

Metallogeny of the Cornwallis Zn-Pb district, Arctic Canada

by

Jordan Mathieu

A thesis submitted in partial fulfillment
of the requirements for the degree of
Doctor of Philosophy (PhD) in Geology

The Faculty of Graduate Studies
Laurentian University
Sudbury, Ontario, Canada

© Jordan Mathieu, 2020

THESIS DEFENCE COMMITTEE/COMITÉ DE SOUTENANCE DE THÈSE
Laurentian University/Université Laurentienne
Faculty of Graduate Studies/Faculté des études supérieures

| | |
|---|---|
| Title of Thesis Titre de la thèse | Metallogeny of the Cornwallis Zn-Pb district, Arctic Canada |
| Name of Candidate Nom du candidat | Mathieu, Jordan Paul |
| Degree Diplôme | Doctor of Philosophy |
| Department/Program Département/Programme | Date of Defence October 22, 2020 Date de la soutenance, |
| Mineral Deposits and Precambrian Geology | |

APPROVED/APPROUVÉ

Thesis Examiners/Examineurs de thèse:

Dr. Elizabeth C. Turner
(Co-Supervisor/Co-directrice de thèse)

Dr. Daniel J. Kontak
(Co-Supervisor/Co-directeur de thèse)

Dr. Iain Samson
(Committee member/Membre du comité)

Dr. Kevin Shelton
(External Examiner/Examineur externe)

Dr. Ramesh Subramanian
(Internal Examiner/Examineur interne)

Approved for the Faculty of Graduate Studies
Approuvé pour la Faculté des études supérieures
Dr. Lace Marie Brogden
Madame Lace Marie Brogden
Acting Dean, Faculty of Graduate Studies
Doyen intérimaire, Faculté des études supérieures

ACCESSIBILITY CLAUSE AND PERMISSION TO USE

I, **Jordan Paul Mathieu**, hereby grant to Laurentian University and/or its agents the non-exclusive license to archive and make accessible my thesis, dissertation, or project report in whole or in part in all forms of media, now or for the duration of my copyright ownership. I retain all other ownership rights to the copyright of the thesis, dissertation or project report. I also reserve the right to use in future works (such as articles or books) all or part of this thesis, dissertation, or project report. I further agree that permission for copying of this thesis in any manner, in whole or in part, for scholarly purposes may be granted by the professor or professors who supervised my thesis work or, in their absence, by the Head of the Department in which my thesis work was done. It is understood that any copying or publication or use of this thesis or parts thereof for financial gain shall not be allowed without my written permission. It is also understood that this copy is being made available in this form by the authority of the copyright owner solely for the purpose of private study and research and may not be copied or reproduced except as permitted by the copyright laws without written authority from the copyright owner.

Abstract

The Cornwallis Zn-Pb district in the Canadian Arctic archipelago contains numerous carbonate-hosted mineralised showings, including the past-producing Polaris Zn-Pb mine on Little Cornwallis Island. The showings' mineralogy is primarily Zn-Pb, with anomalous Cu showings. The volume and geographic/stratigraphic positions of mineralisation are variable, with the majority being hosted by Middle Ordovician Thumb Mountain Formation limestone/dolostone adjacent to extensional faults. Multiple in situ micro-analytical techniques were used on samples from throughout the district to determine the origin, character, flow path, and age of the mineralizing fluid(s) responsible for the showings in the district, and to re-evaluate models of the Polaris deposit.

Geochemical (fluid inclusion microthermometry, trace and rare earth elements, oxygen isotopes) results indicate that a single, regional fluid was involved in mineralisation at all of the showings. Sulphur isotopes indicate that pre-mineralisation sulphur accumulations at individual showings affected early mineralisation $\delta^{34}\text{S}$ values until thermochemical sulphate reduction (TSR) of the regional fluid became the dominant sulphur supply, and that varying degrees of TSR completion resulted in showing-specific $\delta^{34}\text{S}$ values, rather than a uniform regional value. The main control on the volume of mineralisation was the amount of fluid flux that could be accommodated by the showing, with Polaris being much larger than the rest because of its tectonic location, which allowed for copious amounts of mineralising fluid to interact with host rocks.

The Storm copper showing on Somerset Island indicates that Cu showings in the Zn-Pb district are related to the regional fluids of the Zn-Pb showings, but local strata affected the mineralogy. The geochemical signatures of the paragenetic stages indicate that pre-ore fluids were related to the regional Zn-Pb fluid, whereas the main-ore fluid is related to a fluid that displaced the regional Zn-Pb-mineralising fluid during ongoing orogenesis. An underlying Proterozoic redbed contains a record of diagenetic sequences and fluids that is similar to those responsible for the Storm copper showing, indicating that the geographically limited redbed was probably responsible for the anomalous Cu-rich showing in the district.

Keywords: Cornwallis district, Arctic Canada, Polaris, geochemistry, REE, oxygen isotope, sulphur isotope, fluid inclusion microthermometry, diagenesis, redbed copper, carbonate-hosted base-metal deposit.

Co-Authorship Statement

Several co-authors, contributed to the work presented herein. The co-authors provided scientific guidance, and some laboratory analyses. The project was conceived by Drs. Turner and Kontak.

Chapter 2 is co-authored by Drs. Turner, Kontak, and Fayek. Archived samples from Dr. Turner were collected during fieldwork from 2000 to 2002, with supplemental samples collected by the candidate and provided by the GSC. Sample selection and analyses were completed by the candidate. The first draft and initial interpretations were completed by the candidate. The co-authors edited subsequent drafts.

Chapter 3 is co-authored by Drs. Turner, Kontak, Fayek, and Mathur. Chapter 3 is based on samples collected by the candidate as well as supplemental samples provided by Dr. Turner, Aston Bay Holdings, and Apex Geoscience. Sample preparation was done by the candidate. Copper isotope analyses were run by Dr. Mathur who also wrote the method sub-section regarding copper isotope analysis. The first draft and interpretations were completed, with Drs. Turner and Kontak editing subsequent drafts and suggested scientific follow-up topics. Drs. Fayek and Mathur edited final drafts.

Chapter 4 is co-authored by Dr. Turner. Chapter 4 is based on samples collected by the candidate and Dr. Turner during fieldwork in 2016. The candidate completed the analytical work and wrote the first draft of Chapter 4; subsequent drafts were edited by Dr. Turner.

Acknowledgments

Dr. Turner is greatly thanked for providing the opportunity to work on this project, allowing me to teach her paleobiology class, and sending me to many interesting places for conferences and fieldwork. Drs. Turner and Kontak are thanked for putting up with me for the past many years. Funding of this project was provided by a Natural Sciences and Engineering Research Council Discovery and Accelerator grants awarded to Dr. Turner and the Goodman School of Mines Bursary grant to JM. Logistical and field support was provided by Polar Continental Shelf Project and Aston Bay Holdings. R. Sharpe is thanked for running the SIMS analyses and making sure the analyses were completed on time. Drs. Petrus and Leybourne are thanked for running the LA ICP-MS and teaching me how to use it. Drs. Leybourne and Macdonald are thanked for their scientific discussions. R. Poulin is thanked for working so hard to get the cathodoluminescence microscope up and running for me to use. M. Langa and Dr. Hahn are thanked for always being willing to humour me in the office. T. Rzezniczak, C. Campeau, and D. Wong are appreciated for making sure we always had sporting and cultural events to attend to. M. Loney is thanked for providing the use of his camp for much-needed rest and relaxation. My mom and sister are thanked for looking after my dogs while away in the field or at conferences. Thank God my computer lasted throughout the whole processes, even though it crashed several times near the end. My niece and nephews are thanked for using up my free time with playtime; re-kindling my imagination, giving me a better excuse to watch cartoons, and helping me keep proper perspectives on time and what is important. My dogs are greatly thanked for years of their patience and tenacity.

Table of Contents

| | |
|--|------|
| Abstract..... | iii |
| Co-Authorship Statement..... | v |
| Acknowledgments..... | vi |
| Table of Contents..... | vii |
| List of Tables..... | xii |
| List of Figures..... | xiii |
| Chapter 1..... | 1 |
| 1 Introduction to thesis..... | 1 |
| 1.1 Statement of problem..... | 1 |
| 1.2 Research questions..... | 2 |
| 1.3 Regional geology..... | 4 |
| 1.4 Methods..... | 6 |
| 1.5 Structure of thesis..... | 6 |
| 1.6 Statement of responsibilities..... | 8 |
| 1.7 Statement of original contributions..... | 9 |
| 1.8 References..... | 9 |
| Chapter 2..... | 14 |
| 2 Composition, origin, and history of the mineralising, regional fluid responsible for Zn+Pb showings in the Cornwallis Zn-Pb District, Arctic Canada..... | 14 |
| 2.1 Introduction..... | 16 |
| 2.2 Geological history..... | 17 |
| 2.2.1 Tectonic framework..... | 17 |
| 2.2.2 Regional Geology..... | 20 |
| 2.2.3 Showing locations and local geology..... | 22 |

| | | |
|-------|--|----|
| 2.2.4 | Previous work on Polaris and showings | 27 |
| 2.3 | Materials and methods | 30 |
| 2.3.1 | Samples | 30 |
| 2.3.2 | Petrography and SEM | 30 |
| 2.3.3 | Fluid inclusion microthermometry | 31 |
| 2.3.4 | Evaporate mound SEM-EDS | 32 |
| 2.3.5 | Secondary ion mass spectrometry (SIMS)..... | 33 |
| 2.3.6 | LA ICP-MS | 34 |
| 2.4 | Results..... | 34 |
| 2.4.1 | Mineral paragenesis | 34 |
| 2.4.2 | Fluid inclusions | 37 |
| 2.4.3 | SIMS analysis of stable isotopes (O, S)..... | 39 |
| 2.4.4 | Trace element and REE data..... | 42 |
| 2.4.5 | Sulphide trace element data | 46 |
| 2.5 | Interpretation..... | 47 |
| 2.5.1 | Mineral characteristics | 47 |
| 2.5.2 | Fluid inclusions..... | 48 |
| 2.5.3 | Isotopes | 50 |
| 2.5.4 | REE+Y and trace element data..... | 52 |
| 2.5.5 | Sphalerite trace-element chemistry..... | 54 |
| 2.6 | Discussion | 57 |
| 2.6.1 | Fluid origins and metal source(s)..... | 57 |
| 2.6.2 | Sulphur source and reduction mechanism | 61 |
| 2.6.3 | Reconstruction of mineralising system..... | 67 |
| 2.6.4 | Timing of mineralisation..... | 72 |

| | | |
|-----------------|--|-----|
| 2.6.5 | Fluid-driving mechanism | 72 |
| 2.6.6 | Storm copper relationship | 75 |
| 2.6.7 | Interpreted controls on Polaris mineralisation and implications for regional sulphide formation | 76 |
| 2.6.8 | Implication for exploration | 77 |
| 2.7 | Conclusions | 78 |
| 2.8 | Acknowledgements | 79 |
| 2.9 | References | 80 |
| Chapter 3 | | 147 |
| 3 | Atypical Cu mineralisation in the Cornwallis carbonate-hosted Zn district: Storm copper deposit, Arctic Canada | 147 |
| 3.1 | Introduction | 149 |
| 3.2 | Geological history | 151 |
| 3.2.1 | Tectonic framework | 151 |
| 3.2.2 | Regional Geology | 153 |
| 3.2.3 | Local geology of the Storm showing | 154 |
| 3.3 | Materials and methods | 156 |
| 3.3.1 | Sample locations | 156 |
| 3.3.2 | Petrography and SEM | 157 |
| 3.3.3 | Fluid inclusion microthermometry | 157 |
| 3.3.4 | Evaporate mound SEM-EDS | 158 |
| 3.3.5 | Secondary ion mass spectrometry (SIMS) | 159 |
| 3.3.6 | Copper isotopes | 160 |
| 3.3.7 | LA ICP-MS | 160 |
| 3.4 | Results | 161 |
| 3.4.1 | Mineral paragenesis | 161 |

| | | |
|----------------|---|-----|
| 3.4.2 | Fluid inclusions | 166 |
| 3.4.3 | Stable Isotopes | 169 |
| 3.4.4 | Trace and REE Data..... | 171 |
| 3.4.5 | Sulphide trace element geochemistry | 173 |
| 3.5 | Discussion..... | 175 |
| 3.5.1 | Mineral paragenesis at Storm..... | 175 |
| 3.5.2 | Textures and chemistry of Cu phases, with implications for mineralising conditions..... | 176 |
| 3.5.3 | Implications of sulphide trace element data..... | 181 |
| 3.5.4 | Fluid origin and history..... | 183 |
| 3.5.5 | Fluid movement inferred from zonation | 195 |
| 3.5.6 | Timing of mineralisation and fluid-driving mechanism | 196 |
| 3.5.7 | Mineralisation process | 197 |
| 3.6 | Conclusions..... | 202 |
| 3.7 | Acknowledgements..... | 202 |
| 3.8 | References..... | 203 |
| Chapter 4..... | | 256 |
| 4 | Diagenetic evaluation of a possible red-bed source for anomalous Cu in the Paleozoic-carbonate-hosted Cornwallis Zn-Pb district, NU | 256 |
| 4.1 | INTRODUCTION | 257 |
| 4.2 | GEOLOGICAL BACKGROUND..... | 260 |
| 4.3 | MATERIALS and METHODS..... | 264 |
| 4.4 | RESULTS | 266 |
| 4.4.1 | Hand Samples | 266 |
| 4.4.2 | Thin sections | 266 |
| 4.4.3 | Framework grains | 267 |

| | | |
|-----------|---|-----|
| 4.4.4 | Cement | 268 |
| 4.4.5 | Phyllosilicates | 270 |
| 4.4.6 | Porosity | 272 |
| 4.4.7 | Oxygen isotopes..... | 272 |
| 4.5 | INTERPRETATION..... | 272 |
| 4.5.1 | Sandstone composition and fabric | 272 |
| 4.5.2 | Fe-oxide coatings:..... | 273 |
| 4.5.3 | Alteration: | 275 |
| 4.5.4 | Bleaching: | 278 |
| 4.5.5 | Quartz cement and its $\delta^{18}\text{O}$ values..... | 280 |
| 4.6 | DISCUSSION..... | 281 |
| 4.6.1 | Burial history and reddening of the Aston Formation sandstone | 282 |
| 4.6.2 | Timing and origin of quartz cement and its effect on porosity..... | 286 |
| 4.6.3 | Bleaching | 289 |
| 4.6.4 | Aston Formation as an aquifer or aquitard | 291 |
| 4.6.5 | Relationship to Storm mineralising fluids | 292 |
| 4.7 | Conclusions..... | 293 |
| 4.8 | Acknowledgements..... | 294 |
| 4.9 | References..... | 295 |
| Chapter 5 | | 338 |
| 5 | Concluding Statements | 338 |
| 5.1 | Conclusions..... | 338 |
| 5.2 | Future work..... | 340 |
| 5.3 | References..... | 341 |

List of Tables

| | |
|---|-----|
| Table 2-1: Microthermometry results | 134 |
| Table 2-2: SIMS isotope results..... | 136 |
| Table 2-3: REE+Y values of carbonate gangue minerals..... | 143 |
| Table 2-4: Trace element composition of sphalerite..... | 146 |
| Table 3-1: Microthermometric data for Storm..... | 250 |
| Table 3-2: Stable isotope data (SIMS) for Storm sulphides and carbonates | 251 |
| Table 3-3: Copper isotope measurements from Cu minerals from 2750N, 3500N, and 4100N, at different depths. | 253 |
| Table 3-4: Summary of averaged geochemical data for different mineralisation stages..... | 255 |
| Table 4-1: Sample list with associated locations (shown on Figure 6) and colour..... | 337 |

List of Figures

| | |
|---|-----|
| Figure 2-1: Study area..... | 96 |
| Figure 2-2: Paleogeography map of Franklinian Basin | 98 |
| Figure 2-3: Stratigraphic correlation..... | 100 |
| Figure 2-4: Geological map of Little Cornwallis and Truro islands..... | 101 |
| Figure 2-5: Geological map of Bathurst Island..... | 102 |
| Figure 2-6: Geological map of Cornwallis Island..... | 104 |
| Figure 2-7: Geological map of Grinnell Peninsula, Devon Island..... | 105 |
| Figure 2-8: Geological map of Somerset Island | 106 |
| Figure 2-9: Ore-stage paragenesis | 108 |
| Figure 2-10: Petrographic mineral textures and paragenetic relationships..... | 110 |
| Figure 2-11: Representative paragenetic diagram | 112 |
| Figure 2-12: Fluid inclusion photomicrographs | 114 |
| Figure 2-13: Evaporate mound images and composition | 115 |
| Figure 2-14: Dolomite SIMS oxygen isotope results | 117 |
| Figure 2-15: Calcite SIMS oxygen isotope results | 118 |
| Figure 2-16: SIMS sulphur isotope values..... | 119 |
| Figure 2-17: PAAS-normalised REE+Y values of carbonate gangue minerals | 121 |
| Figure 2-18: Dolomite trace element values | 123 |
| Figure 2-19: Anomaly discrimination plot | 124 |

| | |
|--|-----|
| Figure 2-20: Sphalerite trace element composition | 126 |
| Figure 2-21: Laser traverse across sphalerite..... | 129 |
| Figure 2-22: Sulphur isotope fractionation curves..... | 130 |
| Figure 2-23: Interpretive diagram of mineralisation in the Cornwallis district | 133 |
| Figure 3-1: Study location | 223 |
| Figure 3-2: Geological map of Somerset Island | 224 |
| Figure 3-3: Simplified stratigraphy..... | 225 |
| Figure 3-4: Representative Storm copper core photographs..... | 229 |
| Figure 3-5: Simplified paragenetic diagram | 231 |
| Figure 3-6: Storm mineralogy..... | 233 |
| Figure 3-7: Storm mineral textures | 235 |
| Figure 3-8: Storm Cu-sulphide composition..... | 237 |
| Figure 3-9: Storm fluid inclusion photomicrographs..... | 238 |
| Figure 3-10: Evaporate mound images and composition | 239 |
| Figure 3-11: Oxygen isotope diagram | 240 |
| Figure 3-12: PAAS-normalised REE+Y diagram of carbonate gangue minerals | 241 |
| Figure 3-13: Anomaly discrimination diagram..... | 242 |
| Figure 3-14: Trace element composition of carbonate gangue minerals | 243 |
| Figure 3-15: Sulphide trace element composition | 245 |
| Figure 3-16: Water-rock ratio diagram | 246 |

| | |
|--|-----|
| Figure 3-17: Mineralising fluid flow diagram for Storm..... | 247 |
| Figure 3-18: Mineralisation model for Storm..... | 248 |
| Figure 4-1: Study area..... | 314 |
| Figure 4-2: Geological map of Somerset Island | 315 |
| Figure 4-3: Typical exposure of the Aston Formation..... | 317 |
| Figure 4-4: Simplified stratigraphy on Somerset Island | 319 |
| Figure 4-5: Hunting Formation features | 320 |
| Figure 4-6: Simplified local geology of Hunting River, Somerset Island | 322 |
| Figure 4-7: Representative samples of Aston Formation | 323 |
| Figure 4-8: Aston Formation grain contacts | 325 |
| Figure 4-9: K-feldspar diagenetic features | 327 |
| Figure 4-10: Aston Formation opaque grains | 328 |
| Figure 4-11: Aston Formation hematite cement | 329 |
| Figure 4-12: Aston Formation quartz cement..... | 330 |
| Figure 4-13: Aston Formation phyllosilicates | 331 |
| Figure 4-14: Aston Formation void characteristics | 333 |
| Figure 4-15: Aston Formation quartz SIMS oxygen isotope values..... | 334 |
| Figure 4-16: Paragenesis of Aston Formation | 335 |

Chapter 1

1 Introduction to thesis

1.1 Statement of problem

This thesis documents the fluid history in the Cornwallis district in Canada's Arctic archipelago. The Cornwallis district is an area that is 450 km long and 130 km wide and contains the past-producing Polaris deposit (20 MT at 17% Zn+Pb) as well as numerous (>80) base-metal showings (Dewing et al., 2007). A logical assumption that is made with regards to ore districts is that surrounding showings are probably related to the main deposit; however, very little academic attention is allotted to these mineralised showings. By studying the showings in the same detail as the large ore deposit, it would confirm or reject the assumptions typically made and provide explanations regarding the location and volume differences among showings, which are only speculative based on the assumption of related fluids. This study aims to test this assumption through a detailed study of numerous showings throughout the Cornwallis district to determine the genetic relationship among them and the Polaris deposit.

The Polaris deposit was mined from 1982 to 2002 and has undergone several studies in an attempt to explain its ore genesis (Kerr, 1977; Randell, 1994; Randell and Anderson, 1996; Randell et al., 1996; Savard et al., 2000; Reid et al., 2013a,b). Early studies and exploration focused on karst-fill controls (Kerr, 1977), which were subsequently discounted (Randell, 1994; Randell and Anderson, 1996), whereas later studies developed two competing models: fluid mixing (Savard et al., 2000) and in-situ reduction of a single fluid (Randell and Anderson, 1996; Reid et al., 2013a,b). This study attempts to provide a mineralisation model that satisfies the

Polaris deposit as well as the showings. Some showings have received limited study (e.g., Rose, 1999; Turner, 2001; Mitchell et al., 2004; Jober et al., 2007).

Although mineralisation in the Cornwallis district is primarily Zn-Pb, there are a few anomalous Cu showings (Dewing et al., 2007). Copper mineralisation within a Zn-Pb district is not unique to the Cornwallis district, and has been noted in the Viburnum Trend (Cavender et al., 2016).

This study aims to determine if the large Storm Cu showing (Somerset Island) is related to the Zn+Pb mineralisation in the rest of the district.

1.2 Research questions

- *What was the mineralising fluid(s) composition within the Cornwallis Zn-Pb district and what was the mechanism for sulphide precipitation?*

In their summary of sedimentary-rock-hosted Zn-Pb deposits, Leach et al. (2005) showed that the fluids commonly associated with carbonate-rock-hosted Zn-Pb (i.e., MVTs) are high-salinity, low-temperature brines. These brines either carry dissolved metals and sulphate in the same fluid to be reduced at the site of mineralisation, or separately in different fluids to be mixed on site.

The fluid characteristics and histories for showings throughout the district will be determined by using a suite of in situ micro-analytical techniques. This information will then be used to determine the mineralisation mechanism(s) of the different showings.

What was the composition of the fluid(s) of the Storm copper deposit in the district and how does it relate to more regional fluid(s)?

Anomalous copper showings are present in the Cornwallis Zn-Pb district, most notably is the Storm copper deposit. It is questioned whether the mineralisation at Storm copper is related to the Zn-Pb mineralisation in the district. A detailed in-situ micro-analytical study of the sulphides

and carbonate gangue minerals at Storm copper will characterise the fluid(s) and histories involved. The characteristics of the mineralising fluids at Storm copper will then be compared to the fluid(s) associated with the Zn-Pb mineralised showings throughout the district, to determine how they relate.

- *What was the source of copper for the Storm copper deposit?*

Sedimentary-rock-hosted base-metal deposits obtain their metals from source rocks during fluid flow (Leach et al., 2005; Brown et al., 2005; Hitzman et al., 2005). In a Zn-Pb-dominated ore district, however, what produces anomalous Cu showings? By doing a paragenetic study of a probable Cu source for the Storm copper deposit, it will be determined if the Storm copper mineralising fluid interacted with this source rock. Local Cu enrichments may then be explained by local geology in a district.

- *What are the implications of ore district controls and intra-district relationships?*

Showings within ore districts are assumed to be related to one another as well as to the large ore deposit. A detailed analysis of the fluid(s) responsible for the showings in the district will yield information regarding how they are (or are not) related to one another and what controls were in place to dictate the differences in showing composition and/or size.

The results of this study will also aid in the determination of the mechanism of fluid flow within the district. The favourable fluid-driving mechanism related to carbonate-rock-hosted Zn-Pb deposits is the topographically driven model (Garven and Freeze, 1984), based on the majority of these types of deposits being associated with orogenic events (Leach et al., 2005). Other main fluid-driving mechanisms include density-driven and compaction-driven. The age of mineralisation for the Polaris deposit may be related to two major tectonic events: the Ellesmerian orogeny and the opening of the Sverdrup Basin. The results of this study will

elucidate which mode(s) of fluid migration were in place during the mineralisation event(s) in the district.

1.3 Regional geology

The Cornwallis district is composed of the Paleozoic Arctic platform strata and the Boothia Uplift (Trettin, 1991). Strata were deposited in the Franklinian basin, which was divided into a deep-water basin and a shelf, both of which overly a passive margin, with the exception of the southern shelf being deposited on basement rocks of the craton. Proterozoic strata, exposed only on Somerset Island, were deposited in a rift basin associated with a positive relief structure (Tuke et al., 1966; Long and Turner, 2012), which would later influence the Paleozoic Boothia Uplift structure (Okulitch, 1991).

The Franklinian shelf margin was relatively stable from the Cambrian to the Silurian, when far-field, west-directed compressive forces from the Caledonian orogeny (closure of the Iapetus Ocean) caused thrusts and uplift along basement structures, resulting in the Boothia Uplift. This positive relief feature reached from the Boothia Peninsula on the mainland to the Grinnell Peninsula on Devon Island by the Early Devonian. The uplift caused an unconformity and produced local aprons of shed material along the flanks of the uplift (Miall, 1970; Miall and Gibling, 1978). Continued marine sedimentation occurred until the Late Devonian when compressive forces from the present-day north caused the Ellesmerian orogeny, a south-migrating, east-west-trending deformation front. East-west-trending fold belts affected strata as far south as the Parry Islands, but the clastic wedges associated with the orogeny covered most of the Arctic islands (Embry, 1991), reaching a thickness of at least 6 km, and possibly up to 9 km on Banks Island (Dewing and Obermajer, 2009). The Boothia Uplift acted as a buttress

against the southward-directed forces of the orogeny, resulting in interference folds and reactivated Boothia-aged faults (Kerr, 1977).

Following the Ellesmerian orogeny, there were two tectonic events that could have affected the Cornwallis district – development of the Carboniferous-Cretaceous Sverdrup basin (Davies and Nassichuk, 1991) and the Cretaceous-Oligocene Eurekan orogeny (Piepjohn et al., 2016). Rifting to the northwest of the Cornwallis district developed the Sverdrup Basin that extended to northern Grinnell Peninsula, and included salt tectonics and magmatism. Counterclockwise rotation of Greenland with respect to Laurentia caused the Eurekan orogeny in the northern Arctic islands and extension and development of Baffin Bay in the south. Effects of this orogeny on the Cornwallis district are, however, cryptic.

Strata of the Franklinian Basin are predominantly marine carbonate rocks with interbedded clastic rocks (Dewing and Nowlan, 2004). Fluvial and deltaic clastic sediments were deposited along the flanks of the Boothia Uplift (Miall, 1970; Miall and Gibling, 1978). Importantly, the Boothia Uplift was eroded to expose Proterozoic strata that were redeposited in these aprons. Marine carbonate rocks of the Blue Fiord indicate the return to predominantly marine carbonate sedimentation. The foreland basin of the Ellesmerian orogeny was composed entirely of clastic sediments (Embry, 1991).

Mineralisation in the district occurs throughout the Paleozoic strata, as high stratigraphically as strata related to the Ellesmerian orogeny, although it is predominantly hosted in the Middle Ordovician Thumb Mountain Formation (Dewing et al., 2007).

1.4 Methods

Polished thin sections (30 μm thick) were analysed petrographically on a standard petrographic microscope, with scanning electron microscopy (SEM), and on a binocular microscope coupled with a cold cathodoluminescence stage. Fluid inclusion petrography and microthermometry were performed on doubly polished sections (100 μm thick). Major, minor, and trace elements were analysed using in situ laser ablation inductively coupled plasma mass spectrometry (LA ICP-MS) on polished thin sections. Stable isotopes of S and O were analysed in situ with secondary ion mass spectrometry (SIMS) on polished thin sections. Copper isotope analysis was undertaken on powder microdrilled from hand samples and analysed with solution ICP-MS. Each analytical method is outlined in more detail in chapters 2 through 4.

1.5 Structure of thesis

This dissertation is presented in five chapters, with chapters 2-4 written as manuscripts for publication in refereed scientific journals. There is some overlap in the introduction and geological setting of each chapter due to the independent nature of the manuscripts.

Chapter 2 is written as a manuscript entitled “Composition, origin, and history of the mineralising, regional fluid responsible for Zn+Pb showings in the Cornwallis Zn-Pb District, Arctic Canada” This paper presents a multi-analytical in situ approach to determine fluid origin and history for the Cornwallis Zn-Pb district, with emphasis on the relationships among showings. The paper proposes that mineralisation in the Cornwallis district was the result of a regionally uniform fluid that interacted with independent sulphur sources, and experienced various degrees of thermochemical sulphate reduction of the regional fluid, thereby having a large variation in S isotopic composition, whereas maintaining relatively consistent fluid

characteristics. The presence of such a regional fluid favours a topographically driven fluid flow event that was the result of the Ellesmerian orogeny. Showings with major differences are most probably due to local geological differences. The volume of mineralisation at a site was influenced by the presence of a pre-existing sulphur source, the ability to reduce sulphate, and the capability of high fluid flux.

Chapter 3 is a paper published in *Ore Geology Reviews* entitled “Atypical Cu mineralisation in the Cornwallis carbonate-hosted Zn district: Storm copper deposit, Arctic Canada”. Chapter 3 includes a detailed geochemical description of the fluid composition, origin, and history of a copper deposit in the Cornwallis district. Chapter 3 indicates that the main mineralising fluid at Storm copper post-dates the main regional fluid responsible for regional mineralisation in the district, but was likely related to the subsequent meteoric fluid that pervaded the district. Copper mineralisation was facilitated by local copper sources.

Chapter 4 is written as a manuscript entitled “Diagenetic evaluation of a possible redbed source for anomalous Cu in the Paleozoic-hosted Cornwallis Zn district, NU” (formatted for submission to the *Canadian Journal of Earth Sciences*). Chapter 4 is a paragenetic study of the diagenetic events experienced by the Aston Formation sandstone, a possible copper source, to determine if it was involved with the mineralisation in the atypical Storm copper. Timing of key diagenetic events, especially circulation of oxidized fluids that could have mobilized and transported copper, suggests that the Aston Formation may have been the source for copper for the overlying Storm copper deposit.

1.6 Statement of responsibilities

Samples were assembled from a variety of sources. Sulphide-gangue samples from regional Zn showings represent (1) archived samples from the Polaris mine and nearby showings, (2) samples from Zn-Pb showings throughout the Cornwallis district collected by E.C. Turner during a multi-year mapping program supported by Canada-Nunavut Geoscience Office and Polar Continental Shelf Project, and (3) samples from Zn showings on Somerset Island collected by the candidate. Samples of Cu-mineralised material from the Storm deposit were collected by the candidate from core made available by Aston Bay Resources. Samples of Aston Formation sandstone were collected by ECT and the candidate.. All samples collected were cut by the candidate and thin sections were prepared by Willard Desjardins at Laurentian University. Petrography, microthermometry, and SEM-EDS analysis were completed by the candidate at Laurentian University. In situ LA-ICP-MS analysis was completed by the candidate and Dr. Joe Petrus at Laurentian University. LA-ICP-MS data reduction was completed by the candidate. Copper isotope analysis for Chapter 3 was done by Dr. Ryan Mathur at Juniata College, Huntingdon, Pennsylvania. Samples for stable S and O isotopes SIMS analysis were prepared and analysed by the candidate at the University of Manitoba for Chapter 3 and by Ryan Sharpe at the University of Manitoba for Chapters 2 and 4.

The project was designed by Dr. Elizabeth Turner. All initial interpretations of data and the first drafts of chapters 2 to 4 were done by the candidate. Scientific input and edits were provided by co-authors of the respective chapters. Edits for Chapter 3 were provided during the peer-review process by two anonymous reviewers.

1.7 Statement of original contributions

The following points outline the original contributions made by this study:

- Documents the fluid composition for multiple showings throughout the Cornwallis district. Detailed fluid studies have been limited to the Polaris deposit.
- Identifies that showings throughout the Cornwallis district have shared fluid characteristics, indicating a uniform regional fluid. This was previously assumed, but never verified.
- Provides an updated interpretation of the Polaris deposit.
- Adds to current understanding of district-scale processes, such as topographically driven fluid flow.
- Provides the first in-depth study of the Storm copper deposit. Previous work was limited to company reports.
- Provides insight to the occurrence of atypical (Cu) ore deposits within an otherwise uniform (Zn-Pb) ore district.
- Provides the first in-depth diagenetic study of the Aston Formation.
- Provides insight on diagenetic processes and their relationship to mineralising fluid events in order to determine source-rock potential.

1.8 References

Brown. A.C., 2005. Refinements for footwall red-bed diagenesis in the sediment-hosted stratiform copper deposits model. *Economic Geology*, 100, 763-771.

- Cavender, B.D., Shelton, K.L., Schiffbauer, J.D., 2016. An atypical orebody in the Brushy Creek Mine, Viburnum Trend, MVT district, Missouri: Early Cu-(Ni-Co)-Zn-rich ores at the Lamotte sandstone/Bonneterre dolomite contact. *Economic Geology*, 111, 259-269.
- Davies, G.R., Nassichuk, W.W., 1991. Carboniferous and Permian history of the Sverdrup Basin, Arctic Islands, in: Trettin, H.P. (Ed.), *Geology of the Innuitian Orogen and Arctic Platform of Canada and Greenland*, Geological Survey of Canada, *Geology of Canada*, p. 345-368.
- Dewing, K., and Nowlan, G. S., 2004, Correlation chart of Cambrian and Ordovician stratigraphy, Arctic Islands, Nunavut, Canada: Geological Survey of Canada Open File, v. 1837, p. 1.
- Dewing, K., Obermajer, M., 2009. Lower Paleozoic thermal maturity and hydrocarbon potential of the Canadian Arctic Archipelago. *Bulletin of Canadian Petroleum Geology*, 57, 141-166.
- Dewing, K., Sharp, R.J., Turner, E.C., 2007. Synopsis of the Polaris Zn-Pb District, Canadian Arctic Islands, Nunavut, in: Goodfellow, W.D. (Ed.), *Mineral Deposits Division, Special Publication No. 5*, pp. 655-672.
- Embry, A.F., 1991. Middle-Upper Devonian clastic wedge of the Arctic Islands, in: Trettin, H.P. (Ed.), *Geology of the Innuitian Orogen and Arctic Platform of Canada and Greenland*, Geological Survey of Canada, *Geology of Canada*, p. 261-291.
- Garven, G., and Freeze, R. A., 1984, Theoretical analysis of the role of Groundwater flow in the genesis of stratabound ore deposits. 2. Quantitative results: *American Journal of Science*, v. 284, p. 112–1174.
- Hitzman, M.W., Kirkham, R., Broughton, D., Thorson, J., Selley, D., 2005. The sediment hosted stratiform copper ore system. *Economic Geology*, 100, 609-642.
- Jobe, S.-A., Dewing, K., and White, J. C., 2007, Structural geology and Zn-Pb mineral occurrences of northeastern Cornwallis Island: implications for exploration of the Cornwallis Fold Belt, northern Nunavut: *Bulletin of Canadian Petroleum Geology*, v. 55, p. 138–159
- Kerr, J.W., 1977. Cornwallis lead-zinc district: Mississippi Valley-type deposits controlled by stratigraphy and tectonics. *Canadian Journal of Earth Science*, 14, 1402-1426.

- Leach, D. L., Sangster, D. F., Kelley, K. D., Large, R. R., Garven, G., Allen, C. R., Gutzmer, J., and Walters, S., 2005, Sediment-Hosted Lead-Zinc Deposits: A Global Perspective, in One Hundredth Anniversary Volume: Society of Economic Geologists
- Long, D.G.F. and Turner, E.C. 2012: Tectonic, sedimentary and metallogenic re-evaluation of basal strata in the Mesoproterozoic Bylot basins, Nunavut, Canada: are unconformity-type uranium concentrations a realistic expectation?; *Precambrian Research*, v. 214–215, p. 192–209.
- Miall, A.D., 1970. Devonian alluvial fans, Prince of Wales Island, Arctic Canada. *Journal of Sedimentary Petrology*, 40, 556-571.
- Miall, A.D., Gibling, M.R., 1978. The Siluro-Devonian clastic wedge of Somerset Island, Arctic Canada, and some regional paleogeographic implications. *Sedimentary Geology*, 21, 85-127.
- Mitchell, I., Linnen, R.L., Creaser, R.A., 2004. The setting and age of the Bermuda Zn-Pb showing, Grinnell Peninsula, Devon Island: implications for MVT mineralization in the Canadian Arctic. *Exploration Mining Geology*, 13, 109-118.
- Okulitch, A.V., Packard, J.J., Zolnai, A.I., 1991. Late Silurian-Early Devonian deformation of the Boothia Uplift. in: Trettin, H.P. (Ed.), *Geology of the Innuitian Orogen and Arctic Platform of Canada and Greenland*, Geological Survey of Canada, *Geology of Canada*, p. 302-307.
- Piepjohn, K. von Gosen, W., Tessensohn, F., 2016. The Eureka deformation in the Arctic: an outline. *Journal of the Geological Society*, 173, 1007-1024.
- Randell, R.N., Anderson, G.M., 1996. Geology of the Polaris Zn-Pb deposit and surrounding area, Canadian Arctic archipelago. *Society of Economic Geologists Special Publication No. 4*, 307-319.
- Randell, R.N., Héroux, Y., Chagnon, A., Anderson, G.M., 1997. Organic matter and clay minerals at the Polaris Zn-Pb deposit, Canadian Arctic archipelago. *Society of Economic Geologists Special Publication No. 4*, 320-329.

- Reid, S., Dewing, K., Sharp, R., 2013a. Polaris as a guide to northern exploration: Ore textures, paragenesis and the origin of the carbonate-hosted Polaris Zn-Pb mine, Nunavut, Canada. *Ore Geology Reviews*, **51**, 27-42.
- Reid, S., Dewing, K., Sharp, R., 2013. Structural and diagenetic origin of breccias in the carbonate-hosted Polaris Zn-Pb deposit, Nunavut, Canada. *Ore Geology Reviews*, **55**, 110-124.
- Rose, S.R.A., 1999. Sedimentology and diagenesis of the Lower Blue Fiord Formation Carbonates in a prospective Mississippi Valley-type (Pb-Zn) setting. Unpublished M.Sc. thesis, University of Calgary, Calgary, Alberta, Canada, 186 pp.
- Savard, M.M., Chi, G., Sami, T., Williams-Jones, A.E., Leigh, K., 2000. Fluid inclusion and carbon, oxygen, and strontium isotope study of the Polaris Mississippi Valley-type Zn-Pb deposit, Canadian Arctic archipelago: implications for ore genesis. *Mineralium Deposita*, **35**, 495-510.
- Trettin, H.P., 1991. Tectonic Framework. In: Trettin, H.P. (Ed.), *Geology of the Innuitian Orogen and Arctic Platform of Canada and Greenland*. Geological Survey of Canada, *Geology of Canada*, pp. 59–66.
- Tuke, M.F., Dineley, D.L., Rust, B.R., 1966. The basal sedimentary rocks in Somerset Island, N.W.T. *Canadian Journal of Earth Sciences*, **3**: 697–711.
- Turner, E. C., 2001, Investigation of zinc-lead mineralization on eastern Cornwallis Island, Arctic Archipelago, Nunavut: 2001-B2

Chapter 2

2 Composition, origin, and history of the mineralising regional fluid responsible for Zn+Pb showings in the Cornwallis Zn-Pb District, Arctic Canada

Jordan Mathieu^{a,*}, Elizabeth C. Turner^a, Daniel J. Kontak^a, and Mostafa Fayek^b

^aHarquail School of Earth Sciences, Laurentian University, Sudbury, ON P3E 2C6, Canada

^bDepartment of Geological Sciences, University of Manitoba, Winnipeg, MB R3T 2N2, Canada

*jy_mathieu@laurentian.ca

Abstract

The Cornwallis district in Canada's Arctic archipelago contains numerous carbonate-rock-hosted Zn+Pb showings and sparse, anomalous Cu showings in a 450 km x 130 km area. The district is spatially limited to an area of complex but subtle intermittent Paleozoic deformation associated with an episodically active basement high (Boothia uplift) and a major Paleozoic orogenic event (Ellesmerian orogeny). The past-producing Polaris Zn+Pb deposit (20 Mt at 17% Zn+Pb) is in the western part of the district. As in many metallogenic districts, a genetic relationship between the mined deposit and surrounding showings has been assumed but not tested. This study uses an in situ, multi-analytical approach combining optical and SEM petrography, fluid inclusion microthermometry, evaporate mound analysis, LA ICP-MS trace element analysis, and in situ stable isotope analysis on sphalerite and dolomite gangue to characterise the fluid histories of individual showings, regions in the district, and the district as a whole. Mineralisation is not limited to specific strata or to faults, although most showings are hosted by the Thumb Mountain Formation adjacent to faults. Similar T_h values, salinity,

sphalerite chemistry, and $\delta^{18}\text{O}_{\text{dolomite}}$ values are present throughout the district; conversely, $\delta^{34}\text{S}_{\text{sphalerite}}$ values vary throughout the district, but are consistent within each showing. Results indicate that a regional, marine-like fluid dissolved subsurface evaporite minerals and transported metals and sulphate to sites of mineralisation. Differences in main-stage sphalerite sulphur isotope values among different showings indicate a variable degree of thermochemical sulphate reduction at each site. Fluid mixing initially resulted in precipitation of sulphides with lower $\delta^{34}\text{S}$ values, as transported metals encountered pre-existing accumulations of reduced sulphur on site. After the local sulphur pool was exhausted, a change to single-fluid in situ thermochemical reduction of transported sulphate produced a shift to higher $\delta^{34}\text{S}$ values. The mineralised volume of each showing is predominantly a function of local fluid flux and availability of a local reductant. Polaris was a comparatively large sulphide body owing to its location where reductant-rich host strata were under a relatively impermeable cap rock and adjacent to a pre-existing structure that was dilated by Ellesmerian stress, facilitating especially abundant fluid flow during the Ellesmerian orogeny. The partially reduced sulphate from Polaris precipitated a halo of $\delta^{34}\text{S}$ -enriched barite. The consistency of geochemical characteristics throughout the district confirms the genetic relationship between the large deposit and surrounding showings, and indicates a uniform mineralising fluid, topographically mobilised during the Ellesmerian orogeny, was responsible for the main, district-wide mineralisation, after the initial smaller-scale mixing with local fluids.

Keywords: Carbonate-hosted base metal deposit, Arctic Canada, fluid inclusions, stable isotopes, REE geochemistry, Polaris, Cornwallis district, topographically driven fluid flow

2.1 Introduction

The Cornwallis Zn-Pb district in Canada's Arctic archipelago (Fig. 1) has numerous (>80) Zn+Pb showings, including the past-producing Polaris deposit, and spans a 450 km by 130 km area (Dewing et al., 2007). Polaris, a Paleozoic-carbonate-hosted Zn-Pb deposit with a resource of 20 Mt of 17% Zn+Pb, was exploited from 1982 to 2002 (Dewing et al., 2007). A small number of Cu showings are also present in the region, including the Storm carbonate-hosted Cu mineralised system on Somerset Island (Mathieu et al., 2018). District-scale studies of mineralised areas that include research on smaller showings are rare, the work of Field et al. (2018) and Field et al. (2020) on the U.S. mid-continent ore district, Chi et al. (1998) in the Canadian Maritimes, and Wilkinson (2010) in the Irish Orefield being some of the exceptions. Instead, studies generally focus on the large deposits in such districts. The size, fluid(s) responsible, and precipitation mechanism(s) of mineralisation throughout a district are commonly assumed to have resulted from a regional, continuous fluid-flow event (Leach et al., 2005), with different-sized deposits or showings merely assumed to reflect differences in the scales of the fluid flux and ore-forming mechanisms.

The large and richly mineralised Polaris deposit has been the subject of multiple studies (e.g., (Kerr, 1977b; Randell, 1994; Savard et al., 2000; Dewing and Turner, 2003; Turner and Dewing, 2004; Reid et al., 2013a; Reid et al., 2013b), although they are few compared to the research on large carbonate-hosted deposits elsewhere [e.g., Navan (Anderson et al., 1998; Fallick et al., 2001; Wilkinson, 2010; Elliott et al., 2019) and Viburnum (Grundmann, 1977; Roedder, 1977; Leventhal, 1990; Appold and Wenz, 2011; Labotka et al., 2016; Shelton et al., 2020)]. The showings in the Cornwallis district have received limited study (e.g., Turner, 2001; Mitchell et al., 2004; Jober et al., 2007). Limited regional work in the Cornwallis district suggested multiple

possible interpretations for the origin of the mineralisation, including karst-fill (Kerr, 1977), fluid-mixing (Savard et al., 2000), and in situ precipitation resulting from ingress of a single fluid (Reid et al., 2013a; Reid et al., 2013b).

This study revisits the iconic Polaris deposit to examine how its fluid and ore precipitation history relate to the nature and origin of numerous base-metal showings in the surrounding area. Is there some feature present at or in the orebody at Polaris that is absent in the apparently smaller showings, or are they essentially the same? This study addresses the relative importance of fundamental processes in ore deposit studies, and ultimately what differentiates large, rich ore systems from related, but less endowed showings that in many respects appear the same (e.g., Johnson et al., 2009). The work presented here was done using an array of integrated in situ, micro-analytical analyses already tested and applied in comparable settings (Mathieu et al., 2013, 2015; Hahn et al., 2018; Mathieu et al., 2018). Using this approach, this study aims to provide a detailed characterisation of fluid(s) implicated in the less well-mineralised showings across the Cornwallis district, compare them to the large Polaris deposit, and evaluate the factors controlling size and location of sulphide accumulations in the district.

2.2 Geological history

2.2.1 Tectonic framework

The Cornwallis district is composed of the Arctic ‘platform’ and the Boothia uplift (Fig. 2). The Arctic platform, consisting of nearly flat-lying Paleozoic strata underlain by Precambrian basement, extends from the continental mainland in the south to east-trending fold belts of the Ellesmerian orogen, and was deposited in the Franklinian basin (i.e., Laurentia's northern passive margin and nearby epicontinental areas; Fig. 2A; Trettin, 1991a). The Franklinian basin is

divided into a predominantly shallow-marine shelf (Franklinian shelf) in the south and a deep-water zone in the north(west) (Trettin et al., 1991). The shelf-break was abrupt, with no preserved slope, and was relatively stable from the Middle Cambrian to Middle-Late Ordovician, when it spanned ~2500 km from northeastern Greenland to at least northwestern Melville Island (Fig. 2A; Trettin, 1991b; Trettin et al., 1991). The shelf-margin migrated southward to Devon Island, Cornwallis Island, and south of Bathurst Island through the Ordovician – Silurian, as a result of transgression and subsidence (Fig. 2B) (Trettin et al., 1991).

Underlying the Arctic platform is Archean – Paleoproterozoic crystalline and (minor) Mesoproterozoic sedimentary rock, exposed on Somerset and Prince of Wales islands, in the south and on eastern Devon and southern Ellesmere islands (Stewart and Kerr, 1984; Frisch and Trettin, 1991; Trettin et al., 1991; Harrison et al., 2015; Harrison et al., 2016). Paleocurrents of Mesoproterozoic rift-fill strata on Somerset and Prince of Wales islands (Aston Formation) indicate that during their accumulation, a local paleotopographic feature (the Boothia uplift) acted as a sediment source (Dixon et al., 1971).

The Cornwallis district experienced multiple tectonic events both during and after Paleozoic deposition of Arctic platform strata. Far-field, west-directed compression of the Late Silurian Caledonian orogeny (in northern Laurentia developed in eastern Greenland; equivalent to the Acadian orogeny in eastern Laurentia) resulted in the reappearance of the north-trending Boothia uplift (Fig. 2B) (Miall, 1986; Oliver, 2001; Morris et al., 2005), here divided into four regions. The western region, at the western margin of the uplift, consists of a ~35-km-wide belt of conspicuous north-trending thrust or reverse faults and narrow, north-trending folds on Bathurst Island (Harrison and de Freitas, 1999) and Prince of Wales Island (Mayr et al., 2003) (no Zn mineralisation is known from the latter). A long, north-trending axial area on top of the uplifted

Boothia block is subdivided into north (Grinnell Peninsula) and central (Cornwallis Island) regions containing subtler, generally north-trending Caledonian folds and approximately north-trending thrust and reverse faults (Thorsteinsson, 1986; Mayr et al., 1998). The southeastern region (Somerset Island) is where the eastern margin of the uplift is exposed, consisting of basement rock adjacent to a ~10-km-wide north- to northwest-trending zone of thrusts and folds in lower Paleozoic strata, which are overlain by mid-Paleozoic material shed as debris wedges from the uplift margins (Stewart and Kerr, 1984). The interior part of the uplift (the axial zone) in the south is represented by basement rock, where no Paleozoic strata or Zn showings remain; the basement is not exposed north of Somerset Island. The eastern flank of the uplift north of Somerset Island is unknown; it is assumed to be under water east of Cornwallis Island. Paleozoic activity of the uplift initially affected the southern part of the district, leaving areas north of Somerset Island submerged (Fig. 2B); continued uplift into the Early Devonian affected more northern areas including the Grinnell Peninsula (Fig. 2C) (Thorsteinsson, 1980; Okulitch et al., 1991). The full length of the elongate uplift spanned from the mainland (Boothia Peninsula) to Grinnell Peninsula on Devon Island (Okulitch et al., 1991). The Late Devonian – Early Carboniferous Ellesmerian orogeny (Harrison et al., 1991), a south-directed orogenic event, produced a clastic wedge 6-10 km thick over much of the islands (Fig. 2D) (Embry, 1991; Dewing and Obermajer, 2009), west-trending fold belts in the central high Arctic, and reactivated earlier faults (Harrison et al., 1991; Okulitch, 1991; Trettin, 1991a). Ellesmerian folding is present only north of Barrow Strait, and is tightest around the northern end of the Boothia uplift (Fig. 2D), which acted as a buttress against the Ellesmerian orogenic front, resulting in interference-fold structures (Kerr, 1977a). The interaction of the south-vergent deformation front with the Boothia uplift and its structures resulted in north-trending strike-slip

faults with dextral displacement along the eastern margin of the uplift and sinistral displacement on the western margin (Kerr, 1974; Kerr, 1977a; Harrison et al., 1993; Mayr et al., 1998).

Extension in the area northwest of the Cornwallis district followed the Ellesmerian orogeny, producing the Sverdrup basin in the Early Carboniferous (Fig. 2E; Davies and Nassichuk, 1991). Magmatism, in the form of basaltic flows, has been bracketed stratigraphically to be Late Mississippian-Early Pennsylvanian (Serpukhovian-Bashkirian; Thorsteinsson, 1974). The Cretaceous-Oligocene Eurekan orogeny involved the rotation of Greenland relative to Laurentia, causing compression in the (present-day) north (Ellesmere Island) and extension in the southern islands (Kerr, 1967; Tegner et al., 2011; Piepjohn et al., 2016). Effects of this event in the Cornwallis district are inconspicuous to absent.

2.2.2 Regional Geology

Paleozoic strata of the Cornwallis district were deposited on and near the continental shelf and are composed largely of geographically extensive marine carbonate strata with interlayered siliciclastic rocks (Fig. 2F; Embry, 1991; Trettin et al., 1991; Dewing et al., 2007). Geographically variable characteristics resulted in formation names that are not uniform across the islands (Fig. 3; Dewing and Nowlan, 2004). With the exception of Somerset Island, where both crystalline basement and Mesoproterozoic strata are exposed (Aston and Hunting formations), the oldest exposed unmetamorphosed strata are Cambrian.

Middle Cambrian to Early Ordovician mixed carbonate-clastic formations are, with the exception of Somerset Island, overlain by the Early Ordovician evaporitic Baumann Fiord formation, which contains anhydrite up to 500 m thick (Mayr, 1978). The Baumann Fiord Formation is

overlain by the Early Ordovician carbonate-dominated Eleanor River Formation and its lateral equivalent, the Ship Point Formation.

Middle to Late Ordovician strata consist regionally of the evaporitic Bay Fiord (Middle Ordovician; up to hundreds of m of evaporite strata; Mayr, 1978; Miall and Kerr, 1980; Stewart, 1987; Harrison et al., 1999), and carbonate Thumb Mountain (Middle-Late Ordovician) and Irene Bay (Late Ordovician) formations. The locally organic-rich, fossiliferous carbonate strata of the Thumb Mountain Formation are approximately 300 m thick (Harrison et al., 1999; Jober et al., 2007), but thin to <100 m on Somerset Island where they unconformably overlie the Bay Fiord Formation (Stewart, 1987). Interlayered argillaceous shale and carbonate rocks of the Irene Bay Formation conformably overlie the Thumb Mountain Formation with a relatively consistent thickness of approximately 30-60 m throughout the district.

In the northern part of the Cornwallis district, deep-water Ordovician-Silurian carbonate-shale rocks of the Cape Phillips Formation (Devon, Bathurst, Little Cornwallis, Truro, and Cornwallis islands) and later Devon Island Formation are laterally equivalent to the shallow-marine Allen Bay, Cape Storm, and Douro formations (Devon, Cornwallis, and Somerset islands). The deep-water succession is up to 2200 m thick on Cornwallis Island (Thorsteinsson, 1958), but thins to 115-300 m on Bathurst Island (Harrison et al., 1999).

After the compressional (Caledonian) event that produced the Boothia uplift in the Silurian-Devonian, Franklinian shelf carbonates were overlain by Silurian-Devonian siliciclastic deposits that were shed from the Boothia uplift to produce numerous geographically limited formations. Deep-water continental margin strata of the Eids Formation in the northwestern part of the Cornwallis district grade laterally into slope deposits of the Bathurst and Stuart Bay formations

and alluvial fan/shallow marine Prince Alfred Formation (Morrow and Kerr, 1977). With the exception of Quaternary cover, the Early Devonian Peel Sound Formation is the youngest preserved stratigraphic unit on Somerset Island (Stewart, 1987). In the northern part of the Cornwallis district, the largely dolostone Early to Middle Devonian Blue Fiord Formation is a shallow-marine post-Boothia-uplift unit that overlies a Devonian Boothia-related unconformity (Mayr et al., 1998) and is overlain by Devonian clastic successions resulting from the Ellesmerian orogeny (Embry, 1991). Lastly, the northern part of Grinnell Peninsula exposes a suite of Carboniferous and Permian carbonate and clastic rocks associated with development of the Sverdrup basin.

2.2.3 Showing locations and local geology

Showing locations are grouped into four main areas with respect to major tectonic features of the Boothia uplift and the Ellesmerian orogeny. The western region is located along the western margin of the Boothia uplift and includes eastern Bathurst Island, western Little Cornwallis Island, and Truro Island. The central region is situated over the Boothia uplift and includes Cornwallis Island and western Little Cornwallis Island. The northern region is situated over Boothia uplift on Grinnell Peninsula (Devon Island) and Dundas Island. The southeastern region is on Somerset Island along the eastern margin of the Boothia uplift.

2.2.3.1 West –western Little Cornwallis Island and vicinity (Polaris, Truro, Markham Point, and Harrison showings):

The Polaris deposit (557715/8368561) was hosted in the Thumb Mountain Formation on the western shore of Little Cornwallis Island (Fig. 4). Polaris is located near the western border of the Boothia uplift in a dilatational zone where a major west-vergent thrust fault is segmented and offset by west-trending strike-slip (wrench) faults (Turner and Dewing, 2004; Dewing et al., 2007). The Truro showing (554161/8361675), in the Thumb Mountain Formation on Truro Island, southwest of Little Cornwallis Island, is too poorly exposed to allow its structural setting to be determined. Mineralisation at these locations consists of replacement and void-filling sphalerite, galena, marcasite, pyrite, dolomite, and calcite; Polaris has multiple varieties of sphalerite, including colloform texture.

The Harrison (525618/8379593) and Markham Point (532715/8374138) showings on eastern Bathurst Island (Fig. 5) are hosted by the lower petroliferous dolostone member of the Blue Fiord Formation (Devonian) along the western margin of the Boothia uplift. Mineralisation at Harrison spans a strike length of 1930 m and width of 300 m, in outcrops and nearby talus that parallels extensional reactivated thrust faults (Harrison and de Freitas, 1996). Mineralised breccia matrix contains sphalerite, galena, marcasite, bitumen, calcite, and dolomite (Harrison and de Freitas, 1996). The Bass Point showing on Bathurst Island, hosted by Blue Fiord Formation, shares characteristics with Harrison (Rose, 1999).

2.2.3.2 Central - Cornwallis Island and eastern Little Cornwallis Island (Stuart, Rookery, Snowblind, Bacon, and Eclipse showings):

Samples from Cornwallis Island used in this study come from the Rookery Creek (426764/8364328), Stuart River (453686/8389345), Bacon River (458369/8314811), and Snowblind Bay (483380/8349770) showings (Fig. 6). Snowblind is the easternmost showing in

the region, and may be close to the eastern flank of the Boothia uplift. Mineralisation is associated with (predominantly east-vergent) thrust faults, normal faults, Ellesmerian folds, and a sub-Devonian unconformity (Fig. 6; Jober et al., 2007). Four deformation episodes that involve folding and thrust faults occurred on Cornwallis Island (Jober et al., 2007): north-trending folds and thrusts (D1 and D2) related to development of the Boothia uplift (Late Silurian-Middle Devonian), west-trending folds (D3) related to the Ellesmerian orogeny (Late Devonian – Early Carboniferous), and northwest-trending folds (D4) related to the Eurekan orogeny (Paleogene).

The Rookery Creek showing is hosted in the Thumb Mountain Formation close to the sub-Devonian unconformity (Irene Bay was erosionally removed prior to the Devonian) in a complex area of thrust, normal, and strike-slip faults in the interior of the Boothia uplift (Turner and Dewing, 2002; Turner and Dewing, 2004). Mineralisation, primarily sphalerite with rare galena, Fe-sulphides, and pyrobitumen, is locally associated with solution breccia, and showings typically have rusty weathering (Turner and Dewing, 2002).

Stuart River showings, represented by gossanous areas containing galena, marcasite, and zinc carbonates and oxides, are hosted in upper Thumb Mountain Formation (Turner, 2001; Turner, 2015). Showings are predominantly adjacent to normal faults that trend west-southwest or northwest, within a NNW-trending regional anticline (Turner, 2001; Jober et al., 2007).

Bacon River showings are distributed along the length of a graben that juxtaposes Thumb Mountain Formation (Ordovician) against Allen Bay Formation (Silurian) in the centre of the Boothia uplift, and are characterised by extensive (1.5 km-long) gossans that contain galena and sphalerite associated with bitumen (Turner, 2001; Turner, 2015).

Unlike the other showings studied on Cornwallis Island, the Snowblind Bay showing lacks an obvious structural control and may be facies-controlled; mineralisation follows a trend oblique to strike that may represent a subtle structure (Turner, 2001). Sphalerite is present in small (<1 m) areas of pseudo-breccia, which is in situ brecciation of carbonate rock caused by dissolution by hydrothermal fluids (Reid et al., 2013b), and lines vugs and fractures in the Barlow Inlet Formation, with no galena and sparse Fe-sulphides and dolomite.

Eclipse (579006/8386580), on the east side of Little Cornwallis Island, is hosted in the Thumb Mountain Formation. It is situated in the interior of the Boothia uplift and is associated with dilation of previous thrust and/or strike-slip faults (Dewing and Turner, 2003; Turner and Dewing, 2004). Mineralisation consists of replacement and void-filling sphalerite, galena, marcasite, pyrite, dolomite, and calcite.

2.2.3.3 North - Grinnell Peninsula (Trigger, JG, Scheills, Hornby, and Dundas showings):

The Scheills showing (437236/8470086) is on a peninsula on the south side of Grinnell Peninsula at the contact between Thumb Mountain and Bird Fiord formations (Fig. 7). The location is on the east flank of an anticline where north-trending Ellesmerian folds abut less deformed strata of the Boothia uplift; a fault may be present west of the peninsula (Kerr, 1977b; Mayr et al., 1998). Mineralisation consists of sphalerite, smithsonite, and minor marcasite and galena; sparry calcite and saddle dolomite are also present.

The Dundas showings (445359/8442463; Fig. 7), on Dundas Island, are hosted by the upper Thumb Mountain Formation on the east flank of the same anticline as the Scheills showing near the margin of the Boothia uplift; a fault may be west of the showing beneath the adjacent marine channel (Kerr, 1977b). Replacement, vein- and vug-fill, and breccia-matrix mineralisation is

dominated by sphalerite and smithsonite, with minor galena. Showings have rusty patches in the vicinity.

The Trigger and JG showings (4680/8509812; Fig. 7) are in the interior of the Boothia uplift, hosted by the Bird Fiord Formation (Devonian) near the Mt. Parker Fault zone and Ice Fields thrust fault. Mineralisation fills veins and collapse breccia voids, and consists of dolomite, calcite, sphalerite, galena, and minor marcasite. These characteristics were also documented at the Bermuda showing (Mitchell et al., 2004), which is assumed to be related to the JG showing (Fig. 7).

The Hornby showing (463125/8467733) is hosted in weakly dolomitised Bird Fiord Formation or Allen Bay Formation felsenmeer on southern Grinnell Peninsula in the interior of the Boothia uplift. Mineralisation appears to be controlled by north(west)-trending normal faults, and consists of sphalerite with minor galena, sparry dolomite, and late calcite.

2.2.3.4 Southeast - Somerset Island (Seal and Typhoon):

Samples from Somerset Island are from the Seal (438650/8183550) and Typhoon (473018/8115913) showings (Fig. 8), hosted by Ship Point (Lower Ordovician) and Cape Storm (Silurian) formations, respectively. Seal is at the eastern margin of the Boothia uplift, situated between east- and west-vergent thrust faults (Robinson and Atkinson, 2012), whereas Typhoon is in a north-trending anticline adjacent to north-trending normal faults (Stewart and Kerr, 1984) in the uplift's eastern marginal zone. Mineralisation at both locations is replacement and vein-fill and consists of sphalerite, pyrite, dolomite, and calcite, with an apparent lack of galena. Seal is expressed on surface by patches of rusty areas along strike for kilometres, whereas rusty gossans are absent at Typhoon. The Storm Cu showings are located on northern Somerset Island in

Ordovician-Silurian Allen Bay dolostone and have been assumed to be in some way related to the Cornwallis Zn district, based on fluid characteristics (Mathieu et al., 2018).

2.2.4 Previous work on Polaris and showings

2.2.4.1 Mapping

Early work (Kerr, 1977b) related Polaris mineralisation to collapse breccia in the Thumb Mountain Formation, and concluded that pre-mineralisation karstification was a control on ore deposition. It was later reported, however, that mineralisation was cogenetic with dissolution and that there was no pre-mineralisation karst (Randell, 1994; Randell and Anderson, 1996).

Mapping of Little Cornwallis Island (Dewing and Turner, 2003, Turner and Dewing, 2004) concluded that Polaris is situated on a thrust fault block that has been offset from adjacent fault blocks by strike-slip movement during Caledonian compression and experienced torque by south-directed Ellesmerian orogeny forces. Jober et al. (2007) related mineralisation at Polaris and showings on Cornwallis Island (Stuart Bay and Caribou) to east-trending folds associated with the Late Devonian Ellesmerian orogeny.

2.2.4.2 Age of mineralisation

Several techniques have been employed to determine the age of Polaris mineralisation. Paleomagnetic dating of sphalerite and host dolostone (Symons and Sangster, 1992) indicated that mineralisation took place during the Late Devonian. This timing agrees with a 366 ± 15 Ma Rb-Sr (sphalerite) age from Polaris (Christensen et al., 1995) and a Re-Os (bitumen) age of 374 ± 9 Ma for Polaris (Selby et al., 2005). Bitumen associated with mineralisation yielded a Re-Os age of 357 ± 50 Ma for the Bermuda showing (Mitchell et al., 2004). These ages are compatible with the Late Devonian – Early Carboniferous Ellesmerian orogeny (Harrison et al., 1991), but

not the Late Mississippian – Early Pennsylvanian opening of the Sverdrup Basin (Thorsteinsson, 1974).

2.2.4.3 Polaris mineralisation models

Previous interpretations of Polaris mineralisation fall into two categories: a mixing model or an in situ single-fluid model. The mixing interpretation (Kerr, 1977b; Savard et al., 2000) involves mixing of a metal-bearing fluid with a reduced-sulphur-bearing fluid at the site of precipitation. Conversely, the in situ single-fluid interpretation (Randell, 1994; Reid et al., 2013a; Reid et al., 2013b) involves metals and sulphate transported by a single fluid, with sulphide precipitation related to thermochemical sulphate reduction (TSR) on site.

Fluid inclusion work (Jowett, 1975) produced a temperature range of 52° to 103°C that Kerr (1977b) interpreted as two fluids, sourced from different areas, mixing in karst cavities. Savard et al. (2000), using petrography, fluid inclusions, and stable isotopes (O and S), suggested that a warm metal-bearing fluid was focused via the main fault to the base of the overlying impermeable Irene Bay Formation where it reacted with a fluid containing reduced sulphur formed by BSR that was in thermal equilibrium with the host rocks. Fluid mixing was invoked to explain the range in fluid temperatures (62° to 140°C), the constant salinity, the colloform-textured sphalerite, extensive dissolution, and the sharp boundaries between ore and non-ore rocks. Reduction of sulphate by TSR was dismissed because the reduction rate would have been too low at the recorded temperatures to account for the supersaturation textures (e.g., colloform sphalerite).

The single-fluid model suggested by Randell (1994) and Randell and Anderson (1996) was based on fluid inclusion and stable isotopic (O and S) data. Sulphate reduction was attributed to

TSR because the temperature range (typically above 150°C; Yuan et al., 2017b) is at the upper limit of BSR, and it would have been sufficient to have matured organic matter in the upper Thumb Mountain Formation to produce methane needed for sulphate reduction. This interpretation is similar to that of Reid et al. (2013a), in which evaporite-derived sulphate was transported, along with metals, to the site where it was reduced. In situ sulphur isotopic data showed a change in $\delta^{34}\text{S}$ values, from 2 to 10‰, for early and late sphalerite, respectively. This range in $\delta^{34}\text{S}$ values, in combination with temperatures above BSR (>100°C), was attributed to TSR processes, with the reactions related to sulphide precipitation resulting in the dissolution of host dolostone and development of collapse breccias associated with ore minerals. Excess sulphate was also invoked to explain a late barite halo with higher $\delta^{34}\text{S}$ values around the deposit.

The previous studies on Polaris generally agree that fluid-flow was focused along faults and that the fluid was of low to medium temperature (70° to 140°C; Jowett, 1975; Randell, 1994; Savard et al., 2000). There is also a general consensus that at least one of the fluids was derived from seawater, based on the $\delta^{18}\text{O}$ values of gangue dolomite. Although $\delta^{34}\text{S}$ values are consistent among the studies (Randell, 1994; Savard et al., 2000; Reid et al., 2013a), there is no consensus regarding their interpretation. The main problems are the temperature range and mechanism of sulphur reduction, because the documented temperature range (70° to 140°C) is near both the upper theoretical limit of BSR and the lower theoretical limit of TSR (Machel, 2001), and because the amount of fractionation produced by reduction of seawater sulphate is consistent with each of these reduction processes. Mixing models argue that TSR at these temperatures is incapable of reducing sulphate at a sufficient rate to account for the colloform-textured sphalerite, a feature generally attributed to supersaturation (Roedder, 1968; Pfaff et al., 2011)

and most easily explained by fluid mixing. Bacterial sulphate reduction is the preferred explanation for the large degree of fractionation required to produce the measured $\delta^{34}\text{S}$ values, with the temperature limit of BSR overcome by the reduced-sulphur fluid being the lower-temperature fluid and the higher-temperature fluid the metalliferous one. Conversely, the single-fluid interpretation argues that transported reduced sulphur should be homogeneous and would produce homogeneous $\delta^{34}\text{S}$ values in precipitated sulphides if sulphate reduction were complete. Thermochemical sulphate reduction is preferred in the single-fluid model because of temperatures above the BSR range, heterogeneous $\delta^{34}\text{S}$ values, and the presence of organic matter in the Upper Thumb Mountain Formation that could have acted as a reductant.

In summary, deciphering the factors and controls involved in Polaris ore precipitation is difficult because ambiguous geochemical evidence precludes distinguishing between mixed-fluid and single-fluid interpretation.

2.3 Materials and methods

2.3.1 Samples

Samples that are representative of mineralisation from the different showings in the Cornwallis Zn-Pb district (Figs. 4-8) were collected from surface exposures, except for the Polaris mine samples, which are those used by Savard et al. (2000), and the southern showings, for which samples were collected from both surface and exploration drill-core.

2.3.2 Petrography and SEM

Transmitted and reflected-light petrography was undertaken on ~200 polished thin sections (30 μm thick) using an Olympus BX-51 petrographic microscope equipped with a Q-Imaging digital capture system at Laurentian University, Sudbury, Ontario. A scanning electron microscope

(SEM) was used for capturing images, and energy-dispersive spectroscopy (EDS) was used for mineral analysis. Collectively, these methods were used to establish the mineral paragenesis, examine textures, and determine mineral compositions. The latter work used a JEOL 6400 SEM fitted with an Oxford INCA EDS detector housed in the Micro-Analytical Centre (MAC) at Laurentian University. The operating conditions employed were 20 kV accelerating voltage, 1-3 μm incident beam, 1.005 nA beam current, and 5-second counting time.

2.3.3 Fluid inclusion microthermometry

Fluid inclusion petrography and microthermometry were performed on 100- μm -thick, doubly polished thin sections prepared and examined at Laurentian University. Samples of dolomite, calcite, and/or sphalerite were used. Fluid inclusion classification followed the protocol of Goldstein and Reynolds (1994) whereby the concept of fluid inclusion assemblages (FIA) was integrated with petrographic study to classify (i.e., primary, secondary, pseudosecondary, indeterminate) inclusions. A Linkam THMSG600 heating-freezing stage with an automated controller unit coupled to an Olympus BX-51 microscope was used for microthermometric analysis. The heating-freezing stage was calibrated using synthetic fluid inclusions: CO_2 (-56.6°C), freezing point of H_2O (0°C), and critical point of H_2O (374°C). Inclusion salinity was determined using the final melting temperature of ice ($T_{\text{m}}(\text{ice})$) for aqueous inclusions and tables in Bodnar (1993). Final homogenisation temperatures (T_{h}) and salinities, based on ice melting $T_{\text{m}}(\text{ice})$ were determined by repeated runs to ensure that the measurements were accurate and reproducible (i.e., $<\pm 2^\circ\text{C}$ and $<\pm 0.2^\circ\text{C}$, respectively).

2.3.4 Evaporate mound SEM-EDS

The solute chemistry of fluid inclusions was determined using the evaporate mound method (Haynes et al., 1988; Kontak, 2004) with two variants of sample preparation for evaporate mound production and analysis. Both methods involved the rapid heating (100°C/min) of previously studied sample chips in the Linkam THMSG600 heating stage to a temperature of 350°C to induce artificial decrepitation of fluid inclusions. Samples were kept at this temperature for >2 minutes to ensure optimal evaporate mound production from individual fluid inclusions (Haynes and Kesler, 1987). Samples were monitored optically to ensure that primary FIAs were decrepitated for analysis on the SEM. Chips containing two or more intergrown mineral phases, such as dolomite and sphalerite or calcite, were decrepitated and the evaporate mounds analyzed on the chip in order to identify which mounds belonged to which mineral. Monomineralic chips were placed on microscope cover glass (Fisher Brand) and heated, as above, to produce decrepitation; after cooling, the chip was removed, leaving the debris and evaporate mounds on the surface of the glass slip. This was done to preclude any interference the composition of the chip (e.g., Ca and Mg) may have had on mound analyses, because of the small size of the mounds and the penetration depth (i.e., excitation area) of the incident electron beam during analysis. For some samples, evaporate mounds on both the chip and cover glass were analysed to check reproducibility of data. The glass slip used for collecting mounds is not pure silica, but contains small but consistent amounts of Na and K, and so the glass contribution was subtracted from the measured composition of mounds.

The same SEM-EDS system used for imaging was used to analyse evaporate mounds, under similar operating conditions. Mounds were analysed in point-mode unless >5 µm size, in which case raster mode was used to preclude the possible effect of in-situ fractionation (e.g., Na versus

Ca) on mound chemistry (Haynes et al., 1988; Kontak, 2004). In all cases, the wt. % concentrations calculated were for mound and substrate (e.g., quartz, glass slide) and afterwards the contribution of the substrate subtracted to give a final mound analysis which was then normalised to 100 wt. % for plotting purposes. The minimum detection limit for most elements is estimated to be approximately 0.1 wt. %. The latter implies that for a 10 wt. % equiv. NaCl fluid inclusion, an element present in solution at ~200 ppm can be detected in a mound assuming 100% efficiency of solute capture during mound formation.

2.3.5 Secondary ion mass spectrometry (SIMS)

In situ O and S isotope analysis was performed using Secondary Ion Mass Spectrometer (SIMS) at the Manitoba Isotope Research Facility (MIRF), University of Manitoba (Winnipeg, Manitoba). Calcite and dolomite were analysed for their $\delta^{18}\text{O}$ values, and pyrite, sphalerite, and galena for their $\delta^{34}\text{S}$ values. Samples were polished and cleaned in a series of sonic baths and were then thinly sputter-coated with Au. Ion detection was done on a Balzers SEV 1217 electron multiplier coupled with an ion-counting system. The instrument operated with 20 μm sputtering diameter, 300 V sample offset, -9 keV secondary accelerating voltage, 247 μm slit, 18 ns dead time, and mass-resolving power of 347. Oxygen isotopes were analysed using a 2 nA Cs^+ electron gun accelerated at 10 kV. Respective standards were analysed multiple times during the sessions for precision assessment. Data are reported as $\delta^{18}\text{O}$ (VSMOW) and $\delta^{34}\text{S}$ (VCDT) in standard per mil (‰) notation. Spot-to-spot reproducibility for calcite, dolomite, sphalerite, pyrite, and galena were 0.9-1.1‰, 0.7-1.0‰, 0.3-0.7‰, 0.3‰, and 0.3‰, respectively. Further details of the analytical procedure are provided in MacRae (1995) and Fitzsimons et al. (2000).

2.3.6 LA ICP-MS

Trace and rare earth (REE) elements in various minerals were analysed using a Resonetics RESOLUTION M-50, ArF excimer laser with a 193 nm wavelength and two-volume chamber (Laurin Technic) coupled to a Thermo X Series II (quadruple) ICP-MS in the Geochemical Fingerprinting Laboratory, Laurentian University. Samples used were first identified and characterised using petrography and SEM-EDS imaging and analysis. Internal standards for each phase analysed (e.g., Ca, Mg) depended on the target and its composition, based on results of SEM-EDS analysis (e.g., type of carbonate; Fe content of sphalerite). A combination of GSD and GSE glasses (Jochum et al., 2005) and MASS compressed puck (Wilson et al., 2002) standards were used as external standards for rare earth and trace elements. Analyses were done using a beam size that ranged from 15 μm to 124 μm , depending on the size of the minerals analysed, with the following operating conditions: 5 Hz and 7 J/cm², 650 ml/min He, 700 ml/min Ar, and 6 ml/min N₂; washout time between analyses was 30 seconds. Precision error is estimated to be typically <10% of the measured value for trace elements. To obtain an average composition, line traverses across grains were done, rather than numerous point analyses, which on average equated to over 200 seconds of counting time.

2.4 Results

2.4.1 Mineral paragenesis

Zinc showings in the Cornwallis district do not uniformly contain all of the paragenetic elements documented in the region, and so the general mineralogy and paragenetic sequence for the district (Fig. 9) is described first, using the Polaris deposit as a reference, followed by region- and/or showing-specific characteristics. A description of Polaris mineralogy and paragenesis,

following the work of Reid et al. (2013a), as well as the district as a whole, can be grouped into three stages: early, main, and late (Fig.9). Early host-rock dolomitisation produced finely crystalline dolostone accompanied by marcasite (Mar1). The main ore stage involves intergrown saddle dolomite, sphalerite (Sph1-3), and galena (Gal1). The late stage consists of two calcites (Cal1 and 2), galena (Gal2), marcasite (Mar2), and barite. Textural relationships (Fig. 10) indicate that dolomite formed throughout main-stage mineralisation, precipitating both before (Fig. 10A) and after (Fig. 10B) sphalerite 3, and that sphalerite has a nuanced paragenesis within the main stage. In the main stage, discrete, granular, dolostone-replacing sphalerite is typically first (Sph1; Fig. 10C), followed by fine-grained, colloform (Fig. 10C and D) and dendritic (Fig. 10E) Sph2, which is typically replaced by skeletal Gal1 (Fig. 10F), then the last sphalerite is coarsely crystalline Sph3, which typically contains purple patches alternating with pale yellow zones (Fig. 10C, D, G, H, I). Sphalerite 3 is ubiquitous at all showings studied, whereas Sph2 is limited to Dundas, Polaris, Truro, and Eclipse (Fig. 11); Rose (1999) reports colloform sphalerite (Sph2) from the Harrison showing, but it is absent in the samples in this study. Calcite 1 (Cal1) is present as a post-mineralising phase that occupies space among brecciated sphalerite grains (Fig.10 J, K); it is subhedral to euhedral, with crystals up to several centimetres, but locally grades into smaller anhedral crystals (Fig. 10K). Calcite locally replaced saddle dolomite along crystal edges and as patches in dissolution embayments. Calcite 2 (Cal2) is anhedral, with irregular crystal edges, and fills fractures in Cal1 and hematite, which post-dates Cal1 (Fig. 10L).

2.4.1.1 Little Cornwallis Island (Polaris, Eclipse, and Truro):

An early euhedral pyrite/marcasite stage (Py1) is partially preserved in sub- to anhedral Py2 (Fig. 10M). Fine-grained Py2 matrix supports brecciated fragments of sphalerite (Sph1-2; Fig. 10C).

Sphalerite 3, in some samples, has a band characterised by a pitted texture that is overgrown by typical Sph3 (Fig. 10N); this is also documented in Sph3 in Harrison and JG samples.

2.4.1.2 Cornwallis Island (Stuart River, Snowblind Bay, Rookery Creek, and Bacon River):

The mineralogy of showings on Cornwallis Island is similar to that of Little Cornwallis Island, but with local subtle differences. Sphalerites 1 and 2 are absent on Cornwallis Island; Sph3 is apparently the earliest sphalerite stage. Euhedral pyrite is apparently sector-zoned, as revealed on tarnished samples (Fig. 10O).

2.4.1.3 Grinnell Peninsula (Trigger, JG, Scheills, and Dundas):

The Dundas showing in the northern region has dendritic Sph2, which is replaced by fine-grained platy smithsonite 1 (Sm1) that does not replace coarsely crystalline red-orange Sph3 (Fig. 10P, Q). Smithsonite 2 (Sm2) is a coarsely crystalline colourless cement in interstices among brecciated Sph3. It is botryoidal, faintly layered in plane-polarised light (Fig. 10R), and exhibits sweeping extinction.

2.4.1.4 Somerset Island (Seal and Typhoon)

Sphalerites 1 and 2 are apparently absent on Somerset Island. Sphalerite 3 at Seal is generally intergrown with Py2 where the mineralisation is in quartz sandstone (Fig. 10S), but is more red-orange than sphalerite elsewhere. Vein, void-filling, and replacement Sph3 is associated with dolomite gangue, but not intergrown with Py2.

2.4.2 Fluid inclusions

2.4.2.1 Types and distribution of fluid inclusions

Samples from the showings noted above have usable fluid inclusions in dolomite, Sph3, and Cal1. Primary FIAs in sphalerite form planes of fluid inclusions parallel to defined growth zones, some of which are highlighted by purple zones (Fig. 12A-E), whereas secondary FIAs occupy healed fracture planes (Fig. 12F). In all cases, the typically 1-15 μm fluid inclusions are high-density ($\sim 0.9 \text{ g/cm}^3$), two-phase L-V types (Fig. 12). Centres of ore-stage dolomite cement contain both primary and pseudosecondary FIAs of small ($< 5 \mu\text{m}$), high-density ($\sim 0.9 \text{ g/cm}^3$), two-phase L-V inclusions (Fig. 12G, H). Calcite 1 has primary FIAs (Fig. 12I) with high-density ($\sim 0.9 \text{ g/cm}^3$), 5-10 μm , two-phase L-V fluid inclusions. Isolated clusters of fluid inclusions are locally present (indeterminate types; Fig. 12J). No fluid inclusions were documented in Cal2. All samples were examined in UV light to check for the presence of liquid petroleum, either as distinct inclusions or as heterogeneously trapped aqueous-petroleum couplets. There is no evidence suggesting that liquid petroleum was present in of the areas during either burial or mineralising events.

2.4.2.2 Microthermometry

Microthermometric data for the district are summarised in Table 1. With few exceptions, the fluid inclusions were metastable during cooling runs and consequently data for $T_m(\text{ice})$ and derived salinity are limited to the few inclusions that froze. In some cases, repeated cooling to -100°C or holding for 1-2 hours at -100°C initiated freezing of such inclusions. The lack of freezing of inclusions therefore limits the amount of data upon which to characterise chemical

systems using first melting to infer bulk compositions (e.g., NaCl-H₂O versus NaCl-CaCl₂-H₂O) or salinities of trapped fluids.

Primary FIAs in dolomite and sphalerite from the entire district have an overall range in T_h values from 60° to 110°C. In more detail, sphalerite samples from the northern showings have T_h values from 78° to 110°C, with the two FIAs from Hornby having only slightly different average T_h values of 106°C (FIA1; $1\sigma = \pm 8^\circ\text{C}$; $n=4$) and 94°C (FIA2; $1\sigma = \pm 2^\circ\text{C}$; $n=3$). Neither FIA had inclusions that froze, hence no ice-melting data are available. For the Dundas sample, the only measured FIA (FIA3) has T_h values for four inclusions that range from 78° to 90°C and average 84°C ($1\sigma = \pm 6^\circ\text{C}$), with a range in $T_m(\text{ice})$ from -27° to -31°C, with an average of -29°C ($1\sigma = \pm 1.8^\circ\text{C}$).

Rookery (central area) has Sph3 with average T_h values of 89°C (FIA1; range from 85 to 97°C; $1\sigma = \pm 4^\circ\text{C}$; $n=8$), 106°C (FIA2; 105° to 106°C; $n=2$), and 90°C (FIA3; $n=5$). Dolomite from this area has average T_h values of 85°C (FIA4; 83 to 95°C; $1\sigma = \pm 5^\circ\text{C}$; $n=7$) and 90°C (FIA5; 83 to 100°C; $1\sigma = \pm 5^\circ\text{C}$; $n=10$), and average $T_m(\text{ice})$ values of -14°C (FIA1; -7 to -35°C; $1\sigma = \pm 13.2^\circ\text{C}$), -33°C (FIA2; -31 to -35°C; $n = 2$), -31°C (FIA4; -27 to -33°C; $1\sigma = \pm 2.5^\circ\text{C}$; $n = 5$), and -30°C (FIA5; -28 to -30°C; $1\sigma = \pm 0.9^\circ\text{C}$; $n = 5$).

Harrison (western area) has Sph3 with average T_h values of 81°C (FIA1; 70 to 90°C; $1\sigma = \pm 6^\circ\text{C}$; $n=9$) and 87°C (FIA2; 74 to 96°C; $1\sigma = \pm 9^\circ\text{C}$; $n=9$) with average T_{mice} values of -30.3°C (FIA2; -27 to -34°C; $1\sigma = \pm 3.3^\circ\text{C}$; $n=4$).

Seal (southern area) has average T_h values in dolomite of 91°C (FIA1; 88 to 95°C; $1\sigma = \pm 2^\circ\text{C}$; $n = 9$) and in Sph3 of 110°C (FIA2; $n=2$). Only dolomite had fluid inclusions that froze; these yielded a $T_m(\text{ice})$ values of -30°C. Typhoon (south) Sph3 has an average T_h value of 85°C

(FIA3; 82 to 86°C; $1\sigma = \pm 2^\circ\text{C}$; $n = 4$) whereas for Cal1 the average T_h value is 147°C (140 to 158°C; $1\sigma = \pm 5^\circ\text{C}$; $n=9$) and its average $T_m(\text{ice})$ value is -0.3°C (-0.1 to -1.0°C; $1\sigma = \pm 0.3^\circ\text{C}$; $n=7$).

2.4.2.3 Evaporate mound data

Samples with sphalerite and/or dolomite were used for evaporate mound analysis of inclusions in dolomite and sphalerite (Sph3). Examples of the mounds generated (Fig. 13A-D) show highly variable shapes and sizes; domical mounds are either circular (Fig. 13A) or amorphous (Fig. 13B, C), but clusters of irregular crystals are also common (Fig. 13D), all of which is consistent with previously documented examples (see Kontak, 2004) for discussion). The chemical data for each region are summarised in ternary plots for Na-Ca-K (in wt. %) in Figure 13E, F. In general, the cation composition of mounds from both dolomite and sphalerite (Sph3) is predominantly Na-rich (i.e., > 50%), with subordinate amounts of K and Ca. Fewer mounds are dominated by Ca with subordinate Na. No other cations (e.g., Fe, Mg, Mn), including metals (e.g., Zn), were detected, despite the high salinities of the inclusions. Overall, no regional trends are noted in mound composition. The main anion present is Cl, but in some mounds, S is present at levels less than 10 wt. % (normalized to 100 wt. %).

2.4.3 SIMS analysis of stable isotopes (O, S)

The results of SIMS analyses of oxygen and sulphur isotopes (Table 2; Figs. 14 – 16) are discussed separately for each isotope.

2.4.3.1 Oxygen isotopes

The results of 77 analyses of dolomite (Table 2) from 13 samples indicate an overall range for $\delta^{18}\text{O}_{\text{VSMOW}}$ from 19.3 to 30.7‰ (average 23.7 with a $1\sigma = \pm 3\%$). This overall range is not fully expressed in any one area, but instead is the collective variation for all of the data (Fig. 14). Data for the northern showings range from 23.2 to 26.9‰ (average 25.6 ‰; $1\sigma = \pm 1.6\%$, $n = 4$) for Trigger, and 19.3 to 26.7‰ (average 23.2 ‰; $1\sigma = \pm 1.9\%$, $n = 11$) for Dundas. The central showing's data range from 20.2 to 23.1‰ (average 22.1 ‰; $1\sigma = \pm 1\%$, $n = 7$) for Rookery, 23.9 to 26.8‰ (average 25.2 ‰; $1\sigma = \pm 1.4\%$, $n = 5$) for Snowblind, and 21.5 to 24.8‰ (average 23.5 ‰; $1\sigma = \pm 1.5\%$, $n = 4$) for Eclipse. The southeastern showings range from 20.5 to 25.1‰ (average 23.0 ‰; $1\sigma = \pm 1.3\%$, $n = 24$) for Seal, and 19.7 to 26.4‰ (average 23.1 ‰; $1\sigma = \pm 2.6\%$, $n = 13$) for Typhoon. The western showings range from 22.4 to 26.5‰ (average 23.9 ‰; $1\sigma = \pm 2.0\%$, $n = 6$) for Harrison and 23.9 to 26.7‰ (average 25.2 ‰; $1\sigma = \pm 1.1\%$, $n = 5$) for Polaris.

Calcite 1 has $\delta^{18}\text{O}_{\text{VSMOW}}$ values from 6.8 to 21.1‰ (average 14.9 ‰; $1\sigma = \pm 3.8\%$, $n = 45$), a large range that is expressed throughout the district (Fig. 15). The northern showings have ranges of 12.8 to 19.7‰ (average 16.6 ‰; $1\sigma = \pm 2.6\%$, $n = 6$) for JG and 18.9 to 20.5‰ (average 19.9 ‰; $1\sigma = \pm 0.7\%$, $n = 4$) for Dundas. The central Rookery showing ranges from 11.3 to 16.1‰ (average 13.5 ‰; $1\sigma = \pm 2.1\%$, $n = 5$). The western showings have ranges from 10.0 to 11.9‰ (average 10.8 ‰; $1\sigma = \pm 0.7\%$, $n = 5$) for Harrison, 10.1 to 13.8‰ (average 12.4 ‰; $1\sigma = \pm 1.5\%$, $n = 5$) for Truro, and 7.0 to 12.0‰ (average 10.3 ‰; $1\sigma = \pm 2.0\%$, $n = 11$) for Polaris. Southeastern showings range from 13.4 to 20.7‰ (average 16.4 ‰; $1\sigma = \pm 3.0\%$, $n = 6$) at Seal and 16.3 to 21.1‰ (average 19.4 ‰; $1\sigma = \pm 1.9\%$, $n = 5$) at Typhoon.

2.4.3.2 Sulphur isotopes

Sphalerite $\delta^{34}\text{S}_{\text{VCDT}}$ values vary within and among regions but are consistent within each showing (Fig. 16; Table 2). The district has an overall range of values from -6.0‰ to 33.5‰, with no obvious geographic trend. In showings that contain more than one sphalerite generation, there is a slight increase in $\delta^{34}\text{S}$ values from Sph2 to Sph3 (approximately 5‰ magnitude).

Sphalerite $\delta^{34}\text{S}$ values in the north have a total range from -6.0‰ to 26.9‰, with distinct values for each area. Trigger Sph3 ranges from 17.7 to 22.1‰ ($n = 10$) and averages 19.5‰ ($1\sigma = \pm 1.5\%$), whereas galena 2 (Gal2) ranges from 17.6 to 20.2‰ (average 18.7 ‰; $1\sigma = \pm 1.3\%$, $n = 3$). JG Sph3 ranges from 24 to 26.9‰ (average 25.7 ‰; $1\sigma = \pm 1.3\%$; $n = 5$). Dundas Sph2 ranges from -6.0 to -1.6‰ (average -3.7 ‰; $1\sigma = \pm 1.6\%$, $n = 11$), but Sph3 ranges from -2.2 to 1.3‰ (average -0.8 ‰; $1\sigma = \pm 1.2\%$; $n=9$).

Sphalerite $\delta^{34}\text{S}$ values in the central region have a total range from -3.4 to 19.2‰, with partial overlap of the data for two showings. Whereas data for Stuart have a large range from 7.9 to 19.2‰ (average 9.6 ‰; $1\sigma = \pm 4.6\%$; $n = 8$), data for Rookery (range 12.5 to 14.4‰; average 13.3 ‰; $1\sigma = \pm 0.8\%$; $n = 4$) and Bacon (range 8.9 to 10.0‰; average 9.6 ‰; $1\sigma = \pm 0.5\%$; $n = 4$) are more restricted. The $\delta^{34}\text{S}$ values for two sphalerite generations from Eclipse (central) are -3.4 to 4.2‰ (average 0.8 ‰; $1\sigma = \pm 2.6\%$; $n = 12$). Sphalerite 2 values range from -3.4 to 2.2‰ (average -0.9 ‰; $1\sigma = \pm 1.8\%$; $n = 7$), whereas Sph3 has a range from 2.3 to 4.2‰ (average 3.2 ‰; $1\sigma = \pm 0.9\%$; $n = 5$). Galena at Eclipse has a range from -0.4 to 1.5‰ (average of 0.5 ‰; $1\sigma = \pm 1.0\%$, $n=3$).

Sphalerite 3 $\delta^{34}\text{S}$ values in the western region range from 5.1 to 8.2‰ (average 7.1 ‰; $1\sigma = \pm 1.1\%$; $n=6$) for Harrison, 12.7 to 18.6‰ (average 15.9 ‰; $1\sigma = \pm 2.8\%$, $n = 4$) for Markham

Point, 7.7 to 8.6‰ (average 8.2‰; $1\sigma = \pm 0.4\%$; $n = 4$) for Truro, and 5.7 to 6.6‰ (average 6.2‰; $1\sigma = \pm 0.3\%$; $n = 5$), for Polaris. Pyrite 2 at Truro has $\delta^{34}\text{S}$ values ranging from 6.7 to 7.0‰ (average 6.9‰; $1\sigma = \pm 0.1\%$; $n = 3$).

Sphalerite³ $\delta^{34}\text{S}$ in the southeast (Seal showing) ranges from 26.3 to 33.5‰ (average 28.9‰; $1\sigma = \pm 2.2\%$; $n=18$). Pyrite (Py2) coeval with Sph3 has $\delta^{34}\text{S}$ values ranging from 29.5 to 31.6‰ (average 31.1‰; $1\sigma = \pm 1.0\%$; $n = 11$).

2.4.4 Trace element and REE data

Trace and REE data for analysed carbonate phases are summarised in Table 3 and shown graphically in Figures 17 and 18. Shale-normalised values were plotted on the discrimination diagram of Bau and Alexander (2006) (Fig. 19) to verify La and Ce anomalies. For the shale-normalised REE+Y plots (Fig. 17A to D), the ranges and average for each district and showing are shown separately, and the averages are compared in Figure 17E. In these plots, it appears that the results are consistent within each showing. Dolomite cements define three general groups in the shale-normalised REEY plots: (1) one positively sloped ($\text{La}/\text{Yb} < 1$), (2) one negatively sloped ($\text{La}/\text{Yb} > 1$), and 3) one generally flat. Overall there is a large range in $\Sigma\text{REE}+\text{Y}$ from 4.9 ppm to 51.9 ppm (average 21.2 ppm, $1\sigma = \pm 15.3$ ppm, $n=28$; Fig. 17) and in detail there are some geographic differences in the anomalies: (1) positive La anomalies for the western-most (Harrison) and eastern-most (Snowblind) showings; (2) a negative Ce anomaly in the western-most (Harrison) showing; (3) positive Ce anomalies for the southern-most (Typhoon) showing, as well as the central, western, and northern showings; (4) highly variable Eu, with a northern (Dundas) showing characterised by positive Eu anomalies ($\text{Eu}/\text{Eu}^* > 1$) but most others with no anomaly; and (5) highly variable positive Y anomalies ($\text{Y}/\text{Y}^* > 1$) for the central (Snowblind ~ 2), western (Harrison ~ 1.9) and northern (Dundas ~ 1.5 ; Scheills ~ 1.2) showings but flat or weakly

positive ($Y/Y^* = 1$) for the central (Eclipse ~ 1.1 ; Rookery ~ 1.0), and southern (Seal ~ 1.1 ; Typhoon ~ 1.3) showings. The La, Eu and Y anomalies of the showings are more apparent in the summary of the averages for all data (Fig. 17E).

Examining the dolomite data in more detail and with reference to the data table and shale-normalised REE+Y plots (Fig. 17), the northern showings exhibit both negatively sloped (average $La/Yb_{SN} = 4.3$; Dundas) and flat (average $La/Yb_{SN} = 0.93$; Scheills) patterns with $\Sigma REE+Y$ ranges of 27.9 to 51.3 ppm (average of 41.5 ± 12 ppm, $n=3$) for Dundas and 9.8 to 12 ppm (average of 10 ppm; $1\sigma = \pm 1.5$ ppm, $n=4$) for Scheills, and ranges in Y/Ho values of 41 to 47 (average of 43; $1\sigma = \pm 3$, $n=3$) for Dundas and 29 to 34 (average of 33; $1\sigma = \pm 2$, $n=4$) for Scheills. Central showings exhibit both positively sloped (average $La/Yb_{SN} = 0.40$; Rookery) and concave-down (average $La/Yb_{SN} = 1.0$ and 1.1 ; Snowblind and Eclipse, respectively), with ranges in $\Sigma REEY$ of 6.6 to 9.8 ppm (average of 8.2 ppm; $1\sigma = \pm 1.5$ ppm, $n=2$) for Rookery, 6.0 to 9.2 (average of 7.4 ppm; $1\sigma = \pm 1.3$ ppm, $n=4$) for Snowblind, and 21.2 to 22.0 ppm (average of 21.5 ppm; $1\sigma = \pm 0.4$ ppm, $n=3$) for Eclipse, and Y/Ho ranges from 23 to 29 (average of 27; $1\sigma = \pm 3$, $n=2$) for Rookery, 49 to 54 (average of 52; $1\sigma = \pm 2$, $n=4$) for Snowblind, and 27 to 30 (average of 28; $1\sigma = \pm 2$) for Eclipse. The western Harrison showing exhibits positively sloped patterns (average $La/Yb_{SN} = 0.5$) with $\Sigma REE+Y$ of 5.0 to 10.3 ppm (average of 7.3 ppm; $1\sigma = \pm 2.7$ ppm, $n=3$) and Y/Ho from 33 to 54 (average of 44; $1\sigma = \pm 12$, $n=3$). Polaris exhibits a negatively sloped ($La/Yb_{SN} = 3.6$) pattern that has a $\Sigma REEY$ of 313.7 ppm and a Y/Ho value of 36. Southern showings exhibit negatively sloped (average $La/Yb_{SN} = 5.5$ and 3.3 for Seal and Typhoon, respectively) patterns with $\Sigma REE+Y$ ranges of 39 to 52 (average of 44 ppm; $1\sigma = \pm 5$ ppm, $n=4$) for Seal and 18 to 33 (average of 26 ppm; $1\sigma = \pm 8$ ppm, $n=4$) for Typhoon, and

Y/Ho values ranges of 31 to 34 (average of 32; $1\sigma = \pm 1$, $n = 4$) for Seal and 30 to 40 (average of 34; $1\sigma = \pm 4$, $n = 4$) for Typhoon.

The analytical results of other trace elements (Mn, Fe, Sr) in the different carbonates are summarised in Figure 18 and Table 3. Concentrations of Mn and Sr in dolomite are relatively consistent throughout the district. Iron concentration is relatively consistent in all of the regions, except for the Harrison showing (west), which has an order of magnitude lower iron concentration than other showings, and Rookery, which has an order of magnitude higher iron concentration than the other showings. Northern showings have ranges in Fe of 1400 to 19000 ppm (average of 7700 ppm; $1\sigma = \pm 10000$ ppm, $n = 3$) for Dundas and 2300 to 5400 ppm (average of 4400 ppm; $1\sigma = \pm 1400$ ppm, $n = 4$) for Scheills, Mn from 270 to 2600 ppm (average of 1700 ppm; $1\sigma = \pm 840$ ppm, $n = 3$) for Dundas and 140 to 1100 ppm (average of 810 ppm; $1\sigma = \pm 270$ ppm, $n=4$) for Scheills, and Sr values from 14 to 95 ppm (average of 81 ppm; $1\sigma = \pm 23$ ppm, $n=3$) for Dundas and 23 to 65 ppm (average of 49 ppm; $1\sigma = \pm 14$ ppm, $n = 4$) for Scheills. Central showings have ranges in Fe of 13000 to 14000 ppm (average of 14000 ppm; $1\sigma = \pm 370$ ppm, $n=2$) for Rookery, 790 to 2700 ppm (average of 1800 ppm; $1\sigma = \pm 800$ ppm, $n= 4$) for Snowblind, and 2300 to 5500 ppm (average of 3800 ppm; $1\sigma = \pm 1600$ ppm, $n=3$) for Eclipse; Mn ranges from 430 to 590 ppm (average of 510 ppm; $1\sigma = \pm 83$ ppm, $n=2$) for Rookery, 120 to 150 ppm (average of 130 ppm; $1\sigma = \pm 15$ ppm, $n=4$) for Snowblind, and 500 to 760 ppm (average of 670 ppm; $1\sigma = \pm 140$ ppm, $n=3$) for Eclipse; and Sr from 24 to 49 ppm (average of 36 ppm; $1\sigma = \pm 12$ ppm, $n=2$) for Rookery, 33 to 45 ppm (average of 39 ppm; $1\sigma = \pm 5$ ppm, $n=4$) for Snowblind, and 32 to 77 ppm (average of 58 ppm; $1\sigma = \pm 23$ ppm, $n=3$) for Eclipse. The western Harrison showing has Fe from 110 to 180 ppm (average of 150 ppm; $1\sigma = \pm 34$ ppm, $n = 3$), Mn from 180 to 400 ppm (average of 300 ppm; $1\sigma = \pm 110$ ppm, $n=3$), and Sr from 43 to 49 (average

of 47 ppm; $1\sigma = \pm 3$ ppm, $n=3$); Polaris has 1700 ppm Fe, 440 ppm Mn, and 55 ppm Sr. Southern showings has an Fe range of 2600 to 2900 ppm (average of 2800 ppm; $1\sigma = \pm 140$ ppm, $n = 4$) for Seal and 66 to 1600 ppm (average of 820 ppm; $1\sigma = \pm 670$ ppm, $n=4$) for Typhoon, a Mn range of 85 to 640 ppm (average of 590 ppm; $1\sigma = \pm 40$ ppm, $n=4$) for Seal and 85 to 420 ppm (average of 230 ppm; $1\sigma = \pm 150$ ppm, $n = 4$) for Typhoon, and Sr ranges of 18 to 47 ppm (average of 20 ppm; $1\sigma = \pm 1$ ppm, $n = 4$) for Seal and 32 to 48 ppm (average of 42 ppm; $1\sigma = \pm 7$ ppm, $n = 4$) for Typhoon.

Calcite 1 has a large range in $\Sigma\text{REE}+\text{Y}$, from 2.1 ppm to 30.6 ppm throughout the district, with values of 4 ppm at Dundas, 31 ppm at Trigger, 18 ppm at Rookery, 2 ppm at Truro, 29 ppm at Harrison, 15 ppm at Seal, and 20 ppm at Typhoon. Similarly, there are large ranges in Fe (87 ppm to 11000 ppm), Mn (38 ppm to 1300 ppm), and Sr (16 ppm to 780 ppm). Respectively, Fe, Mn, and Sr values (in ppm) include 120, 550, and 75 at Dundas; 180, 1300, and 86 at Trigger; 130, 350 at Rookery, 87 at Truro, 160 at Harrison, 4900, 230, and 130 at Seal, and 11000, 110, and 16 at Typhoon. The shale-normalised patterns (Fig. 17F) vary considerably in their profiles, with approximately flat, concave-down, and positive slopes, although most have $(\text{La}/\text{Yb})_{\text{SN}} < 1.0$, with an exception for the Dundas showing $[(\text{La}/\text{Yb})_{\text{SN}} = 1]$ and the southern showings $[(\text{La}/\text{Yb})_{\text{SN}} = 2.5$ (Seal) and 2.1 (Typhoon)]. There are no appreciable La or Ce anomalies (Fig. 19B), but there are slight positive Eu anomalies (i.e., $\text{Eu}/\text{Eu}^* = 1.1-1.2$), and Y/Ho ranges from 30.9 to 41.8. Examining the data more closely, northern Call has a $\Sigma\text{REE}+\text{Y}$ of 4.2 ppm (Dundas) to 30.6 ppm (Trigger), flat ($\text{La}/\text{Yb} = 1.0$; Dundas) and positive to concave-down ($\text{La}/\text{Yb} = 0.20$; Trigger) shale-normalised patterns with no appreciable La or Ce anomalies, Eu anomalies of 1.4 (Dundas) and 1.1 (Trigger), Y/Ho values from 34.7 (Trigger) to 39.0 (Dundas), and Fe, Mn, and Sr values of 120 ppm, 550 ppm, and 75 ppm, respectively at Dundas and 180

ppm, 1300 ppm, and 86 ppm, respectively at Trigger. Central Cal1 (Rookery Creek) has a $\Sigma\text{REE}+\text{Y}$ of 17.6 ppm, a positively sloped shale-normalised pattern ($\text{La}/\text{Yb} = 0.39$), no appreciable La or Ce anomalies, a Eu anomaly of 1.1, a Y/Ho of 35, and 130 ppm Fe, 350 ppm Mn, and 95 ppm Sr. Western (Harrison) Cal1 has a $\Sigma\text{REE}+\text{Y}$ of 29.2 ppm (Harrison) and 2.1 ppm (Truro), a positively sloped [$\text{La}/\text{Yb} = 0.6$ (Harrison) and 0.5 (Truro)] shale-normalised pattern with no appreciable La or Ce anomalies, Eu anomaly of 1.2 (Harrison and Truro), Y/Ho values of 42 (Harrison) and 34 (Truro), and Fe, Mn, and Sr concentrations (in ppm) of 160, 38, and 780, respectively for Harrison and 87, 82, and 400, respectively for Truro. The southern Cal1 show a general similarity between the two showings (Seal and Typhoon) with $\Sigma\text{REE}+\text{Y}$ of 15.2 ppm and 20.1 ppm, respectively, and have negatively sloped ($\text{La}/\text{Yb} = 2.5$ and 2.1, respectively) shale-normalised patterns. Typhoon has no appreciable La or Ce anomalies, a Eu anomaly of 1.29, Y/Ho of 30.9, and 11000 ppm Fe, 111 ppm Mn, and 16 ppm Sr, whereas Seal has negative La and positive Eu (2.34) anomalies, and Fe, Mn, and Sr concentrations of 4900 ppm, 230 ppm, and 130 ppm Sr, respectively, Y/Ho could not be determined because Ho was below detection limit.

2.4.5 Sulphide trace element data

Trace element data for sphalerite for two showings from the northern (Trigger and Dundas) and western (Harrison and Polaris) regions, three from the eastern region (Snowblind, Rookery, and Eclipse), and one from the southern (Seal) region are provided in Table 4 and plotted in Figures 20 and 21. Data for Ni, As, In, and Sb, which are commonly reported in sphalerite analyses from other settings (e.g., Bellisont et al., 2014; Cook et al., 2009; Pfaff et al., 2011; Slater et al., 2019), are not reported here because they were all below the limit of detection of about 0.4 ppm, 0.1 ppm, 0.004 ppm, and 0.02 ppm, respectively. The Co values are at or near the limit of detection of 0.04 ppm, and may be unreliable.

Using the entire range of Sph3 elemental concentrations throughout the district as a reference, most values are within standard deviation of the average for the respective element (Fig. 20). There are few enrichments or depletions of elements in Sph3; the most notable enrichments are Mn (Harrison and Polaris), Cu (Dundas), Ga (Dundas and Rookery), Ge (Dundas, Seal, and Harrison), Ag (Seal), Pb (Harrison), and Bi (Polaris). With regards to these elevated values, line traverses (representative traverses shown in Figure 21), show that, with the exception of narrow, short-lived spikes (Fig. 21A), the counts are generally uniform throughout the analyses (Fig. 21B, C). Along laser traverses, Ge is generally positively correlated with Ag and Cu (Fig. 21B), but these elements typically seem to be negatively correlated with Cd.

Although there are no geographic trends in element concentration in the district, there is a general decrease temporally in average values of Mn, Fe, Se, Mo, Pb, and Bi, from Sph1 and Sph2 to Sph3. Of particular note is that the purple zoning in plane-polarised petrographic images of Sph3 is spatially associated with an increase in Cd values and decrease in most other elements detected (Pb, Ge, Ga, Ag and possibly Cu) in the laser traverses (Fig. 21C).

2.5 Interpretation

2.5.1 Mineral characteristics

Finely crystalline, colloform, and dendritic sphalerite (Sph2) is thought to be characteristic of supersaturated, rapid growth (Roedder, 1968; Pfaff et al., 2011). Conversely, coarsely crystalline sphalerite (Sph3) may be typical of relatively slower crystal growth. The absence of finely crystalline Sph2 in most showings in the study area implies that the conditions reflected by these textures were not ubiquitous.

Cadmium concentrations in sphalerite, locally to wt. % levels, appear to be correlated with petrographically purple sphalerite (Fig. 20C), but Cd is not typically a chromophore. Previous studies associated Cd with colouration of sphalerite, but attributed the intensity of the colour, rather than the colour itself, to Cd, with other trace elements being responsible for the different colours (Si et al., 2011; Ye et al., 2011). It is possible that the size of the Cd anion distorted the sphalerite crystal to produce vacancies or electron holes, a phenomenon known to cause different colours in fluorite (Murr, 1974; Nassau, 1978; Wright, 2002), but not yet known from sphalerite

The difference in reflected-light colour of tarnished pyrite probably reflects minor variations in its trace-element geochemistry. Oscillatory pyrite zonation is typically interpreted as a rapid growth texture (Ramdohr, 1969; Barker and Cox, 2011) that indicates either cyclic physico-chemical changes in fluid chemistry or the presence of nanoscale inclusions (Pacevski et al., 2012; Li et al., 2018).

2.5.2 Fluid inclusions

Based on stratigraphic thickness, the Polaris orebody formed at ~1 km depth (Randell, 1994). This requires that measured T_h values be pressure-corrected to obtain the true trapping temperature. Corrections are a function of salinity and measured T_h of the fluid. Application of equations from Bodnar and Vityk (1994), using the average salinity of the fluid inclusions (28 wt. % NaCl equiv.) and 1 km of burial, result in corrections of +11°C (for $T_h = 60^\circ\text{C}$), +11°C ($T_h = 80^\circ\text{C}$), +12°C ($T_h = 90^\circ\text{C}$), +12°C ($T_h = 100^\circ\text{C}$), and +22°C ($T_h = 110^\circ\text{C}$). The pressure-correction for Cal1 fluid inclusions, with a low average salinity (0.5 wt. % NaCl equiv.) and using a burial depth of 1 km, calculate to +17°C ($T_h = 140^\circ\text{C}$) and +18°C ($T_h = 156^\circ\text{C}$),

Salinities (in wt. % NaCl equiv.) of FIAs in Sph3 and dolomite, as calculated using the equations and tables from Bodnar (1993) (Table 1), are 26.8 - 28.7 (average 27.6 with $1\sigma = \pm 1.1$) for the north (Dundas), 10.5-32 (average 25.5 ± 7.3) for the east (Rookery), 7.7-31.3 (average 24.6 ± 9.6) for the west (Harrison), and 28.7 for the south (Seal); Savard et al. (2000) reported a salinity range from 26.8 to 40.1 (average 32.7) and Randell (1994) and Randell and Anderson (1996) reported a range from 23 to 31 at Polaris. However, as noted for the $T_m(\text{ice})$ data in this study, the range of salinities in any FIA is very restricted. Inclusions with $T_m(\text{ice})$ values below -30°C suggest the presence of divalent cation(s) in the fluid (Steele-MacInnis et al., 2016), which is identified to be Ca based on evaporate mound analyses (Fig. 13E, F). The mineralising fluids are therefore interpreted as being both highly saline and Ca-rich.

Fluid inclusions in Cal1, which post-dates mineralisation, have calculated salinities of 0.2 to 1.7 wt. %, indicating that a later fluid diluted/supplanted the earlier, more saline fluid. Such a fluid could have a number of origins, including meteoric, magmatic, and metamorphic (White, 1974; Roedder, 1984). The geological history of the Cornwallis district includes neither magmatism nor metamorphism during the Phanerozoic, precluding these fluid types. A fluid of meteoric origin is the most probable diluting fluid.

The analysis of evaporate mounds from dolomite and sphalerite indicates a dominance of Na cations and subordinate Ca and minor K cations, with Cl and S being the dominant and subordinate anions, respectively. Channer et al. (1993) detected appreciable amounts (up to 7.5 mol %) of SO_4^{2-} in fluid inclusions from Polaris, during crush-leach analysis. Fluids that are dominantly NaCl solutions indicate a marine fluid origin, whereas the presence of CaCl_2 , and S (up to 10 wt. %) in the fluid indicates dissolution of evaporite minerals (e.g., anhydrite, gypsum, or calcite), which are present in the stratigraphy (e.g., Bauman Fiord and Bay Fiord formations),

or dissolution of limestone or dolostone. Acquisition of Ca and SO_4^{2-} of a fluid by interaction with subsurface evaporites along the flow path has been documented in groundwater studies (Morales-Casique et al., 2016). Minor K in the fluids may reflect the interaction of the fluid with sedimentary rocks in the subsurface. Fluid compositions between the two end-member reservoirs (Na-dominant and Ca-dominant) indicate variable interaction of the main (Na-dominant) fluid with the Ca reservoir along the fluid flow path.

2.5.3 Isotopes

Temperatures, constrained by T_h , and pressure-corrected to give trapping temperature T_t , as discussed above, were used with average measured $\delta^{18}\text{O}$ values and mineral- H_2O fractionation equations for dolomite (Horita, 2014) and calcite (O'Neil et al., 1969) to calculate the $\delta^{18}\text{O}_{\text{H}_2\text{O}}$ values of the equilibrated fluid (Fig. 14). The $\delta^{18}\text{O}_{\text{H}_2\text{O}}$ values of the fluid that precipitated the northern dolomite range from 4.9‰ ($T_t = 90^\circ\text{C}$) to 8.6‰ ($T_t = 122^\circ\text{C}$) for Trigger, and from 2.5‰ ($T_t = 90^\circ\text{C}$) to 6.2‰ ($T_t = 122^\circ\text{C}$) for Dundas. Central dolomite $\delta^{18}\text{O}_{\text{H}_2\text{O}}$ values range from 1.8‰ ($T_t = 93^\circ\text{C}$) to 4.7‰ ($T_t = 118^\circ\text{C}$) for Rookery, from 4.9‰ ($T_t = 93^\circ\text{C}$) to 7.8‰ ($T_t = 118^\circ\text{C}$) for Snowblind, and from 2.9‰ ($T_t = 91^\circ\text{C}$) to 7.5‰ ($T_t = 122^\circ\text{C}$) for Eclipse. Western (Harrison) dolomite $\delta^{18}\text{O}_{\text{H}_2\text{O}}$ values range from 1.8‰ ($T_t = 80^\circ\text{C}$) to 5.3‰ ($T_t = 107^\circ\text{C}$). Southeastern dolomite $\delta^{18}\text{O}_{\text{H}_2\text{O}}$ values range from 2.7‰ ($T_t = 93^\circ\text{C}$) to 6.0‰ ($T_t = 122^\circ\text{C}$) for both Seal and Typhoon.

The calculated $\delta^{18}\text{O}_{\text{H}_2\text{O}}$ values based on dolomite cement data indicate that either seawater or a low-latitude meteoric water was involved in the mineralisation at each showing. Some showings in which there is slightly elevated $\delta^{18}\text{O}$ value (e.g., Snowblind) suggest that the fluid had interacted with a carbonate rock. In general, however, the overlap of calculated fluid isotopic

values among the various regions suggests that a similar fluid was responsible for precipitation throughout the district, with local fluid-rock interaction in the vicinity of each showing.

The fluid that deposited Cal1 in the southern area has a range of $\delta^{18}\text{O}_{\text{H}_2\text{O}}$ values from 1.2‰ ($T_t = 150^\circ\text{C}$) to 10‰ ($T_t = 173^\circ\text{C}$). However, because T_h data are lacking for Cal1 elsewhere, a range of temperatures from 60° to 173°C, the latter being the highest measured T_h value in the south, were used for calculating $\delta^{18}\text{O}_{\text{H}_2\text{O}}$. The $\delta^{18}\text{O}_{\text{H}_2\text{O}}$ values for Cal1 in the north range from -9.4‰ (60°C) to 8.6‰ (173°C) for JG and -3.3‰ (60°C) to 9.4‰ (173°C) for Dundas. In the central region, Rookery Creek values range from -10.9‰ (60°C) to 5.0‰ (173°C). The western Harrison showing has a range of -12.2‰ (60°C) to 0.8‰ (173°C), and Truro showing has values from -12.1‰ (60°C) to 2.7‰ (173°C). The southeastern showings range from -8.8‰ (60°C) to 9.6‰ (173°C) for Seal and -5.9‰ (60°C) to 10.0‰ (173°C) for Typhoon. The aforementioned $\delta^{18}\text{O}_{\text{H}_2\text{O}}$ values for the fluids that deposited Cal1 over the entire district overlap with the ranges for unmodified, low-latitude meteoric, seawater, and magmatic fluids (Rollinson, 1993).

The $\delta^{34}\text{S}$ sulphide values overall span a large range from -6 to 32‰ throughout the district, but there is a much more limited range within each area. This range of district values indicates possibly different sulphur reservoirs (e.g., seawater or biogenic) or processes (BSR or TSR) for each showing. The limited range at each showing indicates a single, stabilised, showing-specific process. Typically, $\delta^{34}\text{S}$ values $<+5\text{‰}$ are associated with biogenic-derived S, whereas $\delta^{34}\text{S} > +15\text{‰}$ are associated with abiogenic (i.e., TSR) S; values of $+5\text{‰} < \delta^{34}\text{S} < +15\text{‰}$ probably reflect mixed S sources (e.g., Ohmoto and Rye, 1979; Seal, 2006).

Sphalerite 2 has lower $\delta^{34}\text{S}$ values than Sph3 indicating the influence of a ^{32}S -enriched sulphur source. Mixing of a metalliferous fluid with a reduced sulphur-bearing fluid would explain the

supersaturation textures of Sph2 (dendritic and colloform) that are absent in Sph3. The reduced S fluid was probably reduced biogenically to produce its lower $\delta^{34}\text{S}$ values.

Rayleigh fractionation during partial sulphate reduction on site during sulphide precipitation can result in variable $\delta^{34}\text{S}$ values, depending on the degree of reduction (Seal, 2006; Brueckner et al., 2015). Different Sph3 $\delta^{34}\text{S}$ values among the showings throughout the district, assuming the S source for the district was uniform, can be explained by partial reduction of sulphate (Fig. 22).

The availability of $\delta^{34}\text{S}$ data for sulphide pairs allows application of sulphide geothermometry (Ohmoto and Rye, 1979); for this, the average values derived from the measurements are used. For fractionation between sphalerite and galena, data are available for two areas. At Eclipse, the galena replaces Sph2 but apparently not sph3; using average Sph3 values, $\Delta_{\text{sph-gal}} = 2.7\text{‰}$, which gives a temperature of 250°C. For Stuart River, $\Delta_{\text{sph-gal}} = -3.1\text{‰}$ which indicates disequilibrium fractionation. At two localities pyrite-sphalerite data are available. For Seal, the $\Delta_{\text{py-sph}} = 2.2\text{‰}$ which indicates 185°C (Sakai, 1968), or 96°C (Ohmoto and Rye, 1979); however, the pyrite-H₂S fractionation equation from Ohmoto and Rye (1979) is calibrated for a temperature range of 200° to 700°C, but the calculated temperature compares to T_h data of 85-110°C (T_t = 97-123°C) for sphalerite-hosted fluid inclusions. In contrast, at Truro the $\Delta_{\text{py-sph}} = -1.3\text{‰}$, which indicates disequilibrium.

2.5.4 REE+Y and trace element data

The carbonate minerals exhibit a range of PAAS-normalised REE+Y patterns, but there is an internal consistency for each showing. Flat- to negatively sloped patterns (northern, southern, Eclipse, and Polaris) are markedly different from marine carbonate signals (e.g., Alibo and Nozaki, 1999; Nothdurft et al., 2004) indicating high fluid:rock ratios, whereas the westernmost

(Harrison) and easternmost (Snowblind) showings display a typical marine signature (Bau et al., 1997; Nozaki et al., 1997; Alibo and Nozaki, 1999; Nothdurft et al., 2004) and indicate inheritance from the host dolostone under a low F:R system. With the exception of Harrison and Snowblind, the showings have a positive Ce anomaly, indicating reduced fluids. The LREE-enrichment noted in samples from Dundas, Seal, Typhoon, and Polaris (Fig. 17A- C) suggests interaction with LREE-enriched phases or lithologies along the fluid's flow path, such as feldspars, apatite, monazite (Debruyne et al., 2016; Trotter et al., 2016), and/or gypsum (Craddock and Bach, 2010; Inguaggiato et al., 2018; Lin et al., 2019). The northern (Scheills) and western (Eclipse) showings have relatively flat patterns, and represent a fluid:rock system that was between the two end-members. The lack of positive La and Y anomalies, with shale-like Y/Ho values (~ 26) in the otherwise marine signature from Rookery may indicate a small degree of contamination (Kamber and Webb, 2001), rather than a different fluid composition.

The PAAS-normalised REE+Y patterns for Cal1 cement vary, with the most common groups of patterns being positively sloped and concave-down, whereas approximately flat, and negatively sloped are also noted. The positive slopes of Cal1 suggest a system in which the fluid's chemical characteristics were strongly influenced by that of the host rock; flat and negatively sloped patterns indicate that the fluid's chemical characteristics were not influenced by those of the host rock, but instead suggest that the fluids interacted with various basement reservoirs, yielding variable patterns.

The presence of various anomalies in some of the REE+Y data, namely La, Ce, Eu, and Y/Ho, are used to assess aspects of the fluid chemistry, such as degree of rock buffering (fluid:rock) and redox conditions, during carbonate precipitation. The lack of a La anomaly, except for Harrison (west) and Snowblind (east) (Fig. 19A), which is a hallmark of fresh marine carbonate

(Bau and Alexander, 2006), is a measure of the extent of fluid overprinting seen in most samples. The presence of positive Ce anomalies in all of the showings, except for Harrison and single analyses from each of Snowblind and Scheills (Fig. 19A), indicates relatively reducing conditions. In contrast, Eu is enriched in some of the samples (Dundas and Polaris) which indicates a reservoir in which Eu^{2+} was preferentially enriched at some time by interaction with a magmatic source or sedimentary unit derived from igneous or metamorphic parents. Jiang et al. (2015) suggest that positive Eu anomalies may be associated with the redox reactions involved in TSR processes, but homogenisation temperatures in their study ranged from 110° to 220°C and so the comment may not be applicable at the lower temperatures encountered here.

The correlation between Fe and Mn in dolomite and calcite indicates that these elements were controlled by the redox condition of the fluid. The apparent lack of correlation between either Fe or Mn and REE+Y suggests a lack of Fe-(Mn)-oxyhydroxide control on the REE content. That Sr concentration is lower than that of marine carbonates [e.g., 250-500 ppm (Bau et al., 2003); 100-270 ppm (Nothdurft et al., 2004)], but in the typical range of hydrothermal dolomite cement, both associated with MVT ore (Appold and Wenz, 2011) and barren hydrothermal dolomite (Ronchi et al., 2012), suggests that the dolomite has characteristics dominated by those of the precipitating fluid (i.e., high fluid:rock).

2.5.5 Sphalerite trace-element chemistry

The generally consistent values, within standard deviation of the mean district value, for many trace metals in sphalerite suggest a single metal source throughout the district, with minor local variations. Trace element concentrations are in the range of measured values from other studies

on sphalerite (e.g., Cook et al., 2009; Pfaff et al., 2011; Ye et al., 2011; Gagnevin et al., 2014), indicating that the metals were probably not from an anomalously metal-rich source but instead from a typical sedimentary succession. Reduced, organic-rich sedimentary rocks are typically enriched in trace metals (e.g., Gong et al., 1977; Algeo and Maynard, 2004; Large et al., 2011; Turner and Kamber, 2012; Harris et al., 2013; Simbo et al., 2019), and have been suggested as possible metal source for several deposits (e.g., Turner and Kamber, 2012; Simbo et al., 2019). Such units are considered to be the probable source of the metals in the Cornwallis district.

The time-series profiles of laser traverses across sphalerite (Fig. 21) are generally smooth. This indicates that nanoscale mineral inclusions, which are not uncommon in sulphide minerals, are essentially absent, and that it can be assumed that the trace elements are incorporated in the crystal structure (George et al., 2016). An exception to this is the spikes in the Pb profile in one Sph2 grain (Fig. 21A), which probably indicate the presence of nanoscale galena inclusions (George et al., 2016). The presence of such inclusions in Sph1 and Sph2 is probably due to the rapid crystallisation rate of these phases, as reflected by their textures (colloform, banded, dendritic), and with it an increased probability of trapping solid inclusions (Pfaff et al., 2011), which contrasts with an inferred slower precipitation rate for Sph3, as suggested by its texture (coarsely crystalline and euhedral). The decrease in Pb content, even where not due to the presence of micro-inclusions, from Sph1 and Sph2 to Sph3 (Fig. 20) is probably a function of precipitation rate (Pfaff et al., 2011).

The correlation of Ge with Ag and Cu indicates (Fig. 21B) that these elements underwent coupled substitution for Zn, such as $\text{Ge}^{4+} + 2(\text{Ag,Cu})^+ \rightarrow 3\text{Zn}^{2+}$, which has been documented in other studies (e.g., Belissont et al., 2014; Belissont et al., 2016; Bauer et al., 2019). Cadmium does not appear to correlate with other analysed elements, with the exception of a possible

negative correlation with Ge in some samples. Because Cd is preferentially bound to organic matter and is enriched in dark shales, much like other metals (Gong et al., 1977; Algeo and Maynard, 2004; Harris et al., 2013), Cd-enrichment that is decoupled from other elements probably relates to precipitation factors, rather than to different source rocks. For example, it has been observed that Cd-enrichment appears to be favoured by precipitation of sphalerite during (comparatively slow) TSR as opposed to (more rapid) BSR (Barrie et al., 2009; Pfaff et al., 2011; Henjes-Kunst et al., 2017).

Trace-element content of sphalerite has been correlated with host rock lithologies (Pfaff et al., 2011). Because most of the showings in the Cornwallis district are hosted by carbonate rocks, the regional sphalerite composition is expected to be similar, without the effect of different lithological controls. Minor variations are still expected even among the carbonate-hosted showings because of differences in their host formations (Fig. 3). The Ag-poor nature of Harrison sphalerite is probably a function of a silver sink along the local flow path, rather than the lack of silver in the fluid. In general, mineralisation at Seal is the most different from the rest of the district (Fig. 20), which could be the result of its unusually low position in the stratigraphic succession.

Microscale variations of trace-element concentration in sphalerite can also be controlled by variations in temperature, pH, and sulphur activity during precipitation (Gagnevin et al., 2014), which could explain some of the variations documented in the Cornwallis district. The ranges in temperature recorded by the fluid inclusions indicate minor temperature fluctuations during precipitation; minor trace-element variations would therefore also be expected. Variations in trace-element composition of sphalerite due to variable pH conditions is less plausible, however, because of the pH-buffering provided by the host carbonate rocks.

2.6 Discussion

2.6.1 Fluid origins and metal source(s)

This discussion addresses the high fluid:rock showings (i.e., those precipitated from fluids with the least amount of host-rock influence on composition) to determine the main characteristics and history of the mineralising fluid(s), and then addresses the anomalous characteristics of individual showings/regions separately. Fluid characteristics recorded at Polaris, Seal, Typhoon, and Dundas, where systems had high fluid:rock, as indicated by their PAAS-normalised REE+Y patterns (Fig. 17; e.g., Banner et al., 1988), are the most representative of the regional fluid.

Because the carbonate host rocks have oxygenated shale-normalised REE+Y signatures, the marine water in which the sediment initially accumulated was probably not reduced. Therefore, the reduced nature of the precipitating fluid (positive Ce anomaly) does not represent connate water; a different fluid probably displaced the connate water with a reduced formation water.

The range in the inferred $\delta^{18}\text{O}_{\text{H}_2\text{O}}$ values from 1.8 to 7.8‰ for the dolomite-precipitating fluids (Fig. 14) indicates either low-latitude meteoric water or seawater, but the presence of high-salinity fluids (~28 wt. % NaCl equiv.) preserved in dolomite cements precludes involvement of un-modified meteoric water. Enrichment of seawater and meteoric water $\delta^{18}\text{O}$ values by several per mil due to evaporation can, depending on the degree of evaporation (Ward and Halley, 1985; Sun et al., 2009; Passey and Ji, 2019) explain the calculated values. The preserved $\delta^{18}\text{O}$ values therefore probably reflect a reservoir that experienced some degree of evaporation and/or had its signature modified (i.e., enriched in ^{18}O) due to interaction with sedimentary rocks or possibly the dissolution of a subsurface evaporitic unit (e.g., anhydrite or gypsum) (Osselin et al., 2019),

such as the Bay Fiord or Baumann Fiord formations. Crush-leach analyses for material from Polaris indicated evaporation of marine water (Channer et al., 1993), which could represent a marine fluid that was evaporated and replaced the connate water; alternatively, as Randell (1994) and Randell and Anderson (1996) suggested, it could be that the mineralising fluid interacted with connate fluid of the Bay Fiord Formation. Groundwater studies have shown that (meteoric) fluid interacting with evaporite units in the subsurface increases salinity, Ca, and SO_4^{2-} content of the fluid, in addition to affecting $\delta^{18}\text{O}$ values (Morales-Casique et al., 2016). Dissolution of anhydrite or gypsum therefore is a probable explanation, as suggested by three lines of evidence: (1) some fluid inclusions record a Ca-rich, high-salinity signature with rare elevated S; (2) an acquired seawater-like isotopic signature is suggested by isotopic data (O, S); and (3) LREE-enrichment in dolomite indicates high fluid-rock interaction, possibly with evaporite-bearing rocks.

The trace-element contents of sphalerite (Fig. 20), particularly for Sph3, have similar averages across the district. This consistency suggests that a chemically uniform regional fluid, which transported these elements, was present throughout the history of mineralisation. Because crystalline basement is not considered to have contributed to fluid-rock interaction, as indicated by $^{87}\text{Sr}/^{86}\text{Sr}$ values from Polaris (Dewing et al., 2007), the regional fluid must have obtained metals from Paleozoic strata. Certain elements (e.g., Ni, Ag, Zn, Pb, and Se) are preferentially associated with organic matter in sediment (Gong et al., 1977; Algeo and Maynard, 2004) and can be mobilised during fluid interaction. Depending on the fluid-flow path, organic-rich strata may have variably contributed to mineralisation in different showings, which would result in variation among the showings. Sphalerite at the Seal showing (south), for example, is hosted by the Ship Point Formation, which is stratigraphically lower than the other mineralised formations

in the district (Fig. 3) as well as south of the deepwater basin (Fig. 2); the regional fluid may not have interacted with the same organic-rich strata or perhaps the distance from the source allowed for the trace elements to be removed along flow, explaining the showing's relatively low trace-element concentrations. The similarities between Seal and Typhoon, at least in their carbonate cements, suggest that the stratigraphic position may have less of an influence than geography. However, the physico-chemical conditions during sphalerite precipitation appear to be a main factor in trace element composition (Gagnevin et al., 2014), and may obscure geographic/stratigraphic controls on composition.

Dolomite $\delta^{13}\text{C}_{\text{PDB}}$ values at Polaris, Bass Point, and Harrison average approximately 0‰ (Randell, 1994; Randell and Anderson, 1997; Savard et al., 2000; Rose, 1999), which is similar to the Thumb Mountain Formation (Polaris) and Blue Fiord Formation (Bass Point and Harrison) limestone and dolostone, indicating that dolomite inherited its $\delta^{13}\text{C}$ signature from the parent limestone/dolostone. The inheritance of $\delta^{13}\text{C}$ values from the host rock agrees with the dissolution of the Thumb Mountain Formation dolostone that accompanied sulphide precipitation, producing breccias (Reid et al., 2013b), rather than the regional fluid supplying C with these isotopic values. It would be expected that the oxidation of organic matter during gas production would yield more negative, biogenic $\delta^{13}\text{C}$ values, but oxidation of long-chain organic matter during TSR produces intermediate oxidised species that progressively increase $\delta^{13}\text{C}$ value with each oxidation step, resulting in final values approaching 0‰ (Anderson, 2008; Xia et al., 2014; Zhao et al., 2019).

In summary, the main mineralising fluid was derived from formation water that probably was sourced from marine or low-latitude meteoric water that acquired salinity and SO_4^{2-} from evaporite dissolution and metals from deep-water strata (Fig. 23E).

The post-mineralising Cal1-precipitating fluid was a low-salinity fluid relatively depleted in ^{18}O that probably started as a low-latitude meteoric fluid. The unusually high T_h values (150°C) from southeastern (Seal) showings, Polaris (Savard et al., 2000), Bass Point, and Harrison (Rose, 1999) may represent long-distance (~ 500 km) travel of a fluid that was heated during Carboniferous rifting and magmatism in the Sverdrup basin or the deep penetration of meteoric fluid during the Ellesmerian orogeny. Fluid migration of this magnitude due to thermal anomalies has been recorded in the Michigan basin, but there, T_h values progressively decrease towards the basin margin (Haeri-Ardakani et al., 2013). Although T_h data in Cal1 is sparse (four locations), there does not appear to be any geographic trend in temperature (consistently $\sim 150^\circ\text{C}$). The $\delta^{18}\text{O}$ data for Cal1 also show no geographic trend (Fig. 15), indicating that temperature did not vary greatly. The highest $\delta^{18}\text{O}$ values are also associated with nearly flat shale-normalised REE+Y patterns for Cal1 from Dundas (north) and Seal (south) (Fig. 17F) and probably indicate fluid-rock interaction along the flow-path, rather than temperature differences. The elevated temperatures noted are therefore probably derived from deeper fluid penetration across isotherms as the Ellesmerian orogeny progressed.

Calcite $\delta^{13}\text{C}$ values range from 0‰ to -17‰ from Polaris (Randell, 1994; Randell and Anderson, 1996; Savard et al., 2000) and 0‰ to -26‰ from Harrison and elsewhere on Bathurst Island (Rose, 1999). These biogenic signatures could represent the oxidation of simple hydrocarbons or the introduction of ^{12}C -enriched carbon by the fluid. The large range in $\delta^{13}\text{C}$ values may be the result of mixing of different reservoirs or a consequence of bulk analysis. No spatial relationship is noted for the values in order for any systematic change to be detected. For example, as Zhao et al. (2019) conclude, during TSR, $\delta^{13}\text{C}$ value becomes progressively lower as the more simple C species are oxidised, because the more complex C species have been consumed. Therefore, it

could be that most of the complex organic matter was oxidised during sulphide precipitation, leaving simple species (CH_4) to be oxidised during the post-ore calcite precipitation, or that there was a mixing of C sources.

2.6.2 Sulphur source and reduction mechanism

Possible sulphur sources for carbonate-hosted Zn-Pb deposits include magmas, pre-existing sulphides (e.g., diagenetic pyrite; H_2S), connate water, seawater, organically bound sulphur, and/or buried evaporite rocks (Leach et al., 2005). There is no evidence of magmatic activity during the early and middle Paleozoic in the Cornwallis district, but there is Late Mississippian – Early Pennsylvanian magmatism in the form of basaltic flows in the Sverdrup basin on Ellesmere and Axel Heiberg islands (Thorsteinsson, 1974; Trettin, 1988; Davies and Nassichuk, 1991). Geochronology constrains Zn mineralisation in the district to 366-374 Ma (Christensen et al., 1995; Mitchell et al., 2004; Selby et al., 2005), which precludes any Sverdrup magmatic influence on sulphur isotope values. Early pyrite/marcasite at some showings could have contributed to sulphur recycling (replacement of early pyrite by later pyrite; Fig. 10M), but early pyrite is regionally sparse, which limits the volume available to satisfy mass-balance constraints. Thus, the most probable sulphur source involves a seawater signature acquired during deposition of evaporitic sediment, which was subsequently transferred to the fluid via dissolution of primary sulphates and partially retained during reduction of sulphate to sulphide. The two Paleozoic sulphate evaporite units in the Cornwallis district have $\delta^{34}\text{S}$ values of 24-31‰ (Baumann Fiord Formation) and 18-30‰ (Bay Fiord Formation) (Davies and Krouse, 1975; Mossop, 1979; Randell, 1994; Randell and Anderson, 1996). The S-bearing fluid inclusions indicate evaporite (gypsum or anhydrite) dissolution or interaction with a bittern brine, as suggested for Polaris (Channer et al., 1993; Randell, 1994). The contribution of organically bound S to mineralisation

cannot be determined here, but Randell et al. (1996) suggested the possibility of oil and gas generation prior to mineralisation, based on reaction rims around organic matter, in addition to bitumen being associated with mineralisation (Randell, 1994; Randell et al., 1996; Savard et al., 2000; Selby et al., 2005; Reid et al., 2013a); however no S isotope data on organic matter from the Thumb Mountain Formation are available for comparison.

The question of which reduction mechanism generated sulphide at Polaris has long been controversial (e.g., Kerr, 1977b; Randell, 1994; Savard et al., 2000; Reid et al., 2013a; Reid et al., 2013b). The measured range of $\delta^{34}\text{S}$ values for all sphalerite in the Cornwallis district of -6‰ to 30‰ (-7‰ to +36‰ according to Dewing et al., 2007) implies the influence of more than one sulphur reduction mechanism in the district. Given that the original source was probably Early or Middle Ordovician seawater with $\delta^{34}\text{S}$ values of 18-32‰ (Paytan and Gray, 2012), either BSR or TSR processes would be required to reach the much lighter values present in some of the sphalerites. The temperature range of fluid inclusions (70° to 110°C) from main ore-stage mineral phases is within the temperature ranges in which both BSR (high end) and TSR (low end) operate, thus making both processes plausible.

Rayleigh fractionation of H_2S during TSR can cause a large variation of $\delta^{34}\text{S}$ values, depending on the percentage of SO_4^{2-} that was reduced (e.g., Brueckner et al., 2015). Assuming that TSR can operate at low temperatures (e.g., 70-130°C), the range in measured $\delta^{34}\text{S}$ values of sphalerite can be explained by different degrees of fractionation (Fig. 21). By using trapping temperature (T_i) in the equations from Robinson (1973) and a Paleozoic seawater sulphate value of 25‰ (Paytan and Gray, 2012), $\delta^{34}\text{S}$ values <0‰ would require a smaller proportion (less than 40%) of SO_4^{2-} to be reduced, whereas $\delta^{34}\text{S}$ values of 30‰ require a larger proportion (~70%) of the SO_4^{2-} to be reduced. The much lower $\delta^{34}\text{S}$ values for the early sphalerite (Sph2) of -6.0 to +2.2‰

represent a fractionation of ~ -16 to -38% from typical Paleozoic seawater sulphate (18-32‰; Paytan and Gray, 2012) and suggest BSR (Ohmoto and Rye, 1979; Seal, 2006) rather than TSR. Although in situ TSR is capable of producing reduced sulphur (RS_1) at a sufficient rate for ore deposit formation (Thom and Anderson, 2008; Yuan et al., 2017a), it is typically too slow to produce rapid growth textures (Machel, 2001), such as the fine-grained, colloform and dendritic early sphalerites, during sulphate reduction. Development of these textures requires supersaturation (e.g., Roedder, 1968; Pfaff et al., 2011), which in turn demands that a sufficient volume of reduced sulphur existed at the site of mineralisation (RS_0) prior to the delivery of metals. Sulphate reduction to produce RS_0 was therefore independent of the mineralising fluid and was probably controlled by ambient burial conditions, because at the assumed burial depth of 1 km at the time of mineralisation (Randell, 1994; Randell and Anderson, 1996) the temperature would have been approximately 60°C , which is in the optimal temperature range for BSR (Machel, 2001). The low $\delta^{34}\text{S}$ values of early sphalerite, therefore reflect a BSR-dominated RS_0 . The presence of RS_0 and the precipitation of sulphide (via acid-producing reactions) can affect the initiation, temperature, and rate at which TSR can take place (Zhang et al., 2012; Xia et al., 2014; Yuan et al., 2017b), to produce in-situ RS_1 from the regional fluid.

If, however, at the time of fluid mobilisation, reduced sulphur (RS_0) with a lower $\delta^{34}\text{S}$ value was already at the site, metals carried by the sulphate-bearing fluid would precipitate upon contact, and the sulphate would be reduced on site thermochemically via oxidation of organic matter to produce H_2S (RS_1) resulting in intermediate $\delta^{34}\text{S}_{\text{sulphide}}$ values that progressively became enriched in ^{34}S as RS_1 became the dominant sulphide, similar to other deposits (Kuhlemann et al., 2001; Peevler et al., 2003; Henjes-Kunst et al., 2017).

Sphalerite 3, the phase present throughout the district, is characterised by heavier $\delta^{34}\text{S}$ values (5-30‰) than Sph2 and probably records RS_1 produced by TSR rather than BSR. It is possible that the locally seawater-like $\delta^{34}\text{S}$ values of Sph3 represent the reduction of a sulphate fluid that had $\delta^{34}\text{S}$ values of +50‰. Although barite with $\delta^{34}\text{S}$ values \sim 50‰ is present in the district, it is considered to be a by-product of mineralisation (Dewing et al., 2007) rather than a primary product of marine processes. Therefore, it is not plausible to envisage seawater-like values being produced through sulphates with higher ^{34}S being reduced by BSR with large amounts of fractionation. As demonstrated above, Rayleigh fractionation during TSR can produce the higher $\delta^{34}\text{S}$ values without the need for a ^{34}S -enriched sulphate source; this is particularly true for Seal, which has higher $\delta^{34}\text{S}$ values (26-34‰) compared to the rest of the district.

Sphalerite from the northern (Trigger) showing has coarse pale green-tan botryoidal growth zones that are separated by purple bands. These growth bands exhibit $\delta^{34}\text{S}$ values that start at \sim 17‰ after every other purple band and increase towards 22.1‰ before the next purple band (Fig. 10G). This fits with the partial fractionation by TSR in a system that increases in the fraction of SO_4^{2-} being reduced during precipitation, suggesting a partially closed system episodically recharged with fluid.

The largest ranges in sphalerite $\delta^{34}\text{S}$ values are from Stuart and Polaris (Fig. 16). Stuart values probably indicate mixed sulphur sources or a relatively closed system in which the fraction of SO_4^{2-} changed throughout mineralisation, similar to the Trigger showing. Unlike Trigger, however, there is no apparent systematic change in $\delta^{34}\text{S}$ values in the crystals; therefore, mixed sulphur sources are more probable. The large range in sphalerite $\delta^{34}\text{S}$ values previously reported for Polaris (+2.9‰ to +12.3‰; Randell, 1994, Randell and Anderson, 1997) is a consequence of

the bulk sampling method used and probably represents the combination of values from early and late sphalerite.

Polaris has a halo of barite with $\delta^{34}\text{S}$ values of approximately 50‰ (Sharp and Dewing, 2004; Dewing et al., 2007) and is assumed to be the by-product of sphalerite mineralisation. With approximately 45% of SO_4^{2-} being reduced, sphalerite would precipitate with $\delta^{34}\text{S}$ values of approximately 10‰ and produce a residual SO_4^{2-} of approximately 50‰ (Fig. 22E) that could have left the site of mineralisation, precipitating ^{34}S -enriched barite. These values indicate that the partial reduction of SO_4^{2-} by TSR was probably the main reduction mechanism for producing reduced S for the Sph3 at Polaris deposit.

In order for $\delta^{34}\text{S}$ values to be between 0‰ and 10‰ by mixing of a seawater sulphate source (25‰) with a bacteriogenic source (-25‰), a mixing ratio of 50:50 (0‰) to 70:30 (10‰) is required. Showings in this range are predominantly hosted by the Thumb Mountain Formation, which suggests host-rock control, rather than the same mixture being present for these showings. The higher $\delta^{34}\text{S}$ values at JG and Trigger would require no input from a bacteriogenic source, whereas Seal values cannot be attained by mixing of sources, unless an ^{34}S -enriched source was mixed with the seawater sulphate. Therefore, although mixing is possible for some showings, the main sulphur would have been supplied by the regional fluid, with the different $\delta^{34}\text{S}$ values controlled by TSR reactions.

In the richly mineralised East Tennessee district of the USA, a metal and sulphate-bearing fluid was reduced on site by TSR when it contacted a methane gas cap (Peevler et al., 2003). The mixing of H_2S from the gas cap with that being supplied by episodic pulses of the main fluid was suggested to have caused the variable $\delta^{34}\text{S}$ values. The tendency of the $\delta^{34}\text{S}$ values to be higher

(~seawater) in the sulphides indicates that the main S source was from the mineralising fluid, whereas the gas cap H₂S had a minor role in initial mineralisation. Unlike the East Tennessee example, which lacked fine-grained sphalerite, which would have indicated rapid crystallisation due to the predominance of a pre-existing H₂S source (Peevler et al., 2003), the Cornwallis district does have early, fine-grained colloform/dendritic sphalerite; therefore pre-existing H₂S probably played a dominant role, at least initially, in early mineralisation at some showings in the district. Basuki et al. (2008) also noted the precipitation of early, ³²S-enriched, colloform sphalerite in their study of the Florida Canyon and Florcita deposits in Peru was followed by the precipitation of coarsely crystalline, ³⁴S-enriched sphalerite. They concluded that there was an initial influence of a pre-existing H₂S pool (produced by BSR) that was then progressively dominated by in situ TSR processes.

Henjes-Kunst et al. (2017) concluded that mixing between two sulphur reservoirs, one produced by BSR and the other by TSR, was responsible for the Bleiberg deposit in Austria. They argued that the dominant sulphur source changed during mineralisation, as reflected in the changing $\delta^{34}\text{S}$ values from lower (early) to higher (late) mineralisation. A transition from lower (BSR-produced) to higher (TSR-produced) $\delta^{34}\text{S}$ values paragenetically has also been recorded elsewhere (e.g., Kuhlemann et al., 2001; Field et al., 2018; Luo et al., 2020). A change in the BSR:TSR source of sulphur was documented at the Wiensloch MVT deposit in Germany associated with textural changes in the sphalerite (Pfaff et al., 2011). Coarsely crystalline sphalerite from the Wiensloch deposit was precipitated from a TSR-dominant mixture of bacterially reduced formation water sulphide and hydrothermal sulphate; colloform sphalerite precipitated from a BSR-dominant sulphur mixture, as a result of supersaturation from pulses of metal-bearing fluids (Pfaff et al., 2011).

Barrie et al. (2009), Pfaff et al. (2011), and Henjes-Kunst et al. (2017) showed that Cd concentration in sphalerite is higher in coarsely crystalline sphalerite associated with TSR generated sulphur versus fine-grained colloform sphalerite attributed to BSR-generated sulphur. Although Cd concentration in the Cornwallis district is relatively consistent among the sphalerite generations, highest Cd concentrations are associated with purple sphalerite zones, which are limited to Sph3 crystals, and therefore may be related to TSR processes.

Therefore, in the Cornwallis district, pre-existing accumulations of H₂S (probably produced by BSR) at the time of migration of a regional metal and sulphate-bearing fluid would precipitate isotopically light sulphides with supersaturation textures while at the same time supplying an impetus for TSR initiation. Once TSR was established, it could become the dominant H₂S-producing mechanism in the system, precipitating coarsely crystalline, Cd-rich sphalerite with showing-specific $\delta^{34}\text{S}$ values (5 to 32‰) controlled by the proportion of sulphate in the regional fluid being reduced.

2.6.3 Reconstruction of mineralising system

The possible precipitation mechanisms for carbonate-hosted base-metal mineralisation are: (1) mixing of a metalliferous, sulphide-poor fluid with a metal-poor, sulphide-rich fluid, or (2) in situ reduction of a metalliferous sulphate-bearing fluid (Sverjensky, 1986; Leach et al., 2005). It is improbable that multiple, independently sourced but geochemically similar sulphide-bearing fluids would all mobilise at the same time, but in different amounts, to generate mineralisation with similar characteristics at all of the showings throughout the study area. Likewise, it is improbable that a single, metal- and sulphate-bearing fluid was responsible for all of the

mineralisation characteristics, without input from other sulphur sources; otherwise, the same textures and sulphur isotope values would be expected among showings instead of the documented relatively lower $\delta^{34}\text{S}$ values of the early mineralisation.

Although the mixing of multiple fluids is possible, as in southeast Missouri (Appold and Wenz, 2011; Shelton et al., 2020) and East Tennessee (Peevler et al., 2003), the possible fluid convergence mechanisms in those districts are not applicable to the Cornwallis district. Convergence due to permeability contrasts (Freeze and Witherspoon, 1967; Garven et al., 1999) is implausible because mineralisation developed throughout a stratigraphy with variable permeability. Geometric convergence is improbable because of the east-trending, southward-migrating orogenic front. The Boothia basement high, which acted as a buttress, probably would have caused fluid divergence, rather than convergence, making large-scale fluid mixing in the Cornwallis district less probable. Small-scale, local, initial mixing is expected, however, to explain the supersaturation textures and sulphur isotopic compositions of early sphalerite (sph₂).

Individual accumulations of reduced sulphur at the sites of mineralisation that developed owing to the presence of a suitable trap prior to delivery of the main metalliferous regional fluid can explain: (1) supersaturation textures; (2) the different S isotope values; (3) the change from lower to higher $\delta^{34}\text{S}$ values of sulphides; (4) why mineralisation is not restricted to specific (e.g., organic-rich) formations; (5) why mineralisation is not associated with all faults in the district; and (6) why some showings are larger than others (Fig. 23). Individual sulphur pools/sources have also been suggested by Field et al. (2020) to be a control on mineralisation volume in the U.S. mid-continent ore district. The mixing of a regional fluid with such S reservoirs agrees with arguments made by Savard et al. (2000) and Dewing et al. (2007) regarding BSR production of

reduced S via BSR and the need for a mixing hypothesis, in order to account for documented temperatures higher than those typical of BSR.

The main stage of mineralisation in the Cornwallis district was probably the result of in situ reduction of sulphate thermochemically using organic matter as a reductant, in agreement with the arguments made by Randell (1994), Randell and Anderson (1996), and Reid et al. (2013a, b). In summary, the depositional mechanisms for mineralisation were a combination of early fluid mixing followed by main-stage single-fluid, in situ sulphate reduction.

The high-grade zone at Polaris was hosted by an organic-rich part of the Thumb Mountain Formation (the upper member), which encouraged regional exploration programs to focus on that stratigraphic unit (Dewing et al., 2007). Numerous showings are present at other stratigraphic positions (Dewing et al., 2007), however, indicating that mineralisation is not strictly lithology-controlled. Similarly, the lack of mineralisation in the Thumb Mountain Formation where mineralisation is present in subjacent strata shows that formation-scale stratigraphy is not the only control; an ascending fluid would be expected to have precipitated its metals in the lowest favourable unit it encountered regardless of the presence of suitable ore-depositing conditions in overlying strata. It is possible, however, that fluids can utilize faults to by-pass stratigraphy to higher stratigraphic levels (Shelton et al., 2019). Accumulation of reduced sulphur was not restricted to a specific formation, which allowed sulphide bodies to precipitate throughout the stratigraphy. However, the predominance of showings in the Thumb Mountain Formation may be attributed to the organic-rich composition of the upper unit, and possibly more H₂S accumulation, thereby partially controlling mineralisation through the sustainability of RS₁ production.

The data presented here show an apparent correlation among lower $\delta^{34}\text{S}$ values, the presence of Sph₂, and Thumb Mountain Formation being the host, suggesting that this formation may have been more efficient at accumulating RS_0 than other formations. For example, Randell et al. (1996) suggested that the Thumb Mountain Formation at Polaris may have experienced multiple episodes of oil or gas production. However, the $\delta^{34}\text{S}$ values presented in the compilation of Dewing et al. (2007b) show that lower values are present at showings hosted by other formations. It is unclear which sphalerite stage was analysed to produce the data in Dewing et al. (2007b), but RS_0 produced by BSR would be expected to precipitate Sph₂ with lower $\delta^{34}\text{S}$ values; however, some showings that apparently lack Sph₂ but have lower $\delta^{34}\text{S}$ values [e.g., Typhoon (approximately -2‰) and Rookery approximately +4 to +6‰)] could indicate that either a low percentage (30-40%) of sulphate was reduced on site by TSR, with insufficient RS_0 present to allow for supersaturation, or that Sph₂ was not documented at these showings because of poor exposure or weathering. Although no Sph₂ was documented at the Harrison showing in this study, Rose (1999) documented minor amounts of Sph₂, illustrating the possibility that the apparent lack of Sph₂ at a showing may be related to exposure.

Showings in the district are predominantly related spatially to faults, as are most carbonate-hosted Zn-Pb deposits (Leach et al., 2005), but mineralisation is not present along all, or even most of the faults: faults are not the only controlling factor on sulphide distribution. Because faults can act as conduits for fluid movement, it is expected that during the regional fluid-flow event the mineralising fluid would have travelled through available faults (i.e., those with higher hydraulic conductivity) until it encountered a suitable trap, where precipitation took place. It is possible, however, that apparently unmineralised faults may have been mineralised but subsequently eroded, or that mineralisation is not expressed at surface as a showing.

Furthermore, RS_0 accumulations could have acted as chemical traps in an aquifer that lacked a major fault conduit.

Many factors influence the size of showings and orebodies, including sulphur availability, metal availability, accommodation space/traps, and permeability. Because the metal-bearing fluid is thought to have been distributed regionally in the Cornwallis district, metal availability should have been equal per unit volume at all showings, and metal concentration would not be a major influence on showing size. This conclusion was also reached by Field et al. (2020) in the U.S. mid-continent, where uniform trace element compositions of sphalerite from large deposits and showings were measured. A single, fairly chemically homogeneous, metal and sulphate-bearing fluid would be able to supply both metal and sulphur equally to all sites of mineralisation and would be expected to produce equal-sized showings, provided the appropriate reductants were present and fluxes were uniform. Because mineralisation is not restricted to organic-rich, or reductant-rich, strata, it may be suspected that the presence of a trap would control the amount of mineralisation. However, with regards to showings that appear to lack obvious traps (e.g., Snowblind and Scheills), mineralisation seems less probable without a pre-existing supply of reduced sulphur (RS_0). In situations that are incapable of producing RS_1 for continued precipitation (e.g., lack of reductant), the mineralisation would cease after the RS_0 supply was exhausted. Therefore, the general (at least initial) size of the showings was probably controlled by the volume of RS_0 present. In sites that have adequate conditions for producing RS_1 , precipitation can proceed after RS_0 is consumed for as long as RS_1 can be produced at a sufficient rate. The precipitation from RS_0 may provide the impetus to initiate RS_1 production, in otherwise less-than-favourable TSR conditions (Zhang et al., 2012; Xia et al., 2014; Yuan et al., 2017b).

2.6.4 Timing of mineralisation

The absolute timing of mineralisation has been directly and indirectly constrained at Polaris to ca. 360-375 Ma based on paleomagnetic dating of sphalerite and dolomite and radiometric dating (Rb-Sr, Re-Os) of sphalerite (Symons and Sangster, 1992; Christensen et al., 1995; Selby et al., 2005). The low $\delta^{18}\text{O}$ signature and low salinity of the fluid responsible for post-ore calcite cement indicate a low-latitude meteoric fluid. Such an origin for the fluid limits its timing to the Paleozoic between the Ordovician (host-rock depositional age) and Early Carboniferous, based on paleogeographic reconstructions (Torsvik et al., 2012) and present-day meteoric-water $\delta^{18}\text{O}$ values (Yurtsever and Gat, 1981; Luz and Barkan, 2010). These two independent data sets agree with a Late Devonian (Famennian) timing for mineralisation.

2.6.5 Fluid-driving mechanism

The mechanisms that can cause fluid movement in a buried basin are compaction, density, and gravity. Compaction-driven fluid mobilisation involves the compaction of underlying sediment (usually shale) and expels fluids that are in thermal equilibrium upwards to the site of mineralisation (Bethke, 1983; Cathles and Smith, 1983), such as at the Pine Point Zn-Pb deposit. The lack of any substantial shale units in the lower part of the stratigraphic succession in the Cornwallis district (Fig. 3) precludes compaction as a viable driving mechanism for the mineralising fluid. Oxygen isotope values and shale-normalised REE+Y patterns in dolomite gangue do not indicate a fluid that had interacted significantly with a shale-like lithology. Mineralisation associated temporally with orogenesis suggests that most sediment compaction

and fluid expulsion should have already taken place in an earlier burial environment, and that only minimal fluid volumes would have been available to be expelled by further compaction (Garven and Freeze, 1984).

Density-driven fluid mobilisation is initiated by either thermal or salinity contrasts. Magmatic bodies produce increased temperatures that initiate a thermal convection-cell that transports hydrothermal fluids up to the site of precipitation. Fluids can be transported several hundred kilometres from the thermal anomaly, but should show a trend of decreasing fluid temperature with distance (e.g., Haeri-Ardakani et al., 2013). The lack of age-appropriate magmatism in the district (Thorsteinsson, 1974; Davies and Nassichuk, 1991) and the consistency of T_h values in ore-stage minerals throughout the Cornwallis district suggest that thermal convection is improbable. Evaporative environments can cause relatively cool, dense brine to descend and initiate convection cells that can push warm, deep fluids upwards (Garven et al., 2003; Yang, 2006; Yang et al., 2010); this phenomenon has been invoked to explain basin-scale circulation of high-salinity fluids associated with SEDEX deposits, but generally requires syn-sedimentary faults that allow evaporative brine to reach depths and move laterally to reach fluid-dispersion faults (Garven et al., 2003; Yang, 2006; Yang et al., 2010). Although crush-leachate analyses of Polaris fluid inclusions with high Cl/Br ratios indicated evaporation of seawater (Channer et al., 1993), there is no evidence for extensive evaporation around the time of mineralisation (Late Devonian), and so the high-salinity, high Cl/Br fluid was probably derived from interaction with bittern connate brines that formed with the Bay Fiord or Baumann Fiord formations.

Gravity-driven, or topographically driven fluid-mobilisation is triggered by tectonic uplift during an orogenic event (Garven and Freeze, 1984; Garven et al., 1999; Morales-Casique et al., 2016). Accumulation of meteoric water in the exposed part of the orogen produces a considerable

hydrostatic head, which forces the movement of other crustal fluids away from the orogen through aquifers. Downward movement of recharge water pushes warmer deeper water updip towards the basin margin, thereby compressing fluid isotherms and allowing for higher-than-expected fluid temperatures than ambient burial can supply (Garven and Freeze, 1984). Gravity-driven flow can cause regional, long-distance migration of a single fluid, and result in regional episodes of fairly uniform mineralisation; it is the most probable mobilisation mechanism for most carbonate rock-hosted Pb-Zn (MVT) deposits (Leach et al., 2005). Mineralisation at Polaris and the Stuart showing (Cornwallis Island), being controlled by Ellesmerian-related structures (Dewing and Turner, 2003, Turner and Dewing, 2004; Dewing et al., 2007; Jobert et al., 2007), and mineralisation that is geochronologically contemporaneous with the Late Devonian Ellesmerian orogeny (Symons and Sangster, 1992; Christensen et al., 1995; Selby et al., 2005), are compatible with topographically driven fluid-mobilisation. A tectonically influenced, topographically driven regional fluid is therefore the most logical explanation for the generally uniform characteristics of Zn showings throughout the Cornwallis district and can explain the regionally uniform hydrothermal fluid temperature, age of mineralisation, access to subsurface evaporite units by migrating fluid, and long travel distances. Meteoric recharge in the orogen (Garven and Freeze, 1984) may also allow for the documented change from a marine-like formation fluid during the main-ore stage to a (high temperature) meteoric-sourced fluid (assumed shortly) afterwards, in the post-ore stage calcite (Cal1), and may explain why mineralisation ceased; the low salinity post-ore fluid that displaced the formation water was incapable of transporting sufficient metals (Basuki and Spooner, 2002) .

Studies involving topographically driven fluid flow and their relationship to ore deposits are based on numerical modelling (e.g., Garven and Freeze, 1984; Garven et al., 1999; Zhao et al.,

2018) or age relationships between mineralisation and orogenic activity (e.g., Ford and Worley, 2016; Fazli et al., 2019). Studies on present-day groundwater flow from mountainous areas have used numerical modelling and composition of discharge fluid to determine fluid flow path and rock interaction (e.g., Morales-Casique et al., 2016). Against the backdrop of a known Ellesmerian age of sulphide precipitation at Polaris and Stuart River (Christensen et al., 1995; Selby et al., 2005; Jober et al., 2007), the present study is the first to use multiple lines of geochemical evidence to demonstrate that topographically driven fluid was probably responsible for mineralisation throughout this entire metallogenic district.

2.6.6 Storm copper relationship

The rare but conspicuous Cu mineralisation in the district, such as at Storm (Somerset Island), was probably produced through interaction of a post-Zn-mineralising fluid with atypical, geographically restricted underlying strata (Fig. 23F). Although the main-stage Cu mineralisation at Storm is associated with a low-latitude oxidised meteoric fluid (equivalent to Cal1-precipitating fluid in the Zn showings), the pre-mineralisation fluid at Storm (Mathieu et al., 2018) resembled the Cornwallis regional mineralising fluid. Only minor Cu-related mineralisation at Storm is associated with the regional fluid, probably because Cu is less soluble in a reduced fluid, and therefore was less favourable for leaching and transporting sufficient Cu in solution to precipitate Cu-sulphides than Cu solubility in an oxidised, meteoric fluid (Rose, 1989; Brown, 2009), which was responsible for Cal1 precipitation. The underlying red beds (Aston Formation), which are geographically limited, probably supplied the Cu (Mathieu et al., 2018). Copper isotopes and geochemistry from Storm indicate a south-migrating fluid (present-

day co-ordinates; Mathieu et al., 2018), which coincides with the regional tectonically driven fluid flow in the district.

2.6.7 Interpreted controls on Polaris mineralisation and implications for regional sulphide formation

Collectively, the geochemical characteristics of sphalerite and carbonate minerals indicate high fluid:rock at Polaris and at the majority of showings studied, with some showings displaying a host-rock-buffered system (low fluid:rock). It is presumed therefore that a high fluid:rock system was a critical control on the Polaris ore zone. At Polaris, this high fluid-flow was accommodated by reactivation of a Boothia-uplift structure. Polaris is situated where a Caledonian strike-slip (wrench) fault offsets a major north-trending, Boothia-uplift-related thrust fault; the resulting irregularity of the thrust's trend allowed later dilation of the strike-slip fault during sinistral reactivation of the thrust during Ellesmerian compression (Fig. 23C,D; Dewing and Turner, 2003; Turner and Dewing, 2004). Many of the other showings in the district are spatially associated with reactivated, Boothia-related, roughly north-trending thrust faults that probably experienced reactivation or dilation during Ellesmerian compression (e.g., Eclipse, Rookery, Harrison, Stuart), or are near local extensional zones associated with these faults (e.g., JG, Trigger). All of these showings lacked the most favourable geometry for profuse fluid flux that permitted the development of a large deposit like that at Polaris.

The Polaris orebody was the product of three coinciding factors: (1) a large local reservoir of reduced S generated by an earlier process; (2) a structural conduit that facilitated sustained high fluid-flux of a metalliferous fluid; and (3) a reductant-rich host rock that accommodated TSR processes. The accumulation of ^{34}S -depleted sulphide prior to ingress of the regional,

metalliferous fluid ensured that sphalerite supersaturation developed as soon as fluid delivery began. The high fluid flux capacity of the dilated fault and presence of adjacent, reductant- (organic-) rich host rocks allowed for prolonged sulphide precipitation. Other showings in the district do not exhibit all three of these factors, and thus they are smaller than Polaris, even though they have the same mineralisation characteristics and history.

2.6.8 Implications for exploration

Because the main control on mineralisation is fluid flux, the most promising areas to explore would be those that could have facilitated high fluid flux. Snowblind lacks any obvious relation to dilational faults, and its REE+Y content suggests low fluid flux. Similarly, the Harrison showing, located on the western Boothia margin fault zone, may indicate that north-trending, Ellesmerian strike-slip faults generally acted as a regional aquitard, limiting the majority of the mineralising fluid within the Boothia margins. Dilational faults would produce the largest volumes of mineralisation. Ideally, a setting similar to Polaris should be targeted: an offset Caledonian thrust fault block that would have experienced torque from the south-directed stress of the Ellesmerian orogeny. The most probable regional area for renewed mineral exploration in the Cornwallis district would be along the central and northern margins of the Boothia uplift in the vicinity of the Ellesmerian fold belt, the area that would have experienced the most Ellesmerian stress. Areas that have favourable conditions that allow for sustained sulphate reduction, such as reductant-rich strata, that preferably have a trap, would be an appropriate second-order criterion for exploration. Barite with high $\delta^{34}\text{S}$ values, which indicates partial reduction of sulphate, may provide an indication of nearby mineralisation, similar to the barite halo around the Polaris deposit (Dewing et al., 2007).

2.7 Conclusions

Numerous showings throughout the Cornwallis Zn-Pb district (Arctic islands, Canada) were investigated using a suite of in situ analytical techniques that reveal shared characteristics with the past-producing Polaris Zn-Pb deposit in the district's centre. Zinc mineralisation in the district was the product of a regionally uniform, marine-sourced fluid whose flow was topographically driven during the Late Devonian Ellesmerian orogeny. This fluid interacted with subsurface strata, including evaporites, to acquire and transport metals and sulphate to pre-existing sulphide accumulations. After initial mixing and precipitation, H_2S produced by in situ TSR of the regional fluid became the dominant source of reduced S for continued ore sulphide precipitation. These characteristics allowed for: (1) a generally uniform fluid chemistry, except for showing-specific sulphur isotope signatures; (2) textures and geochemical signatures of sphalerite related to two different modes of precipitation (fluid mixing followed by in situ sulphate reduction); and (3) variations in the stratigraphic and geographic position and size of the showings throughout the district. Rare Cu mineralisation in the district is associated with a later fluid event, which locally overprints Zn mineralisation.

Results of this study highlight three factors that controlled the size and location of sulphide bodies in the Cornwallis district, which are attributed to a chemically uniform, regional mineralising-fluid: 1) the ability to sustain sufficient fluid flux supplying metals +/- sulphur; 2) the ability to sustain TSR at a sufficient rate for continued precipitation; and 3) a pre-existing reservoir of sulphide to initiate mineralisation processes. Topographically driven fluid flow links (a) early Zn mineralisation caused by fluid mixing to the main Zn mineralisation stage produced

by in-situ reduction of a single fluid, and (b) the main, formation-water-related, Zn-dominant mineralisation to late, comparatively rare, meteoric-related, Cu-dominated mineralisation. It cannot be assumed that the precipitation mechanism of an ore deposit is uniform throughout its mineralisation history, and that, depending on the paragenetic stage of mineralisation, mineralisation may be categorised under different precipitation models (e.g., mixing and in situ reduction models) for the same deposit.

2.8 Acknowledgements

The Geological Survey of Canada (Calgary and Québec) is acknowledged for the loan of specimens [some previously reported in Savard et al. (2000)] originally collected by R. Sharp and K. Dewing (then employed by Cominco Ltd. and Polaris mine) from Polaris, Eclipse, Truro, and Markham Point. Samples from Seal and Typhoon were collected by JPM; Aston Bay Holdings is gratefully acknowledged for providing site access. Samples from all other showings were collected by ECT during a mapping campaign funded by Canada-Nunavut Geoscience Office. The fluid inclusion microthermometry laboratory at Laurentian University was funded by an NSERC grant to D.J. Kontak. Stipend for PhD study was provided by Goodman School of Mines and NSERC Discovery Grant to E.C. Turner. All analytical work was funded by NSERC-DG grant to E.C. Turner. The authors wish to thank R. Sharpe at the Manitoba Isotope Research Facility (MIRF), University of Manitoba for assistance with SIMS analyses, Dr. J. Petrus at Laurentian University, for help with laser ablation ICP-MS analysis, and Dr. W. Zhe at Laurentian University, for help with the SEM-EDS analysis. W. Desjardins prepared the thin sections at Laurentian University.

2.9 References

- Algeo, T. J., and Maynard, J. B., 2004, Trace-element behavior and redox facies in core shales of Upper Pennsylvanian Kansas-type cyclothems: *Chemical Geology*, v. 206, p. 289–318.
- Alibo, D. S., and Nozaki, Y., 1999, Rare earth elements in seawater: particle association, shale-normalization, and Ce oxidation: *Geochimica et Cosmochimica Acta*, v. 63, p. 363–372.
- Anderson, G. M., 2008, The mixing hypothesis and the origin of Mississippi Valley-type ore deposits: *Economic Geology*, v. 103, p. 1683–1690.
- Anderson, I. K., Ashton, J. H., Boyce, A. J., Fallick, A. E., and Russell, M. J., 1998, Ore depositional process in the Navan Zn-Pb deposit, Ireland: *Economic Geology*, v. 93, p. 535–563.
- Appold, M. S., and Wenz, Z. J., 2011, Composition of ore fluid inclusions from the Viburnum Trend, Southeast Missouri District, United States: Implications for transport and precipitation mechanisms: *Economic Geology*, v. 106, p. 55–78.
- Banner, J. L., Hanson, G. N., and Meyers, W. J., 1988, Rare earth element and Nd isotopic variations in regionally extensive dolomites from the Burlington-Keokuk Formation (Mississippian): implications for REE mobility during carbonate diagenesis: *Journal of Sedimentary Petrology*, v. 58, p. 415–432.
- Barker, S. L. L., and Cox, S. F., 2011, Oscillatory zoning and trace element incorporation in hydrothermal minerals: insights from calcite growth experiments: REE zoning in calcite: experimental insights: *Geofluids*, v. 11, p. 48–56.
- Barrie, C. D., Boyce, A. J., Boyle, A. P., Williams, P. J., Blake, K., Wilkinson, J. J., Lowther, M., McDermott, P., and Prior, D. J., 2009, On the growth of colloform textures: a case study of sphalerite from the Galmoy ore body, Ireland: *Journal of the Geological Society*, v. 166, p. 563–582.
- Basuki, N.I., Spooner, E.T.C., 2002, A review of fluid inclusion temperatures and salinities in Mississippi Valley-type Zn-Pb deposits: Identifying thresholds for metal transport: *Exploration Mining Geology*, v. 11, p. 1-17.
- Basuki, N. I., Taylor, B. E., and Spooner, E. T. C., 2008, Sulfur isotope evidence for thermochemical reduction of dissolved sulfate in Mississippi valley-type zinc-lead mineralization, Bongara area, northern Peru: *Economic Geology*, v. 103, p. 783–799.

- Bau, M., and Alexander, B., 2006, Preservation of primary REE patterns without Ce anomaly during dolomitization of Mid-Paleoproterozoic limestone and the potential re-establishment of marine anoxia immediately after the “Great Oxidation Event”: *South African Journal of Geology*, v. 109, p. 81–86.
- Bau, M., Möller, P., and Dulski, P., 1997, Yttrium and lanthanides in eastern Mediterranean seawater and their fractionation during redox cycling: *Marine Chemistry*, v. 56, p. 123–131.
- Bau, M., Romer, R. L., Lüders, V., and Dulski, P., 2003, Tracing element sources of hydrothermal mineral deposits: REE and Y distribution and Sr-Nd-Pb isotopes in fluorite from MVT deposits in the Pennine Orefield, England: *Mineralium Deposita*, v. 38, p. 992–1008.
- Bauer, M. E., Burisch, M., Ostendorf, J., Krause, J., Frenzel, M., Seifert, T., and Gutzmer, J., 2019, Trace element geochemistry of sphalerite in contrasting hydrothermal fluid systems of the Freiberg district, Germany: insights from LA-ICP-MS analysis, near-infrared light microthermometry of sphalerite-hosted fluid inclusions, and sulfur isotope geochemistry: *Mineralium Deposita*, v. 54, p. 237–262.
- Belissant, R., Boiron, M.-C., Luais, B., and Cathelineau, M., 2014, LA-ICP-MS analyses of minor and trace elements and bulk Ge isotopes in zoned Ge-rich sphalerites from the Noailhac – Saint-Salvy deposit (France): Insights into incorporation mechanisms and ore deposition processes: *Geochimica et Cosmochimica Acta*, v. 126, p. 518–540.
- Belissant, R., Muñoz, M., Boiron, M.-C., Luais, B., and Mathon, O., 2016, Distribution and oxidation state of Ge, Cu and Fe in sphalerite by μ -XRF and K-edge μ -XANES: insights into Ge incorporation, partitioning and isotopic fractionation: *Geochimica et Cosmochimica Acta*, v. 177, p. 298–314.
- Bethke, C. M., 1983, A numerical model of compaction-driven groundwater flow and heat transfer and its application to the paleohydrology of the intracratonic sedimentary basins: *Journal of Geophysical Research*, v. 90, p. 6817–6828.
- Bodnar, R. J., 1993, Revised equation and table for determining the freezing point depression of H₂O-NaCl solutions: *Geochimica et Cosmochimica Acta*, v. 57, p. 683–684.
- Bodnar, R. J., and Vityk, M. O., 1994, Interpretation of microthermometric data for H₂O-NaCl fluid inclusions, in De Vivo, B. and Frezzotti, M. L. eds., *Fluid inclusions in minerals, methods and applications*: Virginia Tech, Blacksburg, V.A., p. 117–30.
- Brown, A. C., 2009, A process-based approach to estimating the copper derived from red beds in the sediment-hosted stratiform copper deposit model: *Economic Geology*, v. 104, p. 857–868.

- Brueckner, S. M., Piercey, S. J., Layne, G. D., Piercey, G., and Sylvester, P. J., 2015, Variations of sulphur isotope signatures in sulphides from the metamorphosed Ming Cu(-Au) volcanogenic massive sulphide deposit, Newfoundland Appalachians, Canada: *Mineralium Deposita*, v. 50, p. 619–640.
- Cathles, L. M., and Smith, A. T., 1983, Thermal constraints on the formation of Mississippi Valley-type lead-zinc deposits, and their implications for episodic dewatering and deposit genesis: *Economic Geology*, v. 78, p. 948–956.
- Channer, D. M., Randell, R. N., Bray, C. J., and Spooner, E. T. C., 1993, Combined gas and ion chromatographic analysis of fluid inclusions: Application to the Polaris MVT Pb-Zn deposit, Canadian Arctic archipelago, Canada: *Geofluids '93 Extended Abstracts*, p. 342–346.
- Chi, G., Kontak, D. J., and Williams-Jones, A. E., 1998, Fluid composition and thermal regime during Zn-Pb mineralization in the lower Windsor Group, Nova Scotia, Canada: *Economic Geology*, v. 93, p. 883–895.
- Christensen, J. N., Halliday, A. N., Leigh, K. E., Randell, R. N., and Kesler, S. E., 1995, Direct dating of sulfides by Rb Sr: A critical test using the Polaris Mississippi Valley-type Zn- Pb deposit: *Geochimica et Cosmochimica Acta*, v. 59, p. 5191–5197.
- Cook, N. J., Ciobanu, C. L., Pring, A., Skinner, W., Shimizu, M., Danyushevsky, L., Saini-Eidukat, B., and Melcher, F., 2009, Trace and minor elements in sphalerite: A LA-ICPMS study: *Geochimica et Cosmochimica Acta*, v. 73, p. 4761–4791.
- Craddock, P. R., and Bach, W., 2010, Insights to magmatic–hydrothermal processes in the Manus back-arc basin as recorded by anhydrite: *Geochimica et Cosmochimica Acta*, v. 74, p. 5514–5536.
- Davies, G. R., and Krouse, H. R., 1975, Sulphur isotope distribution in Paleozoic sulphate evaporites, Canadian Arctic archipelago: *Geological Survey of Canada Paper*, v. 75–1B, p. 221–225.
- Davies, G. R., and Nassichuk, W. W., 1991, Carboniferous and Permian history of the Sverdrup Basin, Arctic Islands, in Trettin, H. P. ed., *Geology of the Inuitian Orogen and Arctic Platform of Canada and Greenland*, p. 345–368.
- Debruyne, D., Hulsbosch, N., and Mucchez, P., 2016, Unraveling rare earth element signatures in hydrothermal carbonate minerals using a source–sink system: *Ore Geology Reviews*, v. 72, p. 232–252.

- Dewing, K., and Nowlan, G. S., 2004, Correlation chart of Cambrian and Ordovician stratigraphy, Arctic Islands, Nunavut, Canada: Geological Survey of Canada Open File, v. 1837, p. 1.
- Dewing, K., and Obermajer, M., 2009, Lower Paleozoic thermal maturity and hydrocarbon potential of the Canadian Arctic Archipelago: *Bulletin of Canadian Petroleum Geology*, v. 57, p. 141–166.
- Dewing, K., and Turner, E. C., 2003, Structural setting of the Cornwallis lead-zinc district, Arctic Islands, Nunavut: 2003-B4.
- Dewing, K., Sharp, R. J., and Turner, E. C., 2007, Synopsis of the Polaris Zn-Pb district, Canadian Arctic Islands, Nunavut, in Goodfellow, W. D. ed., *Mineral Deposits of Canada: A synthesis of major deposit-types, district metallogeny, the evolution of geological provinces, and exploration methods*: p. 655–672.
- Dixon, O. A., Williams, S. R., and Dixon, J., 1971, The Aston Formation (?Proterozoic) on Prince of Wales Island, Arctic Canada: *Canadian Journal of Earth Sciences*, v. 8, p. 732–742.
- Elliott, H. A. L., Gernon, T. M., Roberts, S., Boyce, A. J., and Hewson, C., 2019, Diatremes act as fluid conduits for Zn-Pb mineralization in the SW Irish Ore Field: *Economic Geology*, v. 114, p. 117–125.
- Embry, A. F., 1991, Middle-Upper Devonian clastic wedge of the Arctic Islands, in Trettin, H. P. ed., *Geology of the Inuitian Orogen and Arctic Platform of Canada and Greenland*, p. 261–291.
- Fallick, A. E., Ashton, J. H., Boyce, A. J., Ellam, R. M., and Russell, M. J., 2001, Bacteria were responsible for the magnitude of the world-class hydrothermal base metal sulfide orebody at Navan, Ireland: *Economic Geology*, v. 96, p. 885–890.
- Fazli, S., Taghipour, B., Moore, F., and Lentz, D. R., 2019, Fluid inclusions, S isotopes, and Pb isotopes characteristics of the Kuh-e-Surmeh carbonate-hosted Zn-Pb deposit in the Zagros Fold Belt, southwest Iran: Implications for the source of metals and sulfur and MVT genetic model: *Ore Geology Reviews*, v. 109, p. 615–629.
- Field, J. D., Appold, M. S., Renson, V., and Coveney, R. M., 2018, Lead and sulfur isotope composition of trace occurrences of Mississippi Valley-type mineralization in the U.S. midcontinent: *Journal of Geochemical Exploration*, v. 184, p. 66–81.
- Field, J. D., Appold, M. S., Coveney, R. M., and Bodnar, R. J., 2020, Geochemical characteristics of trace occurrences of Mississippi Valley-type mineralization in the U.S.

- mid-continent: Implications for deposit growth: *Journal of Geochemical Exploration*, v. 213, p. 106514.
- Fitzsimons, I. C. W., Harte, B., and Clark, R. M., 2000, SIMS stable isotope measurement: counting statistics and analytical precision: *Mineralogical Magazine*, v. 64, p. 59–83.
- Ford, T. D., and Worley, N. E., 2016, Mineralization of the South Pennine Orefield, UK—A review: *Proceedings of the Yorkshire Geological Society*, v. 61, p. 55–86.
- Freeze, R. A., and Witherspoon, P. A., 1967, Theoretical analysis of regional groundwater flow. 2. Effects of water-table configuration and subsurface permeability variation: *Water Resources Research*, v. 3, p. 623–634.
- Frisch, T., and Trettin, H. P., 1991, Precambrian successions in the northernmost part of the Canadian Shield, in Trettin, H. P. ed., *Geology of the Innuitian Orogen and Arctic Platform of Canada and Greenland*, p. 101–108.
- Gagnevin, D., Menuge, J. F., Kronz, A., Barrie, C., and Boyce, A. J., 2014, Minor elements in layered sphalerite as a record of fluid origin, Mixing, and crystallization in the Navan Zn-Pb ore deposit, Ireland: *Economic Geology*, v. 109, p. 1513–1528.
- Garven, G., and Freeze, R. A., 1984, Theoretical analysis of the role of groundwater flow in the genesis of stratabound ore deposits. 2. Quantitative results: *American Journal of Science*, v. 284, p. 112–1174.
- Garven, G., Appold, M. S., Toptygina, V. I., and Hazlett, T. J., 1999, Hydrogeologic modeling of the genesis of carbonate-hosted lead-zinc ores: *Hydrogeology Journal*, v. 7, p. 108–126.
- Garven, G., Raffensperger, J. P., Dumoulin, J. A., Bradley, D. A., Young, L. E., Kelley, K. D., and Leach, D. L., 2003, Coupled heat and fluid flow modeling of the Carboniferous Kuna Basin, Alaska: implications for the genesis of the Red Dog Pb-Zn-Ag-Ba ore district: *Journal of Geochemical Exploration*, v. 78–79, p. 215–219.
- George, L. L., Cook, N. J., and Ciobanu, C. L., 2016, Partitioning of trace elements in co-crystallized sphalerite–galena–chalcopyrite hydrothermal ores: *Ore Geology Reviews*, v. 77, p. 97–116.
- Goldhaber, M. B., Church, S. E., Doe, B. R., Aleinikoff, J. N., Brannon, J. C., Podosek, F. A., Mosier, E. L., Taylor, C. D., and Gent, C. A., 1995, Lead and sulfur isotope investigation of Paleozoic sedimentary rocks from the southern Midcontinent of the United States; implications for paleohydrology and ore genesis of the Southeast Missouri lead belts: *Economic Geology*, v. 90, p. 1875–1910.
- Goldstein, R. H., and Reynolds, T. J., 1994, Systematics of fluid inclusions in diagenetic minerals: *Society for Sedimentary Geology Short Course*, v. 31, p. 1–199.

- Gong, H., Rose, A. W., and Suhr, N. H., 1977, The geochemistry of cadmium in some sedimentary rocks: *Geochimica et Cosmochimica Acta*, v. 41, p. 1687–1692.
- Grundmann, W. H., 1977, Geology of the Viburnum No. 27 Mine, Viburnum Trend, Southeast Missouri: *Economic Geology*, v. 72, p. 349–364.
- Haeri-Ardakani, O., Al-Aasm, I., and Coniglio, M., 2013, Fracture mineralization and fluid flow evolution: an example from Ordovician-Devonian carbonates, southwestern Ontario, Canada: *Fracture mineralization and fluid flow evolution: Geofluids*, v. 13, p. 1–20.
- Hahn, K. E., Turner, E. C., Kontak, D. J., and Fayek, M., 2018, Fluid-chemical evidence for one billion years of fluid flow through Mesoproterozoic deep-water carbonate mounds (Nanisivik zinc district, Nunavut): *Geochimica et Cosmochimica Acta*, v. 223, p. 493–519.
- Harris, N. B., Mnich, C. A., Selby, D., and Korn, D., 2013, Minor and trace element and Re–Os chemistry of the Upper Devonian Woodford Shale, Permian Basin, west Texas: Insights into metal abundance and basin processes: *Chemical Geology*, v. 356, p. 76–93.
- Harrison, J. C., and de Freitas, T., 1996, New showings and new geological settings for mineral exploration in the Arctic Islands: 1996-B.
- Harrison, J. C., and de Freitas, T., 1999, Simplified bedrock geology Bathurst Island area, Figure 1 in Overview of bedrock geology: *Geological Survey of Canada Open File*, v. 3714, p. B1–B40.
- Harrison, J. C., Fox, F. G., and Okulitch, A. V., 1991, Late Devonian - Early Carboniferous deformation of the Parry Islands and Canrobert Hills Fold Belts, Bathurst and Melville Islands, in Trettin, H. P. ed., *Geology of the Innuitian Orogen and Arctic Platform of Canada and Greenland*, p. 321–333.
- Harrison, J. C., de Freitas, T., and Thorsteinsson, R., 1993, New field observations on the geology of Bathurst Island, Arctic Canada: Part B, structure and tectonic history: *Geological Survey of Canada Current Research*, v. 93–1B, p. 11–21.
- Harrison, J. C., Dewing, K., Lee, C. C., and Stasiuk, L. D., 1999, New mineral occurrences on northeastern Ellesmere Island and new opportunities for mineral exploration in northern Nunavut: 3822, 1–43 p.
- Harrison, J. C., Gilbert, C., Lynds, T., Ford, A., Thorsteinsson, R., Frisch, T., de Freitas, T., and Kerr, J. W., 2015, Geology, tectonic assemblage map of Alexandra Fiord, central Ellesmere and eastern Axel Heiberg islands, Nunavut: *Canadian Geoscience Map* 30.
- Harrison, J. C., Lynds, T., Ford, A., and Rainbird, R. H., 2016, Geology, Simplified tectonic assemblage map of the Canadian Arctic Islands, Northwest Territories–Nunavut: *Canadian Geoscience Map* 80.

- Haynes, F. M., and Kesler, S. E., 1987, Chemical evolution of brines during Mississippi Valley-type mineralization: evidence from East Tennessee and Pine Point: *Economic Geology*, v. 82, p. 53–71.
- Haynes, F. M., Sterner, S. M., and Bodnar, R. J., 1988, Synthetic fluid inclusions in natural quartz. IV. Chemical analyses of fluid inclusions by SEM/EDA: evaluation of method: *Geochimica et Cosmochimica Acta*, v. 52, p. 969–977.
- Henjes-Kunst, E., Raith, J. G., and Boyce, A. J., 2017, Micro-scale sulfur isotope and chemical variations in sphalerite from the Bleiberg Pb-Zn deposit, Eastern Alps, Austria: *Ore Geology Reviews*, v. 90, p. 52–62.
- Horita, J., 2014, Oxygen and carbon isotope fractionation in the system dolomite–water–CO₂ to elevated temperatures: *Geochimica et Cosmochimica Acta*, v. 129, p. 111–124.
- Inguaggiato, C., Iñiguez, E., Peiffer, L., Kretzschmar, T., Brusca, L., Mora-Amador, R., Ramirez, C., Bellomo, S., Gonzalez, G., and Rouwet, D., 2018, REE fractionation during the gypsum crystallization in hyperacid sulphate-rich brine: The Poás Volcano crater lake (Costa Rica) exploited as laboratory: *Gondwana Research*, v. 59, p. 87–96.
- Jiang, L., Cai, C., Worden, R. H., Li, K., Xiang, L., Chu, X., Shen, A., and Li, W., 2015, Rare earth element and yttrium (REY) geochemistry in carbonate reservoirs during deep burial diagenesis: Implications for REY mobility during thermochemical sulfate reduction: *Chemical Geology*, v. 415, p. 87–101.
- Jobert, S.-A., Dewing, K., and White, J. C., 2007, Structural geology and Zn-Pb mineral occurrences of northeastern Cornwallis Island: implications for exploration of the Cornwallis Fold Belt, northern Nunavut: *Bulletin of Canadian Petroleum Geology*, v. 55, p. 138–159.
- Jochum, K. P., Willbold, M., Raczek, I., Stoll, B., and Herwig, K., 2005, Chemical Characterisation of the USGS Reference Glasses GSA-1G, GSC-1G, GSD-1G, GSE-1G, BCR-2G, BHVO-2G and BIR-1G Using EPMA, ID-TIMS, ID-ICP-MS and LA-ICP-MS: *Geostandards and Geoanalytical Research*, v. 29, p. 285–302.
- Johnson, A.W., Shelton, K.L., Gregg, J.M., Somerville, I.D., Wright, W.R., Nagy, Z.R., 2009, Regional studies of dolomites and their included fluids: recognizing multiple chemically distinct fluids during the complex diagenetic history of Lower Carboniferous (Mississippian) rocks of the Irish Zn-Pb ore field. *Mineralogy and Petrology*, v. 96, p. 1-18.
- Jowett, E. C., 1975, Nature of the ore-forming fluids of the Polaris lead-zinc deposit, Little Cornwallis Island, N.W.T., from fluid inclusion studies:

- Kerr, J. W., 1967, Nares submarine rift valley and the relative rotation of North Greenland: *Bulletin of Canadian Petroleum Geology*, v. 15, p. 483–520.
- Kerr, J. W., 1974, Geology of Bathurst Island Group and Byam Markham Island, Arctic Canada: *Geological Survey of Canada Memoir*, v. 378, p. 152p.
- Kerr, J. Wm., 1977a, Cornwallis Fold Belt and the mechanism of basement uplift: *Canadian Journal of Earth Sciences*, v. 14, p. 1374–1401.
- Kerr, J. Wm., 1977b, Cornwallis Lead–Zinc District; Mississippi Valley-type deposits controlled by stratigraphy and tectonics: *Canadian Journal of Earth Sciences*, v. 14, p. 1402–1426.
- Kontak, D. J., 2004, Analysis of evaporate mounds as a complement to fluid-inclusion thermometric data: case studies from granitic environments in Nova Scotia and Peru: *Canadian Mineralogist*, v. 42, p. 1315–1329.
- Kuhlemann, J., Vennemann, T., Herlec, U., Zeeh, S., and Bechstädt, T., 2001, Variations of sulfur isotopes, trace element compositions, and cathodoluminescence of Mississippi Valley-type Pb-Zn ores from the Drau Range, eastern Alps (Slovenia-Austria): implications for ore deposition on a regional versus microscale: *Economic Geology*, v. 96, p. 1931–1941.
- Labotka, D. M., Panno, S. V., and Locke, R. A., 2016, A sulfate conundrum: Dissolved sulfates of deep-saline brines and carbonate-associated sulfates: *Geochimica et Cosmochimica Acta*, v. 190, p. 53–71.
- Large, R. R., Bull, S. W., and Maslennikov, V. V., 2011, A carbonaceous sedimentary source-rock model for Carlin-type and orogenic gold deposits: *Economic Geology*, v. 106, p. 331–358.
- Leach, D. L., Sangster, D. F., Kelley, K. D., Large, R. R., Garven, G., Allen, C. R., Gutzmer, J., and Walters, S., 2005, Sediment-hosted lead-zinc deposits: A global perspective, in *One Hundredth Anniversary Volume: Society of Economic Geologists*, p. 561-607.
- Leventhal, J. S., 1990, Organic matter and thermochemical sulfate reduction in the Viburnum Trend, southeast Missouri: *Economic Geology*, v. 85, p. 622–632.
- Li, X.-H., Fan, H.-R., Yang, K.-F., Hollings, P., Liu, X., Hu, F.-F., and Cai, Y.-C., 2018, Pyrite textures and compositions from the Zhuangzi Au deposit, southeastern North China Craton: implication for ore-forming processes: *Contributions to Mineralogy and Petrology*, v. 173, p. 73.
- Lin, J., Nilges, M. J., Wiens, E., Chen, N., Wang, S., and Pan, Y., 2019, Mechanism of Gd^{3+} uptake in gypsum ($CaSO_4 \cdot 2H_2O$): Implications for EPR dating, REE recovery and REE behavior: *Geochimica et Cosmochimica Acta*, v. 258, p. 63–78.

- Luo, K., Zhou, J.-X., Huang, Z.-L., Caulfield, J., Zhao, J.-X., Feng, Y.-X., and Ouyang, H., 2020, New insights into the evolution of Mississippi Valley-Type hydrothermal system: A case study of the Wusihe Pb-Zn deposit, South China, using quartz in-situ trace elements and sulfides in situ S-Pb isotopes: *American Mineralogist*, v. 105, p. 35–51.
- Luz, B., and Barkan, E., 2010, Variations of $^{17}\text{O}/^{16}\text{O}$ and $^{18}\text{O}/^{16}\text{O}$ in meteoric waters: *Geochimica et Cosmochimica Acta*, v. 74, p. 6276–6286.
- Machel, H. G., 2001, Bacterial and thermochemical sulfate reduction in diagenetic settings; old and new insight: *Sedimentary Geology*, v. 140, p. 143–173.
- MacRae, N. D., 1995, Secondary-ion mass spectrometry and geology: *The Canadian Mineralogist*, v. 33, p. 219–236.
- Mathieu, J., Kontak, D.J., Turner, E.C., 2013, A fluid inclusion study of diagenetic fluids in Proterozoic and Paleozoic carbonate rocks, Victoria Island, NWT: *Geofluids*, v. 13, p. 559–578.
- Mathieu, J., Kontak, D. J., Turner, E. C., Fayek, M., and Layne, G., 2015, Geochemistry of Phanerozoic diagenesis on Victoria Island, NWT, Canada: *Chemical Geology*, v. 415, p. 47–69.
- Mathieu, J., Turner, E. C., Kontak, D. J., Fayek, M., and Mathur, R., 2018, Atypical Cu mineralisation in the Cornwallis carbonate-hosted Zn district: Storm copper deposit, Arctic Canada: *Ore Geology Reviews*, v. 99, p. 86–115.
- Mayr, U., 1978, Stratigraphy and correlation of Lower Paleozoic formations, subsurface of Cornwallis, Devon, Somerset, and Russell islands, Canadian Arctic Archipelago: *GSC Bulletin* 276, 64p.
- Mayr, U., de Freitas, T., Elisbacher, G. H., and Kerr, J. Wm., 1998, *Geology, Prince Alfred Bay-Cardigan Strait and parts of adjacent sheets, Northwest Territories: Geological Survey of Canada, map 1924A.*
- Mayr, U., Frisch, T., de Freitas, T., Okulitch, A. V., and Kerr, J. W., 2003, *Geology, Eastern Prince of Wales Island and adjacent smaller islands, Nunavut: Map 2016A.*
- Miall, A. D., 1986, Effects of Caledonian tectonism in Arctic Canada: *Geology*, v. 14, p. 904–907.
- Mitchell, I., Linnen, R. L., and Creaser, R. A., 2004, The Setting and Age of the Bermuda Zn-Pb Showing, Grinnell Peninsula, Devon Island: Implications for MVT mineralization in the Canadian Arctic: *Exploration Mining Geology*, v. 13, p. 109–118.

- Morales-Casique, E., Guinzberg-Belmont, J., and Ortega-Guerrero, A., 2016, Regional groundwater flow and geochemical evolution in the Amacuzac River Basin, Mexico: *Hydrogeology Journal*, v. 24, p. 1873–1890.
- Morris, G. A., Page, L., and Martinez, V., 2005, New dates (415 Ma) for the Etive Dyke Swarm and the end of the Caledonian Orogeny in the SW Grampian highlands of Scotland: *Journal of the Geological Society of London*, v. 162, p. 741–744.
- Morrow, D. W., and Kerr, J. W., 1977, Stratigraphy and sedimentology of lower Paleozoic formations near Prince Alfred Bay area, Devon Island: *Geological Survey of Canada Bulletin*, v. 254, p. 122.
- Mossop, G. D., 1979, The evaporites of the Ordovician Baumann Fiord Formation, Ellesmere Island: *Geological Survey of Canada Bulletin*, v. 298, p. 52.
- Murr, L. E., 1974, Ordered lattice defects in colored fluorite: direct observations: *Science*, v. 183, p. 206–208.
- Nassau, K., 1978, The origin of colours in minerals: *American Mineralogist*, v. 63, p. 219–229.
- Nothdurft, L. D., Webb, G. E., and Kamber, B. S., 2004, Rare earth element geochemistry of Late Devonian reefal carbonates, Canning Basin, Western Australia: confirmation of a seawater REE proxy in ancient limestones: *Geochimica et Cosmochimica Acta*, v. 68, p. 263–283.
- Nozaki, Y., Zhang, J., and Amakawa, H., 1997, The fractionation between Y and Ho in the marine environment: *Earth and Planetary Science Letters*, v. 148, p. 329–340.
- Ohmoto, H., and Rye, R. O., 1979, Isotopes of sulfur and carbon, in Barnes, H. L. ed., *Geochemistry of Hydrothermal Ore Deposits*: New York, USA, Wiley, p. 50–567.
- Okulitch, A. V., 1991, Late Devonian - Early Carboniferous deformation of the Central Ellesmere and Jones Sound Fold Belts, in Trettin, H. P. ed., *Geology of the Innuitian Orogen and Arctic Platform of Canada and Greenland*, p. 318–320.
- Okulitch, A. V., Packard, J. J., and Zolnai, A. I., 1991, Late Silurian - Early Devonian deformation of the Boothia Uplift, in Trettin, H. P. ed., *Geology of the Innuitian Orogen and Arctic Platform of Canada and Greenland*, p. 302–307.
- Oliver, G. J. H., 2001, Reconstruction of the Grampian episode in Scotland its place in the Caledonian Orogeny: *Tectonophysics*, v. 332, p. 23–49.
- O’Neil, J. R., Clayton, R. N., and Mayeda, T. K., 1969, Oxygen isotope fractionation in divalent metal carbonates: *The Journal of Chemical Physics*, v. 51, p. 5547–5558.

- Osselin, F., Saad, S., Nightingale, M., Hearn, G., Desautly, A.-M., Gaucher, E. C., Clarkson, C. R., Kloppmann, W., and Mayer, B., 2019, Geochemical and sulfate isotopic evolution of flowback and produced waters reveals water-rock interactions following hydraulic fracturing of a tight hydrocarbon reservoir: *Science of The Total Environment*, v. 687, p. 1389–1400.
- Pacevski, A., Moritz, R., Kouzmanov, K., Marquardt, K., Zivkovic, P., and Cvetkovic, L., 2012, Texture and composition of Pb-bearing pyrite from the Coka Marin polymetallic deposit, Serbia, controlled by nanoscale inclusions: *The Canadian Mineralogist*, v. 50, p. 1–20.
- Passey, B. H., and Ji, H., 2019, Triple oxygen isotope signatures of evaporation in lake waters and carbonates: A case study from the western United States: *Earth and Planetary Science Letters*, v. 518, p. 1–12.
- Paytan, A., and Gray, E. T., 2012, Sulfur isotope stratigraphy, in *The Geologic Time Scale*: Elsevier, p. 167–180.
- Peevler, J., Fayek, M., Misra, K. C., and Riciputi, L. R., 2003, Sulfur isotope microanalysis of sphalerite by SIMS: constraints on the genesis of Mississippi Valley-type mineralization, from the Mascot-Jefferson City district, East Tennessee: *Journal of Geochemical Exploration*, v. 80, p. 277–296.
- Pfaff, K., Koenig, A., Wenzel, T., Ridley, I., Hildebrandt, L. H., Leach, D. L., and Markl, G., 2011, Trace and minor element variations and sulfur isotopes in crystalline and colloform ZnS: Incorporation mechanisms and implications for their genesis: *Chemical Geology*.
- Piepjohn, K., von Gosen, W., and Tessensohn, F., 2016, The Eureka deformation in the Arctic: an outline: *Journal of the Geological Society*, v. 173, p. 1007–1024.
- Pourmand, A., Dauphas, N., and Ireland, T. J., 2012, A novel extraction chromatography and MC-ICP-MS technique for rapid analysis of REE, Sc and Y: Revising CI-chondrite and Post-Archean Australian Shale (PAAS) abundances: *Chemical Geology*, v. 291, p. 38–54.
- Ramdohr, P., 1969, *The Ore minerals and their intergrowths*: Pergamon Press, 1174 p.
- Randell, R. N., 1994, *Geology of the Polaris Zn-Pb Mississippi Valley-type deposit, Canadian Arctic Archipelago*. Unpublished Ph.D. thesis, University of Toronto, Toronto, Ontario, 819 p.
- Randell, R. N., and Anderson, G. M., 1996, Geology of the Polaris Zn-Pb Deposit and surrounding area, Canadian Arctic archipelago, in *Carbonate-hosted lead-zinc deposits*: Society of Economic Geologists, p. 307–319.

- Randell, R. N., Héroux, Y., Chagnon, A., and Anderson, G. M., 1996, Organic matter and clay minerals at the Polaris Zn-Pb Deposit, Canadian Arctic archipelago, in Carbonate-hosted lead-zinc deposits: Society of Economic Geologists, p. 320–329.
- Reid, S., Dewing, K., and Sharp, R., 2013a, Polaris as a guide to northern exploration: Ore textures, paragenesis and the origin of the carbonate-hosted Polaris Zn–Pb Mine, Nunavut, Canada: Ore Geology Reviews, v. 51, p. 27–42.
- Reid, S., Dewing, K., and Sharp, R., 2013b, Structural and diagenetic origin of breccias in the carbonate-hosted Polaris Zn–Pb deposit, Nunavut, Canada: Ore Geology Reviews, v. 55, p. 110–124.
- Robinson, B. W., 1973, Sulfur isotope equilibrium during sulfur hydrolysis at high temperatures: Earth and Planetary Science Letters, v. 18, p. 443–450.
- Robinson, J., and Atkinson, B., 2012, Technical report on the exploration history and current status of the Storm Project, Somerset Island, Nunavut.
- Roedder, E., 1968, The non-colloidal origin of “colloform” textures in sphalerite ores: Economic Geology, v. 63, p. 451–471.
- Roedder, E., 1977, Fluid inclusion studies of ore deposits in the Viburnum Trend, Southeast Missouri: Economic Geology, v. 72, p. 474–479.
- Roedder, E., 1984, Interpretation and utilization of inclusion measurements - compositional data on liquid and gas inclusions, in Fluid inclusions: An introduction to studies of all types of fluid inclusions, gas, liquid, or melt, trapped in materials from Earth and space, and their application to the understanding of geologic processes: Mineralogical Society of America, p. 644.
- Rollinson, H. R., 1993, Using geochemical data; evaluation, presentation, interpretation: Longman Scientific and Technical, Harlow, United Kingdom, 352 p.
- Ronchi, P., Masetti, D., Tassan, S., and Camocino, D., 2012, Hydrothermal dolomitization in platform and basin carbonate successions during thrusting: A hydrocarbon reservoir analogue (Mesozoic of Venetian Southern Alps, Italy): Marine and Petroleum Geology, v. 29, p. 68–89.
- Rose, A. W., 1989, Mobility of copper and other heavy metals in sedimentary environments, in Boyle, R. W., Brown, A. C., Jefferson, C. W., Jowett, E. C., and Kirkham, R. eds., Geological Association of Canada Special Paper, p. 97–110.
- Rose, S., 1999, Sedimentology and diagenesis of the lower Blue Fiord Formation carbonates in a prospective Mississippi-Valley-type (Pb-Zn) setting M.Sc.: Calgary, Alberta, University of Calgary: 189 p.

- Savard, M. M., Chi, G., Sami, T., Williams-Jones, A. E., and Leigh, K., 2000, Fluid inclusion and carbon, oxygen, and strontium isotope study of the Polaris Mississippi Valley-type Zn-Pb deposit, Canadian Arctic Archipelago: implications for ore genesis: *Mineralium Deposita*, v. 35, p. 495–510.
- Seal, R. R., 2006, Sulfur Isotope Geochemistry of Sulfide Minerals: *Reviews in Mineralogy and Geochemistry*, v. 61, p. 633–677.
- Selby, D., Creaser, R., Dewing, K., and Fowler, M., 2005, Evaluation of bitumen as a Re–Os geochronometer for hydrocarbon maturation and migration: A test case from the Polaris MVT deposit, Canada: *Earth and Planetary Science Letters*, v. 235, p. 1–15.
- Shelton, K.L., Hendry, J., Gregg, J.M., Truesdale, J.P., Somerville, I.D., 2019, Fluid circulation and fault- and fracture-related diagenesis in Mississippian synrift carbonate rocks on the northeast margin of the metalliferous Dublin Basin, Ireland, *Journal of Sedimentary Research*, v, 89, p. 508-536.
- Shelton, K. L., Cavender, B. D., Perry, L. E., Schiffbauer, J. D., Appold, M. S., Burstein, I., and Fike, D. A., 2020, Stable isotope and fluid inclusion studies of early Zn-Cu-(Ni-Co)-rich ores, lower ore zone of Brushy Creek mine, Viburnum Trend MVT district, Missouri, U.S.A.: Products of multiple sulfur sources and metal-specific fluids: *Ore Geology Reviews*, v. 118, 26p.
- Si, R., Gu, X., Xiao, C., Yu, H., Wang, Z., Chen, Y.-J., and Qiu, N., 2011, Geochemical character of trace elements in sphalerite from Fule Pb-Zn Deposit, Yunnan Province: *Journal of Mineralogy and Petrology*, v. 31, p. 34–40.
- Simbo, C. W., Potra, A., and Samuelsen, J. R., 2019, A geochemical evaluation of the genetic relationship between Ouachita Mountains Paleozoic rocks and the Mississippi Valley-type mineralization in the southern Ozark Region, USA: *Ore Geology Reviews*, v. 112, 18p.
- Steele-MacInnis, M., Ridley, J., Lecumberri-Sanchez, P., Schlegel, T. U., and Heinrich, C. A., 2016, Application of low-temperature microthermometric data for interpreting multicomponent fluid inclusion compositions: *Earth-Science Reviews*, v. 159, p. 14–35.
- Stewart, W. D., 1987, Late Proterozoic to Early Tertiary stratigraphy of Somerset Island and northern Boothia Peninsula, District of Franklin, N.W.T.: *Geological Survey of Canada Paper*, v. 83–26, p. 85.
- Stewart, W. D., and Kerr, J. W., 1984, *Geology of Somerset Island north, District of Franklin: Geological Survey of Canada, map 1595A.*

- Sun, X., Chen, J., Tan, H., Rao, W., Wang, Y., Liu, X., and Su, Z., 2009, Study on the mechanism of isotope fractionation in soil water during the evaporation process under equilibrium condition: *Chinese Journal of Geochemistry*, v. 28, p. 351–357.
- Sverjensky, D.A., 1986, Genesis of Mississippi Valley-type lead-zinc deposits: *Annual Review of Earth and Planetary Science*, 14, p. 177-199.
- Symons, D. T. A., and Sangster, D. F., 1992, Late Devonian paleomagnetic age for the Polaris Mississippi Valley-type Zn-Pb deposit, Canadian Arctic Archipelago: *Canadian Journal of Earth Sciences*, v. 29, p. 15–25.
- Tegner, C., Storey, M., Holm, P. M., Thorarinsson, S. B., Zhao, X., Lo, C.-H., and Knudsen, M. F., 2011, Magmatism and Eureka deformation in the High Arctic large igneous province: ^{40}Ar – ^{39}Ar age of Kap Washington Group volcanics, North Greenland: *Earth and Planetary Science Letters*, v. 303, p. 203–214.
- Thom, J., and Anderson, G. M., 2008, The role of thermochemical sulfate reduction in the origin of Mississippi Valley-type deposits. I. Experimental results: *Geofluids*, v. 8, p. 16-26
- Thorsteinsson, R., 1958, Cornwallis and Little Cornwallis islands district of Franklin Northwest Territories: v. 294, p. 144.
- Thorsteinsson, R., 1974, Carboniferous and Permian stratigraphy of Axel Heiberg Island and western Ellesmere Island, Canadian Arctic Archipelago: *Geological Survey of Canada Bulletin*, v. 224, p. 115.
- Thorsteinsson, R., 1980, Part 1. Contributions to stratigraphy, in *Stratigraphy and conodonts of Upper Silurian and Lower Devonian rocks in the environs of the Boothia Uplift, Canadian Arctic Archipelago*, p. 1–38.
- Thorsteinsson, R., 1986, *Geology of Cornwallis Island and neighbouring smaller island, District of Franklin, Northwest Territories: Map 1626A.*
- Torsvik, T. H., Van der Voo, R., Preeden, U., Mac Niocaill, C., Steinberger, B., Doubrovine, P. V., van Hinsbergen, D. J. J., Domeier, M., Gaina, C., Tohver, E., Meert, J. G., McCausland, P. J. A., and Cocks, L. R. M., 2012, Phanerozoic polar wander, palaeogeography and dynamics: *Earth-Science Reviews*, v. 114, p. 325–368.
- Trettin, H. P., 1988, Early Namurian (or older) alkali basalt in the Borup Fiord Formation, northern Axel Heiberg Island, Arctic Canada: *Geological Survey of Canada Paper*, v. 88–1D, p. 21–26.

- Trettin, H. P., 1991a, Middle Devonian to Early Carboniferous deformations, northern Ellesmere and Axel Heiberg islands, in Trettin, H. P. ed., *Geology of the Innuitian Orogen and Arctic Platform of Canada and Greenland*, p. 309–317.
- Trettin, H. P., 1991b, Tectonic framework, in *Geology of the Innuitian Orogen and Arctic Platform of Canada and Greenland*, p. 57–66.
- Trettin, H. P., Mayr, U., Long, D. G. F., and Packard, J. J., 1991, Cambrian to Early Devonian basin development, sedimentation and volcanism, in Trettin, H. P. ed., *Geology of the Innuitian Orogen and Arctic Platform of Canada and Greenland*, p. 163–238.
- Trotter, J. A., Barnes, C. R., and McCracken, A. D., 2016, Rare earth elements in conodont apatite: Seawater or pore-water signatures? *Palaeogeography, Palaeoclimatology, Palaeoecology*, v. 462, p. 92–100.
- Turner, E., and Dewing, K., 2002, *Geology of Rookery Creek zinc-lead showings, Cornwallis Island, Nunavut: 2002-B2*.
- Turner, E. C., 2001, *Investigation of zinc-lead mineralization on eastern Cornwallis Island, Arctic Archipelago, Nunavut: 2001-B2*.
- Turner, E. C., 2015, *Gossans of the Cornwallis District, central high Arctic Islands, Canada: Geological Survey of Canada Open File*, v. 7718, p. 54–57.
- Turner, E. C., and Dewing, K., 2004, *Geology of Little Cornwallis Island and Rookery Creek (Cornwallis Island), Nunavut: Geological Survey of Canada Open File*, v. 1780.
- Turner, E. C., and Kamber, B. S., 2012, Arctic Bay Formation, Borden Basin, Nunavut (Canada): Basin evolution, black shale, and dissolved metal systematics in the Mesoproterozoic ocean: *Precambrian Research*, v. 208–211, p. 1–18.
- Ward, W. C., and Halley, R. B., 1985, Dolomitization in a mixing zone of near-seawater composition, Late Pleistocene, northeastern Yucatan Peninsula: *Journal of Sedimentary Petrology*, v. 55, p. 407–420.
- White, D.E., 1974, Diverse origins of hydrothermal ore fluids, *Economic Geology*, 69, p. 954–973.
- Wilkinson, J. J., 2010, A review of fluid inclusion constraints on mineralization in the Irish Ore Field and implications for the genesis of sediment-hosted Zn-Pb deposits: *Economic Geology*, v. 105, p. 417–442.
- Wilson, S. A., Ridley, W. I., and Koenig, A. E., 2002, Development of sulfide calibration standards for the laser ablation inductively-coupled plasma mass spectrometry technique: *J. Anal. At. Spectrom.*, v. 17, p. 406–409.

- Wright, C., 2002, Spectroscopic characterization of fluorite: relationships between trace element zoning, defects and color. MSc Thesis: Oxford, OH, Miami University: 190 p.
- Xia, X., Ellis, G. S., Ma, Q., and Tang, Y., 2014, Compositional and stable carbon isotopic fractionation during non-autocatalytic thermochemical sulfate reduction by gaseous hydrocarbons: *Geochimica et Cosmochimica Acta*, v. 139, p. 472–486.
- Yang, J., 2006, Finite element modeling of transient saline hydrothermal fluids in multifaulted sedimentary basins: implications for ore-forming processes: *Canadian Journal of Earth Sciences*, v. 43, p. 1331–1340.
- Yang, J., Feng, Z., Luo, X., and Chen, Y., 2010, Three-dimensional numerical modeling of salinity variations in driving basin-scale ore-forming fluid flow: Example from Mount Isa Basin, northern Australia: *Journal of Geochemical Exploration*, v. 106, p. 236–243.
- Ye, L., Cook, N. J., Ciobanu, C. L., Yuping, L., Qian, Z., Tiegeng, L., Wei, G., Yulong, Y., and Danyushevskiy, L., 2011, Trace and minor elements in sphalerite from base metal deposits in South China: A LA-ICPMS study: *Ore Geology Reviews*, v. 39, p. 188–217.
- Yuan, G., Cao, Y., Zhang, Y., and Gluyas, J., 2017a, Diagenesis and reservoir quality of sandstones with ancient “deep” incursion of meteoric freshwater—An example in the Nanpu Sag, Bohai Bay Basin, East China: *Marine and Petroleum Geology*, v. 82, p. 444–464.
- Yuan, S., Ellis, G. S., Chou, I.-M., and Burruss, R. C., 2017b, Experimental investigation on thermochemical sulfate reduction in the presence of 1-pentanethiol at 200 and 250 °C: Implications for in situ TSR processes occurring in some MVT deposits: *Ore Geology Reviews*, v. 91, p. 57–65.
- Yurtsever, Y., and Gat, J. R., 1981, Atmospheric waters, in Gat, J. R. and Gofiantini, R. eds., *Stable isotope hydrology deuterium and oxygen-18 in the water cycle*, p. 103–142.
- Zhang, T., Ellis, G. S., Ma, Q., Amrani, A., and Tang, Y., 2012, Kinetics of uncatalyzed thermochemical sulfate reduction: *Geochimica et Cosmochimica Acta*, v. 96, p. 1–17.
- Zhao, C., Hobbs, B. E., and Ord, A., 2018, Modeling of mountain topography effects on hydrothermal Pb-Zn mineralization patterns: Generic model approach: *Journal of Geochemical Exploration*, v. 190, p. 400–410.
- Zhao, H., Liu, W., Borjigin, T., Zhang, J., Luo, H., and Wang, X., 2019, Study of thermochemical sulfate reduction of different organic matter: Insight from systematic TSR simulation experiments: *Marine and Petroleum Geology*, v. 100, p. 434–446.

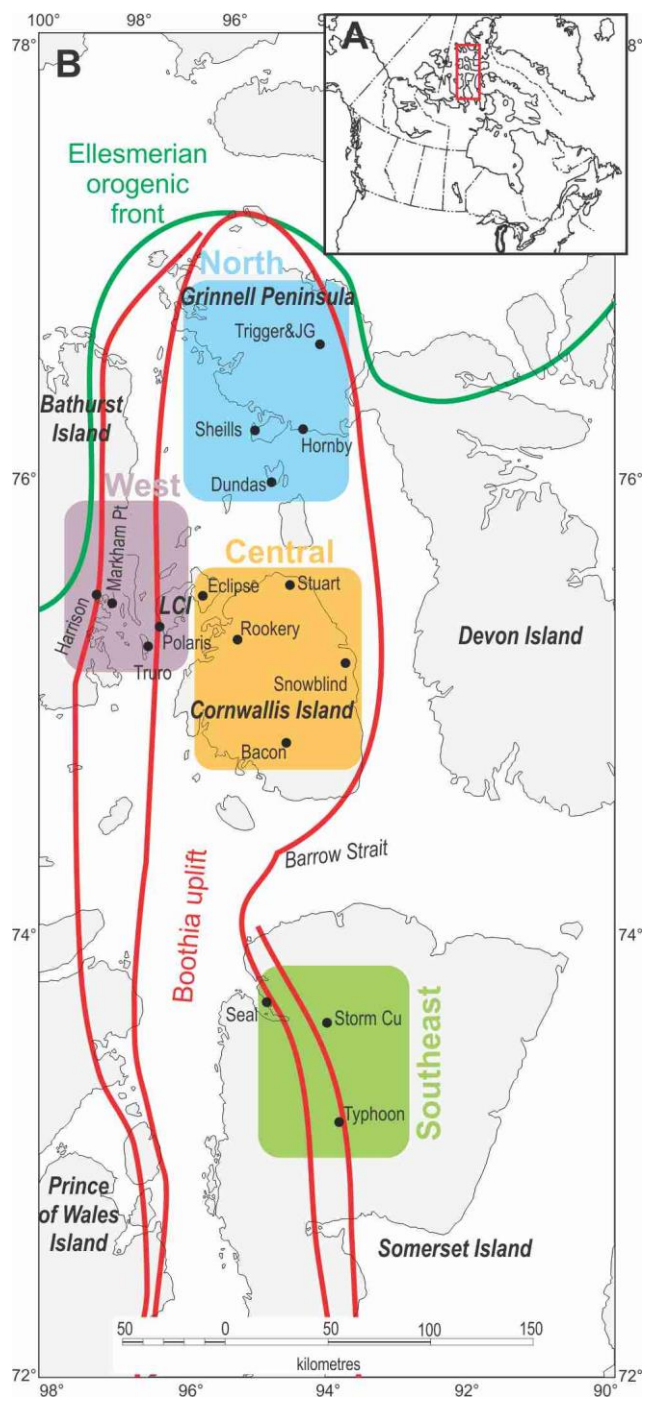


Figure 2-1: Study area

Location of study area in the Arctic islands of Canada. Rectangle is enlarged in (B). (B) Part of the Canadian Arctic archipelago, showing location of the Cornwallis district (rectangle) and base-metal showings in the district (modified from Dewing et al., 2007) form four geographic

regions; colour-coding for northern, southern, western, and central regions is also used in ensuing figures.

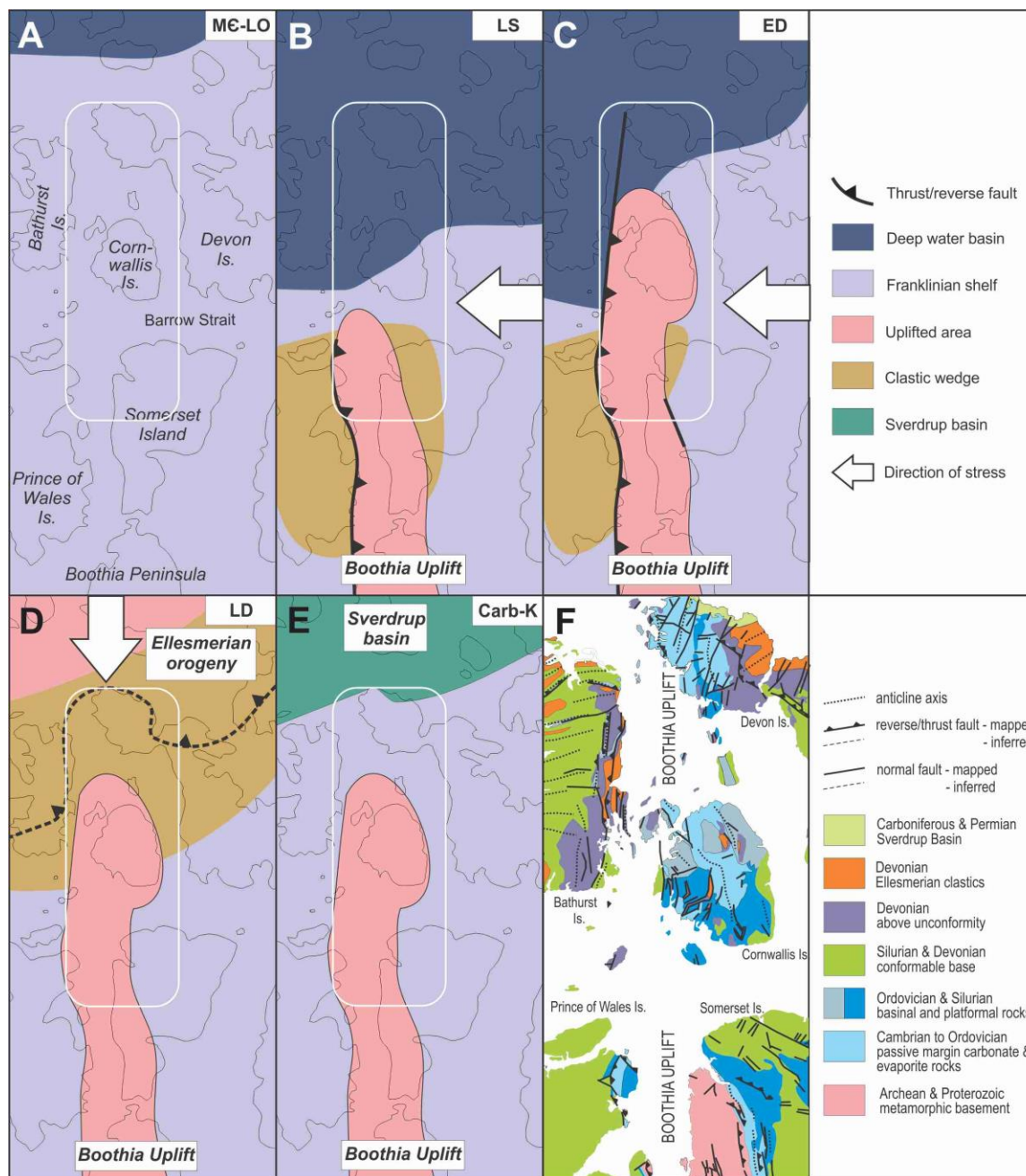


Figure 2-2: Paleogeography map of Franklinian Basin

Simplified maps of the Franklinian basin show paleogeography of continental margin depositional settings through the early to mid-Paleozoic (after Trettin et al., 1991); Cornwallis district outlined in white rectangle. (A) Margin between deep-water basin and shelf was relatively stable from Middle Cambrian to Late Ordovician, but started to migrate craton-wards (present-day south) in the Silurian. West-directed compressive far-field stress associated with the

Caledonian orogeny caused uplift in the central Arctic islands, in a north-trending elongate area termed the Boothia uplift, extending from the mainland (south) to northern Somerset Island in the (B) Late Silurian but reaching Grinnell Peninsula (Devon Island) by the Early Devonian (C). Sediment shed from the uplift was deposited as adjacent clastic aprons. (D) Late Devonian to Early Carboniferous south-directed compression caused by the Ellesmerian orogeny produced a large clastic wedge that covered many of the Arctic Islands. (E) Extension in the Carboniferous resulted in the Sverdrup basin northwest of the Cornwallis district. (F) The present-day exposure of the Cornwallis district shows the distribution of the different tectonic elements inherited from this depositional and deformational history composed of mixed carbonate-clastic successions (figure modified from Dewing et al., 2007).

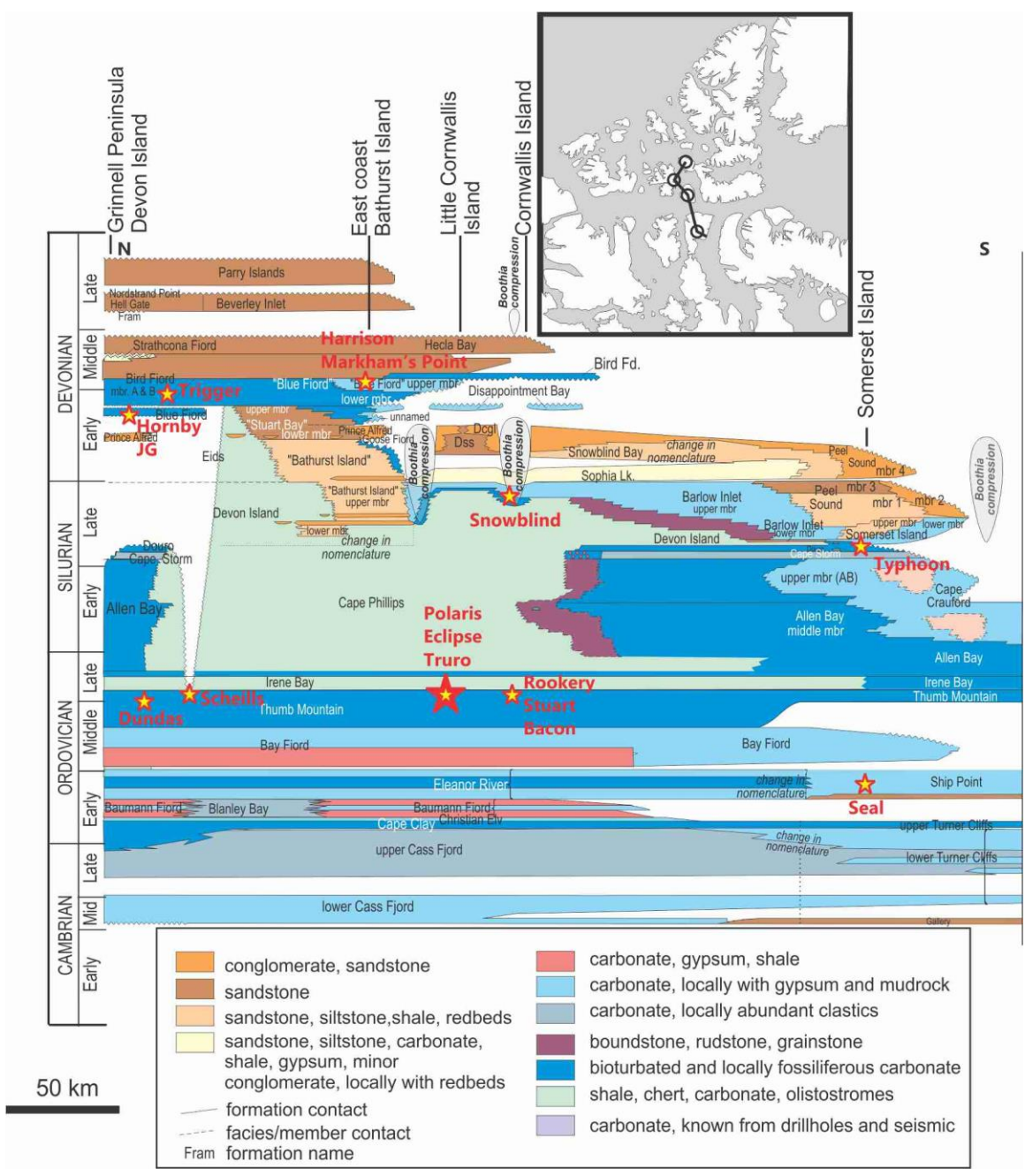


Figure 2-3: Stratigraphic correlation

North-south stratigraphic correlation panel that shows temporal and geographic distribution of early and middle Paleozoic formal stratigraphic units in the Cornwallis district [modified from Mayr et al. (1998) and Dewing et al. (2007)]. Stars indicate the stratigraphic and geographic positions of studied showings.

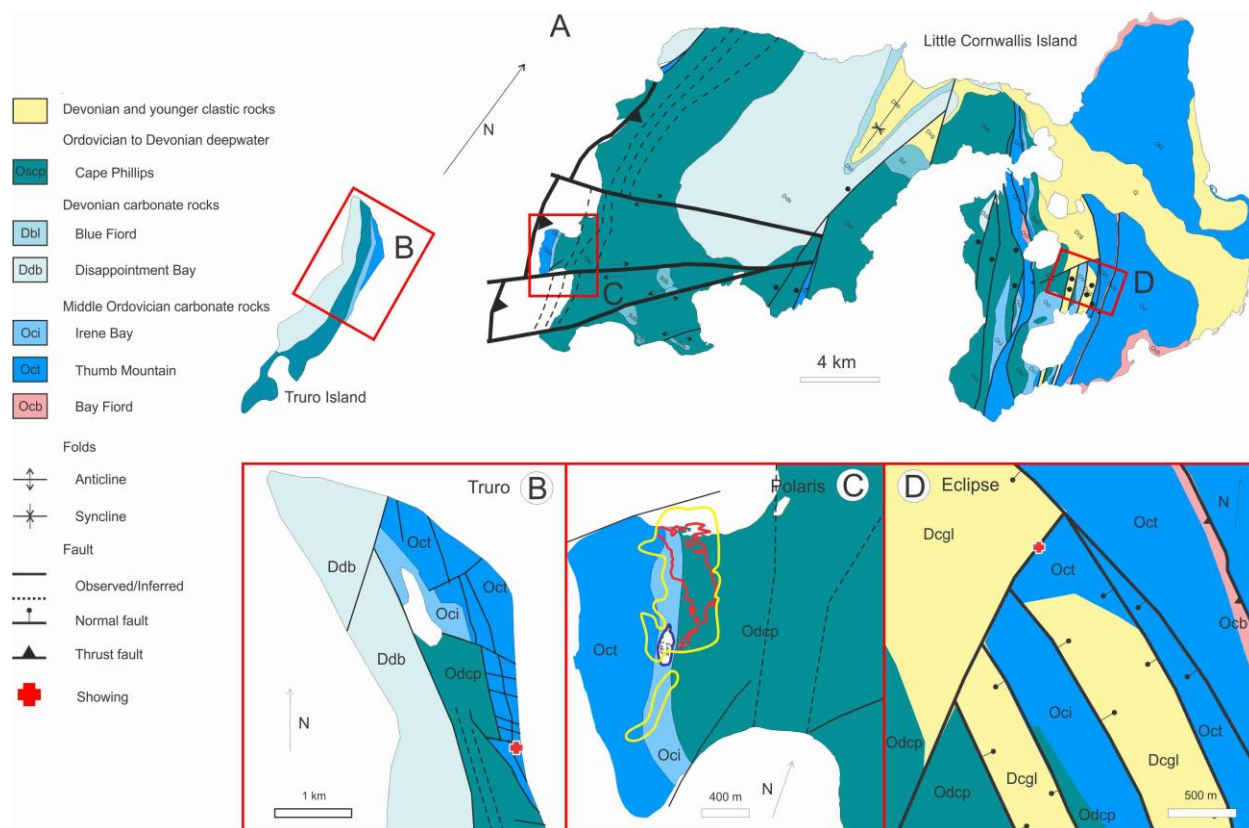


Figure 2-4: Geological map of Little Cornwallis and Truro islands

(A) Simplified geological maps of Little Cornwallis and Truro islands, showing locations of Zn-Pb showings addressed in this study (Truro, Polaris, Eclipse). Rectangles in (A) indicate detailed maps of showing areas in (B), (C), and (D). Geologic map of Little Cornwallis Island after Turner and Dewing (2004); Truro Island map after Randell (1994). Red outline in (C) is area of Polaris ore-body projected to surface (Dewing et al., 2007).

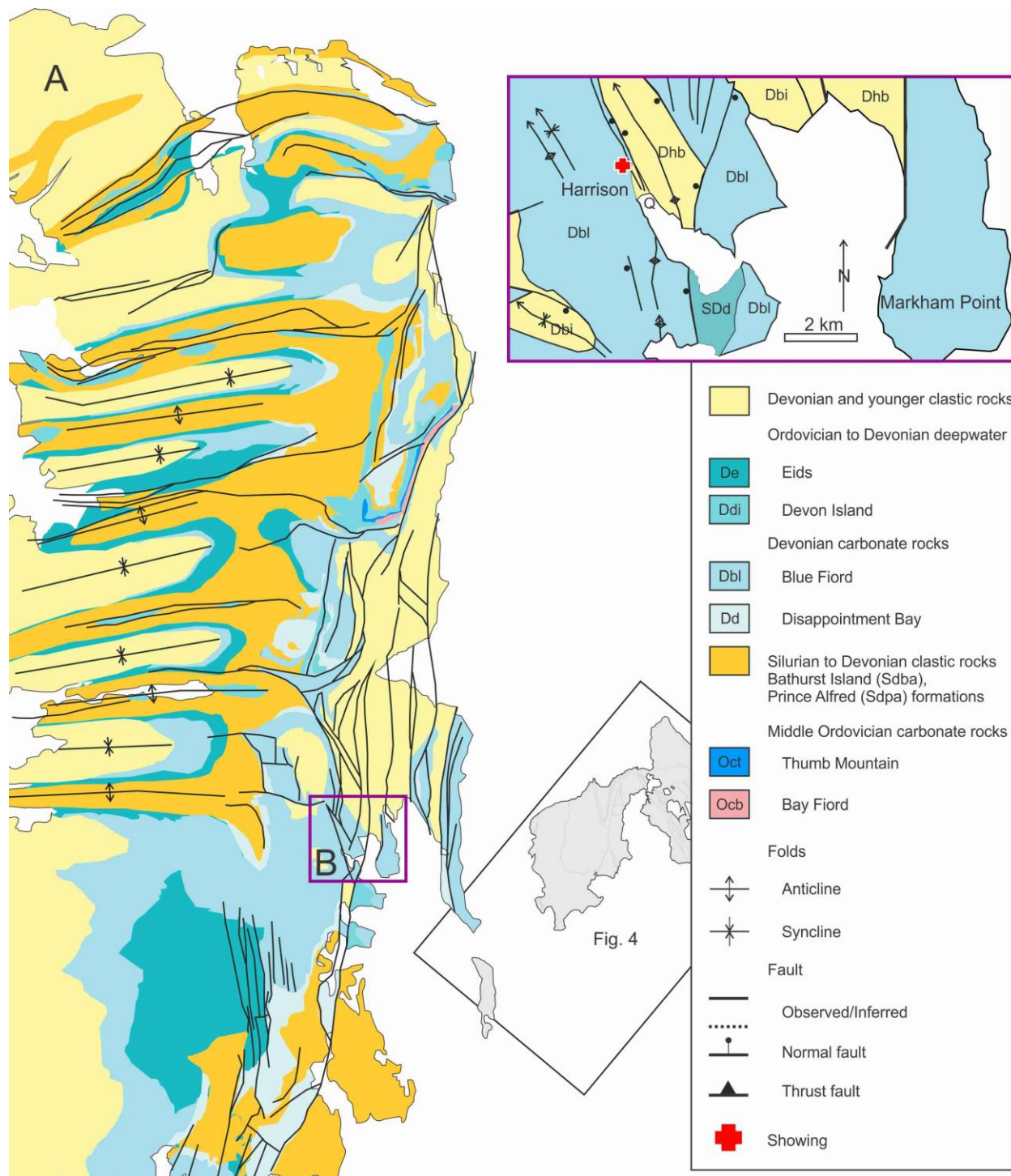


Figure 2-5: Geological map of Bathurst Island

Simplified geological map of Bathurst Island (Western region of study); modified from Harrison and de Freitas (1999), indicating location of the Zn-Pb showing addressed in this study (Harrison). Detailed map of showing area modified from Harrison and de Freitas (1996).

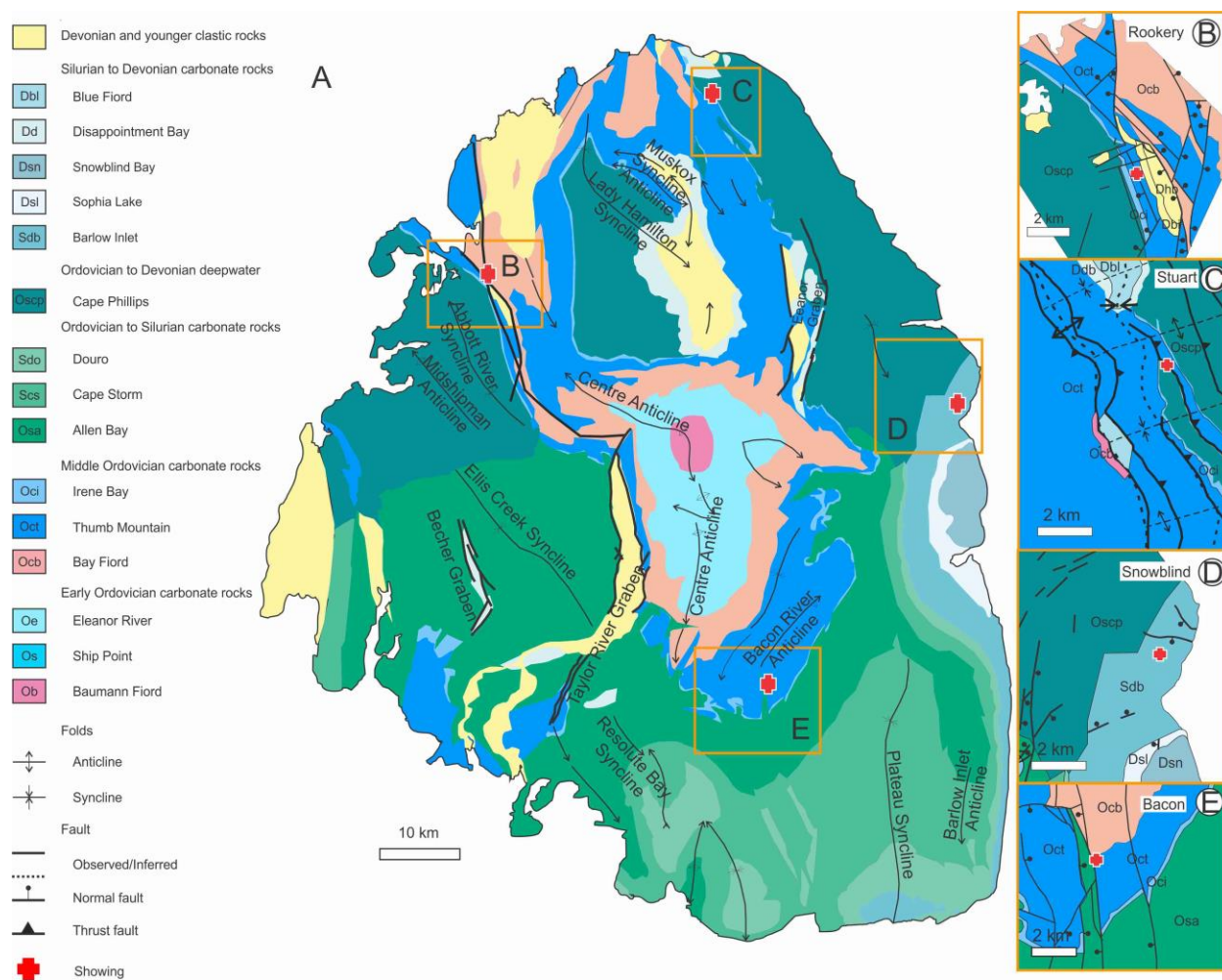


Figure 2-6: Geological map of Cornwallis Island

Simplified geological map of Cornwallis Island (central Cornwallis district), indicating locations of Zn-Pb showings used in this study (Rookery, Stuart, Snowblind, Bacon). Cornwallis Island map and detailed maps of Snowblind and Bacon showings are modified after Harrison et al. (2015); detailed maps of Rookery and Stuart showings are modified after Turner and Dewing (2004) and Jober et al. (2007), respectively.

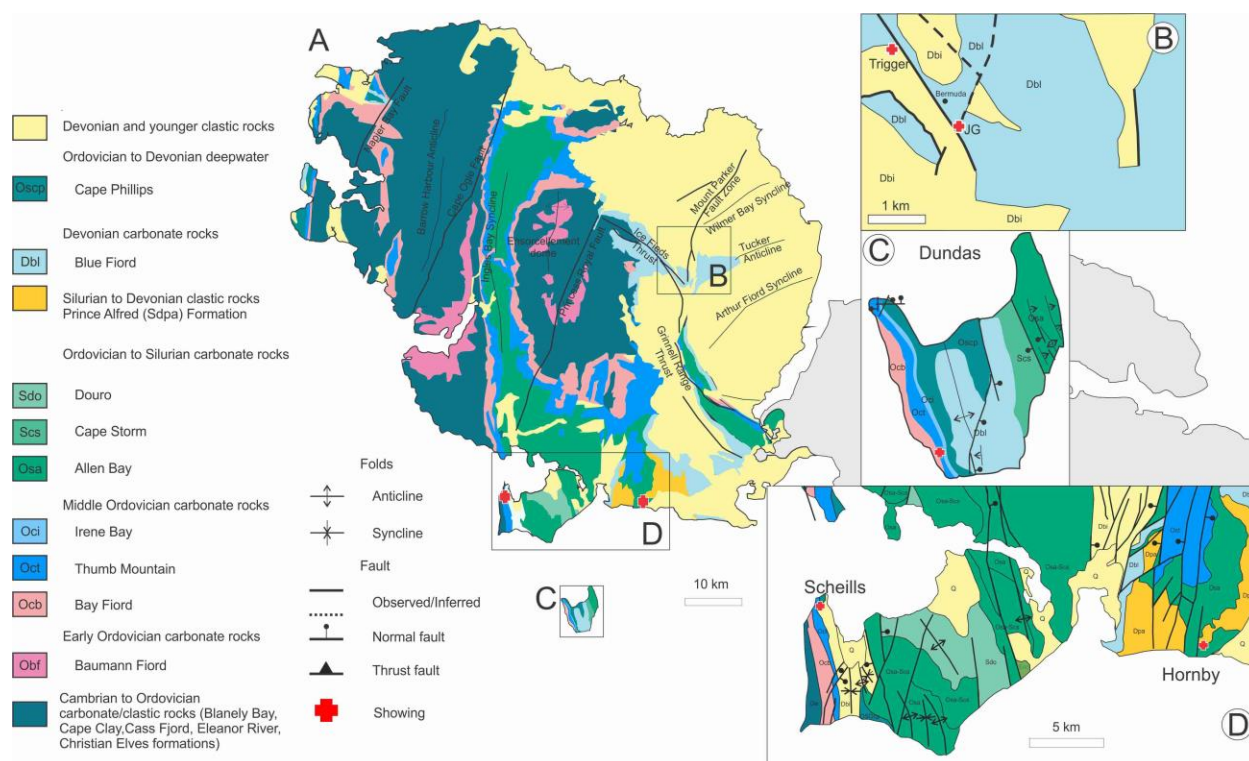


Figure 2-7: Geological map of Grinnell Peninsula, Devon Island

Simplified geological map of northern region of the Cornwallis district (Grinnell Peninsula of Devon Island; Dundas Island), indicating locations of Zn-Pb showings used in the study (Trigger, JG, Dundas, Scheills, Hornby). General geology map and detailed map of Scheills and Hornby showings are modified from Mayr et al. (1998); detailed map of Dundas Island modified after (Thorsteinsson, 1986); and detailed map of Trigger and JG showings modified from Mitchell et al. (2004).

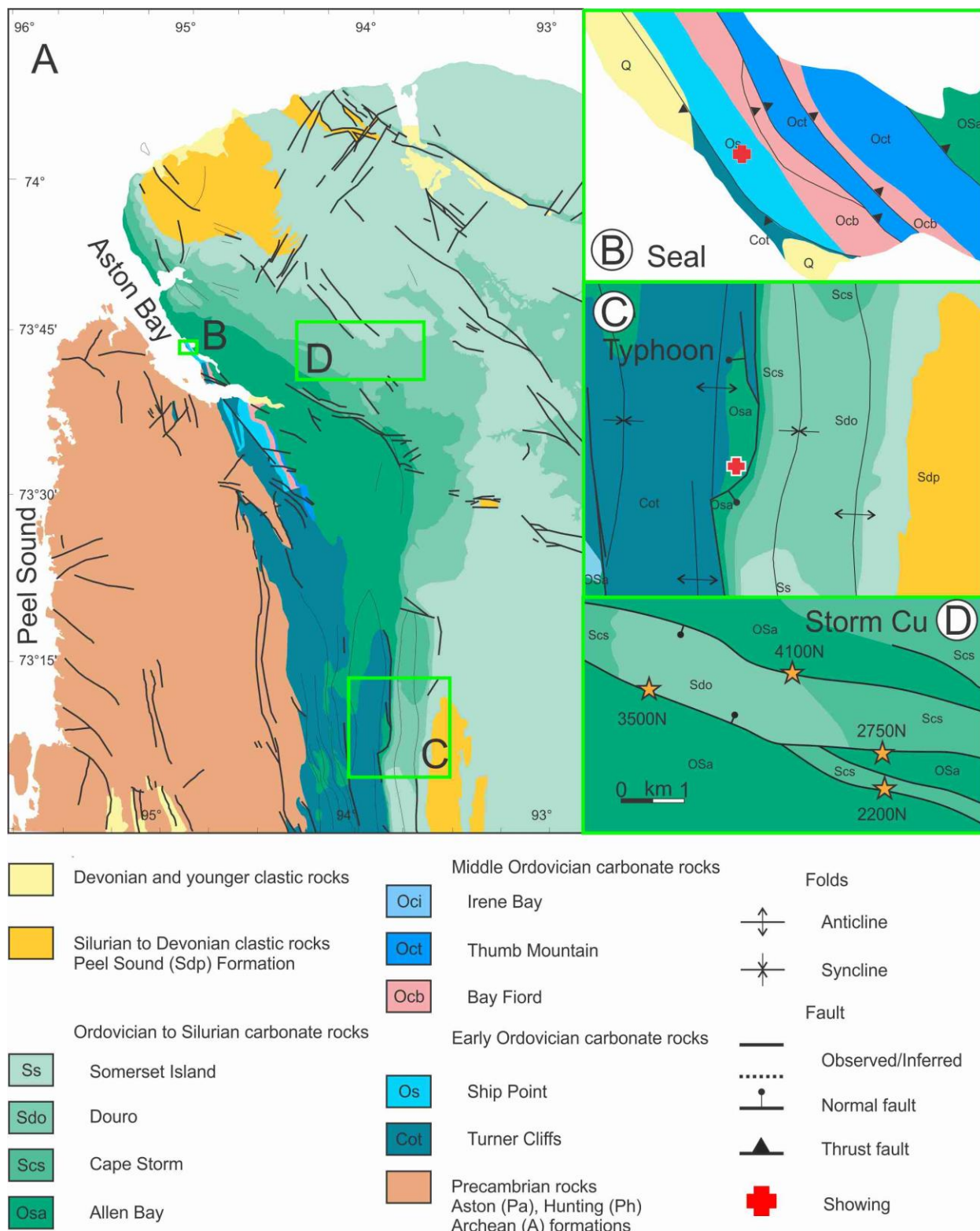


Figure 2-8: Geological map of Somerset Island

Simplified geological map of the southeastern region of the Cornwallis district (Somerset Island; modified from (Stewart and Kerr, 1984)), indicating locations of base-metal showings addressed in this paper. Detailed maps of Typhoon, Seal, and Storm showing areas are modified from Stewart and Kerr (1984), (Robinson and Atkinson, 2012), and Mathieu et al. (2018), respectively.

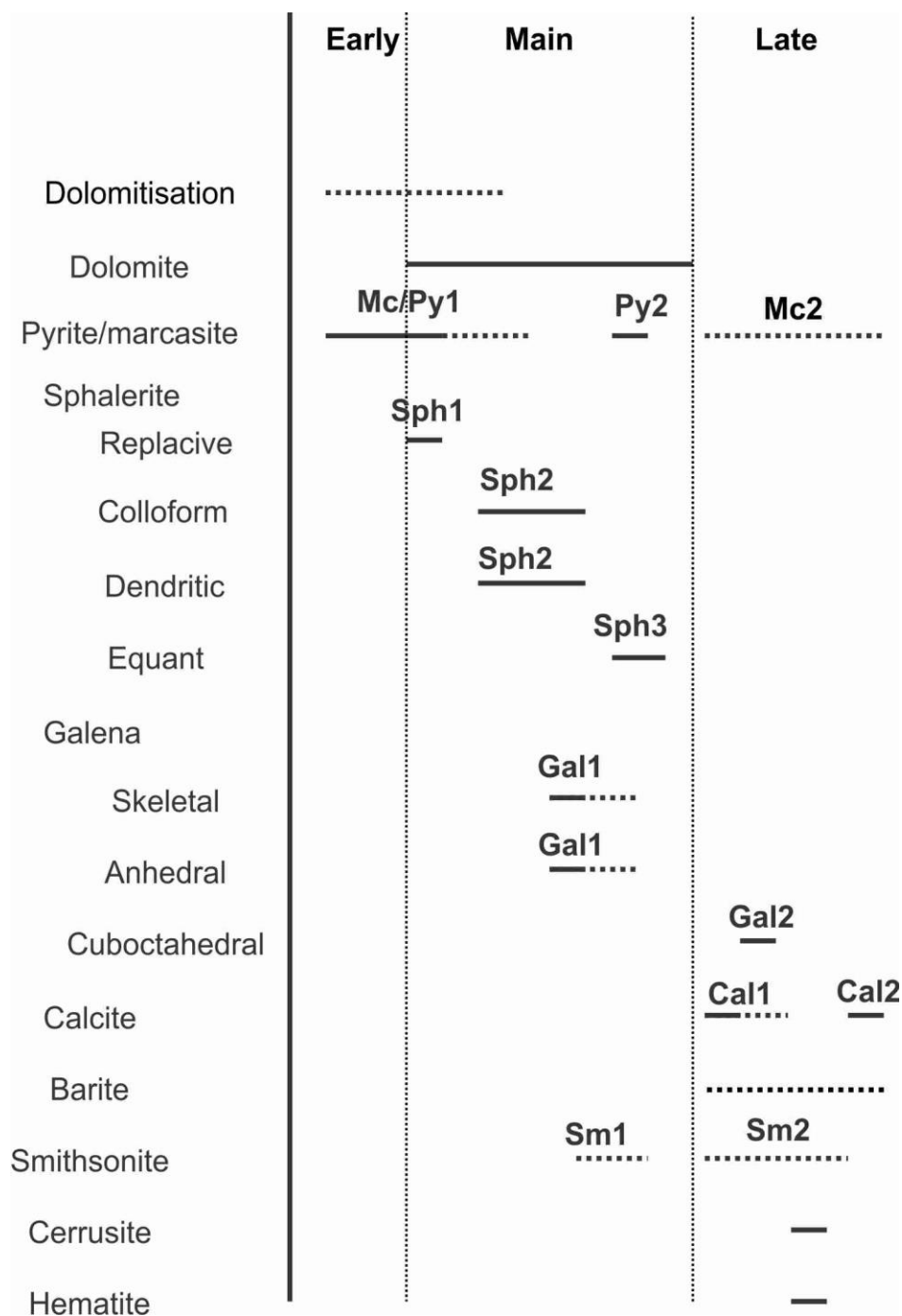
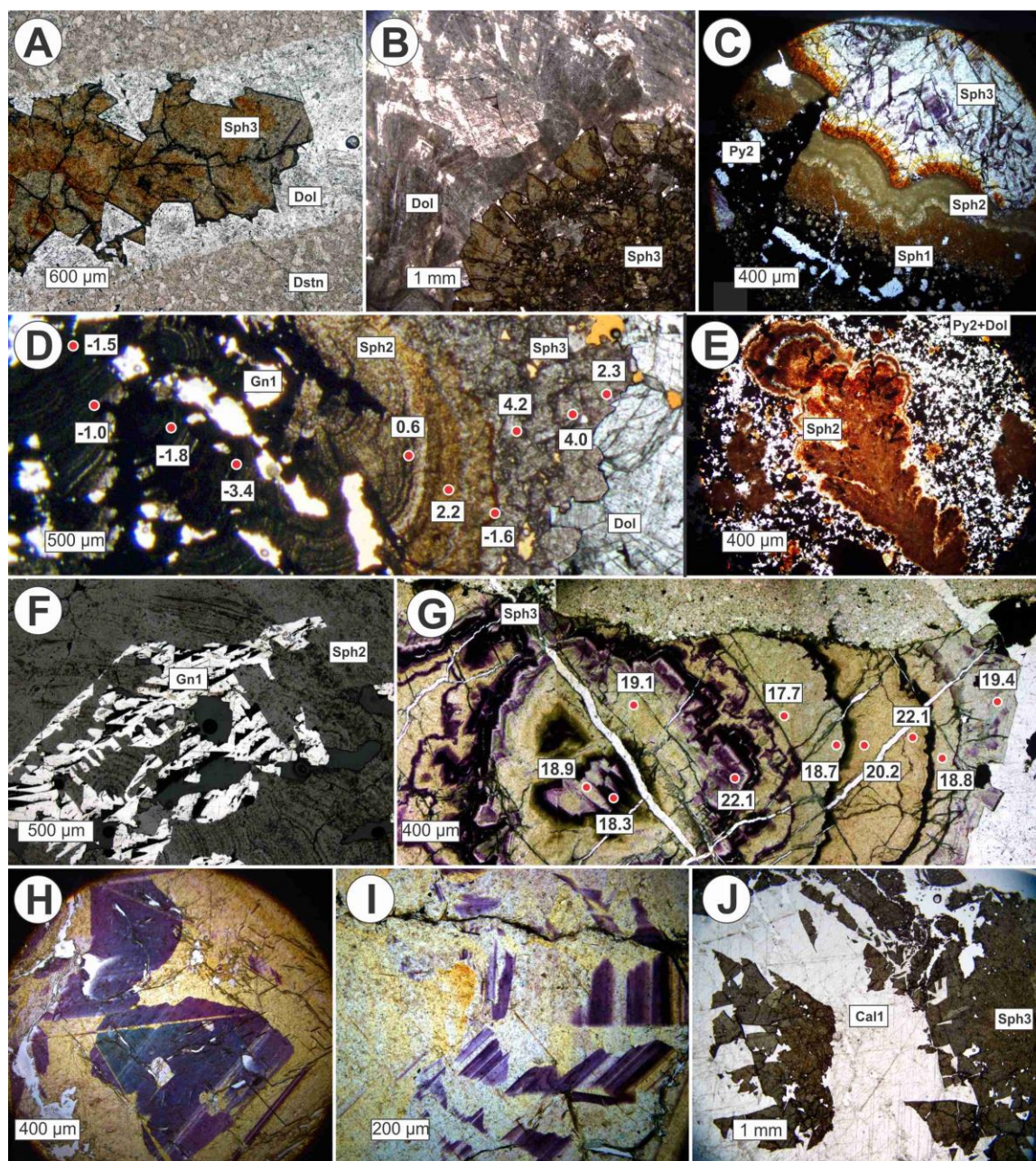


Figure 2-9: Ore-stage paragenesis

Ore-stage paragenesis for the Cornwallis district. Not all phases are present at every showing in the district.



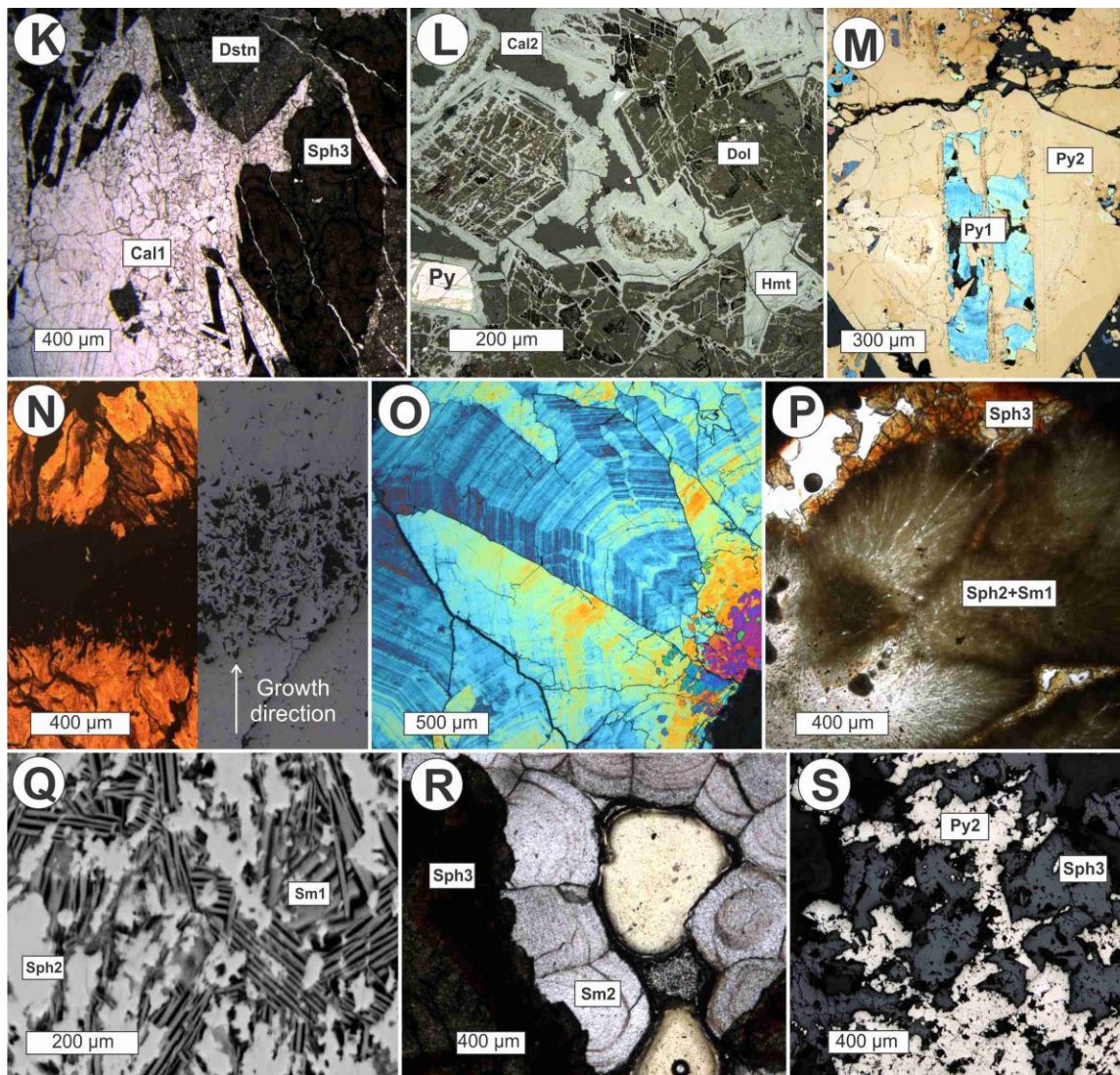


Figure 2-10: Petrographic mineral textures and paragenetic relationships

Images of typical mineral textures and paragenetic relationships in the Cornwallis district. (A and B) Void-filling dolomite (Dol) both underlies (A) and overlies (B) sphalerite 3 (Sph3) (PPL). (C and D) Three stages of sphalerite are present: finely crystalline replacement sphalerite 1 (Sph1), finely crystalline colloform Sph2, and coarsely crystalline Sph3, with typical purple zones (visible in C). Pyrite2 (Py2) fills fractures in Sph1 and Sph2 in (C) (both PPL). (D) Sulphur isotope spots analysed on Sph2 by SIMS and their respective values (in per mil relative to V-CDT) are indicated by red spots (PPL). (E) Sphalerite 2 locally forms fine-grained, dendritic masses (PPL). (F) Skeletal galena is associated with Sph2 (RL) (G-I) Coarsely crystalline Sph3 typically has purple zones that as bands (G), large areas in a crystal (H), or discontinuous zones

scattered within a crystal (I) (all PPL). SIMS analyses of crystals (shown in G) indicate that isotopic composition is not affected by the purple colour. (J) Coarsely crystalline calcite 1 (Cal1) is generally inclusion-free, up to several mm across and euhedral that grades into smaller anhedral crystals (K), and fills fractures in Sph3, indicating a post-mineralising timing (PPL). (L) Anhedral finely to medium-crystalline calcite 2 (Cal2) fills fractures in post-Cal1 hematite (RL). (M) Reflected-light image shows tarnished Py2 replacing earlier euhedral Py1. Tarnish colour may be related to trace element distribution. (N) Combined plane-polarised transmitted-light and reflected-light photomicrograph of a pitted texture in some Sph3 that causes dark bands in transmitted light. (O) Tarnished Py2 with micron-scale laminae and possible sector-zoning; lamination may indicate rapid pyrite precipitation (RL). (P and Q) Smithsonite (Sm) replaces Sph2. (Q) Back-scattered electron image shows that Sm1 replacing Sph2 in (P) is bladed. (R) Botryoidal pore-filling Sm2 overlies Sph3 (RL). (S) Intergrown Py2 and Sph3 shows that they are cogenetic (RL). Images are from the following locations: Rookery (A,I), Polaris (B,C,E), Eclipse (D, F), Trigger (G,K), Dundas (H, P, Q, R), Harrison (J, N), Truro (M), Stuart (L, O), Seal (S). PPL = plane-polarised transmitted light; RL = reflected light.

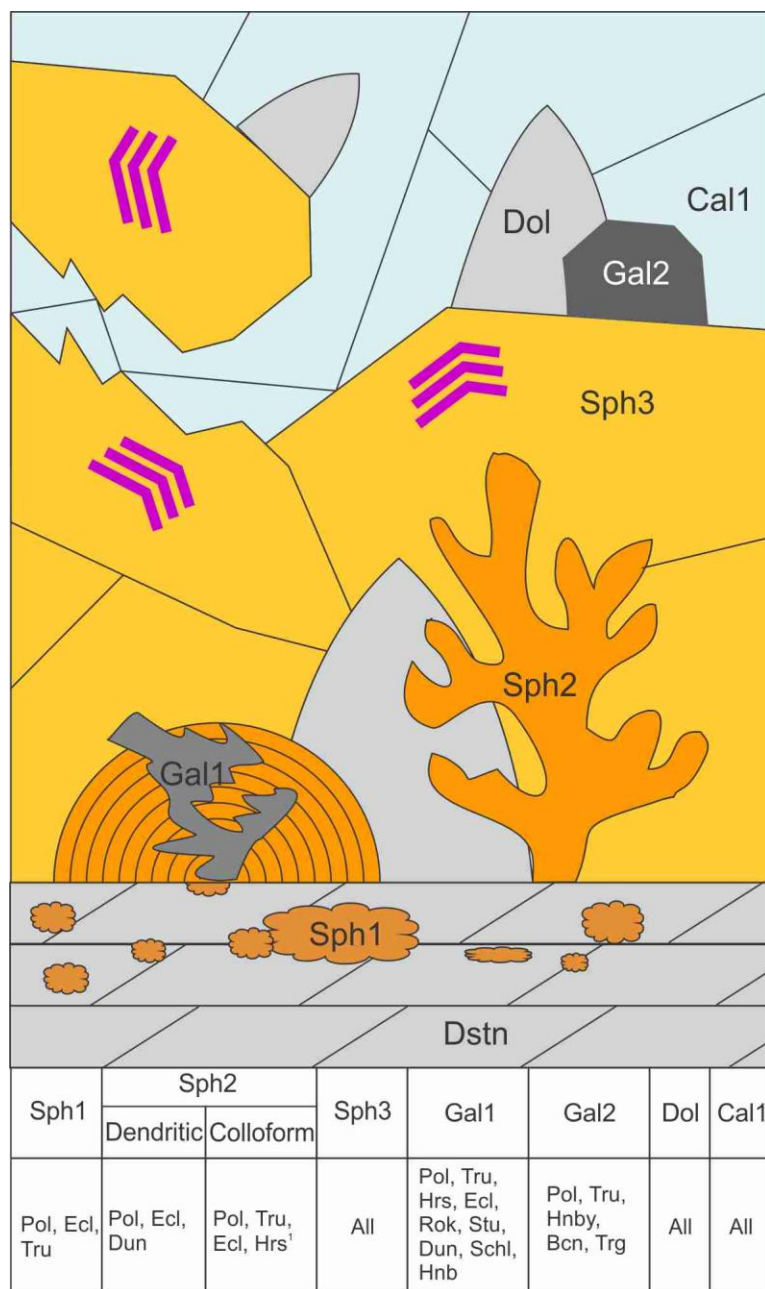


Figure 2-11: Representative paragenetic diagram

Representative diagram of main-ore paragenesis and table of which showings contain these mineral stages. ¹Reported in Rose (1999). (Pol = Polaris; Ecl = Eclipse; Tru = Truro; Dun = Dundas; Hrs = Harrison; Rok = Rookery; Stu = Stuart; Schl = Scheills; Hnb = Hornby; Bcn = Bacon; Trg = Trigger)

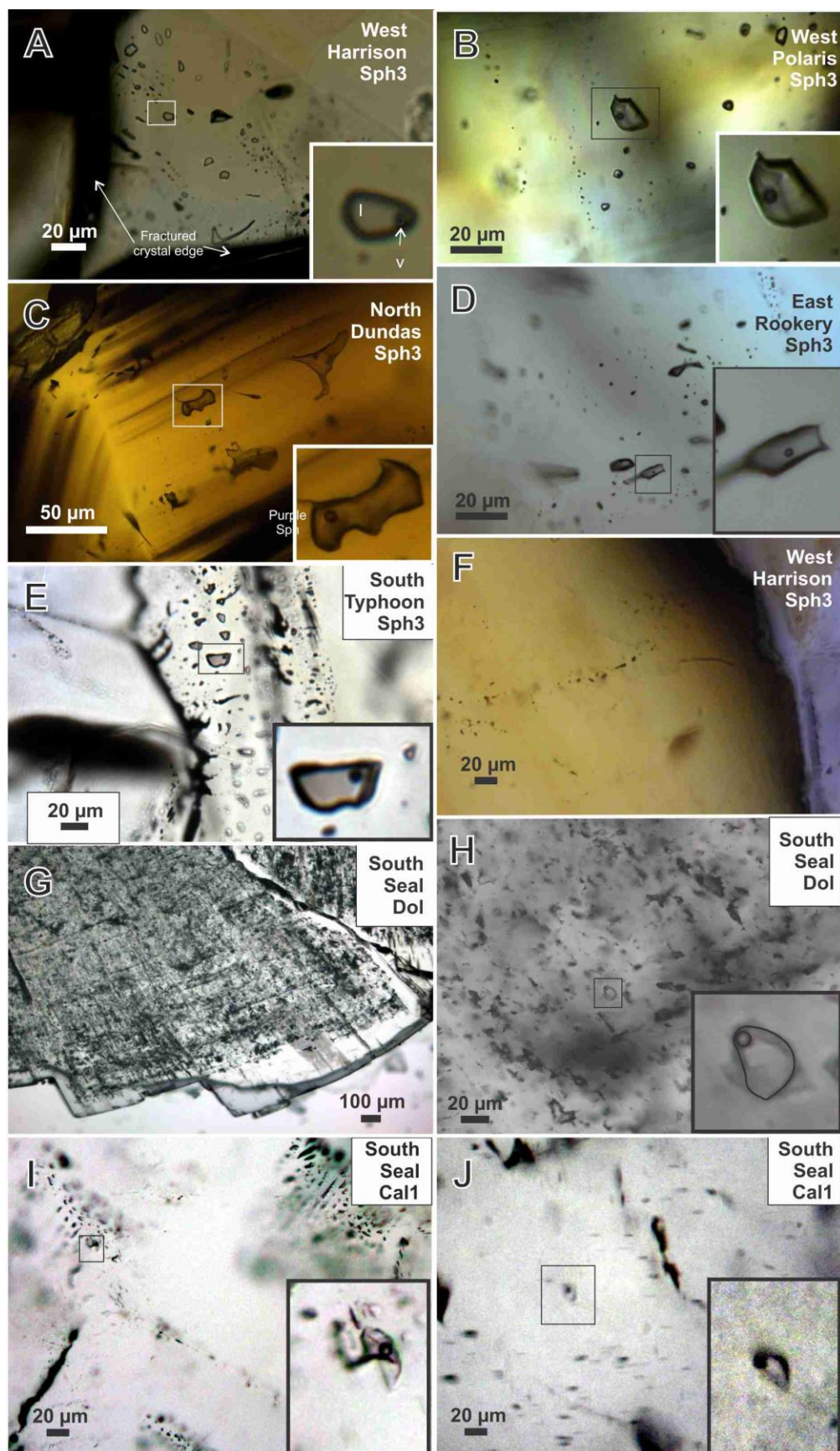


Figure 2-12: Fluid inclusion photomicrographs

Transmitted-light photomicrographs depicting petrographic characteristics of fluid inclusion assemblages (FIAs) and similarity of liquid-vapour ratios in sphalerite 3 (Sph3) and ore-stage dolomite (Dol) in all regions of the Cornwallis district. The largest inclusions are approximately 20 μm , but typical size is $<10 \mu\text{m}$. Insets depict typical fluid inclusion shape, size, and liquid-vapour ratio. Primary sphalerite 3-hosted fluid inclusions from (A) Harrison, (B) Polaris, (C) Dundas, (D) Rookery, and (E) Typhoon. (F) Secondary fluid inclusions follow cross-cutting healed fractures. (G and H) Primary and pseudo-secondary fluid inclusions in dolomite cement are generally densely distributed in crystal centres, causing (G) a cloudy appearance. Primary fluid inclusions in post-ore calcite 1 follow growth zones, whereas (J) isolated inclusions are of indeterminate origin. Similarity of fluid characteristics throughout the district suggests the same fluid present at all showings.

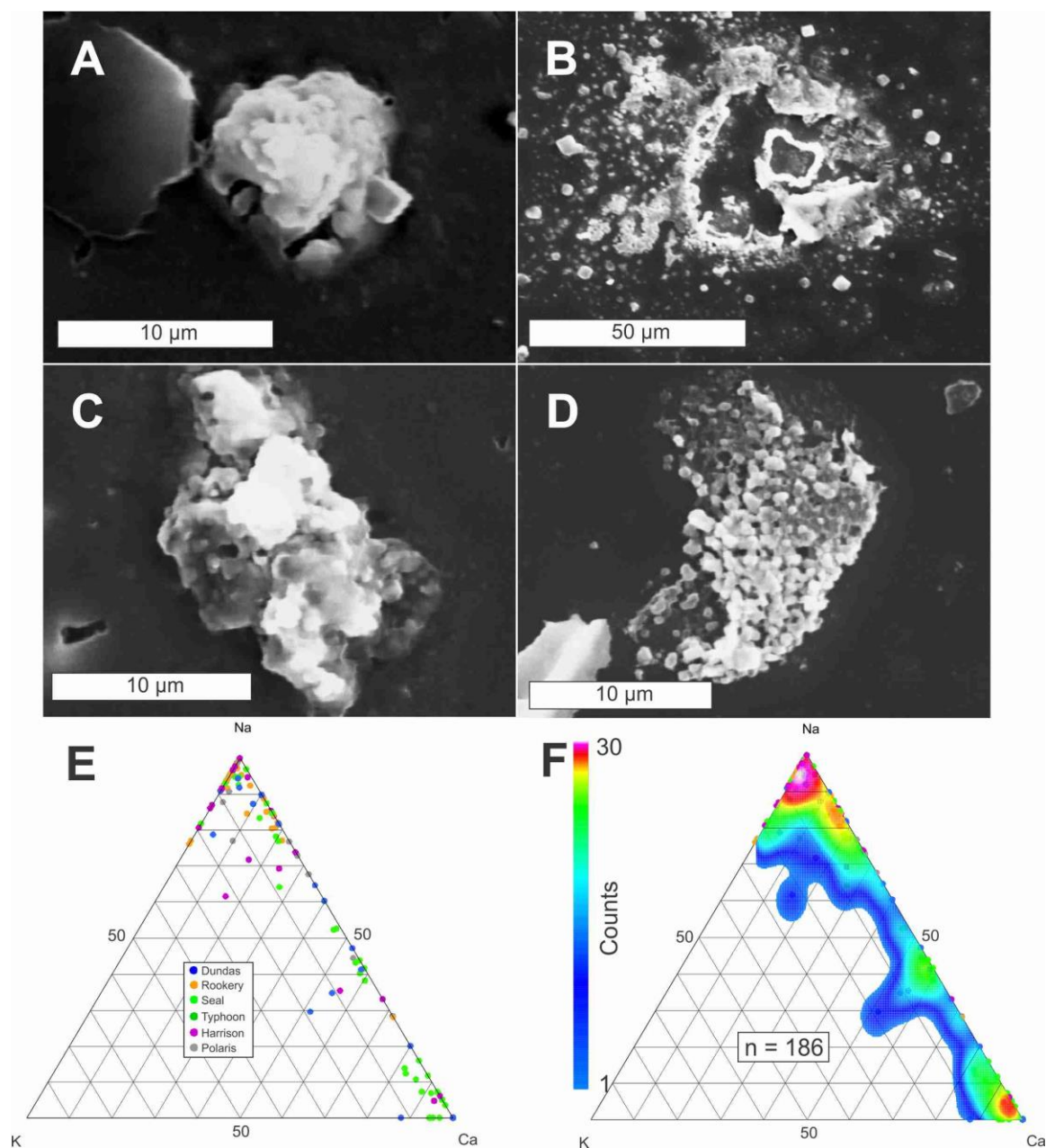


Figure 2-13: Evaporate mound images and composition

(A-E) Back-scattered electron images of evaporate mound morphologies, including (A) circular domes and (B) amorphous mounds, (C) irregular areas of dispersed microcrystals, and (D) irregular areas of densely clustered microcrystals. (E and F) Na-Ca-K ternary diagrams of evaporate mound compositions from ore-stage sphalerite 3 and dolomite in normalised wt. % obtained by SEM-EDS analysis plotted as (E) individual mound analyses from respective samples and (F) density lots of all samples analysed, showing that two end-member fluid

compositions (Na- and Ca-dominated) were present. Minor potassium is present in many inclusions. The presence of Ca in the fluids indicates subsurface interaction with Ca-bearing rocks.

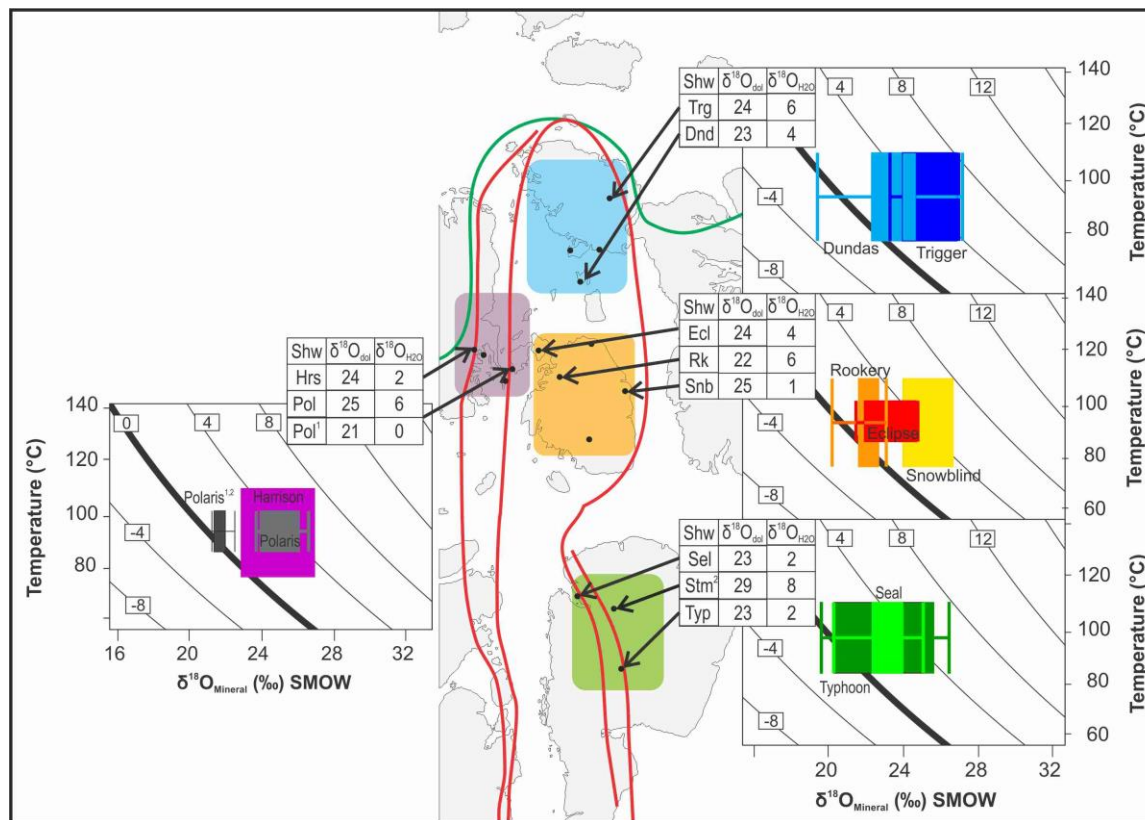


Figure 2-14: Dolomite SIMS oxygen isotope results

Box-and-whisker plots of oxygen isotope values measured by SIMS combined with mineral-water fractionation diagrams for dolomite showing range of possible $\delta^{18}\text{O}$ values of the precipitating fluids in the different geographic regions. Curved lines represent isopleths of $\delta^{18}\text{O}_{\text{H}_2\text{O}}$ values calculated using Horita (2014) for dolomite-water fractionation. Homogenisation temperatures from dolomite/sphalerite were corrected for 1 km burial depth and used as the temperature constraints in the fractionation equation. Most showings have similar $\delta^{18}\text{O}_{\text{H}_2\text{O}}$ values, indicating a similar fluid source. ¹Values reported by Savard et al. (2000). ²Values reported by Mathieu et al. (2018).

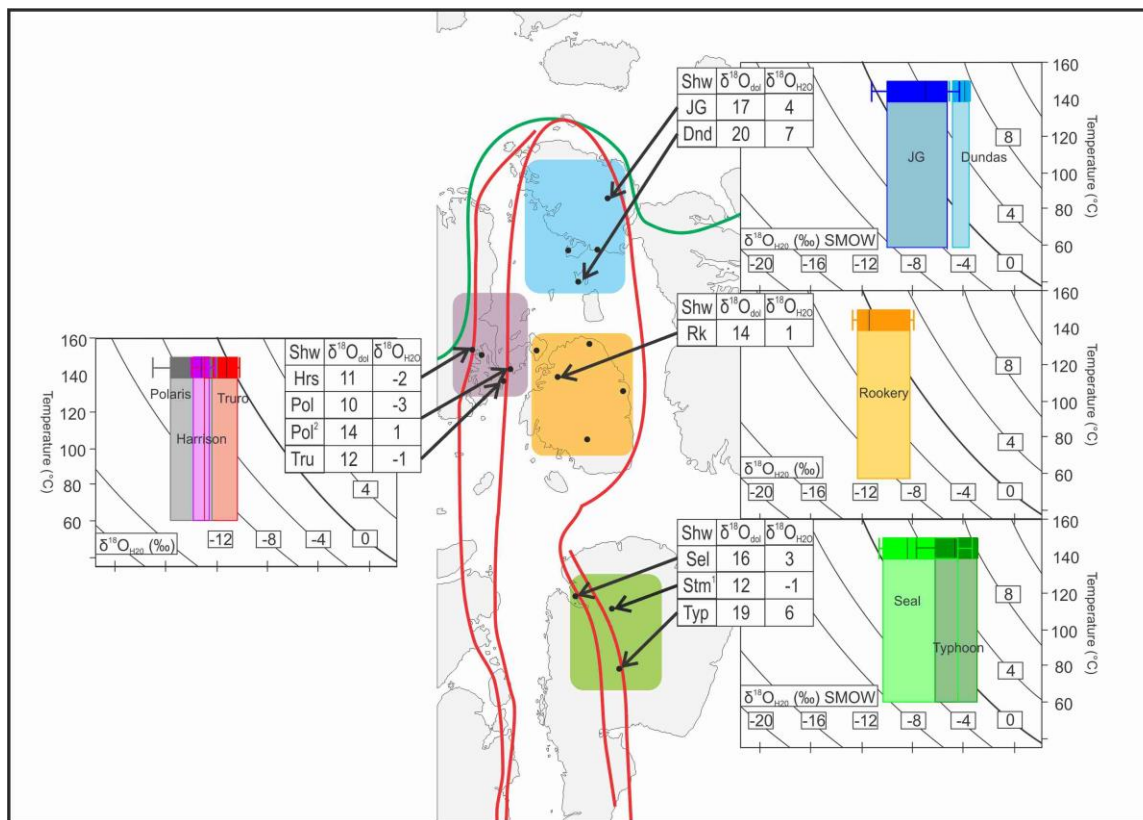


Figure 2-15: Calcite SIMS oxygen isotope results

Box-and-whisker plots of oxygen isotope values measured by SIMS combined with mineral-water fractionation diagrams for calcite showing the range of possible $\delta^{18}\text{O}$ values of the precipitating fluids for the five geographic regions. Curved lines represent isopleths of $\delta^{18}\text{O}_{\text{H}_2\text{O}}$ values calculated using O'Neil et al. (1969) for calcite-water fractionation. Homogenisation temperatures were corrected for burial of 1 km from calcite (darker boxes) and reasonable burial temperatures (lighter boxes) were used as temperature constraints. Most showings have similar fluid values indicating a single fluid source. ¹Values reported by Mathieu et al. (2018). ²Values reported by Savard et al. (2000).

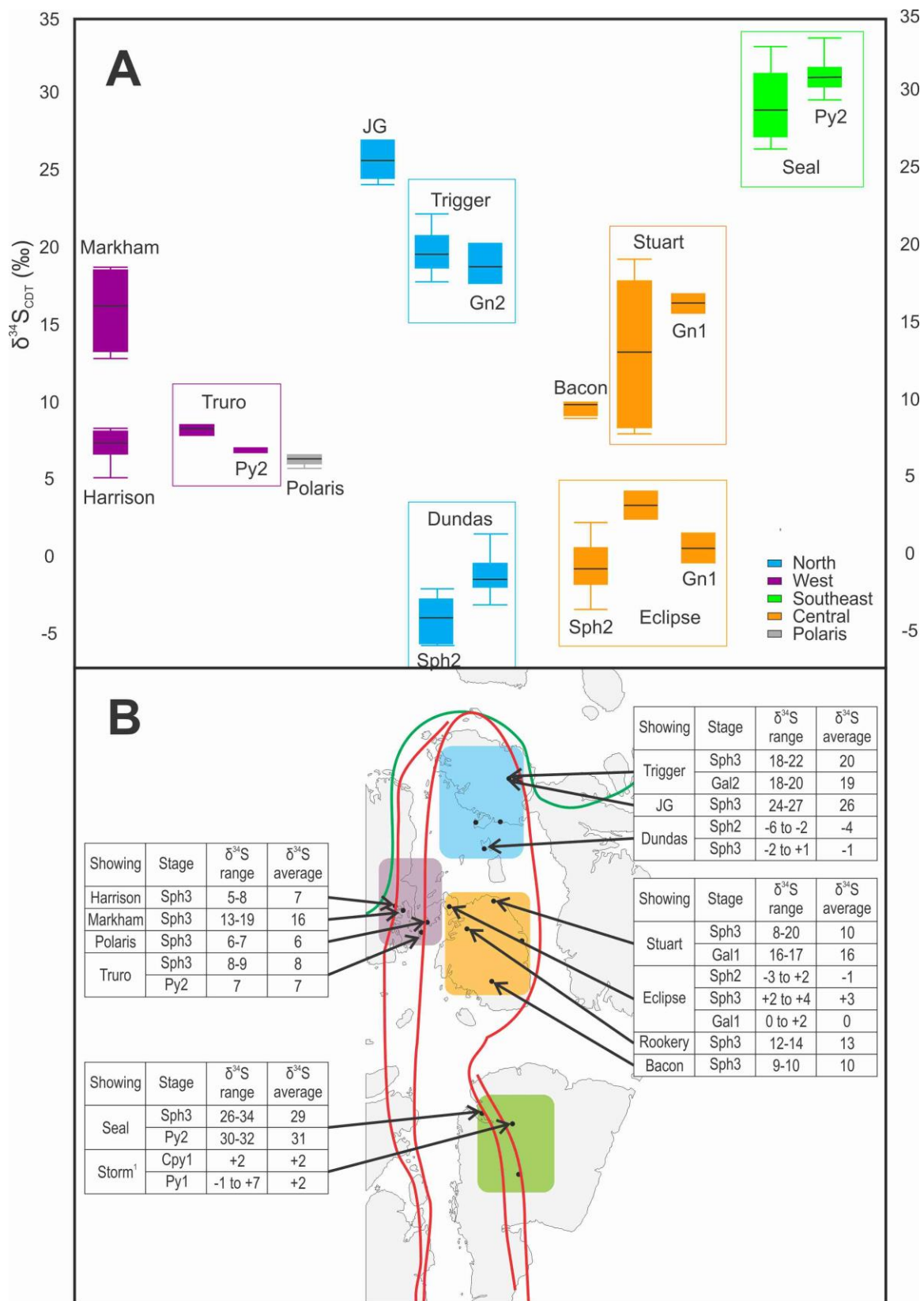


Figure 2-16: SIMS sulphur isotope values

(A) Box-and-whisker plots of measured $\delta^{34}\text{S}_{\text{VCDT}}$ values from the five geographic regions for sphalerite 3 (not labelled), sphalerite 2 (Sph2), galena (Gn), and pyrite (Py) show substantial variation in the district, but a limited range of values at each showing. (B) Geographic distribution of showings with their respective average $\delta^{34}\text{S}$ values. In each showing, earlier stages have typically lower values than later stages. The showing-specific ranges indicate the geographically limited influence of local S sources. ¹Values reported by Mathieu et al. (2018).

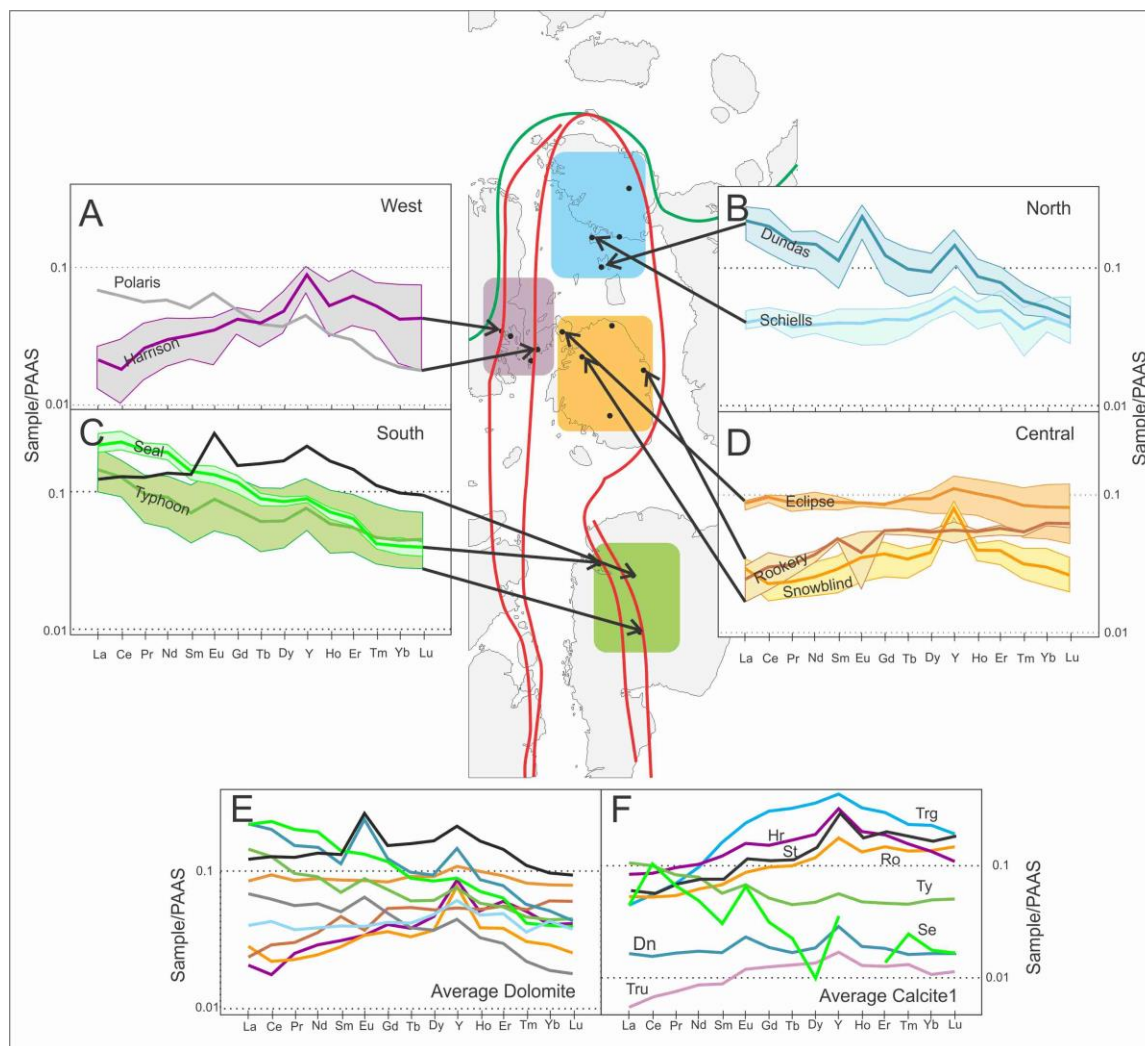


Figure 2-17: PAAS-normalised REE+Y values of carbonate gangue minerals

PAAS-normalised REE+Y diagrams for carbonate gangue in showings from the five geographic regions of the Cornwallis district, at the same vertical scale. (A-E) Dolomite. (F) Calcite 1. The fields represent the range in values for individual showings, with the average represented by a heavy line. Data for Storm Cu showing are from Mathieu et al. (2018). The three categories of patterns (positively sloped, negatively sloped, and approximately flat) represent different fluid:rock systems. Positively sloped and flat patterns indicate low fluid:rock systems (fluid characteristics influenced by host-rock composition); negatively sloped patterns represent high fluid:rock systems (fluid characteristics not influenced by host rock composition). PAAS values from Pourmand et al. (2012). The diversity of the patterns indicates that fluid flux was not

consistent among showings. Trg = Trigger, Hr = Hornby, St = Storm, Ro = Rookery, Ty = Typhoon, Dn = Dundas, Se = Seal, Tru = Truro.

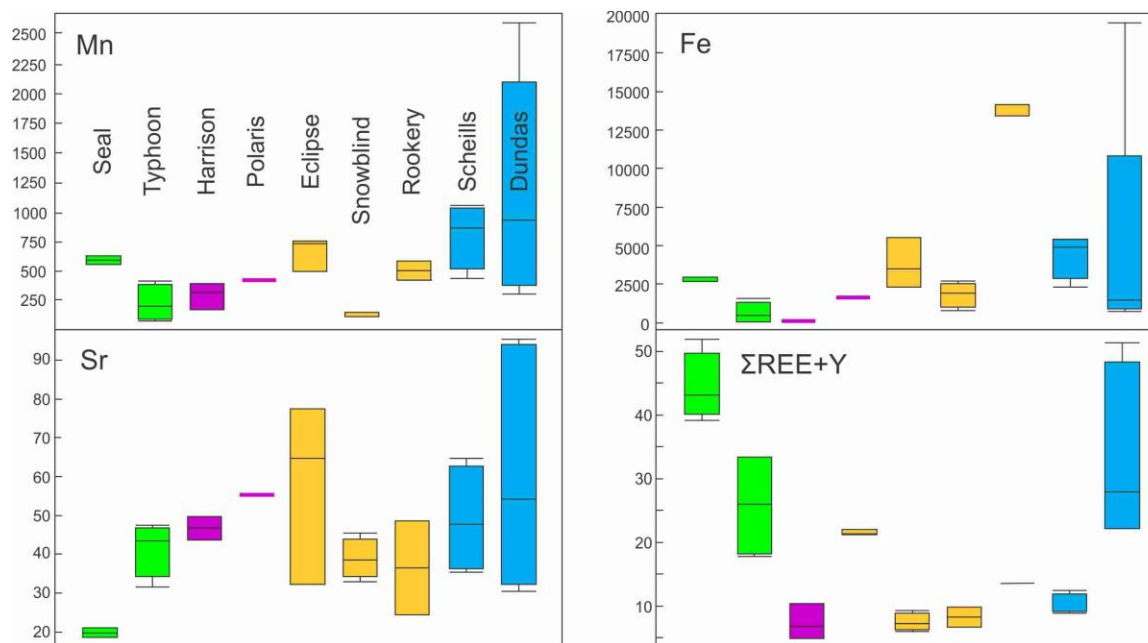


Figure 2-18: Dolomite trace element values

Box-and-whisker plots of trace elements in dolomite gangue for five Cornwallis district regions show that, with the exception of Fe in the western showing, gangue-precipitating fluids were similar throughout the district, indicating a regional fluid.

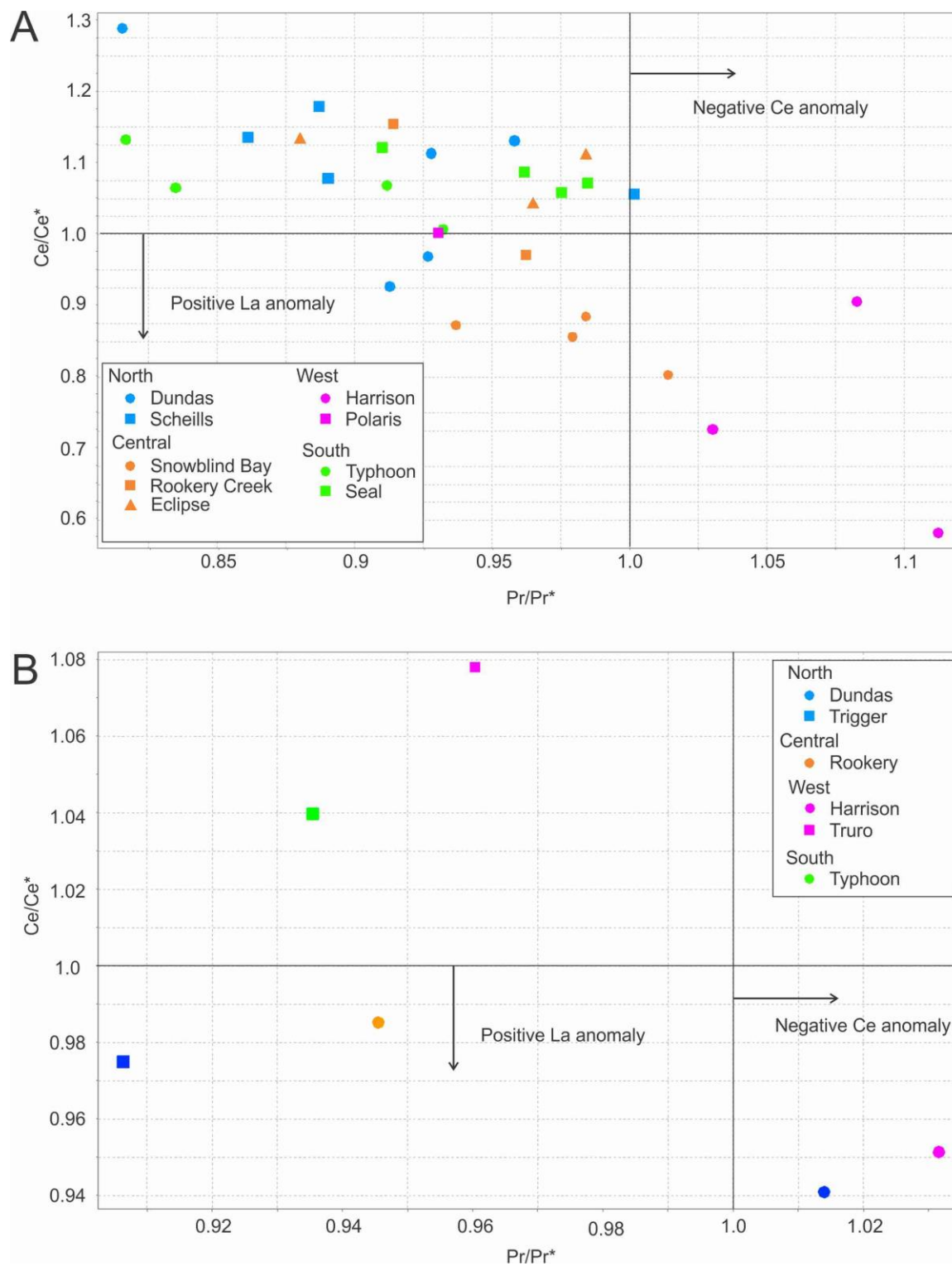


Figure 2-19: Anomaly discrimination plot

Discrimination plots (Bau and Alexander (2006)) quantify shale-normalised La and Ce anomalies for (A) dolomite and (B) calcite 1. Dolomite generally has positive Ce anomalies and negative La anomalies. $Pr^* = Pr_N / (0.5 * (Ce_N + Nd_N))$. $Ce^* = Ce_N / (0.5 * (La_N + Pr_N))$. The negative Ce anomaly indicates that the regional fluid was reduced.

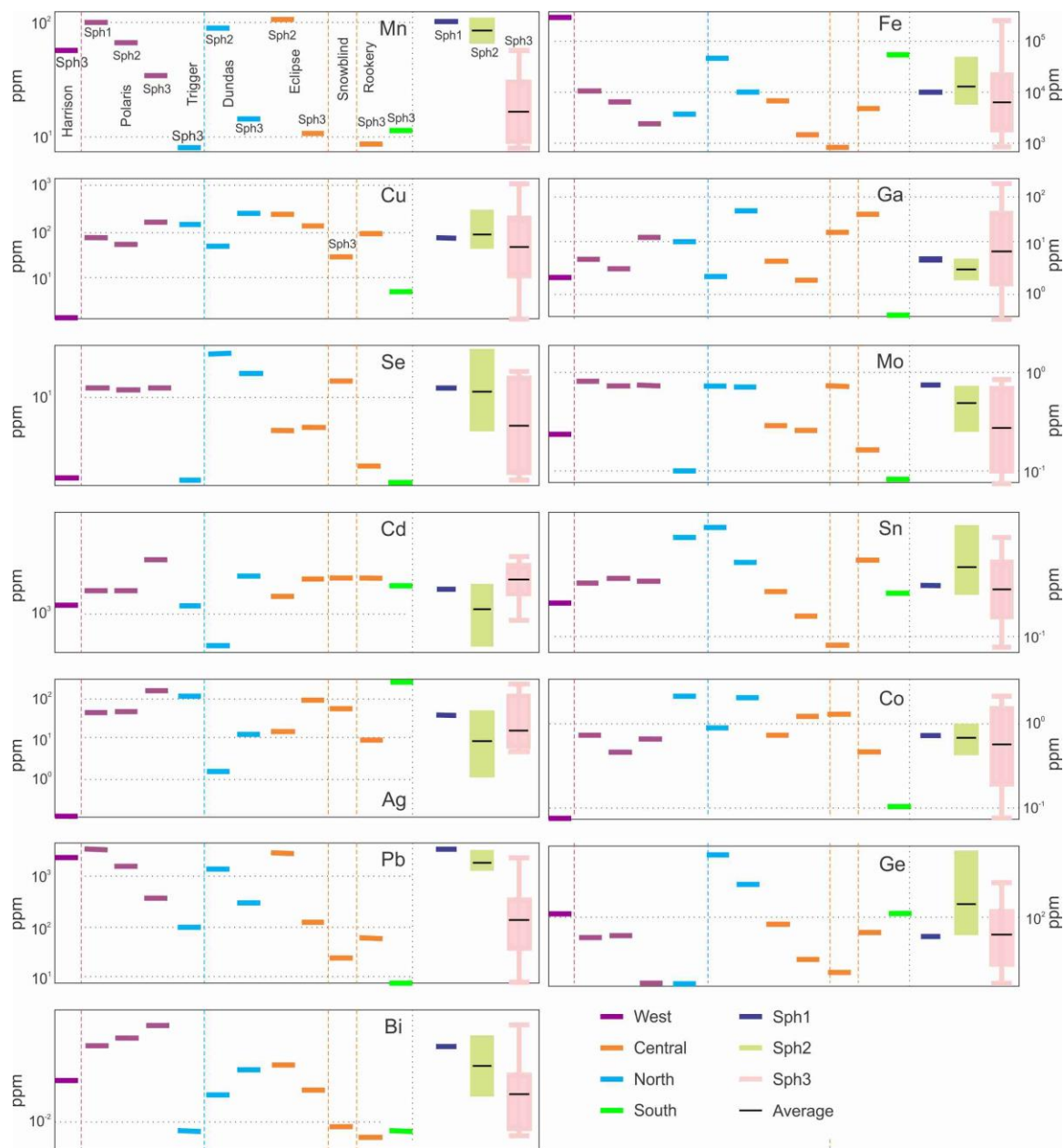


Figure 2-20: Sphalerite trace element composition

Box-and-whisker plots summarising average trace element concentration of sphalerite (LA-ICP-MS) grouped into five regions and three sphalerite stages. Most elements are relatively constant throughout the district, indicating a shared metal source; variations probably reflect local influences, rather than different sources. Generally, trace element content decreases from early sphalerite (Sph1 and 2) to main Sph3, possibly as a function of precipitation rates.

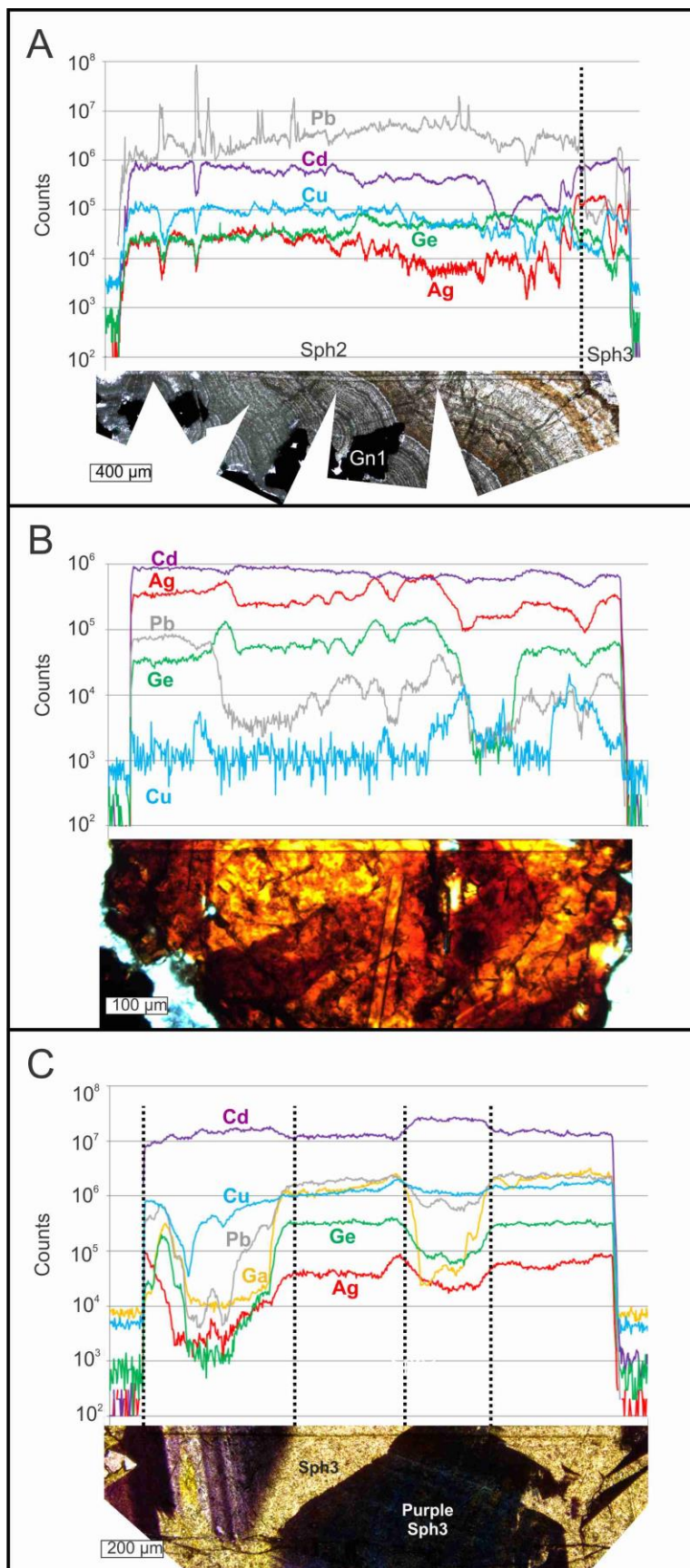


Figure 2-21: Laser traverse across sphalerite

Laser traverses across sphalerite show comparatively smooth profiles, indicating that trace elements are structurally bound. (A) Spikes in Pb counts along Sph2 traverse (Eclipse) are probably caused by micro-inclusions that were trapped during rapid precipitation. (B) Sph3 (Seal) shows that Ge, Ag, and Cu are locally correlated, possibly indicating coupled substitution. (C) Traverses across purple sphalerite zones typically show increased Cd and decreased Ge, Ga, and Ag counts (here from Dundas), suggesting that interplay among these elements may have affected development of purple colour.

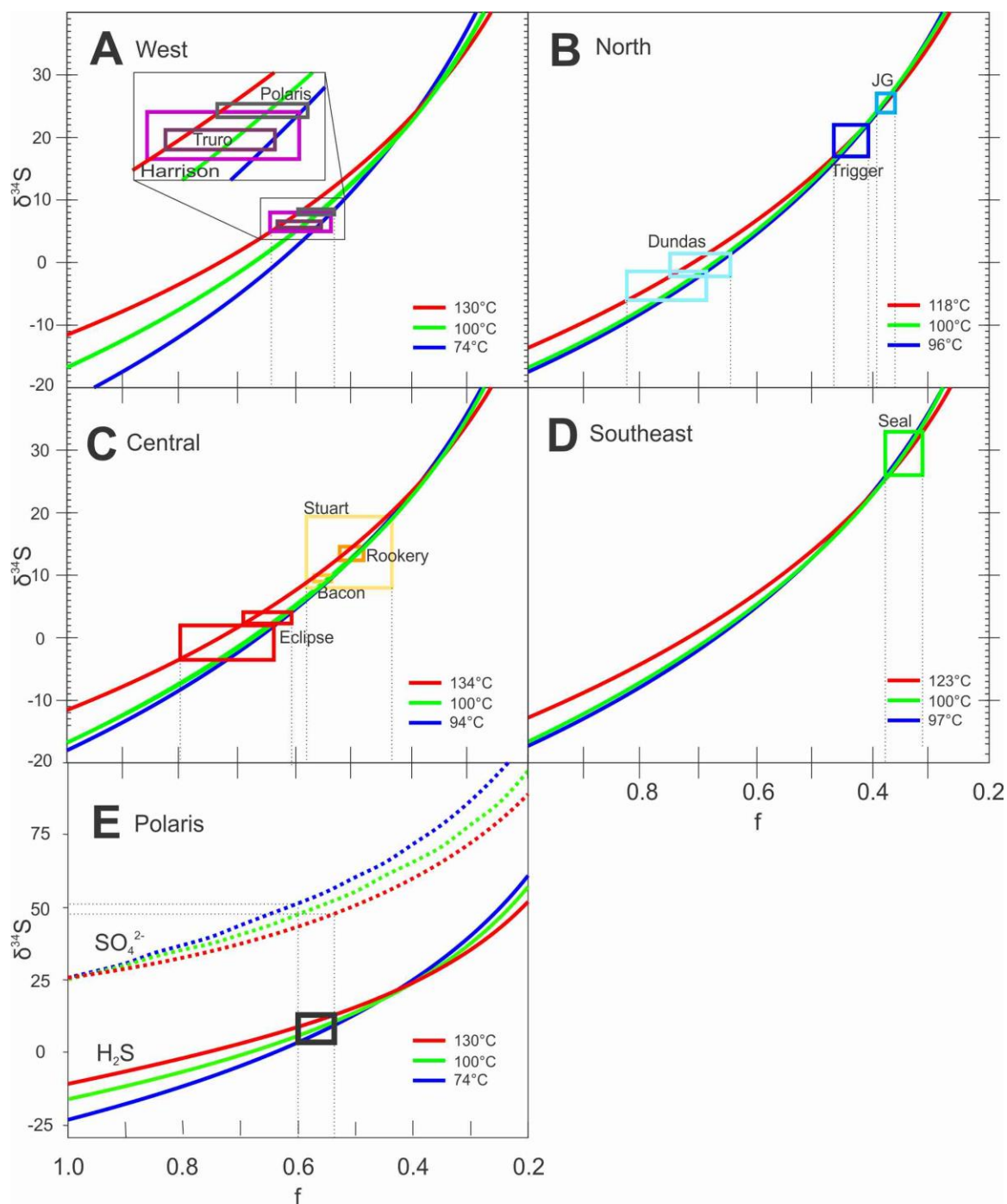


Figure 2-22: Sulphur isotope fractionation curves

(A-D) Sulphur fractionation curves for the four regions during partial sulphate reduction to sulphide thermochemically. (E) Sulphate-sulphide partial fractionation curves for the Polaris deposit shows that residual sulphate in the fluid after 40–45% reduction has a $\delta^{34}\text{S}$ value of 48–51‰. Temperature ranges are the lowest and highest measured T_h values for each region, with

100°C being used as a common T. Initial $\delta^{34}\text{S}_{\text{SO}_4}$ ($\delta^{34}\text{S}_o$) value in calculations was 25‰. Residual $\delta^{34}\text{S}_{\text{SO}_4}$ value after fractionation ($\delta^{34}\text{S}_{\text{SO}_4f}$) = $(\delta^{34}\text{S}_o + 1000) \times (f^{\alpha-1}) - 1000$. Isotopic composition of H_2S produced by partial reduction ($\delta^{34}\text{S}_{\text{H}_2\text{S}f}$) = $(\delta^{34}\text{S}_{\text{SO}_4f} + 1000) \times (\alpha_{\text{H}_2\text{S}-\text{SO}_4} - 1)$. f = proportion of sulphate remaining after reduction. Equation for $\alpha_{\text{SO}_4-\text{H}_2\text{S}}$ fractionation is from Robinson (1973).

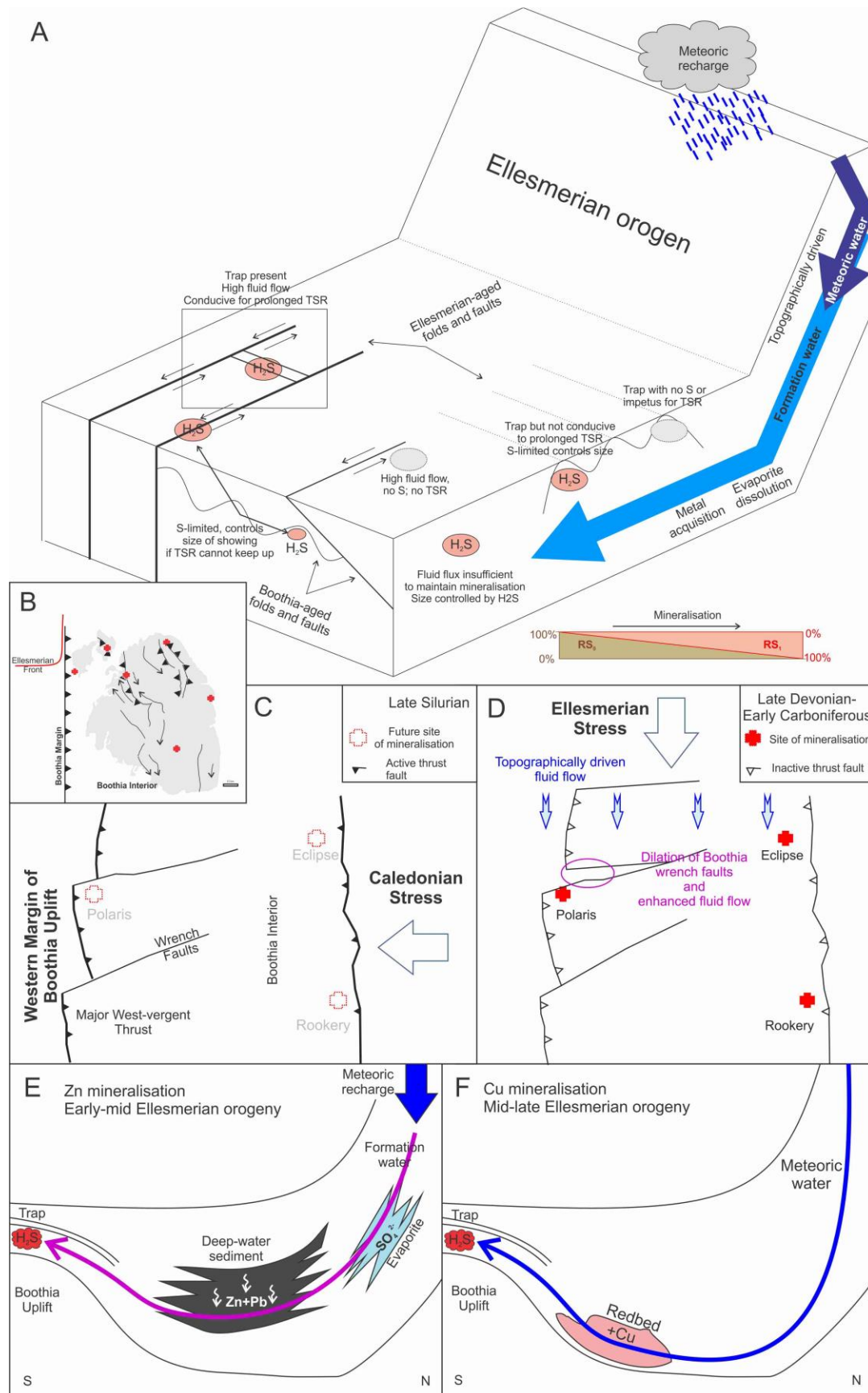


Figure 2-23: Interpretive diagram of mineralisation in the Cornwallis district

(A) Interpretive diagram illustrating how a regional fluid was mobilised by the topographic recharge and descent of meteoric fluid. Formation waters were displaced by meteoric water and obtained extra salinity through subsurface evaporite dissolution and transported metals to sites of previously accumulated sulphide (RS_0), probably reduced via BSR. If conditions were favourable, TSR could have reduced additional sulphate from the fluid (RS_1), eventually becoming the predominant mode of sulphate reduction. The volume of mineralisation is dependent on (a) initial volume of RS_0 , (b) sustainability of TSR and production of RS_1 , and (c) the efficiency of fluid delivery. Polaris was a large sulphide body because metals were copiously supplied by fluid delivered through an orogenically dilated cross-fault, were focussed into and trapped under an impermeable cap rock (Irene Bay and Cape Phillips formations), and interacted with a large volume of organic matter reductant in the host rock (Upper Thumb Mountain Formation). After an initial episode of sulphide precipitation that used pre-existing localised and isotopically distinct BSR pools that had accumulated at each eventual showing location, yielding early, light sulphur isotopic values, a larger volume of sulphides was produced through TSR of sulphate carried with the metals in the regional fluid using sedimentary organic matter as a reductant. (B) Simplified map of Cornwallis and Little Cornwallis islands indicating the location of showings and main structural features. (C) Due to west-directed forces in the Late Silurian, segmented thrust faults were offset by sinistral strike-slip movement on wrench faults. (D) South-directed stress in the Late Devonian caused torque on the offset fault blocks causing dilation to allow for substantial fluid flux. (E) Zn mineralisation during the early to middle Ellesmerian orogeny was the result of formation waters being pushed through the subsurface by descending meteoric recharge, interacting with evaporite and deep-marine sedimentary rocks to acquire sulphate and base-metals, respectively. The fluid moved up the Boothia structure to the site of precipitation. (F) Cu mineralisation is associated with the middle to late Ellesmerian orogeny, when the meteoric recharge fluid became the dominant regional fluid. This fluid penetrated deep in the subsurface and interacted with geographically limited red beds to acquire Cu.

Table 2-1: Microthermometry results

Microthermometric data for diagenetic minerals in the Cornwallis district.

FIA = fluid inclusion assemblage, FI = fluid inclusion, Avg = average, T_h = homogenization temperature, T_m = ice melting temperature

| Region | Showing | Mineral | Stage | FIA# | #Flincs | Range T_h | Average T_h | Range T_m | Average T_m | Salinity (wt. % NaCl equiv.) |
|--------|----------|------------|-------|------|---------|----------------|------------------|-------------------|------------------|---------------------------------------|
| North | Hornby | Sphalerite | Sph3 | 1 | 4 | 95 to 110 | 106 | - | - | - |
| North | Hornby | Sphalerite | Sph3 | 2 | 3 | 92 to 96 | 94 | - | - | - |
| North | Dundas | Sphalerite | Sph3 | 1 | 4 | 78 to 90 | 84 | -27.0 to -30.0 | -28.3 | 27.6 |
| East | Rookery | Dolomite | Dol | 1 | 7 | 83 to 95 | 85 | -27.0 to -33.0 | -31.0 | 29.3 |
| East | Rookery | Dolomite | Dol | 2 | 10 | 83 to 100 | 90 | -28.0 to -30.0 | -30.0 | 28.7 |
| East | Rookery | Sphalerite | Sph3 | 1 | 8 | 82 to 97 | 89 | -7.0 to - 35.0 | -14.0 | - |
| East | Rookery | Sphalerite | Sph3 | 2 | 2 | 105 to 106 | 105 | -31.0 to -35.0 | -33.0 | - |
| East | Rookery | Sphalerite | Sph3 | 3 | 5 | 90 | 90 | - | - | - |
| West | Harrison | Sphalerite | Sph3 | 1 | 9 | 70 to 90 | 81 | - | - | - |
| West | Harrison | Sphalerite | Sph3 | 2 | 5 | 60 to 65 | 62 | -4.9 | -4.9 | - |
| West | Harrison | Sphalerite | Sph3 | 3 | 9 | 74 to 96 | 87 | -27.0 to -34.0 | -30.0 | - |
| South | Seal | Dolomite | Dol | 1 | 9 | 88 to 95 | 85 | - | - | - |
| South | Seal | Sphalerite | Sph3 | 1 | 2 | 110 | 110 | - | - | - |

| | | | | | | | | | | |
|-------|---------|------------|------|---|---|---------------|-----|------------------|------|-----|
| South | Seal | Calcite | Cal1 | 1 | 9 | 140 to 156 | 148 | -0.1 to - 1.0 | -0.3 | 0.5 |
| South | Typhoon | Sphalerite | Sph3 | 1 | 4 | 82 to 86 | 85 | - | - | - |

Table 2-2: SIMS isotope results

Stable isotope data, presented to 1σ (0.3‰ and 1.2‰ for S and O isotopes, respectively) for dolomite, calcite, pyrite, galena, and sphalerite as determined by SIMS.

| Location | Showing | Sulfide | Stage | $\delta^{34}\text{S}_{\text{CDT}}$ (‰) | Carbonate | Stage | $\delta^{18}\text{O}_{\text{SMOW}}$ (‰) |
|----------|---------|------------|-------|---|-----------|-------|--|
| North | Trigger | Sphalerite | Sph3 | 18.9 | Dolomite | Dol | 26.9 |
| North | Trigger | Sphalerite | Sph3 | 18.3 | Dolomite | Dol | 23.2 |
| North | Trigger | Sphalerite | Sph3 | 19.1 | Dolomite | Dol | 26.5 |
| North | Trigger | Sphalerite | Sph3 | 22.1 | Dolomite | Dol | 25.9 |
| North | Trigger | Sphalerite | Sph3 | 17.7 | | | |
| North | Trigger | Sphalerite | Sph3 | 18.7 | | | |
| North | Trigger | Sphalerite | Sph3 | 20.2 | | | |
| North | Trigger | Sphalerite | Sph3 | 22.1 | | | |
| North | Trigger | Sphalerite | Sph3 | 18.8 | | | |
| North | Trigger | Sphalerite | Sph3 | 19.4 | | | |
| North | Trigger | Galena | Gal | 20.2 | | | |
| North | Trigger | Galena | Gal | 17.6 | | | |
| North | Trigger | Galena | Gal | 18.3 | | | |
| North | JG | Sphalerite | Sph3 | 26.9 | Calcite | C1 | 18.1 |
| North | JG | Sphalerite | Sph3 | 26.8 | Calcite | C1 | 12.8 |
| North | JG | Sphalerite | Sph3 | 26.0 | Calcite | C1 | 19.7 |
| North | JG | Sphalerite | Sph3 | 24.7 | Calcite | C1 | 15.9 |
| North | JG | Sphalerite | Sph3 | 24.0 | Calcite | C1 | 14.4 |
| North | JG | | | | Calcite | C1 | 18.4 |
| North | Dundas | Sphalerite | Sph2 | -5.9 | Dolomite | Dol | 22.3 |
| North | Dundas | Sphalerite | Sph2 | -6.0 | Dolomite | Dol | 23.2 |
| North | Dundas | Sphalerite | Sph2 | -5.7 | Dolomite | Dol | 24.3 |

| | | | | | | | |
|-------|---------|------------|------|------|----------|-----|------|
| North | Dundas | Sphalerite | Sph2 | -4.1 | Dolomite | Dol | 22.2 |
| North | Dundas | Sphalerite | Sph2 | -2.5 | Dolomite | Dol | 27.1 |
| North | Dundas | Sphalerite | Sph2 | -4.3 | Dolomite | Dol | 22.3 |
| North | Dundas | Sphalerite | Sph2 | -3.1 | Dolomite | Dol | 24.6 |
| North | Dundas | Sphalerite | Sph2 | -2.5 | Dolomite | Dol | 26.7 |
| North | Dundas | Sphalerite | Sph2 | -1.9 | Dolomite | Dol | 23.2 |
| North | Dundas | Sphalerite | Sph2 | -1.6 | Dolomite | Dol | 19.9 |
| North | Dundas | Sphalerite | Sph2 | -3.1 | Dolomite | Dol | 19.3 |
| North | Dundas | Sphalerite | Sph3 | 0.7 | Calcite | C1 | 18.9 |
| North | Dundas | Sphalerite | Sph3 | 1.3 | Calcite | C1 | 20.3 |
| North | Dundas | Sphalerite | Sph3 | -1.0 | Calcite | C1 | 19.9 |
| North | Dundas | Sphalerite | Sph3 | -0.5 | Calcite | C1 | 20.5 |
| North | Dundas | Sphalerite | Sph3 | -0.6 | Calcite | C2 | 9.4 |
| North | Dundas | Sphalerite | Sph3 | -1.1 | Calcite | C2 | 10.1 |
| North | Dundas | Sphalerite | Sph3 | -2.2 | Calcite | C2 | 8.0 |
| North | Dundas | Sphalerite | Sph3 | -2.0 | Calcite | C2 | 10 |
| North | Dundas | Sphalerite | Sph3 | -2.2 | Calcite | C2 | 7.6 |
| North | Dundas | | | | Calcite | C2 | 8.8 |
| North | Dundas | | | | Calcite | C2 | 8.2 |
| North | Dundas | | | | Calcite | C2 | 6.8 |
| North | Dundas | | | | Calcite | C2 | 8.6 |
| East | Rookery | Sphalerite | Sph3 | 12.8 | Dolomite | Dol | 22.7 |
| East | Rookery | Sphalerite | Sph3 | 13.4 | Dolomite | Dol | 23.1 |
| East | Rookery | Sphalerite | Sph3 | 12.5 | Dolomite | Dol | 22.6 |
| East | Rookery | Sphalerite | Sph3 | 14.4 | Dolomite | Dol | 20.2 |
| East | Rookery | | | | Dolomite | Dol | 21.6 |
| East | Rookery | | | | Dolomite | Dol | 22.7 |

| | | | | | | | |
|------|-----------|------------|------|------|----------|-----|------|
| East | Rookery | | | | Dolomite | Dol | 21.7 |
| East | Rookery | | | | Calcite | C1 | 16.1 |
| East | Rookery | | | | Calcite | C1 | 11.3 |
| East | Rookery | | | | Calcite | C1 | 15.5 |
| East | Rookery | | | | Calcite | C1 | 12.6 |
| East | Rookery | | | | Calcite | C1 | 12.1 |
| East | Stuart | Sphalerite | Sph3 | 9.0 | Calcite | C2 | 8.8 |
| East | Stuart | Sphalerite | Sph3 | 7.9 | Calcite | C2 | 7.7 |
| East | Stuart | Sphalerite | Sph3 | 16.3 | Calcite | C2 | 8.9 |
| East | Stuart | Sphalerite | Sph3 | 14.7 | Calcite | C2 | 8.2 |
| East | Stuart | Sphalerite | Sph3 | 11.7 | | | |
| East | Stuart | Sphalerite | Sph3 | 8.1 | | | |
| East | Stuart | Sphalerite | Sph3 | 19.2 | | | |
| East | Stuart | Sphalerite | Sph3 | 18.3 | | | |
| East | Stuart | Galena | Gn1 | 15.7 | | | |
| East | Stuart | Galena | Gn1 | 17 | | | |
| East | Bacon | Sphalerite | Sph3 | 9.9 | Dolomite | Dol | 30.3 |
| East | Bacon | Sphalerite | Sph3 | 9.7 | Dolomite | Dol | 27.7 |
| East | Bacon | Sphalerite | Sph3 | 8.9 | Dolomite | Dol | 30.7 |
| East | Bacon | Sphalerite | Sph3 | 10 | Dolomite | Dol | 30.1 |
| East | Snowblind | | | | Dolomite | Dol | 26.6 |
| East | Snowblind | | | | Dolomite | Dol | 23.9 |
| East | Snowblind | | | | Dolomite | Dol | 25 |
| East | Snowblind | | | | Dolomite | Dol | 23.9 |
| East | Snowblind | | | | Dolomite | Dol | 26.8 |
| West | Harrison | Sphalerite | Sph3 | 8.0 | Dolomite | Dol | 22.6 |
| West | Harrison | Sphalerite | Sph3 | 5.1 | Dolomite | Dol | 22.9 |

| | | | | | | | |
|---------|----------|------------|------|------|----------|-----|------|
| West | Harrison | Sphalerite | Sph3 | 7.1 | Dolomite | Dol | 26.5 |
| West | Harrison | Sphalerite | Sph3 | 7.0 | Dolomite | Dol | 22.5 |
| West | Harrison | Sphalerite | Sph3 | 7.4 | Dolomite | Dol | 22.4 |
| West | Harrison | Sphalerite | Sph3 | 8.2 | Dolomite | Dol | 26.4 |
| West | Harrison | Sphalerite | Sph3 | 14.4 | Calcite | C1 | 10 |
| West | Harrison | Sphalerite | Sph3 | 17.8 | Calcite | C1 | 11 |
| West | Harrison | Sphalerite | Sph3 | 18.6 | Calcite | C1 | 10.4 |
| West | Harrison | Sphalerite | Sph3 | 12.7 | Calcite | C1 | 10.8 |
| West | Harrison | | | | Calcite | C1 | 11.9 |
| West | Harrison | | | | Calcite | C1 | 19.1 |
| West | Harrison | | | | Calcite | C1 | 15.6 |
| West | Harrison | | | | Calcite | C1 | 17.8 |
| West | Harrison | | | | Calcite | C1 | 17 |
| Central | Eclipse | Sphalerite | Sph2 | -1.5 | Dolomite | Dol | 21.5 |
| Central | Eclipse | Sphalerite | Sph2 | -1.0 | Dolomite | Dol | 23.2 |
| Central | Eclipse | Sphalerite | Sph2 | -1.8 | Dolomite | Dol | 24.8 |
| Central | Eclipse | Sphalerite | Sph2 | -3.4 | Dolomite | Dol | 24.5 |
| Central | Eclipse | Sphalerite | Sph2 | 0.6 | | | |
| Central | Eclipse | Sphalerite | Sph2 | 2.2 | | | |
| Central | Eclipse | Sphalerite | Sph2 | -1.6 | | | |
| Central | Eclipse | Sphalerite | Sph3 | 4.2 | | | |
| Central | Eclipse | Sphalerite | Sph3 | 4.0 | | | |
| Central | Eclipse | Sphalerite | Sph3 | 2.3 | | | |
| Central | Eclipse | Sphalerite | Sph3 | 3.3 | | | |
| Central | Eclipse | Sphalerite | Sph3 | 2.4 | | | |
| Central | Eclipse | Galena | Gn1 | 0.5 | | | |
| Central | Eclipse | Galena | Gn1 | 1.5 | | | |

| | | | | | | | |
|---------|---------|------------|------|------|----------|-----|------|
| Central | Eclipse | Galena | Gn1 | -0.4 | | | |
| Central | Polaris | Sphalerite | Sph3 | 6.3 | Dolomite | Dol | 24.3 |
| Central | Polaris | Sphalerite | Sph3 | 6.2 | Dolomite | Dol | 23.9 |
| Central | Polaris | Sphalerite | Sph3 | 5.7 | Dolomite | Dol | 25.7 |
| Central | Polaris | Sphalerite | Sph3 | 6.4 | Dolomite | Dol | 25.2 |
| Central | Polaris | Sphalerite | Sph3 | 6.6 | Dolomite | Dol | 26.7 |
| Central | Polaris | | | | Calcite | C1 | 12 |
| Central | Polaris | | | | Calcite | C1 | 11.3 |
| Central | Polaris | | | | Calcite | C1 | 9.8 |
| Central | Polaris | | | | Calcite | C1 | 7.0 |
| Central | Polaris | | | | Calcite | C1 | 11.3 |
| Central | Truro | Pyrite | Py2 | 6.9 | Calcite | C1 | 10.1 |
| Central | Truro | Pyrite | Py2 | 7.0 | Calcite | C1 | 12.8 |
| Central | Truro | Pyrite | Py2 | 6.7 | Calcite | C1 | 13.5 |
| Central | Truro | Sphalerite | Sph3 | 8.4 | Calcite | C1 | 13.8 |
| Central | Truro | Sphalerite | Sph3 | 7.7 | Calcite | C1 | 12.0 |
| Central | Truro | Sphalerite | Sph3 | 8.6 | | | |
| Central | Truro | Sphalerite | Sph3 | 8.1 | | | |
| South | Seal | Sphalerite | Sph3 | 27.1 | Dolomite | Dol | 22.2 |
| South | Seal | Sphalerite | Sph3 | 32.0 | Dolomite | Dol | 24.2 |
| South | Seal | Sphalerite | Sph3 | 32.9 | Dolomite | Dol | 24.0 |
| South | Seal | Sphalerite | Sph3 | 26.4 | Dolomite | Dol | 25.1 |
| South | Seal | Sphalerite | Sph3 | 31.9 | Dolomite | Dol | 22.9 |
| South | Seal | Sphalerite | Sph3 | 30.0 | Dolomite | Dol | 24.0 |
| South | Seal | Sphalerite | Sph3 | 27.5 | Dolomite | Dol | 24.5 |
| South | Seal | Sphalerite | Sph3 | 29.3 | Dolomite | Dol | 23.0 |
| South | Seal | Sphalerite | Sph3 | 27.1 | Dolomite | Dol | 23.4 |

| | | | | | | | |
|-------|---------|------------|------|------|----------|-----|------|
| South | Seal | Sphalerite | Sph3 | 26.8 | Dolomite | Dol | 22.7 |
| South | Seal | Sphalerite | Sph3 | 26.3 | Dolomite | Dol | 23.4 |
| South | Seal | Sphalerite | Sph3 | 27.8 | Dolomite | Dol | 20.5 |
| South | Seal | Sphalerite | Sph3 | 28.5 | Dolomite | Dol | 21.5 |
| South | Seal | Sphalerite | Sph3 | 27.3 | Dolomite | Dol | 20.3 |
| South | Seal | Sphalerite | Sph3 | 27.6 | Dolomite | Dol | 21.1 |
| South | Seal | Sphalerite | Sph3 | 30.0 | Dolomite | Dol | 23.7 |
| South | Seal | Sphalerite | Sph3 | 31.2 | Dolomite | Dol | 23.1 |
| South | Seal | Sphalerite | Sph3 | 31.2 | Dolomite | Dol | 22.7 |
| South | Seal | Pyrite | Py1 | 33.5 | Dolomite | Dol | 23.3 |
| South | Seal | Pyrite | Py1 | 30.9 | Dolomite | Dol | 21.9 |
| South | Seal | Pyrite | Py1 | 31.6 | Dolomite | Dol | 24.6 |
| South | Seal | Pyrite | Py1 | 31.5 | Dolomite | Dol | 23.3 |
| South | Seal | Pyrite | Py1 | 30.3 | Dolomite | Dol | 23.5 |
| South | Seal | Pyrite | Py1 | 31.6 | Dolomite | Dol | 24.0 |
| South | Seal | Pyrite | Py1 | 31.1 | Calcite | C1 | 20.7 |
| South | Seal | Pyrite | Py1 | 30.7 | Calcite | C1 | 19.2 |
| South | Seal | Pyrite | Py1 | 29.5 | Calcite | C1 | 13.4 |
| South | Seal | Pyrite | Py1 | 30.3 | Calcite | C1 | 15.3 |
| South | Seal | Pyrite | Py1 | 30.6 | Calcite | C1 | 13.8 |
| South | Seal | | | | Calcite | C1 | 15.9 |
| South | Typhoon | | | | Dolomite | Dol | 20.5 |
| South | Typhoon | | | | Dolomite | Dol | 19.7 |
| South | Typhoon | | | | Dolomite | Dol | 19.9 |
| South | Typhoon | | | | Dolomite | Dol | 20.2 |
| South | Typhoon | | | | Dolomite | Dol | 20.6 |
| South | Typhoon | | | | Dolomite | Dol | 25.8 |

| | | | | |
|-------|---------|----------|-----|------|
| South | Typhoon | Dolomite | Dol | 24.5 |
| South | Typhoon | Dolomite | Dol | 26.4 |
| South | Typhoon | Dolomite | Dol | 23.5 |
| South | Typhoon | Dolomite | Dol | 26.2 |
| South | Typhoon | Dolomite | Dol | 25.5 |
| South | Typhoon | Dolomite | Dol | 23.8 |
| South | Typhoon | Dolomite | Dol | 23.9 |
| South | Typhoon | Calcite | C1 | 21.0 |
| South | Typhoon | Calcite | C1 | 16.3 |
| South | Typhoon | Calcite | C1 | 19.2 |
| South | Typhoon | Calcite | C1 | 19.3 |
| South | Typhoon | Calcite | C1 | 21.1 |

Table 2-3: REE+Y values of carbonate gangue minerals

Summary of the averaged geochemical data (reported in ppm) of the different carbonate stages in mineralization. $Ce_N^* = 0.5*(La_N+Pr_N)$; $Pr_N^* = 0.5*(Ce_N+Nd_N)$; $Eu_N^* = (2/3)*Sm_N+(1/3)*Tb_N$

| Region | West | West | West | North | North | North | North | North | North | North | Central | Central | Central |
|---------|----------|----------|----------|----------|----------|----------|----------|--------|--------|--------|---------|---------|---------|
| Showing | Harrison | Harrison | Harrison | Schiells | Schiells | Schiells | Schiells | Dundas | Dundas | Dundas | Eclipse | Eclipse | Eclipse |
| Stage | Dol | Dol | Dol | Dol | Dol | Dol | Dol |
| Mn | 320 | 400 | 180 | 960 | 440 | 1100 | 780 | 940 | 1600 | 2600 | 500 | 760 | 730 |
| Fe | 180 | 110 | 140 | 5400 | 2300 | 5400 | 4400 | 2100 | 1400 | 19000 | 5500 | 2300 | 3500 |
| Sr | 43.7 | 46.9 | 49.6 | 64.6 | 38.8 | 56.8 | 35.5 | 95.5 | 92.6 | 54.3 | 32.1 | 77.5 | 64.6 |
| La | 0.59 | 1.19 | 0.99 | 1.61 | 1.62 | 1.77 | 2.19 | 12.40 | 7.08 | 10.20 | 3.45 | 3.95 | 3.92 |
| Ce | 0.91 | 2.64 | 1.11 | 3.68 | 3.37 | 3.60 | 4.52 | 18.30 | 11.30 | 23.50 | 8.70 | 8.24 | 7.77 |
| Pr | 0.15 | 0.40 | 0.21 | 0.35 | 0.31 | 0.36 | 0.49 | 1.70 | 1.10 | 1.90 | 1.0 | 0.77 | 0.82 |
| Nd | 0.71 | 1.60 | 0.94 | 1.37 | 1.25 | 1.48 | 1.66 | 6.13 | 3.66 | 6.88 | 3.90 | 2.94 | 2.94 |
| Sm | 0.15 | 0.29 | 0.20 | 0.27 | 0.21 | 0.28 | 0.34 | 0.81 | 0.49 | 1.05 | 0.67 | 0.57 | 0.53 |
| Eu | 0.020 | 0.050 | 0.050 | 0.060 | 0.030 | 0.060 | 0.040 | 0.350 | 0.200 | 0.320 | 0.100 | 0.100 | 0.110 |
| Gd | 0.20 | 0.30 | 0.24 | 0.28 | 0.17 | 0.30 | 0.27 | 0.77 | 0.47 | 0.99 | 0.49 | 0.50 | 0.50 |
| Tb | 0.024 | 0.042 | 0.036 | 0.036 | 0.028 | 0.038 | 0.046 | 0.081 | 0.055 | 0.120 | 0.070 | 0.087 | 0.086 |
| Dy | 0.178 | 0.352 | 0.220 | 0.222 | 0.219 | 0.254 | 0.311 | 0.454 | 0.353 | 0.680 | 0.390 | 0.487 | 0.575 |
| Y | 1.8 | 2.8 | 2.5 | 1.6 | 1.3 | 1.7 | 2.0 | 3.9 | 2.9 | 5.0 | 2.0 | 3.1 | 3.8 |
| Ho | 0.033 | 0.083 | 0.045 | 0.054 | 0.038 | 0.051 | 0.058 | 0.082 | 0.068 | 0.120 | 0.074 | 0.100 | 0.140 |
| Er | 0.116 | 0.293 | 0.146 | 0.140 | 0.131 | 0.124 | 0.210 | 0.216 | 0.193 | 0.311 | 0.189 | 0.285 | 0.375 |
| Tm | 0.015 | 0.035 | 0.019 | 0.014 | 0.010 | 0.017 | 0.023 | 0.022 | 0.021 | 0.034 | 0.022 | 0.037 | 0.051 |
| Yb | 0.060 | 0.225 | 0.084 | 0.120 | 0.112 | 0.104 | 0.183 | 0.144 | 0.132 | 0.186 | 0.144 | 0.214 | 0.357 |
| Lu | 0.008 | 0.033 | 0.014 | 0.012 | 0.012 | 0.015 | 0.027 | 0.018 | 0.016 | 0.023 | 0.019 | 0.032 | 0.052 |
| EREE | 4.95 | 10.31 | 6.76 | 9.82 | 8.84 | 10.19 | 12.36 | 45.31 | 27.93 | 51.28 | 21.23 | 21.39 | 21.97 |
| Ce/Ce* | 0.73 | 0.91 | 0.58 | 1.20 | 1.10 | 1.10 | 1.10 | 0.93 | 0.97 | 1.30 | 1.10 | 1.10 | 1.00 |
| Pr/Pr* | 1.0 | 1.1 | 1.1 | 0.9 | 0.9 | 0.9 | 1.0 | 0.9 | 0.9 | 0.8 | 1.0 | 0.9 | 1.0 |
| Eu/Eu* | 0.9 | 1.0 | 1.2 | 1.3 | 0.9 | 1.2 | 0.7 | 2.6 | 2.4 | 1.8 | 0.9 | 1.0 | 1.0 |
| Y/Ho | 54 | 34 | 55 | 30. | 35 | 34 | 35 | 47 | 42 | 41 | 27 | 30. | 28 |

| Region | Polaris | East | East | East | East | East | East | South | South | South | South | South | South |
|---------|---------|---------|---------|-----------|-----------|-----------|-----------|-------|-------|-------|-------|---------|---------|
| Showing | Polaris | Rookery | Rookery | Snowblind | Snowblind | Snowblind | Snowblind | Seal | Seal | Seal | Seal | Typhoon | Typhoon |
| Stage | Dol | Dol | Dol | Dol | Dol | Dol | Dol | Dol | Dol | Dol | Dol | Dol | Dol |
| Mn | 440 | 590 | 430 | 140 | 150 | 120 | 130 | 620 | 560 | 560 | 640 | 130 | 85 |
| Fe | 1700 | 13000 | 14000 | 1600 | 2200 | 2700 | 790 | 2800 | 2800 | 2900 | 2600 | | |
| Sr | 55.4 | 24.3 | 48.6 | 39.1 | 45.4 | 38.1 | 33.0 | 18.8 | 20.4 | 18.7 | 20.9 | 44.6 | 47.5 |
| La | 3.04 | 0.74 | 1.36 | 1.29 | 1.53 | 1.17 | 1.08 | 9.66 | 8.55 | 11.70 | 9.15 | 4.54 | 9.05 |
| Ce | 5.49 | 1.80 | 3.35 | 1.97 | 2.51 | 1.78 | 1.50 | 19.40 | 17.70 | 24.10 | 19.30 | 8.06 | 14.80 |
| Pr | 0.57 | 0.26 | 0.36 | 0.24 | 0.30 | 0.20 | 0.18 | 2.00 | 1.80 | 2.30 | 2.00 | 0.60 | 1.10 |
| Nd | 2.16 | 1.21 | 1.45 | 0.94 | 1.21 | 0.84 | 0.69 | 6.98 | 6.33 | 8.23 | 7.13 | 2.02 | 3.80 |
| Sm | 0.35 | 0.33 | 0.31 | 0.19 | 0.25 | 0.20 | 0.13 | 0.93 | 0.83 | 1.10 | 1.02 | 0.29 | 0.49 |
| Eu | 0.080 | 0.030 | 0.070 | 0.040 | 0.060 | 0.040 | 0.030 | 0.150 | 0.140 | 0.190 | 0.160 | 0.060 | 0.120 |
| Gd | 0.30 | 0.33 | 0.31 | 0.22 | 0.27 | 0.23 | 0.15 | 0.67 | 0.58 | 0.80 | 0.76 | 0.28 | 0.44 |
| Tb | 0.034 | 0.051 | 0.045 | 0.030 | 0.036 | 0.031 | 0.022 | 0.076 | 0.070 | 0.086 | 0.086 | 0.033 | 0.051 |
| Dy | 0.198 | 0.261 | 0.295 | 0.192 | 0.234 | 0.203 | 0.163 | 0.430 | 0.417 | 0.487 | 0.467 | 0.207 | 0.299 |
| Y | 1.2 | 1.2 | 1.7 | 2.2 | 2.5 | 2.0 | 1.9 | 2.4 | 2.3 | 2.5 | 2.5 | 1.4 | 2.1 |
| Ho | 0.034 | 0.052 | 0.058 | 0.040 | 0.047 | 0.041 | 0.035 | 0.074 | 0.066 | 0.079 | 0.080 | 0.038 | 0.053 |
| Er | 0.091 | 0.157 | 0.184 | 0.118 | 0.144 | 0.113 | 0.096 | 0.200 | 0.172 | 0.202 | 0.208 | 0.112 | 0.139 |
| Tm | 0.010 | 0.023 | 0.024 | 0.014 | 0.018 | 0.012 | 0.011 | 0.017 | 0.018 | 0.020 | 0.020 | 0.014 | 0.013 |
| Yb | 0.057 | 0.185 | 0.181 | 0.088 | 0.123 | 0.073 | 0.066 | 0.105 | 0.110 | 0.130 | 0.139 | 0.084 | 0.091 |
| Lu | 0.008 | 0.025 | 0.028 | 0.011 | 0.016 | 0.009 | 0.009 | 0.015 | 0.019 | 0.018 | 0.018 | 0.012 | 0.013 |
| EREE | 13.63 | 6.66 | 9.76 | 7.53 | 9.21 | 6.94 | 6.04 | 43.12 | 39.13 | 51.91 | 43.04 | 17.78 | 32.64 |
| Ce/Ce* | 1.0 | 0.97 | 1.2 | 0.86 | 0.88 | 0.87 | 0.80 | 1.1 | 1.1 | 1.1 | 1.1 | 1.1 | 1.1 |
| Pr/Pr* | 0.93 | 0.96 | 0.91 | 0.98 | 0.98 | 0.94 | 1.0 | 0.98 | 0.98 | 0.91 | 0.96 | 0.82 | 0.83 |
| Eu/Eu* | 1.4 | 0.41 | 1.1 | 1.2 | 1.2 | 1.0 | 1.1 | 1.1 | 1.1 | 1.1 | 1.0 | 1.3 | 1.5 |
| Y/Ho | 36 | 23 | 30. | 54 | 53 | 49 | 53 | 33 | 34 | 32 | 31 | 38 | 40. |

| Region | South | South | West | North | North | East | Centre | South |
|---------|---------|---------|----------|--------|---------|---------|--------|---------|
| Showing | Typhoon | Typhoon | Harrison | Dundas | Trigger | Rookery | Truro | Typhoon |
| Stage | Dol | Dol | Cal1 | Cal1 | Cal1 | Cal1 | Cal1 | Cal1 |
| Mn | 420 | 290 | 38 | 550 | 1300 | 350 | 82 | 110 |
| Fe | | | 160 | 120 | 180 | 130 | 87 | 11000 |
| Sr | 42.4 | 31.7 | 785.0 | 74.8 | 86.3 | 94.8 | 399.0 | 16.0 |
| La | 7.59 | 4.47 | 3.72 | 0.73 | 1.99 | 2.35 | 0.24 | 4.69 |
| Ce | 13.40 | 8.47 | 7.53 | 1.37 | 4.88 | 4.64 | 0.62 | 8.62 |
| Pr | 1.30 | 0.81 | 0.97 | 0.17 | 0.70 | 0.55 | 0.08 | 0.84 |
| Nd | 4.84 | 2.91 | 3.85 | 0.64 | 3.60 | 2.30 | 0.32 | 2.95 |
| Sm | 0.77 | 0.37 | 0.84 | 0.12 | 1.10 | 0.47 | 0.06 | 0.39 |
| Eu | 0.170 | 0.080 | 0.190 | 0.030 | 0.290 | 0.110 | 0.010 | 0.080 |
| Gd | 0.75 | 0.29 | 0.91 | 0.11 | 1.80 | 0.58 | 0.08 | 0.31 |
| Tb | 0.095 | 0.038 | 0.150 | 0.015 | 0.290 | 0.089 | 0.012 | 0.040 |
| Dy | 0.562 | 0.232 | 1.010 | 0.099 | 1.910 | 0.626 | 0.073 | 0.251 |
| Y | 3.4 | 1.4 | 8.8 | 0.8 | 12.0 | 4.8 | 0.5 | 1.5 |
| Ho | 0.110 | 0.047 | 0.210 | 0.020 | 0.340 | 0.140 | 0.014 | 0.050 |
| Er | 0.292 | 0.131 | 0.578 | 0.057 | 0.915 | 0.452 | 0.039 | 0.143 |
| Tm | 0.036 | 0.019 | 0.070 | 0.007 | 0.100 | 0.061 | 0.006 | 0.020 |
| Yb | 0.218 | 0.138 | 0.401 | 0.050 | 0.688 | 0.411 | 0.032 | 0.149 |
| Lu | 0.031 | 0.023 | 0.048 | 0.007 | 0.084 | 0.065 | 0.005 | 0.022 |
| EREE | 33.62 | 19.45 | 29.23 | 4.21 | 30.62 | 17.65 | 2.06 | 20.10 |
| Ce/Ce* | 1.0 | 1.1 | 1.0 | 0.9 | 1.0 | 1.0 | 1.1 | 1.0 |
| Pr/Pr* | 0.9 | 0.9 | 1.0 | 1.0 | 0.9 | 1.0 | 1.0 | 0.9 |
| Eu/Eu* | 1.3 | 1.2 | 1.2 | 1.4 | 1.1 | 1.1 | 1.2 | 1.3 |
| Y/Ho | 32 | 30 | 42 | 39 | 35 | 35 | 34 | 31 |

Table 2-4: Trace element composition of sphalerite

Trace element content measured by LA ICP-MS for sphalerite from representative showings throughout the district.

| Region | Showing | Stage | Mn (ppm) | Fe (ppm) | Co (ppm) | Cu (ppm) | Ga (ppm) | Ge (ppm) | Se (ppm) | Mo (ppm) | Ag (ppm) | Cd (ppm) | In (ppm) | Sn (ppm) | Pb (ppm) | Bi (ppm) |
|---------|-----------|-------|----------|----------|----------|----------|----------|----------|----------|----------|----------|----------|----------|----------|----------|----------|
| Central | Polaris | Sph1 | 100 | 12000 | 0.70 | 75 | 4.9 | 57 | 11 | 0.86 | 48 | 1600 | 0.009 | 0.22 | 3100 | 0.021 |
| Central | Polaris | Sph2 | 69 | 7100 | 0.45 | 52 | 3.2 | 61 | 11 | 0.77 | 48.0 | 1600 | 0.008 | 0.23 | 1500 | 0.023 |
| Central | Eclipse | Sph2 | 110 | 7400 | 0.73 | 250 | 4.4 | 87 | 6 | 0.30 | 15.0 | 1400 | 0.079 | 0.19 | 2600 | 0.018 |
| North | Dundas | Sph2 | 88 | 49000 | 0.87 | 51 | 2.1 | 610 | 20. | 0.79 | 1.6 | 440 | b.d. | 0.49 | 1300 | 0.013 |
| West | Harrison | Sph3 | 56 | 320000 | 0.08 | 1.3 | 2.1 | 110 | 3 | 0.26 | 0.1 | 1100 | b.d. | 0.17 | 2100 | 0.015 |
| North | Dundas | Sph3 | 8 | 4600 | 1.60 | 1100 | 180.0 | 110 | 14 | 0.96 | 6.4 | 7400 | 0.140 | 0.42 | 280 | 0.013 |
| North | Trigger | Sph3 | 7 | 2500 | 3.80 | 280 | 8.4 | 1 | 2 | 0.10 | 100.0 | 1400 | 0.440 | 0.74 | 120 | 0.008 |
| East | Snowblind | Sph3 | b.d. | 840 | 1.20 | 29 | 17.0 | 21 | 13 | 0.78 | 53.0 | 2100 | b.d. | 0.09 | 27 | 0.009 |
| East | Rookery | Sph3 | 9 | 4900 | 0.45 | 86 | 38.0 | 64 | 3 | 0.17 | 9.1 | 2200 | 0.077 | 0.30 | 65 | 0.008 |
| South | Seal | Sph3 | 11 | 54000 | 0.10 | 4.8 | 0.3 | 110 | 3 | 0.09 | 240.0 | 1800 | 0.100 | 0.19 | 10 | 0.009 |
| Central | Polaris | Sph3 | 35 | 2600 | 0.64 | 170 | 13.0 | 15 | 11 | 0.80 | 160.0 | 3300 | 0.013 | 0.23 | 360 | 0.026 |
| Central | Eclipse | Sph3 | 11 | 1600 | 1.20 | 130 | 1.8 | 32 | 6 | 0.27 | 92.0 | 2000 | b.d. | 0.14 | 130 | 0.013 |

Chapter 3

3 Atypical Cu mineralisation in the Cornwallis carbonate-hosted Zn district: Storm copper deposit, Arctic Canada

Jordan Mathieu^{a,*}, Elizabeth C. Turner^a, Daniel J. Kontak^a, Mostafa Fayek^b, and Ryan Mathur^c

^aHarquail School of Earth Sciences, Laurentian University, Sudbury, ON P3E 2C6, Canada

^bDepartment of Geological Science, University of Manitoba, Winnipeg, MB R3T 2N2, Canada

^cJuniata College, Huntingdon, PA 16652, USA

*jy_mathieu@laurentian.ca

Abstract

The metallogenetically important Cornwallis Zn district, in Canada's Arctic islands, includes the past-producing Polaris mine and numerous base-metal showings, including Storm copper. Storm is unusual because it is near the southern limit of the district, is Cu- versus Zn-dominated, is overlain and underlain by red sandstone, and is hosted by Silurian strata (rather than Ordovician strata, as at Polaris). Mineralisation styles are primarily carbonate replacement and breccia, and consist of geerite, covellite, bornite, and chalcopyrite, all of which are associated with calcite and dolomite gangue. Multiple in situ micro-analytical techniques (fluid inclusion microthermometry, evaporate mound SEM-EDS, LA ICP-MS, SIMS), plus conventional Cu isotopic analysis were integrated to characterise the nature of the mineralising fluids and events. Fluid inclusions yielded low-temperature ($T_h < 130^\circ\text{C}$), moderate- to low-salinity (17.0 to 0.4 wt. % NaCl equiv.) fluids. Evaporate mound SEM-EDS analysis, which quantified the solute

chemistry, show a change from bimodal Na- and Na+K-dominated fluid mixture to a Na+K-dominated fluid. The $\delta^{18}\text{O}_{\text{H}_2\text{O}}$ signature of the mineralising fluid involved reservoirs reflecting involvement of meteoric (<0‰) and rock-equilibrated (8‰) fluids, respectively. The $\delta^{34}\text{S}$ values are nearly homogeneous for pre-ore and second generation sulphides at 0‰ and 10‰, respectively, whereas the third generation (recrystallised) sulphides are more variable, with values from 8.8 to 23.4‰. The majority of Cu sulphides have $\delta^{65}\text{Cu}$ values near 0‰, but second-generation chalcopyrite shows elevated $\delta^{65}\text{Cu}$ values from +1.31‰ in the north to +3.44 ‰ in the south, suggesting a probable southward fluid flow. Positive Eu PAAS-normalised anomalies in early dolomite cements, which indicate basement involvement, are absent in succeeding cements, suggesting a change in fluid pathways and hence the mineralogical nature of the reservoir. Negative Ce_{SN} anomalies in main-stage calcite cement indicate an oxidised fluid, but the lack of similar Ce anomalies in the dolomite cements indicates reduced fluids. These data suggest that Storm copper mineralisation is related to basement-equilibrated fluids mobilised during the Ellesmerian orogeny (Devonian), which acquired heat and leached Cu from underlying Proterozoic red sandstone (Aston Formation) and were then focussed up faults where Cu sulphides precipitated. Prolonged meteoric fluid movement from the north, with intermittent episodes of basin-equilibrated fluid influx, produced hypogene and supergene mineralisation. Fluid movement resumed in the Cenozoic, when high-latitude fluids altered Cu minerals to atacamite. Storm copper mineralisation shares characteristics with both red-bed and Irish-type Cu deposit sub-types, but may also highlight a relationship with carbonate-replacement Zn-Pb deposits. Timing of mineralisation is comparable to that of Zn ore precipitation at Polaris, suggesting that Storm may be an integral part of the Cornwallis district, in spite of its unusual composition.

Keywords: Carbonate-hosted copper deposit, Arctic Canada, fluid inclusions, stable isotopes, REE geochemistry, geerite

3.1 Introduction

The Canadian Arctic once had two world-class carbonate-hosted Zn-Pb mines: Polaris (Little Cornwallis Island; mid-late Paleozoic mineralisation age; Christensen et al., 1995) and Nanisivik (Baffin Island; Mesoproterozoic mineralisation age; Hnatyshin et al., 2016; Fig. 1). Multiple Zn and Pb showings are associated with each of these mines (Dewing et al., 2007b), but Cu is scarce. The most conspicuous Cu site (Storm) is hosted in mid-Paleozoic carbonate rocks in a narrow, northwest-trending graben system (Aston-Batty line; Dewing et al., 2007a) on central Somerset Island (Fig. 2). Western Somerset Island is known to be underlain by Mesoproterozoic strata that are putatively equivalent to “rift”-related strata of the Borden basin on nearby northern Baffin Island (Fig. 1).

Sedimentary-rock-hosted Cu deposits are, along with porphyry Cu deposits, the most economically significant base-metal deposits globally because of the central African copperbelt (approximately 190 Mt Cu; Hitzman et al., 2005; Selley et al., 2005). Sub-types of these sedimentary-rock-hosted deposits arise from variability in host rock and reductant types, as well as different temporal relationships to volcanic activity. Kupferschiefer-type deposits (e.g., Jowett, 1986) are hosted in reduced, shallow-marine sedimentary rocks overlying oxidised, hematite-bearing, coarse-grained, continental siliciclastic rocks (Hitzman et al., 2005). Red-bed

type deposits (e.g., Kennecott; Bateman and McLaughlen, 1920) are in reduced, continental siliciclastic rocks in a red-bed succession with mineralisation localised to the interface between reduced and oxidised strata (Hitzman et al., 2005).

The most unusual aspect of the Storm copper showing is its regional setting in a carbonate-replacement Zn district and the host rock that differs from the rest of the district (Dewing et al., 2007a). Drilling provided significant intersections in several zones (Fig. 2B): 110 m of 2.45% Cu (2750N), 49 m of 1.79% Cu (2200N), and 16 m of 3.07 % Cu (4100n). This showing also has characteristics of each of the deposit sub-types previously mentioned. Thus this significant occurrence of this unusual Cu mineralisation is important because it may relate sedimentary-rock-hosted stratiform Cu deposits to carbonate-hosted Zn-Pb deposits.

This paper contributes to the current understanding of carbonate-hosted Cu mineralisation.

Archived material from past drilling programs (section 3.1) formed the basis of the present study, with mineralised samples used for a multi-analytical investigation (petrography, SEM-EDS, fluid inclusions, evaporate mound analysis, LA-ICP-MS, O and S isotope analysis with SIMS, and Cu isotopes). These data were used to constrain the evolution of the mineralising fluid(s) and are used to interpret the origin of the deposit. Integration of these complementary techniques has been successful in other recent studies that unravelled complex fluid histories in comparable sedimentary settings (Hahn, 2016; Hahn et al., 2018; Mathieu et al., 2015, 2013).

3.2 Geological history

3.2.1 Tectonic framework

Rocks of the Canadian Arctic archipelago have undergone repeated tectonic activity since the Proterozoic. Late Mesoproterozoic assembly of Rodinia (Li et al., 2008) left a sedimentary record of base-metal-hosting intracratonic rift-basins in northern Laurentia that developed as a result of orogenic far-field stress (the “Bylot basins”; Fig. 1; Fahrig et al., 1981; Turner et al., 2016). During and after deposition of the Paleozoic “Arctic platform”, multiple Phanerozoic orogenic events took place, including the Caledonian (Late Silurian; Miall, 1986; Morris et al., 2005; Oliver, 2001), Ellesmerian (Late Devonian; (Embry, 1991a), and Eurekan (Cretaceous-Oligocene; Kerr, 1967; Piepjohn et al., 2016; Tegner et al., 2011) orogenies, as well as extension during the development of the Sverdrup basin (Early Carboniferous; Davies and Nassichuk, 1991).

Both Proterozoic and Phanerozoic strata and tectonic events may be relevant to Paleozoic-hosted base-metals of the southern Cornwallis district (central Arctic islands; Fig. 1). Mesoproterozoic development of the Bylot ‘rift’ basins (Fig. 1) was associated with repeatedly reactivated northwest-trending fault systems (Jackson and Cumming, 1981; Dewing et al., 2007b), and host the Nanisivik deposit and associated Zn and Cu showings (Hnatyshin et al., 2016; Turner, 2011). Somerset Island exposes Mesoproterozoic strata of the Aston-Hunting basin, as well as vestiges of lineaments in Phanerozoic strata that are co-linear with basin-bounding faults in the nearby Borden basin (north Baffin Island; Fig. 1). There is no known record of Neoproterozoic sedimentation or tectonism in the area.

Collision of Laurentia with Baltica in the Silurian resulted in the Caledonian orogeny, producing far-field compressional effects in the central Canadian Arctic islands, known as the “Boothia uplift” (Kerr and Christie, 1965; Miall, 1986; Morris et al., 2005; Oliver, 2001), a north-trending structure that stretches from the mainland to Devon Island (Fig. 1). The Boothia uplift was important to development of the Cornwallis Zn district, including the Polaris Zn-Pb deposit (Dewing et al., 2007a; Jober et al., 2007; Turner and Dewing, 2004).

In the Late Devonian, an unknown landmass to the north (present-day orientation) collided with Laurentia to cause the Ellesmerian orogeny (Embry, 1991a), producing a south-moving deformation front that had structural effects as far south as Melville, Bathurst, and Cornwallis islands (Fig. 1; Okulitch et al., 1991). No structures related to this orogen are known south of Barrow Strait. The foreland basin adjacent to the orogen covered most of the present-day central and southern islands, and locally reached 9 km thickness (Dewing and Obermajer, 2009; Embry, 1991a; Miall, 1976). Ellesmerian stress, combined with inherited structures of the Boothia uplift, mobilised and focussed mineralising fluids in the Cornwallis Zn-Pb district (Dewing et al., 2007a; Jober et al., 2007; Turner and Dewing, 2004).

The Sverdrup basin (northern Arctic islands) was initiated by extension (Forsyth et al., 1979) following the Ellesmerian orogeny in the Early Carboniferous (Davies and Nassichuk, 1991). The basin was the main regional depocentre during most of its history (Carboniferous to Eocene; Embry, 1991b). Multiple salt-cored anticlines, flood basalts, and dykes formed in this basin (Dewing et al., 2007b; Embry, 1991b).

During multi-stage deformation in the Eocene, compression (northern islands) and extension (southern islands) resulted in the Eurekan orogeny and opening of Baffin Bay, respectively (Kerr, 1967; Okulitch and Trettin, 1991; Piepjohn et al., 2016; Tegner et al., 2011). Somerset Island, in the southernmost Cornwallis district, contains subtle expressions of most of these events, from Mesoproterozoic to Eocene.

3.2.2 Regional Geology

Archean quartzo-feldspathic and mafic gneisses from the amphibolite-granulite facies of the Rae province on Somerset Island are overlain by the Mesoproterozoic Aston and Hunting formations (Brown et al., 1969). The Aston Formation consists of red sandstone cross-cut by Neoproterozoic diabase sills (Dixon et al., 1971; Tuke et al., 1966; Jones and Fahrig, 1978) presumed to be related to the Mackenzie igneous event (~1270 Ma). The combined thickness of Aston Formation and contained sills is 1.1 km. The overlying Hunting Formation, deposited between 1270 and 723 Ma (cross-cutting dyke ages; Dixon, 1974; Heaman et al., 1992; Mayr et al., 2004), is 1.3 km of marine dolostone (Dixon, 1974; Tuke et al., 1966). The Hunting Formation is presumed to be related to similar strata in the nearby Borden basin (ca. 1.1 Ga; Jackson and Iannelli, 1981).

Approximately 3 km of predominantly dolomitic Paleozoic strata unconformably overlie the Proterozoic units (Miall and Kerr, 1980, 1977): the Cambro-Ordovician Turner Cliffs Formation; Ordovician Ship Point, Bay Fiord, Thumb Mountain, and Irene Bay formations; and Silurian

Allen Bay, Cape Storm, Douro, Read Bay, Somerset Island, and Peel Sound formations (Fig. 2, 3; (Miall and Kerr, 1980, 1977). The Bay Fiord Formation is interbedded finely crystalline, partly argillaceous dolostone, shale, and anhydrite (Miall and Kerr, 1980). The Thumb Mountain Formation, host-rock of the Polaris zinc-lead deposit on Little Cornwallis Island (Dewing et al., 2007a), consists of fossiliferous carbonate rock (Miall and Kerr, 1980). The Irene Bay Formation consists of interbedded argillaceous limestone and shale (Miall and Kerr, 1980) that was probably deposited in a deep subtidal environment (Stewart, 1983). The Allen Bay Formation, which hosts the Storm orebodies and unconformably overlies various older Paleozoic strata consists of buff dolostone that is organic- and pyrite-poor, commonly bioclastic, stromatolitic, and interlayered with evaporites at the top of the formation. The Allen Bay Formation is overlain by argillaceous, silty carbonate of the Cape Storm Formation (Mayr et al., 2004). The Late Silurian Somerset Island and Peel Sound formations are clastic wedge deposits associated with uplift of the Boothia uplift in the Late Silurian and have conspicuous red clastic members (Miall et al., 1978). Preserved in some grabens, the Eureka Sound Formation (Tertiary) has a thickness up to 300 m (Miall and Kerr, 1977).

3.2.3 Local geology of the Storm showing

Storm is located in one of several northwest-trending grabens on northwestern Somerset Island (Fig. 2). Outcrops are minimal, with surface expressions of mineralisation limited to felsenmeer, rubble, gossans, and malachite staining. Except for a few mineralised float samples, all of the material studied is from drill-core.

Cominco Ltd. (Teck Resources Ltd.), who worked at the site from 1964 to 2007, informally divided the Allen Bay Formation into three members (Fig. 3): varied stromatoporoid (VSM), brown dolopackstone and dolofloatstone (BPF), and alternating dolomudstone and dolowackestone (ADMW).

The VSM consists of interbedded dolofloatstone and dolorudstone with stromatoporoid boundstone/framestone; three distinctive marker units are identified by reef and ooid lithofacies and skeletal hash layers.

The BPF consists of medium- to dark brown, fossiliferous dolopackstone and dolowackestone with chert nodules at two levels. The base of the BPF is where buff stromatoporoid facies (VSM) first appear.

The ADMW consists of alternating dolomitic mudstone and grey, silty dolostone.

Copper mineralisation is present in four zones (2200N, 2750N, 3500N, and 4100N) in the Allen Bay Formation near the contact with the overlying Cape Storm Formation (Figs. 2B, 3). Little to no mineralisation is present in the Cape Storm Formation, but local veins are present in the overlying Douro Formation. The size and geometry of the orebodies are at present not clearly defined, but surface expressions of mineralisation trend parallel to faults and lineaments.

In general, mineralisation consists of carbonate replacement in the Allen Bay Formation, but also includes vein, disseminated, stringer, and breccia types (Fig. 4). The overlying Douro Formation

contains less mineralisation, primarily as stringers and disseminated sulphides; little mineralisation is present in the Cape Storm Formation. The main replacement-style mineralisation is hosted by the BPF, whereas breccia and vein-type mineralisation are dominant in the ADMW; various mineralisation types are present in the basal VSM (Fig. 4). The ore mineralogy (see 4.1) does not seem to be controlled by the host unit. Most mineralisation is associated spatially with graben faults near the contact of Allen Bay and Cape Storm formations.

A crude vertical zonation of minerals is present, as well as a general horizontal zonation. Within each ore zone, the deepest mineralisation is typified by the predominance of geerite, followed upward by bornite- and chalcopyrite-geerite-dominated zones. Native Cu is present locally in all the ore zones. Bornite and chalcopyrite are more prominent in the southern part of the graben (2750N) versus the northern (4100N) and western (3500N) zones. Malachite is present in all ore zones, but cuprite and atacamite are apparently exclusive to the 3500N ore zone.

3.3 Materials and methods

3.3.1 Sample locations

Core samples of representative mineralisation from the 2750N, 3500N, and 4100N zones (Figs. 2 and 4) include material from each informal member.

3.3.2 Petrography and SEM

Transmitted and reflected light petrography was undertaken on 30 polished thin sections (30 μm thickness) using an Olympus BX-51 petrographic microscope equipped with a Q-Imaging digital capture system at Laurentian University (Sudbury, Ontario). Imaging and analysis of sections was done using a JEOL 6400 SEM fitted with an Oxford INCA EDS detector at Laurentian University using the following operating conditions: accelerating voltage of 20 kV, beam current of 1.005 nA, and 5-second counting time.

3.3.3 Fluid inclusion microthermometry

Fluid inclusion petrographic studies and microthermometry were performed using 100- μm -thick, doubly polished thin sections. Fluid inclusion classification (i.e., primary, pseudosecondary, secondary) followed the protocol of Goldstein and Reynolds (1994) using their concept of fluid inclusion assemblages (FIA). Microthermometric analysis was done using a Linkham THMSG600 heating-freezing stage with an automated controller unit and Olympus BX-51 microscope equipped with a Q-Imaging digital capture system at Laurentian University. The heating-freezing stage was calibrated using synthetic fluid inclusions. Inclusion salinity was determined using the final melting temperature of ice ($T_{\text{m}}(\text{ice})$) for aqueous inclusions and tables in Bodnar (1993). Repeated runs for T_{h} and $T_{\text{m}}(\text{ice})$ were made on inclusions in FIAs to ensure that the measurements were reproducible (i.e., $< 2^{\circ}\text{C}$ and $< 0.2^{\circ}\text{C}$, respectively).

3.3.4 Evaporate mound SEM-EDS

The solute chemistry of fluid inclusions was determined using the evaporate mound method (Haynes et al., 1988; Kontak, 2004), with two variants of sample preparation for evaporate mound production and analysis. Both methods involved rapid heating (100°C/min) of samples to 350°C to induce fluid inclusion decrepitation, with samples then kept at this temperature for >2 minutes to ensure optimal evaporate mound production (Haynes and Kesler, 1987). Chips that had two or more inseparable minerals were decrepitated and their evaporate mounds were analysed on the chip to identify which mounds belonged to which mineral. Mound composition was calculated by subtracting the substrate's composition, in this case Ca and Mg from the host dolostone, from the measured mound composition. To remove the influence of the carbonate host mineral on SEM-EDS analysis of the evaporate mounds, fluid inclusion chips of a single carbonate mineral were also placed on a Fisher brand microscope cover glass and heated to produce decrepitation; after cooling, the chip was removed, leaving the debris and evaporate mounds on the cover glass. For some samples, evaporate mounds on both the chip and cover glass were analysed for reliability. The cover glass used was not pure silica, but contained small but consistent amounts of Na and K, in which case mounds analysed on the glass subsequently had the glass composition subtracted from their measured compositions.

The JEOL 6400 SEM-EDS system was used to image and analyse samples and evaporate mounds. With a voltage of 20 kV, the minimum detection limit for most elements was approximately 0.2 wt. %. Because in situ fractionation of evaporate phases can occur during

inclusion decrepitation and subsequent mound formation (Haynes et al., 1988; Kontak, 2004), rastering of the entire mounds for 5 seconds was done to provide an average composition, thereby minimising any fractionation effects.

3.3.5 Secondary ion mass spectrometry (SIMS)

Samples with the appropriate paragenetic minerals were selected for in situ O (carbonates) and S (sulphides) isotopic analysis using a secondary ion mass spectrometer (SIMS) at the University of Manitoba (Winnipeg, Manitoba). Samples were polished and cleaned in a series of sonic baths and were then sputter-coated with a thin Au coating. Ion detection was done on a Balzers SEV 1217 electron multiplier coupled with an ion-counting system. The instrument operated with a 20 μm sputtering diameter, a 300 V sample offset, a -9 keV secondary accelerating voltage, a 247 μm slit, an 18 ns dead time, and a mass resolving power of 347. Oxygen isotopes were analysed using a 2 nA Cs^+ electron gun accelerated at 10 kV. Standards used were calcite (Joplin; Mahon et al., 1998), dolomite (Brumado; Plummer, 2006), pyrite (Balmat; Crowe and Vaughn, 1996), and chalcopyrite (Trout Lake; Crowe and Vaughn, 1996). The relevant standards were analysed multiple times during the sessions for precision assessment. The data are reported as $\delta^{18}\text{O}$ (SMOW) and $\delta^{34}\text{S}$ (CDT) in per mil (‰), with errors of 1.2‰ and 0.3‰ for O and S, respectively. Spot-to-spot reproducibility on the respective standards for calcite, dolomite, pyrite, and chalcopyrite were 0.4‰, 0.6‰, 0.2‰, and 0.3‰, respectively.

3.3.6 Copper isotopes

Copper minerals were chosen that lacked oxidative rims, and larger masses of non-weathered Cu were chosen for analysis because oxidation of Cu minerals can change the Cu isotope value (Mathur et al., 2014, 2005). Approximately 0.05 g of Cu minerals was dissolved in 4 ml of heated ultrapure aquaregia. Copper was purified using the ion exchange chromatography described in Mathur et al. (2009) and with isotopic analysis, which was determined using the Neptune multi-collector at Pennsylvania State University (Pennsylvania, USA), similar to that presented in Mathur et al. (2009, 2005). Samples were corrected for mass bias by bracketing with NIST 976 standard. Samples are reported as $\delta^{65}\text{Cu}$ as per mil (‰) variations compared to NIST 976. Reported values are an average of 1 block of 30 ratios measured at separate times in the analytical session. An in-house standard (USA penny from 1838, as reported in Mathur et al., 2009) was interleaved throughout the session with analysis yielding an average $\delta^{65}\text{Cu} = -0.04 \pm 0.07\text{‰}$ (n=5); this value overlapped with results of previous values reported. The error of the NIST 976 bracketed by itself throughout the measuring session varied by 0.09‰ (2 σ). This is considered the error for analysis reported here, because none of the replicates fell outside the reported errors.

3.3.7 LA ICP-MS

Trace and rare-earth (REE) elements were analysed using a Resonetics RESolution M-50, ArF excimer laser with a 193 nm wavelength and two-volume chamber (Laurin Technic) coupled to a

Thermo X Series II (quadrupole) ICP-MS at Laurentian University. Samples were identified through petrography and SEM-EDS imaging and analysis. Internal standards depended on the mineral analysed and were chosen based on SEM-EDS analysis. A combination of NIST 610, 612, and BHVO2G glass and MASS compressed puck were used as external standards. Analyses were performed using a beam size that ranged from 15 μm to 124 μm , depending on the size of the minerals analysed, with the following operating conditions: 5 Hz and 7 J/cm², 650 ml/min He, 700 ml/min Ar, and 6 ml/min N₂. Accuracy was typically <10% error, with the HREE at ~20% error. Precision error is estimated to be typically <10% for trace elements.

3.4 Results

3.4.1 Mineral paragenesis

Mineral paragenesis, (Fig. 5) was established based on examination of hand samples, transmitted and reflected light microscopy, and SEM-EDS imaging and analysis. Three distinct stages are present: pre-ore, main-stage, and post-ore. The main stage is complicated, and could be subdivided into a more complex assemblage of sub-stages, given that there is an apparent mixture of deposition from fluids of varied origins (see discussion).

3.4.1.1 Pre-ore stage:

The pre-ore stage is characterised by chalcopyrite, pyrite, and marcasite, with dolomite gangue. Dolomite 1 (D1) is present as both pore- and vein-filling cement. The crystals are euhedral where pore-filling, but anhedral where vein-filling, and typically progress from inclusion-rich cores to relatively inclusion-poor margins (Fig. 6A). Early pyrite (Py1) is large (up mm scale) with both euhedral and anhedral crystals and later marcasite pseudomorphs. Both of these iron sulphide minerals are commonly fractured and replaced by Cu sulphides (Fig. 6B). The earliest chalcopyrite (Cpy1) is massive, non-porous, associated with D1, and replaces dolostone, but is also locally void-filling (Fig. 6C).

3.4.1.2 Main stage:

Main stage mineralisation included precipitation of various Cu (geerite and covellite), Cu-Fe (bornite and chalcopyrite), and Fe sulphides (pyrite), with calcite, dolomite, and quartz as gangue. Early calcite (C1) is anhedral, replaces dolomite along its margins, and is intergrown with Cu sulphides (Fig 6E, 7I), although its presence is limited to a few samples. Later-stage calcite (C2) is anhedral, coarsely crystalline pore-filling cement with few mineral and fluid inclusions. This cement has embayed contacts with D1 (Fig. 6A) and sharp contacts with bornite. Quartz is present as euhedral and anhedral pore fillings and vein cements (Fig. 6G) and locally as silicified dolostone; it contains few fluid inclusions. Second-generation dolomite (D2) cement is coarse, anhedral to euhedral void-filling saddle dolomite, typically densely populated by fluid inclusions (Fig. 6L), and exhibits undulatory extinction.

Second-stage pyrite (Py2) commonly forms a halo of crystals radiating from Py1 (Fig. 7F), whereas later Py3 forms euhedral crystals with sharp boundaries against Cu sulphides.

Geerite, present in two stages (G1, G2), is recognised in reflected light by its pale grey-blue colour and isotropy. It is present as disseminations replacing carbonate, and also as vein- and void-fill in all three mineralised zones (Figs. 4, 6D, E, F, G, M, N). G1 has sharp contacts with calcite (C1) cement (Fig. 6E) and is coeval with Py2. This generation of geerite (G1) exhibits no intergrowths with other Cu-sulphide minerals. Although its composition centres on its ideal composition ($\text{Cu}_{1.6}\text{S}$; Goble and Robinson, 1980), some analyses approach spionkopite ($\text{Cu}_{1.4}\text{S}$; Fig. 8A). The Fe content of G1 is typically below 1 atomic % in all three of the mineralised zones, but ranges from 0.0 to 8.5 (2750N), and 0.0 to 6.5 (3500N), whereas at 4100N it is consistently 0.0%. The second generation of geerite (G2) forms intergrowths/replacement of spionkopite and covellite (Fig. 7A-C, G) at the 2750N and 4100N zones, but is absent at the 3500N zone. Spionkopite is present as fine, bireflectant (pale to medium blue) lamellae in geerite (Fig. 7A, B). The composition of G2 is more Cu-depleted than G1, ranging from $\text{Cu}_{1.25}\text{S}$ to $\text{Cu}_{1.65}\text{S}$, with most compositions clustering at $\text{Cu}_{1.5}\text{S}$ and $\text{Cu}_{1.3}\text{S}$ (Fig. 8B), but still within the natural range of geerite (Goble and Robinson, 1980). The Fe in G2 is predominantly 0 atomic%, but can be up to 5%.

Chalcopyrite 2 (Cpy2) is a porous aggregate of chalcopyrite needles intergrown with calcite (C2) and amorphous carbon (Fig. 7I), which resembles chalcopyrite exsolution from bornite (Figs. 6H, I, T; 7H-J). In some samples, Cpy2 appears to grade into the exsolved chalcopyrite (Fig. 7J),

which may indicate that it is the same phase. It replaces Py1 and is coeval with Py2; G1 and G2 have not been documented in the same sample as Cpy2.

Bornite is predominantly present in the 2750N zone, but locally present in 4100N; bornite is absent from 3500N zone, although others have reported it (Robinson and Atkinson, 2012). It is most common at shallower depths (i.e., ~200-250 m above present-day sea-level). Bornite is purple to purple-orange with poor reflectance. It forms finely or coarsely crystalline cement, massive replacement, or rims on geerite and/or spionkopite (Fig. 7A, C, D) and fills cracks in Py2. Small bornite grains are locally present in C2 where it appears more blue-purple than replacement bornite, which is purple-orange. Chalcopyrite exsolution, in the form of needles, blebs, and lenses (Fig. 7C, D), is common in the replacement (orange) bornite, but absent in bornite cement (purple). Bornite composition falls on a line between ideal bornite (Cu_5FeS_4) and idaite (Cu_3FeS_4), with no obvious relationship between the bornite colours and types.

Covellite (Fig. 6O-T) appears as strongly bireflectant (pale-blue to deep-blue), anisotropic (blue to red-orange) lamellae concentrated along the edges of geerite crystals (2750N) or laths in geerite (4100N) (Fig. 7A-C, G); it is also present as non-pleochroic dark blue covellite in G2 (Fig. 7C). Covellite composition ranges from $\text{Cu}_{0.9}\text{S}$ to $\text{Cu}_{1.06}\text{S}$, but centres on CuS (2750N) and $\text{Cu}_{0.9}\text{S}$ (4100N; Fig. 8C); its Fe content is typically less than 0.9 at. % in both zones. Covellite is a common by-product of alteration of bornite to chalcopyrite (e.g., Large et al., 1995; Sillitoe and Clark, 1969), and is interpreted as contemporaneous with chalcopyrite exsolution or bornite replacement.

Chalcopyrite 3 (Cpy3) is massive and non-porous (Figs. 6J, K, P, 7K). The major element composition of the three chalcopyrite phases is very uniform and close to ideal chalcopyrite; exsolved chalcopyrite trends from Cpy2 towards bornite, which is similar to the Cpy2 from 4100N that replaced sphalerite. A late-stage, massive geerite precipitation event post-dates one of the chalcopyrite phases (Cpy3?) and Py2; this geerite has the same composition as G1 ($\text{Cu}_{1.6}\text{S}$), but has unknown relationships with all other minerals.

Sphalerite is preserved as small irregular fragments surrounded by Cpy2. The paragenetic timing of this phase is unknown, except for predating Cpy2.

3.4.1.3 Post-ore stage:

Post-ore minerals include native Cu, Cu- and Fe oxides, and calcite gangue (Fig. 6U). The latest stage carbonate (C3) is an anhedral replacement phase that locally has relict structure (solid inclusions) inherited from precursor dolomite cement (Figs. 6Q-S; 7L). Copper minerals in this stage include native Cu, cuprite, malachite, and atacamite. Native Cu is dendritic and spatially related to goethite, which may be related to C3 (Fig. 6V). Cuprite (Cp), red in plane-polarised light and pale blue in reflected light (Fig. 6W), is in sharp contact with a carbonate mineral recrystallised and/or replaced by C3. This is also the case with malachite, native Cu, and C3. Malachite forms fan-like aggregates of blue-green needles and anhedral masses around Cu sulphides. Atacamite, a euhedral, pale green-blue-green, finely crystalline phase in plane-polarised light, is present in and around cuprite (Fig. 6W). There is no sense of timing between it

and the latest recrystallising calcite, but it is possible that these two minerals are contemporaneous, because both post-date cuprite.

3.4.2 Fluid inclusions

3.4.2.1 Petrography

Fluid inclusions in all carbonate cements are very small, averaging 2-5 μm (Fig. 9). Dolomite 1 cement contains two-phase L-V inclusions with a high degree of fill ($F = \text{Volume}_{\text{liquid}}/\text{Volume}_{\text{fluid inclusion}}$) (i.e., $F = 0.9$ with $L = 90\%$) that are concentrated in their centres, as both primary and secondary types (Fig. 9A, B). Single-phase, secondary liquid inclusions are also present.

Dolomite 2 cements also have two-phase L-V inclusions with $F = 0.9$ and are present in both primary and secondary FIAs (Fig. 9C, D). Primary L-V inclusions present in C2 cement (Fig. 9E, F) appear to have been necked, based on their variable L:V ratios, producing variable F values. Fluid inclusions in C3 cement (Fig. 9G) are sparse and/or too small to distinguish their L-V ratios with confidence. No fluid inclusions are present in C1 cement. Hydrocarbons have not been observed in any of the fluid inclusions.

3.4.2.2 Microthermometry

Microthermometric data (Table 1) indicate that, with few exceptions, Storm fluid inclusions were metastable during cooling runs, and so $T_{\text{m(ice)}}$ data and therefore salinity are limited to the

few inclusions that froze. Neither repeated cooling nor holding for long duration at low temperature (i.e., 1-2 hours at -100°C) initiated freezing of such inclusions.

Three FIAs in dolomite 1 were analysed. The total range in T_h values was from 77° to 130°C , with an average of 83°C ($n = 12$), 117°C ($n = 6$), and 104°C ($n = 2$). These average T_h values, although similar in their low temperatures, are distinct, and record an overall variation of 34°C . Only one FIA provided useful $T_m(\text{ice})$ data, with two inclusions giving an identical value of -13.0°C , which equates to a fluid salinity of 17 wt. % equiv. NaCl.

Dolomite 2 yielded T_h values from two FIAs, but due to metastability these inclusions did not freeze and thus salinity data are lacking. T_h values range from 97° to 130°C , with average values of 115°C ($n = 7$) and 107°C ($n = 7$).

Calcite 2 had a single FIA in which data could be measured. T_h values range from 102° to 190°C . The T_h data form three groups: 105°C ($n=3$), 140°C ($n=3$), and 180°C ($n=2$), with the first two similar to the T_h data for D1 cement, whereas the third is very different. Only two inclusions froze upon cooling, yielding T_m values of -0.1°C and -0.2°C , reflecting salinities of 0.3 wt. % equiv. NaCl.

3.4.2.3 Evaporate mounds

Compositions of evaporate mounds were determined for the two dolomite cements (D1, D2) and one calcite cement (C2). No mounds were produced from C1 or C3. In general, the mounds vary in size and shape, which is consistent with their variable chemistry (see Kontak, 2004 for discussion): domes, irregular clusters of crystals, and dendritic shapes are present (Fig. 10A, B, C). Dolomite-hosted fluid inclusions produced large, abundant mounds compared to calcite-hosted fluid inclusions, which is consistent with the dolomite-precipitating fluid being more saline than the calcite-precipitating fluid. The mounds are predominantly Na- and K-dominated, with subordinate amounts of Mg and Ca; minor S (<10 wt. % when data are normalised to 100%) was detected in dolomite-derived mounds, but only one S-bearing mound was noted from C2 cement.

The chemistry of D1 mounds forms two groups, one Na-dominated and the other Na+K-dominated (Fig. 10D, E), with the two populations overlapping. In addition, a few Ca+Mg-rich mounds define a distinct population (Fig. 10E).

Calcite 2 produced few evaporate mounds, which were primarily Na-dominated, with variable K content (Fig. 10F).

The chemistry of D2 mounds vary from K-dominated to Na-dominated, with the mode being K-dominated (Fig. 10G, H).

3.4.3 Stable Isotopes

3.4.3.1 Oxygen

Analyses of the cement phases indicate the following results (Table 2 and Fig. 11) The Allen Bay Formation dolostone has a consistent $\delta^{18}\text{O}_{\text{SMOW}}$ value of 25.7‰ for all members (ADMW, BPF, and VSM), except for a sample close to vein mineralisation (10s of microns) which yielded 31.6‰. Dolomite 1 $\delta^{18}\text{O}_{\text{SMOW}}$ values are 23.8 to 32.0‰ (average = 28.8‰, n=9), whereas D2 $\delta^{18}\text{O}_{\text{SMOW}}$ values are 24.0 to 30.0‰ (average = 27.2‰, n=6). Calcite 1 $\delta^{18}\text{O}_{\text{SMOW}}$ values are 6.3 to 8.6‰ (average = 7.5‰, n=5) in the north (4100N), and 14.8 to 19.4‰ (average = 17.3‰, n=5) in the south (2750N). Calcite 2 $\delta^{18}\text{O}_{\text{SMOW}}$ values are 12.0 to 15.0‰ (average = 13.6‰, n = 3), whereas C3 $\delta^{18}\text{O}_{\text{SMOW}}$ values are 9.7 to 10.7‰ (average = 10.2‰, n = 6).

Fractionation equations for dolomite-water (Horita, 2014) and calcite-water (O'Neil et al., 1969) along with T_h data (where available) were used to calculate the $\delta^{18}\text{O}_{\text{H}_2\text{O}}$ of the fluid in equilibrium with the various cements phases during their precipitation (D1, D2, C1, C2, and C3). The $\delta^{18}\text{O}_{\text{H}_2\text{O}}$ values of the fluid that precipitated D1 and D2 are 12.6‰ ($T_h = 114^\circ\text{C}$) and 11.4‰ ($T_h = 111^\circ\text{C}$), respectively (Fig. 11). The Allen Bay dolostone, C1, C2, and C3 cements have no T_h values to constrain fractionation, and thus temperatures bracketed from 20°C to 120°C are used as constraints (reasonable range based on inferred burial depth and fluid temperatures of earlier phases); maximum temperature constraints for C3 are set at 30°C because of its association with atacamite. Using these temperature limits, $\delta^{18}\text{O}_{\text{H}_2\text{O}}$ values for the fluids range from -7.7‰ (20°C) to 8.5‰ (120°C) for the Allen Bay dolostone, -26.1‰ (20°C) to -6.5‰

(120°C) for C1 (north), -14.9‰ to 4.3‰ (120°C) for C1 (south); -15.9‰ (20°C) to -1.5‰ (120°C) for C2, and -19.3‰ (20°C) to -16.7‰ (30°C) for C3 (Fig. 11).

3.4.3.2 Sulphur

Sulphur isotopic analyses (Table 2) for primary sulphide minerals Py1 and Cpy1 show $\delta^{34}\text{S}_{\text{CDT}}$ values from -1.4‰ to 6.9‰ (average of 1.7‰, n=6; Py1; Fig. 7F) and 1.5‰ to 2.2‰ (average 1.8‰, n = 3; Cpy1; Fig. 6C). In contrast, replacement pyrite (Py2) and chalcopyrite (Cpy2) values range from 10.2‰ to 11.2‰ (average of 10.7‰, n=3) and 8.7 to 13.5 (average 11.4, n=4), respectively (Fig. 6I). Recrystallised chalcopyrite (Cpy3) has $\delta^{34}\text{S}_{\text{CDT}}$ values of 8.8‰ to 23.4‰ (average 16.9‰, n = 4; Fig. 6K).

3.4.3.3 Copper

Isotopic values (Table 3) for the three zones (2750N, 3500N, and 4100N) indicate that the majority of $\delta^{65}\text{Cu}$ values (G1, G2, Cpy1, Cpy2, Bn, and cuprite) are around 0‰. Chalcopyrite 2 has the highest values of any mineral in all three zones (3.44‰, 2750N; 0.99‰, 3500N; 1.31‰, 4100N). Covellite 2 (2750N) also has a high value (1.31‰), whereas covellite 1 did not produce reliable results. Native Cu had $\delta^{65}\text{Cu}$ values from 0.04‰ (4100N) to 0.22‰ (3500N).

Using present-day sea-level as a reference point for depth, enrichment of $\delta^{65}\text{Cu}$ values is evident in the north (4100N) at 294 m above sea level (masl; G1 = 0.43 ‰) and increases (Cpy2 = 1.31 ‰) downwards to 283 masl. The greatest enrichment of $\delta^{65}\text{Cu}$ values is in the south (2750 N; Cpy2 = 3.44 ‰) at 221 masl, where it then decreases with depth to 2.18 ‰ (Cpy2) and 1.31 ‰

(Cv2) at 180 masl and 158 masl, respectively. Chalcopyrite 2, with a $\delta^{65}\text{Cu}$ value of 0.99 ‰, is the highest value in the west (3500 N), at 212 masl. Post-ore malachite (3500 N) with a $\delta^{65}\text{Cu}$ value of 0.78 ‰ from 197 masl has the highest value of any mineral at that elevation.

3.4.4 Trace and REE Data

Post-Archean Australian shale (PAAS)-normalised REE patterns of diagenetic minerals (Fig. 12) and La and Ce anomalies (Fig 13), and trace element content of gangue minerals (Fig. 14) are discussed below, following the established mineral paragenesis (Fig. 5).

Allen Bay Formation dolostone and dolomitised stromatoporoid boundstone form two compositional groups having different ΣREEY (2.3 ppm, $n = 8$; and 15 ppm, $n = 3$, respectively), but similar PAAS_N patterns. In general, the samples have nearly flat REE patterns and slight HREE enrichment ($(\text{La}/\text{Yb})_\text{N} = 0.73$). Samples have variable Eu and Y anomalies, with values of 1.24 and 1.19 (dolostone and stromatoporoid boundstone, respectively). With one exception, negative Ce anomalies are absent. The Y/Ho values range from 25.07 to 34.43, with an average of 29.04 ($n=11$).

Dolomite 1 cements show a large overall range in ΣREEY (2.7 ppm to 141.8 ppm; average 43.5, $n = 17$) but with very similar patterns, except for a single sample. The patterns are generally flat, with slight LREE-enrichment ($(\text{La}/\text{Yb})_\text{N} = 1.67$). All but one sample have positive Eu anomalies between 1.02 and 6.82. There is a general absence of negative Ce and positive La anomalies,

except for a few samples. The Y/Ho values range from 27.23 to 39.9, with an average of 33.30 (n = 16); the outlier sample has a Y/Ho value of 60.42.

Calcite 1 shows a large overall range in Σ REEY (55.1 ppm to 300.6 ppm; average 170.9 ppm, n = 3) with very different patterns, and all have slight positive Ce anomalies. Two samples are LREE-enriched, with negative La anomalies and positive Eu anomalies. In contrast, the third sample is LREE-depleted and has a slight HREE-enrichment ($(La/Yb)_N = 0.42$); it also has positive Eu and Y anomalies. The Y/Ho values range from 29.78 to 30.31, with an average of 30.09 (n = 3).

Calcite 2 shows a large range in Σ REEY (1.0 ppm to 327.3 ppm; average 53.7 ppm, n = 13) but all samples have similar patterns that are moderately fractionated with HREE-enrichment ($(La/Yb)_N = 0.64$). Small negative Ce anomalies and a few slight positive La anomalies are indicated. The Y/Ho values range from 29.35 to 50.63, with an average of 36.33 (n = 13).

Dolomite 2 shows a range in Σ REEY (17.2 ppm to 156.6 ppm; average 50.1 ppm, n = 7) but all have similar patterns with either a slight positive slope ($(La/Yb)_N = 0.43$) or a convex shape. The samples also have a slightly positive to no Ce anomalies and both positive and negative La anomalies. The Y/Ho values range from 22.76 to 32.89 with an average of 26.36 (n = 7).

The low elemental concentrations of REEY in C3 make the normalised patterns irregular and discontinuous, but the more coherent data appear to define two groups based on their very different Σ REEY and degrees of fractionation. The more REE-enriched group (5.2 ppm, n = 5)

has a nearly flat pattern ($(\text{La}/\text{Yb})_N = 2$) with subtle positive Eu anomalies. The Y/Ho values of this group range from 26.85 to 53.24, with an average of 38.59 ($n = 4$). In contrast, samples with lower ΣREEY (0.08 ppm, $n = 7$) have a slight positive slope ($(\text{La}/\text{Yb})_N = 0.76$), with subtle variable La, Ce, and Y anomalies, but these may be analytical artifacts owing to the abundances. The Y/Ho is limited to a single sample with a value of 36.11.

Later cement stages (C1, C2, and D2) show the greatest enrichments in Fe and Mn compared to earlier dolomites (D_{stn} and D1; Fig. 14). Cements C1, D2 and C2 markedly enriched in both Fe (19.0 ppm, 5162.5 ppm, and 2586.3 ppm, respectively) and Mn (710.3 ppm, 817.5 ppm, and 1007.2 ppm, respectively), as compared to the host dolostone (Fe: 893.7 ppm; Mn: 113.0 ppm) and D1 cement (Fe: 773.7 ppm; Mn: 298.7 ppm).

3.4.5 Sulphide trace element geochemistry

Trace element data for sulphides (Fig. 15) show that Cpy1, which pre-dates the main ore stage, has detectable amounts of Co (2.44 ppm), Zn (89 ppm), Se (102.28 ppm), Ag (1.46 ppm), Au (0.19 ppm), and Pb (72.04 ppm), with Ni and In below detection limits. Pyrite 1, which also predates the main ore stage, is anomalously enriched, with respect to the other minerals, in (maximum values given) Co (2445 ppm), Zn (400 ppm), Se (1235 ppm), Ag (13280 ppm), Au (74.50 ppm), and Pb (108750.00 ppm). Exceptional values in Py1 probably relate to micro-inclusions.

Main ore-stage geerite shows a general increase in trace metal abundances from G1 to G2, as follows: Se = 5.69 ppm to 20.94 ppm, Ag = 69.14 ppm to 1232.43 ppm, In = ND to 10.12 ppm, Au = 0.43 ppm to 27.25 ppm, and Pb = 175.92 ppm to 827.55 ppm. In contrast, the following metals show a decrease from G1 to G2: Co = 18.18 ppm to 0.23 ppm, Ni = 0.19 ppm to BD, and Zn = 19.14 ppm to 1.96 ppm.

Chalcopyrite phases do not show any general trends, except that Cpy2 and Cpy3 are trace-metal enriched relative to Cpy1. Chalcopyrite 2 is also slightly enriched, relative to Cpy3, for Co (23.25 ppm vs. 12.10 ppm), Se (40.88 ppm vs. 5.84 ppm), Ag (25.58 ppm vs. 2.33 ppm), In (1.12 ppm to 0.20 ppm), and Pb (643.04 ppm vs. 257.32 ppm), but depleted in Ni (9.04 ppm vs. 12.10 ppm), Zn (8.75 ppm vs. 33.43 ppm), and Au (0.60 ppm vs. 0.84 ppm).

Pyrite 2 is depleted in trace metals compared to Py1, but still generally enriched in Co (1367.2 ppm), Zn (11.76 ppm), Se (24.42 ppm), Ag (142.84 ppm), Au (2.11 ppm), and Pb (2290.80 ppm), relative to the other sulphides. Where pyrite data are available from the different zones, the south (2750N) is generally enriched relative to both the north (4100N) and west (3500N).

In addition, as a group, the trace element data show a general enrichment in Zn, Co and Se, but decrease in Ag from 4100N to 2750N. There is a strong positive correlation between Pb and Ag, and a weak positive correlation between Pb and Au.

3.5 Discussion

Key features throughout the paragenesis (Fig. 5), such as textures and composition (Table 4), can be used to constrain fluid origin, interactions, conditions of precipitation, relative timing, and flow direction, which are then used to interpret the history of mineralisation at Storm. An important feature is the transition from geerite to bornite to chalcopyrite (Fig. 5), which is a typical redox-related phenomenon common in other sedimentary-rock-hosted Cu deposits (e.g., stratiform deposits; Hitzman et al., 2005), although most deposits are chalcocite- versus geerite-dominated.

3.5.1 Mineral paragenesis at Storm

The paragenesis (Fig. 5), constructed using combined petrography, SEM-EDS, and geochemistry (isotopes, trace elements, and REEs), is sub-divided into three stages (pre-, main-, and post-ore) containing either geerite-dominated or chalcopyrite-dominated areas, because Cpy2 is not present in association with geerite minerals. Similar S isotope values between Cpy2 ($\delta^{34}\text{S} = 11.4\text{‰}$) and Py2 associated with geerite ($\delta^{34}\text{S} = 10.7\text{‰}$), along with the association of both minerals with C1, C2, Cpy2 and G1/G2, which all have a similar timing in the paragenesis. Massive Cpy3 overprints bornite, with chalcopyrite exsolution in chalcopyrite-dominated samples, but apparently is absent in geerite-dominated samples. Because bornite with chalcopyrite exsolution is present in both types of samples, it is inferred that Cpy3 is younger than G1/2, which has the same timing as Cpy2. Solid inclusions that are unidentifiable in C3

outline its crystal edges, but the irregular C3 crystal boundaries cross-cut in which solid inclusions outline the extent of the previous mineral phase.

3.5.2 Textures and chemistry of Cu phases, with implications for mineralising conditions

The association of calcite (C1 and 2) with G1 → bornite → Cpy2 (Fig. 5), which records a continuous sequence of minerals with progressively lower Cu/S ratios and more reduced state, probably records a protracted fluid event accompanied by chemical change, such as pH and redox, due to ongoing interaction with surrounding carbonate rocks, similar to calculated stability trends (Reed and Palandri, 2006). The dissolution of early pyrite (Py1) during Cu-sulphide (G1, G2) and Cu-Fe-sulphide (bornite followed by Cpy2, 3) precipitation suggests that the S and Fe were at least partly derived from the earlier pyrite. The further addition of S and/or Fe from the ingressing fluid accompanying mineralisation may have been responsible for the heterogeneous mineralogy in the three zones. At the Kennecott Cu deposit in Alaska (Bateman and Lasky, 1932; Bateman and McLaughlen, 1920), the presence/absence of bornite, chalcocite, and covellite may have been controlled by local variations in Fe and/or S. Pyrite dissolution generally produces acidic solutions, which facilitate Cu transport. Acidic fluids are interpreted to have been present during main-stage ore precipitation at Storm, because dolomite corrosion is associated with pyrite dissolution and Cu (-Fe) sulphide precipitation.

Chalcopyrite exsolution from bornite has been shown experimentally to occur during low-temperature annealing (<200°C; Yund and Kullerud, 1966). Low-temperature alteration of Storm sulphides could have occurred after bornite precipitation, such as the replacement of bornite by chalcopyrite, which is known to produce contemporaneous covellite (e.g., Kupferschiefer; Large et al., 1995). The associated covellite and chalcopyrite exsolution-like texture in bornite suggests that this was a late fluid event rather than exsolution initiated by cooling.

The bladed texture of Cpy2 may be related to the exsolution-like texture of chalcopyrite from bornite (Figs. 7C,D), in that the “exsolved” chalcopyrite lamellae could have acted as nucleation sites for replacement; alternatively, replacement of an earlier bladed mineral could also result in bladed chalcopyrite. Another explanation of the bladed/porous texture of Cpy2 could be replacement along crystallographic planes, similar to exsolution. The apparently bladed and porous texture of Cpy2 may reflect the removal of the less-stable bornite parent mineral, leaving the more-stable chalcopyrite behind. Alternatively, because the unit cell of bornite (2621.31 \AA^3) is an order of magnitude larger than that of chalcopyrite (290.21 \AA^3), the fractured texture may be related to volume reduction during replacement. A similar crackled texture related to volume-reducing replacement was documented by Sillitoe and Clark (1969) in Cu-rich ore from the Copiapó district (Chile).

Copper composition in G1 is clustered at $\text{Cu}_{1.6}\text{S}$ for all three mineralisation zones (Fig. 8A), with the largest range in the west (3500N). Because compositions are homogeneous and centre near ideal geerite, with no intermediate values between geerite and chalcocite, it is unlikely that G1 represents a chalcocite mineral that had its Cu leached, turning it into geerite. Instead, a Cu-

depleted (relative to chalcocite) fluid (i.e., to stabilise a geerite composition) probably precipitated G1 from solution. In contrast, the depleted Cu composition of G2 from ideal geerite indicates Cu-leaching. This depletion is associated with visible intergrowths of spionkopite and covellite (Fig. 7A, B), which represent Cu-leaching of G1. The leached Cu may have reacted with the Fe and S in the fluid (pyrite dissolution) to produce bornite rims. The most Cu-depleted samples from 3500N are small grains surrounded by replacement cuprite and atacamite; there, Cu could have been removed during oxidation alteration. Copper leaching is also suggested by Cu isotopic compositions of atacamite, which indicate enrichment from oxidised leaching of a previous Cu mineral and short transport distance. Samples with Cu depletion, relative to natural geerite ($\text{Cu}_{1.5}\text{S}$ to $\text{Cu}_{1.6}\text{S}$; Goble and Robinson, 1980), may be a result of fine spionkopite ($\text{Cu}_{1.4}\text{S}$) or yarrowite ($\text{Cu}_{1.2}\text{S}$) intergrowths.

The Cu enrichment noted at 3500N between geerite and anilite compositions may suggest the presence of anilite. Because anilite is not stable above 39°C (Grønvold et al., 1987), this mineral must have precipitated recently, post-dating burial, or alternatively early in the diagenetic history of the deposit area and was later altered while maintaining its composition; the latter explanation is improbable. The recent precipitation of anilite (T less than 39°C after burial) that later altered to geerite to produce the enriched Cu/S geerite would not allow for the T_h values (~100°C) of associated minerals or post-geerite events. An early precipitation of anilite is also unlikely because there is no other evidence of anilite, and temperatures exceeded 39°C throughout mineralisation. The most probable explanation is the alteration of geerite increasing the Cu content locally. Because the crystals analysed were partly replaced by cuprite and atacamite, Cu-enriched heterogeneities could have developed in them.

Sikka et al. (1991) noted that Cu(-Fe)-sulphides (from a porphyry deposit) developed a tarnish with geerite composition after five months at surface conditions. It is possible that the predominance of geerite over the typical chalcocite mineralogy at Storm could be the result of alteration during the several years at surface from the time of drilling. It is not probable, however, that every sample that has subsequently been cut to expose a fresh surface has been completely altered, not just tarnished, to be entirely of geerite composition. If this degree of alteration were the case, it would be expected that geerite would be much more common in the literature. Geerite at Storm is almost certainly primary and the product of mineralisation, rather than an alteration product resulting from surface conditions.

Covellite shows Cu-depletion from $\text{Cu}_{1.0}\text{S}$ (2750N) to $\text{Cu}_{0.9}\text{S}$ (4100N; Fig. 8C) in analysed samples. Copper-leaching experiments Whiteside and Goble (1986) resulted in metastable Cu-S phases with depleted Cu:S from covellite (down to $\text{Cu}_{0.5}\text{S}$). After several hours of continued leaching, the phases reverted back to typical covellite compositions and equilibrated with the leaching fluid in this closed-system experiment. It is possible that the Cu-depleted values at Storm could represent an interrupted leaching sequence in which chemical reactions were halted prior to reversion to the covellite composition, or that it represents disequilibrium of an open system.

Iron content is conspicuous in some geerite and covellite samples. Although these minerals' formulae do not contain Fe, Fe may be incorporated in the structure due to alteration. When chalcocite, djurleite, and digenite are altered to anilite, the anilite has no Fe, but anillite altered from a Fe-bearing mineral (e.g., chalcopyrite) may contain Fe (Sikka et al., 1991). A solid

solution exists between digenite and bornite (Grguric et al., 2000; Grguric and Putnis, 1999), and Fe is required for low digenite to be stable (Morimoto and Koto, 1970). It is possible therefore that some Fe could be incorporated in geerite in this manner. Similarly, hypogene covellite from the Chuquicamata porphyry deposit in Chile was shown to have up to 5 wt. % Fe (Lewis, 1996); therefore, it is possible for natural covellite to contain Fe, as documented here.

Bornite is depleted in Cu relative to ideal bornite (Cu_5FeS_4), and could represent either Cu-loss or Fe-S-gain of G2. Although the Cu contents of G2 and Cv at 4100N are depleted, indicating Cu-loss, bornite is uniquely spatially associated with dissolved pyrite (Fig. 7E). Iron and S released during pyrite dissolution could have reacted with Cu from G2/Cv to precipitate Cu-depleted bornite. Bornite from 2750N, conversely, formed rims on Cu-poor G2 (Fig. 7A-C), and probably records Cu-loss because, in the absence of a ready source of Fe and S (e.g., pyrite), it is simpler to remove one component (Cu) than to add two (Fe and Cu). Copper-depleted bornite rims from the Kupferscheifer have been similarly interpreted (Large et al., 1995).

The presence of atacamite points to an oxidised Cl-rich fluid in an arid environment (Hannington, 1993; Palacios et al., 2011; Sillitoe, 2005), which may have been attained at Somerset Island's current geographic location, indicating comparatively recent precipitation. The co-precipitation of C3 probably balanced the CO_2 content of the fluid to promote atacamite precipitation, rather than the expected malachite from a CO_2 fluid (Hannington, 1993), although some malachite is still present.

3.5.3 Implications of sulphide trace element data

Trace metal analysis of sulphide phases (pyrite, chalcopyrite, geerite) provides insight into elemental enrichment in addition to yielding implications for metal sources. The enrichment of early pyrite (Py1) in Co (Fig. 15) suggests leaching of an appropriate source (i.e., mafic igneous rock), as documented for sulphides in other sedimentary-rock-hosted Cu deposits (e.g., Chen et al., 2011) or derived from a red-bed (Wilkinson et al., 2005). In a somewhat analogous study, Jowitt et al. (2012) suggest, in their study of the Troodos VMS deposit, that alteration of sulphides in the underlying sheeted dykes released base-metals (particularly Cu) to a hydrothermal fluid, which controlled the sulphide budget of the deposit. A similar model may be invoked for sourcing metals in sedimentary-rock-hosted base-metal deposits, including Storm.

The trace element concentrations (Ag, Au, Zn, and Pb) of early pyrite (Py1) fall in the diagenetic field (Fig. 15A) based on data in Large et al. (2009). Like pyrite from sedimentary-rock-hosted hydrothermal Au systems (Large et al., 2012, 2009), subsequent fluid events (diagenesis) and successive pyrite growth (Py2) can deplete the initial trace-metal content of early pyrite, although they apparently remain largely in the diagenetic field. This elemental depletion and remobilisation agrees with mixing of S implied by the S isotope data, discussed below (section 5.4). This decrease in metals from Py1 to Py2 is complemented by the relatively high concentrations in geerite associated with Py2.

Certain elements (e.g., Ni, Ag, Zn, Pb, and Se) are preferentially bonded to organic material in sediment (Algeo and Maynard, 2004) and can be mobilised during fluid interaction. Positive correlation between Au and these elements led Large et al. (2009) to conclude that Au in

orogenic Au deposits reflects such mobilisation. Gold content in Storm pyrite and other sulphides (with the exception of Cpy3) shows a weak positive correlation (Fig. 15) with Ag, Pb, and, with the exception of Cpy2, Se; Ni appears to be disconnected from the other elements. This correlation, as with the study of Large et al. (2009), could relate to the liberation of these elements from organic matter during diagenesis.

Analyses that form distinct groups and/or unusually high contents outside of the trends (Fig. 15) may indicate the presence of nanoparticles; this can be seen particularly with Au and Ag in G2. Silver can be incorporated into digenite and chalcopyrite (Reich et al., 2013, 2010) and can then be assumed to also be in geerite. The laser profile of a spot through the sample (not shown) appears to indicate discrete enrichments of Ag, rather than uniform values through the geerite, which suggests micro-inclusions. The two Cu-sulphides with the highest Ag content (Cpy2 and G2) are those associated with precipitation/alteration from an oxidised fluid (REE signature and $\delta^{65}\text{Cu} \sim +2\%$), consistent with supergene chalcocite and covellite being more Ag-enriched than their hypogene counterparts (Reich et al., 2013, 2010).

Chalcopyrite 3 displays different trends from the other sulphides, and may thus reflect a different fluid source and/or interaction by this fluid. This fluid transporting “new” elements to the system agrees with other geochemical data explored below.

3.5.4 Fluid origin and history

The major sources of diagenetic fluids on Somerset Island after deposition of the Allen Bay Formation include seawater, meteoric water, and formation water. No metamorphism or magmatic activity is recorded on Somerset Island during the Phanerozoic, although magmatism did take place in the distant Sverdrup basin during the Mesozoic (Davies and Nassichuk, 1991).

3.5.4.1 Allen Bay Formation dolostone

Shale-normalised REE patterns of Allen Bay Formation dolostone (Fig. 12) do not preserve an original signature acquired during marine deposition (e.g., Bau and Alexander, 2006), which indicates either contamination of the dolostone or diagenetic alteration. Siliciclastic and/or oxyhydroxide contamination, which can affect REE abundances in carbonate minerals (Nothdurft et al., 2004), is the cause of flat shale-normalised REE patterns, because there is no apparent correlation between LREE-enrichment and major elements (e.g., Fe or Mn; Fig. 14). The calculated high $\delta^{18}\text{O}_{\text{H}_2\text{O}}$ values, assuming diagenesis at $>60\text{-}80^\circ\text{C}$, are greater than that attained through evaporation (+6‰; Lloyd, 1966; Ward and Halley, 1985), which suggests instead that the modified shale-normalised REE patterns and Y/Ho values that equate to typical shale (26; Pourmand et al., 2012) reflect alteration of the dolostone by a reduced, basement-derived fluid that had extensively interacted with a shale-like unit or rock of similar bulk composition. The nature and origin of such a fluid is further explored below.

If seawater was the main source of the dolomitising fluid (i.e., $\delta^{18}\text{O}_{\text{H}_2\text{O}} = 0\text{‰}$), the inferred temperature of dolomitisation would have been $\sim 60^\circ\text{C}$, based on the constraints imposed by the $\delta^{18}\text{O}$ for dolostone (Fig. 11). Using a standard geothermal gradient ($25^\circ\text{C}/\text{km}$; Allen and Allen, 2005), such temperatures would place dolomitisation in the intermediate burial regime (Machel, 1999). The lack of a negative Ce anomaly agrees with a reduced dolomitising fluid, which would be expected in this burial regime. Assuming that the paragenetically ensuing D1-precipitating fluid was in part responsible for dolomitisation (i.e., maximum value of 12.6‰ ; see Fig. 11), a temperature of 160°C would be required. This temperature is well in excess of the measured T_h values (80 to 100°C) for D1 cement, hence dolomitisation of the Allen Bay Formation must have occurred prior to mineralisation.

Dolostone cross-cut by mineralising veins has high $\delta^{18}\text{O}$ values (D1 of 31.6‰ ; Table 2) that, at temperatures similar to the T_h values recorded for D1 cement, indicate the $\delta^{18}\text{O}_{\text{H}_2\text{O}}$ of the dolostone overlaps with values calculated for D1 (12.6‰). It is possible, therefore, that D1-precipitating fluid recrystallised the dolostone, which can be evaluated using the $\delta^{18}\text{O}$ data available, assuming a $\delta^{18}\text{O}_{\text{H}_2\text{O}}$ value of the fluid and limiting temperatures. Using the closed water:rock equation from (Taylor, 1977), a W:R between 2 and 20 (depending on temperature) would be sufficient for D1 fluid to alter the $\delta^{18}\text{O}$ of the dolostone (Fig. 16) assuming the water had a value of about 12‰ .

3.5.4.2 Pre-ore-stage (D1, Cpy1, and Py1)

Evaporation of seawater can fractionate O isotopes up to +6‰ (Lloyd, 1966; Ward and Halley, 1985). Assuming a seawater fluid source ($\delta^{18}\text{O}_{\text{H}_2\text{O}} = 0\text{‰}$), temperatures of formation would be in the range of 29° to 68°C in order to accommodate the $\delta^{18}\text{O}$ data for D1. However, this temperature is at odds with both the measured T_h values and salinities (17 wt. % equiv. NaCl vs. 3.5 wt. % for seawater) of D1 and its reduced shale-normalised REE signature (positive Ce and Eu anomalies, both of which suggest burial deeper than 1 km; Machel, 1999). Thus the hydrothermal fluid responsible for D1 could not have been unmodified seawater. Using the pressure-corrected T_h data, which indicate trapping temperatures up to 170°C for maximum assumed burial depth, and the isotopic composition of the precipitating fluid (i.e., maximum $\delta^{18}\text{O}_{\text{H}_2\text{O}}$ value of 18‰; Fig. 11) then a more crustal-involved signature is indicated.

The geochemical signature of D1 cement differs markedly from the Allen Bay Formation dolostone, which suggests interaction with a very different fluid from that responsible for dolomitisation. The enrichment of LREE, and lack of any appreciable La or Ce, but minor Y anomalies in PAAS-normalised patterns for D1, indicates interaction with a fluid that had equilibrated with a reduced rock. The positive to absent Ce anomaly and strongly positive Eu anomalies furthermore indicate a reduced fluid (Bao et al., 2008; Torres-Ruiz, 2006), or reaction with a sulphidic, igneous, or gneissic unit in a reduced setting (Göb et al., 2013; Leybourne et al., 2000; Schwinn and Markl, 2005). Furthermore, the lack of correlation between Ba and Eu values indicates that Eu values are not related to any interference from Ba in the analysis, and that the recorded positive Eu anomaly is real. The lack of spreading ridges and magmatic activity in the Phanerozoic on Somerset Island argue against the signal representing vent or magmatic fluid;

therefore, fluid-rock interaction along the fluid's flow-path is the preferred explanation for modifying fluid chemistry. In general, Eu^{2+} is not very mobile in low-temperature fluids (Sverjensky, 1984), and so, fluid transport must not have been far, despite its migration through the graben. The most reasonable source would then be underlying mafic gneiss or dykes (Mackenzie- or Franklin-aged) and rapid transport facilitated by faults.

In terms of modifying the LREE signal of D1 cement, phosphates typically incorporate LREE (Debruyne et al., 2016). If a fluid interacts with such a mineral phase, it becomes enriched in LREE, which can be inherited by carbonate minerals that precipitate from such a fluid. With phosphates being abundant in crustal rocks, such as granite or shale, multiple subsurface units could have supplied the LREE.

Enrichment of K in a diagenetic fluid (based on the evaporate mound data) may originate from interaction with a K-rich source in the subsurface (e.g., granite or shale; Mathieu et al., 2013). Lastly, the intermediate Y/Ho values (34) indicate interaction with a source having a low Y/Ho value, such as basalt or shale (Nothdurft et al., 2004; Turner and Kamber, 2012). Given that no mafic rocks (with the exception of the dykes) or abundant shale units are locally present in the buried Mesoproterozoic to Silurian stratigraphy, basement gneiss may be the most reasonable source for these characteristics. Alternatively, shale interbeds in the Irene Bay Formation may have been sufficient to produce these characteristics, depending on the extent of shale abundance underlying the local geology.

Homogeneous $\delta^{34}\text{S}_{\text{Py,Cpy}}$ values for sulphides cogenetic with D1 cement (Fig. 6C) centre on a magmatic reservoir (0‰) and could have been derived from a magmatic fluid, interaction with an igneous or sulphidic unit in the subsurface, or from isotopic fractionation. Alternative explanations include bacterial sulphate (BSR) and thermochemical sulphate (TSR) reduction. As to the former, the pressure-corrected T_h values of associated D1 FIAs approach 170°C, assuming maximum burial, precluding BSR. However, at the burial depths experienced by the Allen Bay Formation (up to 3 km), the ambient temperature would lie in the optimal range for BSR (Machel, 2001) and therefore BSR may have generated sulphide prior to introduction of the metal-bearing fluid, with some $\delta^{34}\text{S}$ values theoretically around 0‰. However, because BSR commonly produces heterogeneous $\delta^{34}\text{S}$ values in associated minerals (Kohn et al., 1998; Riciputi et al., 1996), the homogeneous $\delta^{34}\text{S}$ values in the sulphides argue against this mechanism. As for TSR, fractionation of $\delta^{34}\text{S}$ at recorded homogenisation temperatures (~100°C) is insufficient to reduce a seawater sulphate from values of about 20‰, based on the global seawater sulphate isotope curve (Claypool et al., 1980; Paytan and Gray, 2012), to magmatic values (~0‰; Machel, 2001; Ohmoto and Rye, 1979). Thus the $\delta^{34}\text{S}_{\text{Py,Cpy}}$ data probably reflect a signature inherited from sulphide dissolution in an igneous unit.

The $\delta^{65}\text{Cu}$ values of Cpy1 (~0‰) are typical of a mantle-derived source (Wall et al., 2011) and imply that Cu either came directly from a magmatic fluid or indirectly via its leaching from a mantle-derived rock (e.g., basalt). A reduced fluid has the ability to leach and transport Cu from a source rock without fractionating $\delta^{65}\text{Cu}$, whereas an oxidised fluid would induce fractionation (Albarède, 2004; Ehrlich et al., 2004; Mathur et al., 2009, 2005; Pękala et al., 2011; Seo et al., 2007; Wall et al., 2011)

Owing to the lack of magmatism on Somerset Island in the Phanerozoic (Miall and Kerr, 1977), the Cu, as with the S argued above, must have been acquired through interaction of a reduced fluid with an igneous source in the subsurface.

The geochemical features of early cement (D1) and sulphides, which include its REE patterns and anomalies, high $\delta^{18}\text{O}_{\text{H}_2\text{O}}$ and low $\delta^{34}\text{S}$ values, bimodal Na and K-Na fluid inclusion mound chemistry, and Y/Ho ratios, indicate that the precipitating fluid was a mixture of fluids that had interacted with crustal rocks along their flow paths. Proterozoic sills and dykes in the Aston and Hunting formations, together with basement gneiss (Fig. 2), are assumed to continue under the Phanerozoic cover. During the Ellesmerian orogeny, Paleozoic strata would have been approximately 6 km thick (Dixon, 1974; Dixon et al., 1971; Miall and Kerr, 1977), and with a normal geothermal gradient, the maximum inferred temperatures of 170°C could have been reached at the basement nonconformity. Thermally equilibrated, reduced hydrothermal fluids could have interacted with the basement gneiss and/or the Aston Formation to acquire Cu, S, K, and Eu^{2+} . Because the transport capacity of Cu in a reduced sulphide fluid is low, Cu and S were probably transported separately. As with most other low-temperature Cu mineralising fluids, Cu was probably transported as CuCl_2^- (Rose et al., 1986; Rose, 1989). Both fluids must have been reduced, otherwise Cu would have been fractionated during leaching, and the $\delta^{34}\text{S}$ fractionated during reduction. Following the recent model proposed by Large et al. (2012, 2009) for sedimentary-rock-hosted gold deposits whereby metals are sourced from nearby sedimentary units (i.e., sulphidic shale), it is possible that the metal-rich fluid had interacted with sedimentary rocks, such as the Aston Formation (red bed), whereas S was transported from a basement reservoir. Because positive Eu anomalies, which are related to interaction with igneous bodies

(or their clastic equivalent), are present only in D1 cements, which is associated with magmatic S, S was probably derived from basement rocks. If Cu were sourced from the basement, D2 would be expected to express a positive Eu anomaly.

3.5.4.3 Main-stage ore (C1, C2, G1, G2, Cv1, Bn, and Cpy2)

Calcite 1 is characterised by low $\delta^{18}\text{O}$ values, LREE-enrichment, positive Ce and Eu anomalies, and moderate Mn enrichment. The $\delta^{18}\text{O}_{\text{H}_2\text{O}}$ values indicate a low-latitude meteoric water. The PAAS-normalised REE data reflect only slightly the signature of the preceding D1 cement, suggesting that C1 characteristics were, at least partially, inherited during precipitation at a low fluid-rock ratio, and reflected also in the rock-buffered $\delta^{18}\text{O}$ values.

The PAAS--normalised REE patterns of C2, the main gangue mineral, together with its ambiguous $\delta^{18}\text{O}_{\text{H}_2\text{O}}$ values, indicate the possibility of a seawater or low-latitude meteoric origin, which is similar to C1 fluid. Because $\delta^{18}\text{O}$ values of C1 and C2 are similar, but the PAAS-normalised signatures of C1 (i.e., +Eu and +Ce anomalies) are absent in C2, the precipitation of C2 may indicate a change from low W:R to high W:R. The small, sparse evaporate mounds produced by C2 reflect its low-salinity (0.3 wt. % equiv. NaCl) inclusions. The low-salinity fluids, with consistently Na-dominated composition, favour a meteoric fluid that interacted with evaporite units along its flow path. Assuming a seawater origin instead, a temperature approaching 140°C would have been required to account for the $\delta^{18}\text{O}$ data. Such temperature could have been reached in the buried strata, but burial would have had to be $\gg 1$ km, and hence

in the reduced environment (Machel, 1999). Although some of the C2 cements exhibit negative Ce anomalies, which contradict the latter possibility, these anomalies are weak and not present in all examples of C2. The relatively high $\delta^{65}\text{Cu}_{\text{Cpy}}$ values (+1.0 to +3.4‰) indicate that Cu was leached from the surrounding rocks, suggesting an oxidised fluid (Albarède, 2004; Ehrlich et al., 2004; Mathur et al., 2005, 2009; Pękala et al., 2011; Seo et al., 2007; Wall et al., 2011). The Cu may have been leached from oxyhydroxide cements in the underlying red clastic unit (Aston Formation). The enriched Mn content in C2 (Fig. 14) requires oxidised fluid for transport and could reflect Mn incorporation into the fluid from oxyhydroxide cements, which are good Mn sinks.

Although Cl^- is the main anion in the fluid, based on evaporate mound analysis, S was also detected (to 1 wt. %). The $\delta^{34}\text{S}$ sulphide values (10‰) suggest the involvement of seawater sulphate, consistent with sulphate anions in the fluid, and with seawater or meteoric $\delta^{18}\text{O}$ values. Homogeneous $\delta^{34}\text{S}$ values (10‰) that fall between pre-ore sulphide values of 0‰ (see above) and Paleozoic seawater (20-25‰) may suggest that S was remobilised and recycled from the pre-ore sulphides and mixed with seawater-derived sulphate. The remobilisation of S has been shown to homogenise large ranges in $\delta^{34}\text{S}$ values to its mean value (Chang et al., 2008). As suggested by Large et al. (2012, 2009), metal enrichment can be produced by remobilisation of metals from earlier sulphides, primarily pyrite. As noted above, Py1 is enriched in trace elements (Pb, Ag, and Au) compared to later pyrite (Fig. 15), which is consistent with an explanation invoking remobilisation and also suggests that S was remobilised. The replacement of earlier sulphides (pyrite +/- chalcopyrite) is common in stratiform Cu deposits (Muechez and Corbella, 2012).

Because geerite (Cu_8S_5) has no covalently bonded S layers, like covellite, in its unit cell (Goble, 1985), Cu(I) and Cu(II) are required to balance charge ($\text{Cu}_6^+\text{Cu}_2^{2+}\text{S}_5^{2-}$), with an average charge of $\text{Cu}^{1.25+}$. With the dominance of Cu(I) in geerite, it is most probable that Cu was transported as a Cu-chloride complex, likely CuCl_3^{2-} or CuCl_2^- , depending on a_{Cl} (Muechez and Corbella, 2012; Rose, 1976, 1989; Xiao et al. 1998).

3.5.4.4 Recrystallisation of main-stage ore (D2, Cpy3)

Similar T_h and $\delta^{18}\text{O}$ values in D1 and D2 may indicate a similar fluid source, but, the difference in $\delta^{34}\text{S}$ values and lack of a Eu anomaly suggest that magmatic basement rock no longer dominated in the fluid mixture. Unfractionated Cu isotopes indicate a reduced fluid (Albarède, 2004; Ehrlich et al., 2004; Mathur et al., 2005, 2009; Pękala et al., 2011; Seo et al., 2007; Wall et al., 2011), whereas the higher $\delta^{34}\text{S}$ values (i.e., up to 23‰) indicate a relatively oxidised sulphate-bearing fluid (Ohmoto and Rye, 1979). A large compositional range of the fluid (evaporate mounds) and a lower abundance and lack of correlation among trace elements in Cpy3 (e.g., Pb and Ag) indicates the interaction of multiple fluids from different sources. These characteristics suggest that hypogene precipitation resulted from mixing of at least two fluids: a reduced Cu-bearing fluid and a sulphate-bearing fluid, both of which probably carried different trace-element concentrations.

Assuming an initial seawater fluid source ($\delta^{18}\text{O} = 0\text{‰}$), the temperature of formation would be in the range of 42° to 65°C to account for the $\delta^{18}\text{O}$ data (Fig. 11). This temperature range does not agree with T_h values from fluid inclusions or with reduced shale-normalised REE signatures (positive Ce anomaly); therefore, the hydrothermal fluid could not have originated purely from seawater. The large range of $\delta^{18}\text{O}_{\text{H}_2\text{O}}$ values, which implicates crustal fluid, could be obtained through either mixing of reservoirs or equilibration of a single fluid with crustal rocks. A single source for the fluid has already been dismissed based on Cu and S isotopes and the large variation in evaporate mounds, which favours the mixing of (at least) two fluids. The sulphate-bearing fluid would probably have had a lighter, seawater-like $\delta^{18}\text{O}$ composition, whereas the Cu-bearing fluid would have had the rock-equilibrated signature. A seawater mixture with a reduced rock-equilibrated fluid is reflected in the PAAS-normalised, intermediate pattern that lacks any appreciable anomalies and has chondritic Y/Ho values (~27).

The S isotopic data were the product of one of the following processes: (1) high $\delta^{34}\text{S}$ sulphate (e.g., 50‰) that underwent large degrees of fractionation (e.g., -25 to -40‰) through BSR; (2) seawater sulphate (~25‰) that experienced a lower degree of fractionation (0 to -20‰); (3) seawater sulphate that mixed with recycled S from previous sulphides; or (4) a combination of these. In the first case, heterogeneous $\delta^{34}\text{S}$ values such as those of Cpy3 are common in reduced seawater sulphates (Chang et al., 2008) and are a common byproduct of BSR (Machel, 2001; Riciputi et al., 1996). Transport of bacterially reduced S by D2 fluid is improbable, however, because the T_h values are beyond the thermal regime of BSR (Machel et al., 1995; Machel, 2001). In the latter two cases, evaporites of the underlying Bay Fiord Formation have $\delta^{34}\text{S}$ values that range from +20 to +30 (Dewing et al., 2007a), and although evaporite layers are a minor

component in this unit on Somerset Island (Miall and Kerr, 1980), both formation thickness and anhydrite abundance increases to the present-day north of Somerset Island (Trettin et al., 1991). Evaporite beds in the upper Allen Bay Formation (Cape Crauford Formation; Miall and Kerr, 1977, 1980) could, however, also have produced the high values documented here. Because the measured $\delta^{34}\text{S}$ values are similar to those of the evaporite units, little or no fractionation need have occurred. Reduction by TSR is more probable because it operates at temperatures $>100^\circ\text{C}$ and fractionates less than BSR, allowing for higher $\delta^{34}\text{S}$ values. The range in $\delta^{34}\text{S}$ values within single crystals (Fig. 6K), as noted here, has also been documented in low-temperature base-metal deposits (e.g., Basuki et al., 2008) and was interpreted as the result of S source mixing. Thus the documented $\delta^{34}\text{S}$ values for Cpy3 may reflect mixing of recycled S from earlier sulphides (Cpy1, Py1) with reduced seawater sulphate via TSR. Rayleigh fractionation of S isotopes is improbable because there does not appear to be any systematic spatial variation in the values (Fig. 6K), which would be expected during crystal growth.

The magmatic $\delta^{65}\text{Cu}$ values ($\sim 0\text{‰}$) of Cpy3 indicate an input of new Cu, rather than recycling of Cu from sulphides. Because no sulphate was detected in this fluid (based on mound chemistry), it is suggested that Cu and S were not transported together in a single sulphate fluid and then reduced on site; instead, Cu was transported as a chloride complex and S was supplied by a different fluid. Both fluids transported metals, based on the scatter of trace elements in Cpy3 (Fig. 15).

3.5.4.5 Post-ore alteration (C3, cuprite, native copper, atacamite, malachite)

Because of the paucity of evaporate mounds from C3 and the relationship between mound size and salinity (Haynes et al., 1988; Kontak, 2004), a low-salinity fluid is assumed for C3. The inferred low salinity, very light $\delta^{18}\text{O}_{\text{H}_2\text{O}}$ values ($\ll 0\text{‰}$), and PAAS-normalised REE signatures along with low ΣREE all suggest that C3-precipitating fluid was high-latitude meteoric water. The co-precipitation of cuprite, native Cu, and goethite with C3 indicate that the fluid was oxidised. Seawater could not, therefore, have been the source, because burial in excess of 1 km and likely much deeper (i.e., a reduced environment; Machel, 1999) would be required to produce the temperatures needed to fractionate seawater to obtain the $\delta^{18}\text{O}$ values of C3 (Fig. 11), a depth beyond oxidised fluid penetration (Machel, 1999) and a temperature beyond atacamite stability (Hannington, 1993). The Y/Ho ratios are much lower than typical seawater or meteoric water in C3, which may be due to fluid-rock interaction along its flow path. The fluid was probably a deeply penetrating, oxidised, modified meteoric water. Lastly, Cu in post-ore minerals was probably derived from the leaching of previous Cu phases. Slightly elevated $\delta^{65}\text{Cu}$ values (0.2 to 0.78‰) indicate that only low temperatures and few leaching events took place, and that the Cu was not transported great distances from the leached source material (Mathur et al., 2009).

3.5.5 Fluid movement inferred from zonation

Initial fluid movement appears to have originated in the present-day north and moved southward (Fig. 17), because of the crude metal zonation: geerite-rich (north), versus geerite-bornite-chalcopyrite (south). If fluid originated in the south instead, the Cu zonation would have resulted from pH or redox changes (Reed and Palandri, 2006), and the natural mineral zonation described by Hitzman et al. (2005) (i.e., chalcocite-group minerals followed by bornite and then chalcopyrite from origin outwards), would produce the opposite trend to that documented at Storm. The $\delta^{65}\text{Cu}$ data indicate southwestward fluid migration, with a progressive increase from +1.31‰ at 294 masl (4100N) to +3.44 ‰ and 2.18 ‰ at 221 and 180 masl, respectively (2750N), and +0.99 ‰ at 212 masl (3500N). The increase in ^{65}Cu along the flow path suggests increasing exposure time to Cu leaching from source rocks, a process that has also been recorded at the Meiduk porphyry (Asadi et al., 2015). Increasing $\delta^{18}\text{O}$ values in C1 cement from north (7.5‰) to south (17.3‰) also indicate an increasingly rock-buffered system, and thus, north- to south-movement. The decrease in $\delta^{65}\text{Cu}$ values with depth in the south (2750N) may indicate that fluid ascended along faults. The southward increase in $\delta^{65}\text{Cu}$ values reflects progressive leaching of the Cu source (Aston Formation), enhanced by leaching of deeper sulphides, while moving up faults at 2750N. The greater depletion of Cu in the northern sulphide minerals (covellite, $\text{Cu}_{0.9}\text{S}$), like the $\delta^{65}\text{Cu}$ values, records increased fluid interaction and therefore fluid flow from the north.

Post-ore oxidising meteoric fluid was focussed in the western part of the Storm graben (3500N), precipitating native Cu, cuprite, and atacamite. Although native Cu is present throughout the graben, cuprite and atacamite are limited to the western part. This may reflect the more oxidised

nature of cuprite relative to native Cu: as the fluid moved through the system it became more reduced and cuprite was no longer stable.

3.5.6 Timing of mineralisation and fluid-driving mechanism

Three orogenic events (Caledonian, Ellesmerian, and Eurekan) and an extensional event (Sverdrup basin) took place after Allen Bay Formation deposition. Each event could have mobilised fluid. By utilizing all available data, a probable age, and therefore mobilising agent, can be identified.

Low-latitude meteoric water present throughout ore mineralisation, inferred from geochemical arguments above, limits precipitation of main-stage ore between the Silurian (host-rock depositional age) and Early Carboniferous, based on paleogeographic reconstructions (Torsvik et al., 2012). This Paleozoic mineralisation age precludes both the Eurekan orogeny (Cenozoic) and Sverdrup basin extension and magmatism (Mesozoic) from involvement. No Paleozoic magmatism is known in the region, and so thermal convection driven by a magma body or an exsolved magmatic fluid is not a viable driving force behind fluid migration. Basement-equilibrated fluid temperatures displayed by pre-ore-stage (D1) fluids suggest that maximum burial was attained at the time of the Ellesmerian orogeny (late Devonian; Embry, 1991a). The pre-ore fluid was probably mobilised during early orogenic activity, after which the fluid pathway changed during continued orogenesis. This interpretation could explain the basement involvement (+Eu anomaly and 0‰ $\delta^{34}\text{S}$ values) with pre-ore fluid, and its absence from subsequent fluids.

Very low $\delta^{18}\text{O}$ values for C3, which implicate meteoric water, indicate a relatively high-latitude fluid. Somerset Island initially reached a high latitude in the mid-late Mesozoic (Torsvik et al., 2012). Atacamite mineralisation requires arid and/or saline conditions (Sillitoe, 2005); such arid conditions are facilitated in the Arctic, where Somerset Island has been situated since the Cenozoic. Fossilised tree forests, beetles, and molluscs on Ellesmere Island indicate that there was a transition from a warm humid climate in the Eocene to a more arid, cool climate in the Pliocene (Csank et al., 2011; Elias et al., 2006; Jahren et al., 2003). Calculated meteoric water isotopic values reveal that surficial water in the Pliocene had values in the range of -10 to -22‰, with an average of -16‰ (Csank et al., 2011), similar to the values obtained for C3. Somerset Island was covered, primarily from cold-based glaciers (Dyke, 1978) during the Late Pleistocene. This would limit the timing of supergene alteration to the Pliocene-Late Pleistocene. Because the solubility of atacamite increases above 25°C (Hannington, 1993), it would have formed below 25°C, and would require near-surface (i.e., no burial) conditions.

3.5.7 Mineralisation process

The Storm showing is a carbonate-rock-hosted stratiform Cu deposit that resembles red-bed Cu deposits, based on the initial tectonic setting (mini-graben), stratigraphic succession (relatively impermeable argillaceous Cape Storm strata overlying permeable carbonate strata, all of which overlie red clastic strata), absence of a relationship with igneous activity, both metal and mineral zonation, the presence of an oxidised fluid that leached Cu and transported metals to a reductant (Hitzman et al., 2005, 2010), and textural similarities to other deposits (e.g., Bateman and

McLaughlen, 1920; Bernstein and Cox, 1986; Branum and Ripley, 1990; Hitzman, 1986; Large et al., 1995). The carbonate-rock-hosted Kipushi-type deposits, which are generally polymetallic and Co-rich (Bernstein and Cox, 1986; Hitzman, 1986; Hitzman et al., 2005), are unlike Storm, which apparently lacks Co minerals or other characteristic metals (e.g., Ge, As, Sb, and V), with the exception of Ag. The early pyrite (Py1) is relatively enriched in Co, but there is no apparent association with Au. With the exception of being carbonate-rock-hosted, the ore setting of Storm does not strongly resemble that of Kipushi (Turner et al., 2018).

Clastic units that underlie sedimentary-rock-hosted ore deposits are credited as the main source of base-metals for some red-bed (Hitzman et al., 2005), MVT (Peru; Basuki et al., 2008; Viburnum Trend; Appold et al., 2004), and Irish-type (Wilkinson et al., 2005) deposits. In the case of the Storm setting, there are red clastic units both above (Peel Sound and Somerset Island formations) and below (Aston Formation) the mineralised Allen Bay Formation. Bleached zones in Aston Formation sandstone clearly indicate post-depositional alteration, which may have included leaching of particular metals, hence establishing a setting that is in some respects akin to the Irish ore district, where bleaching is noted in the underlying "old red sandstone" unit (Wilkinson et al., 2005). Interaction of basement igneous rocks, in addition to underlying sandstone, has been noted as a base-metal source for Irish-type deposits (Everett et al., 2003) and the Viburnum trend (Shelton et al., 1995, 2009). The diagenetic history of the Aston Formation sandstone and its possible role as a metal source have yet to be investigated, and so the true source of metals remains undetermined.

3.5.7.1 Pre-ore

Based on textural and geochemical data (Table 4), pre-ore mineralisation resulted when two reduced fluids mixed on-site (Fig. 18A). High temperatures, +Eu PAAS-normalised anomalies, and $\delta^{34}\text{S}$ values ($\sim 0\%$) indicate a fluid that had equilibrated with basement gneiss and/or mafic dykes was rapidly transported (to preserve the Eu^{+2} signatures) along graben faults to the site of precipitation. Sulphur (along with Eu^{+2} +/- Co) that had been leached from the basement mixed with a second reduced fluid. The second fluid, having equilibrated with red clastic rocks (probably Aston Formation), transported unfractionated Cu as a chloride complex to the site of mineralisation. The ranges in $\delta^{18}\text{O}$ and fluid compositions (evaporate mounds) indicate mixing of two fluids; the relatively consistent fluid temperature may indicate that the two fluids had similar temperatures (similar temperatures in both basement and Aston Formation).

3.5.7.2 Main ore

Continued orogenesis affected fluid flow paths established during pre-ore mineralisation, and the basement-equilibrated fluid (Eu anomaly, $\delta^{34}\text{S}$, and Co) was no longer prominent. Using red-bed Cu deposit type mineralisation as an analogy, the sequence of events that resulted in mineralisation commenced with an oxidised fluid circulating through igneous basement (Blundell et al., 2003; Koziy et al., 2009) and/or red beds (Hitzman, 2000; Hitzman et al., 2010), leaching Cu and transporting it to a reductant where precipitation would occur. At Storm, a downward-migrating, oxidised, low-latitude meteoric fluid (0 wt. % NaCl equiv.) dissolved

evaporite units to become enriched in Na, and leached Cu (and Mn) from the underlying red-bed and transported Cu as a chloride complex along faults to sites of mineralisation (Fig. 18B).

Prolonged fluid flow from the north(west) resulted in Cu-depletion in the north (geerite and covellite compositions) and southward ^{65}Cu -enrichment. Deeper mineralisation has lower $\delta^{65}\text{Cu}$ values than the more shallow sulphides and reflects the remobilisation of Cu up the faults.

Sulphur was provided by dissolution of pre-ore sulphides (primarily pyrite) mixed with seawater/evaporite sulphate ($\delta^{34}\text{S} = \sim 20\text{‰}$) that was reduced by TSR to result in intermediate $\delta^{34}\text{S}$ values ($\sim 10\text{‰}$).

There is little evidence for the presence of organic matter or abundant pyrite to act as a reductant in the Allen Bay Formation. However, the former presence of hydrocarbons is suggested from the amorphous carbon associated with Cpy2 and calcite (Fig. 7I) that may be the end-product of hydrocarbon degradation.

The argillaceous Cape Storm Formation acted as a trap for the mineralising fluids. The permeability contrast between the Allen Bay Formation and the Cape Storm Formation was sufficient to cause fluid(s) to pool to initiate mineralisation, but still allowing for some fluid to leak into the overlying Douro Formation, where stringers of mineralisation formed.

Pulses of a basement-equilibrated fluid, similar to pre-ore fluids (T, salinity, $\delta^{18}\text{O}$, REE patterns, K-enrichment), introduced unfractionated Cu ($\delta^{65}\text{Cu} = 0\text{‰}$) and $\delta^{34}\text{S}$ -enriched S ($\delta^{34}\text{S} = 20\text{‰}$). This fluid was also responsible for the Cpy3 and D2 minerals at 2750N.

3.5.7.3 Post-ore

The post-ore assemblage records alteration from a downward-migrating, oxidised, high-latitude meteoric water. Copper was locally leached from pre-existing sulphides and precipitated as secondary oxides, carbonates, and native Cu.

In summary, hypogene mineralisation at Storm was the result of two fluids (Cu-bearing and S-bearing) that migrated along graben faults and mixed in a carbonate host beneath a semi-impermeable argillaceous unit during the Ellesmerian orogeny. Copper was probably derived from an underlying red clastic unit and transported as a chloride complex; S, on the other hand, was probably derived from seawater or evaporite dissolution, underwent TSR, and also mixed with pre-ore sulphides. Prolonged fluid movement from the present-day north produced a globally familiar zonation in sulphide mineralogy (geerite [chalcocite] → bornite → Cpy). Later (Cenozoic) supergene mineralisation was the result of downward-penetrating high-latitude surficial water locally remobilised copper. The Devonian-Carboniferous timing of pre- and main-stage mineralisation, based on combined paragenetic and analytical criteria, is compatible with the geochronology of Zn mineralisation elsewhere in the Cornwallis district (Christensen et al., 1995; Selby et al., 2005), suggesting that the Storm copper deposit may be closely related to other showings in the district despite its contrasting mineral composition and stratigraphic position.

3.6 Conclusions

Integration of detailed petrography and SEM-EDS studies with multiple in situ microanalytical analyses on ore and gangue minerals from a Cu showing in the Cornwallis Zn district constrains the source and history of its diagenetic and mineralizing fluids, which collectively span the Silurian (early diagenesis), Devonian-Carboniferous (main ore precipitation) and Cenozoic (oxidation of the sulphide mineralisation). Whereas pre-ore mineralisation resulted from mixing of two reduced fluids on-site, with one fluid transporting Cu and the other reduced S, the main mineralising fluid was a southward-migrating, descending, meteoric fluid that leached Cu from the underlying Proterozoic red sandstone (Aston Formation) and was reduced on site. The latest fluid event, which remobilised Cu from the sulphides and precipitated supergene minerals, is related to descending meteoric water during the Cenozoic. The timing of the main ore event is comparable with dates for Zn mineralisation elsewhere in the Cornwallis district, suggesting that the Storm Cu deposit is genetically related to the Zn deposits in spite of their obvious differences. The ultimate source of metals in the deposit, and its relationship to the Zn-dominated showings that dominate the Cornwallis district, are the subjects of ongoing work.

3.7 Acknowledgements

Primary funding for this work was through Natural Resources Canada's GEM (Geoscience for Energy and Minerals) program and from NSERC Discovery and Accelerator Grants to ECT. The Goodman School of Mines (Laurentian University) partially supports JM. Additional sample material was kindly provided by Aston Bay Holdings and Apex Geoscience. The fluid inclusion microthermometry laboratory at Laurentian University was funded by an NSERC grant to DJK. The authors wish to thank R. Sharpe at the University of Manitoba (Winnipeg, Manitoba), for assistance with SIMS analyses, and Drs. J. Petrus and M. Leybourne at Laurentian University (Sudbury, Ontario) for laser ablation ICP-MS analyses.

3.8 References

Albarède, F., 2004. The stable isotope geochemistry of copper and zinc. *Rev. Mineral. Geochem.* 55, 409–427.

Algeo, T.J., Maynard, J.B., 2004. Trace-element behavior and redox facies in core shales of Upper Pennsylvanian Kansas-type cyclothems. *Chem. Geol.* 206, 289–318.
<https://doi.org/10.1016/j.chemgeo.2003.12.009>

Allen, A.A., Allen, J.R., 2005. *Basin analysis: Principles and applications*. Blackwell Publishing.

Appold, M.S., Numelin, T.J., Shepherd, T.J., Chenery, S.R., 2004. Limits on the metal content of fluid inclusions in gangue minerals from the Viburnum Trend, southeast Missouri, determined by laser ablation ICP-MS. *Econ. Geol.* 99, 185–198.

- Asadi, S., Mathur, R., Moore, F., Zarasvandi, A., 2015. Copper isotope fractionation in the Meiduk porphyry copper deposit, Northwest of Kerman Cenozoic magmatic arc, Iran. *Terra Nova* 27, 36–41. <https://doi.org/10.1111/ter.12128>
- Bao, S.-X., Zhou, H.-Y., Peng, X.-T., Ji, F.-W., Yao, H.-Q., 2008. Geochemistry of REE and yttrium in hydrothermal fluids from the Endeavour segment, Juan de Fuca Ridge. *Geochem. J.* 42, 359–370.
- Basuki, N.I., Taylor, B.E., Spooner, E.T.C., 2008. Sulfur isotope evidence for thermochemical reduction of dissolved sulfate in Mississippi valley-type zinc-lead mineralization, Bongara area, northern Peru. *Econ. Geol.* 103, 783–799.
- Bateman, A.M., Lasky, S.G., 1932. Covellite-chalcocite solid solution and ex-solution. *Econ. Geol.* 27, 52–86.
- Bateman, A.M., McLaughlen, D.H., 1920. Geology of the ore deposits of Kennecott Alaska. *Econ. Geol.* 15, 1–80.
- Bau, M., Alexander, B., 2006. Preservation of primary REE patterns without Ce anomaly during dolomitization of Mid-Paleoproterozoic limestone and the potential re-establishment of marine anoxia immediately after the “Great Oxidation Event”. *S. Afr. J. Geo.* 109, 81–86.
- Bau, M., Möller, P., Dulski, P., 1997. Yttrium and lanthanides in eastern Mediterranean seawater and their fractionation during redox cycling. *Mar. Chem.* 56, 123–131.
- Bernstein, L.R., Cox, D.P., 1986. Geology and Sulfide Mineralogy of the Number One Orebody, Ruby Creek Copper Deposit, Alaska. *Econ. Geol.* 81, 1675–1689.

- Blundell, D.J., Karnkowski, P.H., Alderton, D.H.M., Oszczepalski, S., Kucha, H., 2003. Copper mineralization of the Polish Kupferschiefer: a proposed basement fault-fracture system of fluid flow. *Econ. Geol.* 98, 1487–1495.
- Bodnar, R.J., 1993. Revised equation and table for determining the freezing point depression of H₂O-NaCl solutions. *Geochim. Cosmochim. Acta* 57, 683–684.
- Branum, T.D., Ripley, E.M., 1990. Genesis of sediment-hosted copper mineralization in South-Central Kansas: sulfur/carbon and sulfur isotope systematic. *Econ. Geol.* 85, 601–621.
- Brown, R.L., Dalziel, I.W., Rust, B.R., 1969. The structure, metamorphism, and development of the Boothia Arch, Arctic Canada. *Can. J. Earth Sci.* 6, 525–543.
- Chang, Z., Large, R.R., Maslennikov, V., 2008. Sulfur isotopes in sediment-hosted orogenic gold deposits: Evidence for an early timing and a seawater sulfur source. *Geology* 36, 971–974.
- Chen, H., Tian, W., Falloon, T.J., Chen, M., 2011. Pyrite trace element geochemistry of mafic granulite xenoliths from Xikeer: implications for the source of Cu in the sediment-hosted mineralization in the northwestern Tarim Basin (Northwest China). *Miner. Deposita* 46, 1001–1006. <https://doi.org/10.1007/s00126-011-0387-y>
- Christensen, J.N., Halliday, A.N., Leigh, K.E., Randell, R.N., Kesler, S.E., 1995. Direct dating of sulfides by Rb-Sr: a critical test using the Polaris Mississippi Valley-type Zn-Pb deposit. *Geochim. Cosmochim. Acta* 59, 5191-5197.
- Claypool, G.E., Holser, W.T., Kaplan, I.R., Sakai, H., Zak, I., 1980. Age curves of sulfur and oxygen isotopes in marine sulfate and their mutual interpretation. *Chem. Geol.* 28, 199–260.

Corbella, M., Ayora, C., Cardellach, E., 2004. Hydrothermal mixing, carbonate dissolution and sulfide precipitation in Mississippi Valley-type deposits. *Miner. Deposita* 39, 344–357.

<https://doi.org/10.1007/s00126-004-0412-5>

Crowe, D.E., Vaughan, R.G., 1996. Characterization and use of isotopically homogeneous standards for in situ laser microprobe analysis of $^{34}\text{S}/^{32}\text{S}$ ratios. *American Mineralogist* 81, 187-193.

Csank, A.Z., Patterson, W.P., Eglington, B.M., Rybczynski, N., Basinger, J.F., 2011. Climate variability in the Early Pliocene Arctic: Annually resolved evidence from stable isotope values of sub-fossil wood, Ellesmere Island, Canada. *Palaeogeography, Palaeoclimatology, Palaeoecology* 308, 339-349.

Davies, G.R., Nassichuk, W.W., 1991. Carboniferous and Permian history of the Sverdrup Basin, Arctic Islands, in: Trettin, H.P. (Ed.), *Geology of the Innuitian Orogen and Arctic Platform of Canada and Greenland*, Geological Survey of Canada, *Geology of Canada*. pp. 345–368.

Debruyne, D., Hulsbosch, N., Muchez, P., 2016. Unraveling rare earth element signatures in hydrothermal carbonate minerals using a source–sink system. *Ore Geol. Rev.* 72, 232–252.

<https://doi.org/10.1016/j.oregeorev.2015.07.022>

Dewing, K., Obermajer, M., 2009. Lower Paleozoic thermal maturity and hydrocarbon potential of the Canadian Arctic Archipelago. *Bull. Can. Pet. Geol.* 57, 141–166.

Dewing, K., Sharp, R.J., Turner, E.C., 2007a. Synopsis of the Polaris Zn-Pb district, Canadian Arctic Islands, Nunavut, in: Goodfellow, W.D. (Ed.), *Mineral Deposits of Canada: A Synthesis of Major Deposit-Types, District Metallogeny, the Evolution of Geological Provinces, and*

Exploration Methods, Geological Association of Canada, Mineral Deposits Division, Special Publication. pp. 655–672.

Dewing, K., Turner, E.C., Harrison, J.C., 2007b. Geological history, mineral occurrences, and mineral potential of the sedimentary rocks of the Canadian Arctic archipelago, in: Goodfellow, W.D. (Ed.), *Mineral Deposits of Canada: A Synthesis of Major Deposit-Types, District Metallogeny, the Evolution of Geological Provinces, and Exploration Methods*, Geological Association of Canada, Mineral Deposits Division, Special Publication. pp. 733–753.

Dixon, J., 1974. Revised stratigraphy of the Hunting Formation (Proterozoic), Somerset Island, Northwest Territories. *Can. J. Earth Sci.* 11, 635–642.

Dixon, O.A., Williams, S.R., Dixon, J., 1971. The Aston Formation (?Proterozoic) on Prince of Wales Island, Arctic Canada. *Can. J. Earth Sci.* 8, 732–742.

Dyke, A.S., 1978. Glacial history of and marine limits on Somerset Island, District of Franklin.

Geological Survey of Canada Current Research 78-1B, 218-223.

Ehrlich, S., Butler, I., Halicz, L., Rickard, D., Oldroyd, A., Matthews, A., 2004. Experimental study of the copper isotope fractionation between aqueous Cu(II) and covellite, CuS. *Chem. Geol.* 209, 259–269. <https://doi.org/10.1016/j.chemgeo.2004.06.010>

Elias, S.A., Kuzmina, S., Kiselyov, S., 2006. Late Tertiary origins of the Arctic beetle fauna. *Palaeogeography, Palaeoclimatology, Palaeoecology* 241, 373-392.

Embry, A.F., 1991a. Middle-Upper Devonian clastic wedge of the Arctic Islands, in: Trettin, H.P. (Ed.), *Geology of the Innuitian Orogen and Arctic Platform of Canada and Greenland*, Geological Survey of Canada, Geology of Canada. pp. 261–291.

- Embry, A.F., 1991b. Mesozoic history of the Arctic Islands, in: Trettin, H.P. (Ed.), *Geology of the Innuitian Orogen and Arctic Platform of Canada and Greenland*, Geological Survey of Canada, *Geology of Canada*. pp. 369–433.
- Everett, C.E., Rye, D.M., Ellam, R.M., 2003. Source or sink? An assessment of the role of the Old Red Sandstone in the genesis of the Irish Zn-Pb deposits. *Econ. Geol.* 98, 31–50.
- Fahrig, W.F., Christie, K.W., Jones, D.L., 1981. Paleomagnetism of the Bylot basins: evidence for Mackenzie continental tensional tectonics. *Geol. Surv. Can. Pap.* 81–10, 303–312.
- Forsyth, D.A., Mair, J.A., Fraser, I., 1979. Crustal structure of the central Sverdrup Basin. *Can. J. Earth Sci.* 16, 1581–1598.
- Göb, S., Loges, A., Nolde, N., Bau, M., Jacob, D.E., Markl, G., 2013. Major and trace element compositions (including REE) of mineral, thermal, mine and surface waters in SW Germany and implications for water–rock interaction. *Appl. Geochem.* 33, 127–152.
<https://doi.org/10.1016/j.apgeochem.2013.02.006>
- Goble, R.J., Robinson, G., 1980. Geerite, Cu_{1.6}S, a new copper sulfide from Dekalb township. *Can. Mineral.* 18, 519–523.
- Goldstein, R.H., Reynolds, T.J., 1994. Systematics of fluid inclusions in diagenetic minerals. *Soc. Sediment. Geol. Short Course* 31, 1–199.
- Grguric, B.A., Harrison, R.J., Putnis, A., 2000. A revised phase diagram for the bornite–digenite join from in situ neutron diffraction and DSC experiments. *Mineral. Mag.* 64, 213–231.
- Grguric, B.A., Putnis, A., 1999. Rapid exsolution behaviour in the bornite–digenite series, and implications for natural ore assemblages. *Mineral. Mag.* 63, 1–12.

Grønvold, F., Stølen, S., Westrum, E.F., Galeas, C.G., 1987. Thermodynamics of copper sulphides III. Heat capacities and thermodynamic properties of $\text{Cu}_{1.75}\text{S}$, $\text{Cu}_{1.80}\text{S}$, $\text{Cu}_{1.85}\text{S}$ from 5 to about 700K. *J. Chem. Thermodyn.* 19, 1303–1324.

Hahn, K.E., 2016. Sedimentology, stratigraphy, geochemistry, geochemistry and diagenesis of giant lacustrine carbonate seep mounds (Ikpiarjuk Formation), Mesoproterozoic Borden Basin, Nunavut, Arctic Canada (PhD Thesis). Laurentian University of Sudbury.

Hahn, K.E., Turner, E.C., Kontak, D.J., Fayek, M., 2018. Fluid-chemical evidence for one billion years of fluid flow through Mesoproterozoic deep-water carbonate mounds (Nanisivik zinc district, Nunavut). *Geochim. Cosmochim. Acta* 223, 493-519.

Hannington, M.D., 1993. The formation of atacamite during weathering of sulfides on the modern seafloor. *Can. Mineral.* 31, 945–956.

Haynes, F.M., Kesler, S.E., 1987. Chemical evolution of brines during Mississippi Valley-Type mineralization: evidence from East Tennessee and Pine Point. *Econ. Geol.* 82, 53–71.

Haynes, F.M., Sterner, S.M., Bodnar, R.J., 1988. Synthetic fluid inclusions in natural quartz. IV. Chemical analyses of fluid inclusions by SEM/EDA: evaluation of method. *Geochim. Cosmochim. Acta* 52, 969–977.

Heaman, L.M., Lecheminant, A.N., Rainbird, R.H., 1992. Nature and timing of Franklin igneous events, Canada: implications for a late Proterozoic mantle plume and the break-up of Laurentia. *Earth Planet. Sci. Lett.* 109, 117–131.

Heijlen, W., Banks, D.A., Muchez, P., Stensgard, B.M., Yardley, B.W., 2008. The nature of mineralizing fluids of the Kipushi Zn-Cu deposit, Katanga, Democratic Republic of Congo:

quantitative fluid inclusion analysis using laser ablation ICP-MS and bulk crush-Leach methods. *Econ. Geol.* 103, 1459–1482.

Hitzman, M.W., 2000. Source basins for sediment-hosted stratiform Cu deposits: implications for the structure of the Zambian Copperbelt. *J. Afr. Earth Sci.* 30, 855–863.

Hitzman, M.W., 1986. Geology of the Ruby Creek Copper Deposit, Southwestern Brooks Range, Alaska. *Econ. Geol.* 81, 1644–1674.

Hitzman, M.W., Kirkham, R., Broughton, D., Thorson, J., Selley, D., 2005. The sediment-hosted stratiform copper ore system. *Econ. Geol.* 100, 609–642.

Hitzman, M.W., Selley, D., Bull, S., 2010. Formation of sedimentary rock-hosted stratiform copper deposits through Earth history. *Econ. Geol.* 105, 627–639.

Hnatyshin, D., Kontak, D.J., Turner, E.C., Creaser, R.A., Morden, R., Stern, R.A., 2016. Geochronologic (Re-Os) and fluid-chemical constraints on the formation of the Mesoproterozoic-hosted Nanisivik Zn Pb deposit, Nunavut, Canada: Evidence for early diagenetic, low-temperature conditions of formation. *Ore Geol. Rev.* 79, 189–217.
<https://doi.org/10.1016/j.oregeorev.2016.05.017>

Horita, J., 2014. Oxygen and carbon isotope fractionation in the system dolomite–water–CO₂ to elevated temperatures. *Geochim. Cosmochim. Acta* 129, 111–124.
<https://doi.org/10.1016/j.gca.2013.12.027>

Jackson, G.D., Cumming, L.M., 1981. Evaporites and folding in the Neohelikian Society Cliffs Formation, northeastern Bylot Island, Arctic Canada. *Geol. Surv. Can. Pap.* 81–1C, 35–44.

Jackson, G.D., Iannelli, T.R., 1981. Rift-related cyclic sedimentation in the Neohelikian Borden Basin, northern Baffin Island, in: Campbell, F.H.A. (Ed.), Proterozoic basins of Canada, Geological Survey of Canada Paper 81-10, pp. 269-302.

Jahren, A.H., Stenberg, L.S.L., 2003. Humidity estimate for the middle Eocene Arctic rain forest. *Geology* 31, 463-466.

Jober, S.-A., Dewing, K., White, J.C., 2007. Structural geology and Zn-Pb mineral occurrences of northeastern Cornwallis Island: implications for exploration of the Cornwallis Fold Belt, northern Nunavut. *Bull. Can. Pet. Geol.* 55, 138–159.

Jones, D.L., Fahrig, W.F., 1978. Paleomagnetism and age of the Aston dykes and Savage Point sills of the Boothia Uplift, Canada. *Can. J. Earth Sci.* 15, 1605–1612.

Jowitt, S.M., Jenkin, G.R.T., Coogan, L.A., Naden, J., 2012. Quantifying the release of base metals from source rocks for volcanogenic massive sulfide deposits: Effects of protolith composition and alteration mineralogy. *J. Geochem. Explor.* 118, 47–59.

<https://doi.org/10.1016/j.gexplo.2012.04.005>

Kerr, J.W., 1967. Nares submarine rift valley and the relative rotation of North Greenland. *Bull. Can. Pet. Geol.* 15, 483–520.

Kerr, J.W., Christie, R.L., 1965. Tectonic history of Boothia uplift and Cornwallis fold belt, Arctic Canada. *Bull. Am. Assoc. Pet. Geol.* 49, 905–926.

Kohn, M.J., Riciputi, L.R., Stakes, D., Orange, D.L., 1998. Sulfur isotope variability in biogenic pyrite: Reflections of heterogeneous bacterial colonization? *Am. Mineral.* 83, 1454–1468.

- Kontak, D.J., 2004. Analysis of evaporate mounds as a complement to fluid-inclusion thermometric data: case studies from granitic environments in Nova Scotia and Peru. *Can. Mineral.* 42, 1315–1329.
- Koziy, L., Bull, S., Large, R., Selley, D., 2009. Salt as a fluid driver, and basement as a metal source, for stratiform sediment-hosted copper deposits. *Geology* 37, 1107–1110.
- Large, D.J., MacQuaker, J., Vaughan, D.J., Sawlowicz, Z., Gize, A.P., 1995. Evidence for low-temperature alteration of sulfides in the Kupferschiefer copper deposits of southwestern Poland. *Econ. Geol.* 90, 2143–2155.
- Large, R., Thomas, H., Craw, D., Henne, A., Henderson, S., 2012. Diagenetic pyrite as a source for metals in orogenic gold deposits, Otago Schist, New Zealand. *N. Z. J. Geol. Geophys.* 55, 137–149. <https://doi.org/10.1080/00288306.2012.682282>
- Large, R.R., Danyushevsky, L., Hollit, C., Maslennikov, V., Meffre, S., Gilbert, S., Bull, S., Scott, R., Emsbo, P., Thomas, H., 2009. Gold and trace element zonation in pyrite using a laser imaging technique: implications for the timing of gold in orogenic and Carlin-style sediment-hosted deposits. *Econ. Geol.* 104, 635–668.
- Lewis, M.H., 1996. Characterisation of hypogene covellite assemblages at the Chuquicamata porphyry copper deposit, Chile, Section 4500N (MSc). Dalhousie, Halifax, Nova Scotia.
- Leybourne, M.I., Goodfellow, W.D., Boyle, D.R., Hall, G.M., 2000. Rapid development of negative Ce anomalies in surface waters and contrasting REE patterns in groundwaters associated with Zn–Pb massive sulphide deposits. *Appl. Geochem.* 15, 695–723.

Li, Z.X., Bogdanova, S.V., Collins, A.S., Davidson, A., De Waele, B., Ernst, R.E., Fitzsimons, I.C.W., Fuck, R.A., Gladkochub, D.P., Jacobs, J., Karlstrom, K.E., Lu, S., Natapov, L.M., Pease, V., Pisarevsky, S.A., Thrane, K., Vernikovsky, V., 2008. Assembly, configuration, and break-up history of Rodinia: A synthesis. *Precambrian Res.* 160, 179–210.

<https://doi.org/10.1016/j.precamres.2007.04.021>

Lloyd, R.M., 1966. Oxygen isotope enrichment of sea water by evaporation. *Geochim. Cosmochim. Acta* 30, 801–814.

Machel, H.G., 2001. Bacterial and thermochemical sulfate reduction in diagenetic settings; old and new insight. *Sediment. Geol.* 140, 143–173.

Machel, H.G., 1999. Effects of groundwater flow on mineral diagenesis, with emphasis on carbonate aquifers. *Hydrogeol. J.* 7, 94–107.

Machel, H.G., Krouse, H.R., Sassen, R., 1995. Products and distinguishing criteria of bacterial and thermochemical sulfate reduction. *Appl. Geochem.* 10, 373–389.

Mahon, K.I., Harrison, T.M., McKeegan, K.D., 1998. The thermal and cementation histories of a sandstone petroleum reservoir, Elk Hills, California Part 2: in situ oxygen and carbon isotopic results. *Chemical Geology* 152, 257-271.

Mathieu, J., Kontak, D.J., Turner, E.C., 2013. A fluid inclusion study of diagenetic fluids in Proterozoic and Paleozoic carbonate rocks, Victoria Island, NWT. *Geofluids* 13, 559–578.

<https://doi.org/10.1111/gfl.12063>

- Mathieu, J., Kontak, D.J., Turner, E.C., Fayek, M., Layne, G., 2015. Geochemistry of Phanerozoic diagenesis on Victoria Island, NWT, Canada. *Chem. Geol.* 415, 47–69. <https://doi.org/10.1016/j.chemgeo.2015.08.016>
- Mathur, R., Munk, L.A., Townley, B., Gou, K.Y., Gómez Miguélez, N., Titley, S., Chen, G.G., Song, S., Reich, M., Tornos, F., Ruiz, J., 2014. Tracing low-temperature aqueous metal migration in mineralized watersheds with Cu isotope fractionation. *Appl. Geochem.* 51, 109–115. <https://doi.org/10.1016/j.apgeochem.2014.09.019>
- Mathur, R., Ruiz, J., Titley, S., Liermann, L., Buss, H., Brantley, S., 2005. Cu isotopic fractionation in the supergene environment with and without bacteria. *Geochim. Cosmochim. Acta* 69, 5233–5246. <https://doi.org/10.1016/j.gca.2005.06.022>
- Mathur, R., Titley, S., Barra, F., Brantley, S., Wilson, M., Phillips, A., Munizaga, F., Maksaev, V., Vervoort, J., Hart, G., 2009. Exploration potential of Cu isotope fractionation in porphyry copper deposits. *J. Geochem. Explor.* 102, 1–6. <https://doi.org/10.1016/j.gexplo.2008.09.004>
- Mayr, U., Brent, T.A., de Freitas, T., Frisch, T., Nowlan, G.S., Okulitch, A.V., 2004. Geology of eastern Prince of Wales Island and adjacent smaller islands, Nunavut. *Geol. Surv. Can. Bull.* 574, 1–99.
- Miall, A.D., 1991. Late Cretaceous and Tertiary basin development and sedimentation, Arctic islands, in: Trettin, H.P. (Ed.), *Geology of the Inuitian Orogen and Arctic Platform of Canada and Greenland*, Geological Survey of Canada, *Geology of Canada*. pp. 369–433.
- Miall, A.D., 1986. Effects of Caledonian tectonism in Arctic Canada. *Geology* 14, 904–907.

- Miall, A.D., 1976. Devonian geology of Banks Island, Arctic Canada, and its bearing on the tectonic development of the circum-Arctic region. *Geol. Soc. Am. Bull.* 87, 1599–1608.
- Miall, A.D., Kerr, J.W., 1980. Cambrian to Upper Silurian stratigraphy, Somerset Island and northeastern Boothia Peninsula, District of Franklin, N.W.T. *Geol. Surv. Can. Bull.* 315, 1–17.
- Miall, A.D., Kerr, J.W., 1977. Phanerozoic stratigraphy and sedimentology of Somerset Island. *Geol. Surv. Can. Pap.* 77–1A, 99–106.
- Miall, A.D., Kerr, W.M., Gibling, M.R., 1978. The Somerset Island Formation: an upper Silurian to ?Lower Devonian intertidal/supratidal succession, Boothia Uplift region, Arctic Canada. *Can. J. Earth Sci.* 15, 181–189.
- Morimoto, N., Koto, K., 1970. Phase relations of the Cu-S system at low temperatures: stability of anilite. *Am. Mineral.* 55, 106–117.
- Morris, G.A., Page, L., Martinez, V., 2005. New dates (415 Ma) for the Etive Dyke Swarm and the end of the Caledonian Orogeny in the SW Grampian highlands of Scotland. *J. Geol. Soc. Lodon* 162, 741–744.
- Muchez, P., Corbella, M., 2012. Factors controlling the precipitation of copper and cobalt minerals in sediment-hosted ore deposits: Advances and restrictions. *J. Geochem. Explor.* 118, 38–46. <https://doi.org/10.1016/j.gexplo.2012.04.006>
- Nothdurft, L.D., Webb, G.E., Kamber, B.S., 2004. Rare earth element geochemistry of Late Devonian reefal carbonates, Canning Basin, Western Australia: confirmation of a seawater REE proxy in ancient limestones. *Geochim. Cosmochim. Acta* 68, 263–283. [https://doi.org/10.1016/S0016-7037\(03\)00422-8](https://doi.org/10.1016/S0016-7037(03)00422-8)

- Ohmoto, H., Rye, R.O., 1979. Isotopes of sulfur and carbon, in: Barnes, H.L. (Ed.), *Geochemistry of Hydrothermal Ore Deposits*. Wiley, New York, USA, pp. 50–567.
- Okulitch, A.V., Packard, J.J., Zolnai, A.I., 1991. Late Silurian - Early Devonian deformation of the Boothia Uplift, in: Trettin, H.P. (Ed.), *Geology of the Innuitian Orogen and Arctic Platform of Canada and Greenland*, Geological Survey of Canada, *Geology of Canada*. pp. 302–307.
- Okulitch, A.V., Trettin, H.P., 1991. Late Cretaceous – Early Tertiary deformation, Arctic Islands, in: Trettin, H.P. (Ed.), *Geology of the Innuitian Orogen and Arctic Platform of Canada and Greenland*, Geological Survey of Canada, *Geology of Canada*. pp. 469–490.
- Oliver, G.J.H., 2001. Reconstruction of the Grampian episode in Scotland its place in the Caledonian Orogeny. *Tectonophysics* 332, 23–49.
- O’Neil, J.R., Clayton, R.N., Mayeda, T.K., 1969. Oxygen Isotope Fractionation in Divalent Metal Carbonates. *J. Chem. Phys.* 51, 5547–5558. <https://doi.org/10.1063/1.1671982>
- Palacios, C., Rouxel, O., Reich, M., Cameron, E.M., Leybourne, M.I., 2011. Pleistocene recycling of copper at a porphyry system, Atacama Desert, Chile: Cu isotope evidence. *Miner. Deposita* 46, 1–7. <https://doi.org/10.1007/s00126-010-0315-6>
- Paytan, A., Gray, E.T., 2012. Sulfur isotope stratigraphy, in: Gradstein, F.M., Ogg, J.G., Schmitz, M.D., Ogg, G.M. (Eds.), *The geologic time scale 2012*, Elsevier Publishing, pp.167-180.
- Pękala, M., Asael, D., Butler, I.B., Matthews, A., Rickard, D., 2011. Experimental study of Cu isotope fractionation during the reaction of aqueous Cu(II) with Fe(II) sulphides at temperatures between 40 and 200°C. *Chem. Geol.* 289, 31–38. <https://doi.org/10.1016/j.chemgeo.2011.07.004>

- Piepjohn, K., von Gosen, W., Tessensohn, F., 2016. The Eureka deformation in the Arctic: an outline. *J. Geol. Soc.* 173, 1007–1024. <https://doi.org/10.1144/jgs2016-081>
- Plummer, K., 2006. Contact metamorphism of calc-silicate rocks in the Belmont contact aureole, central Nevada (MSc thesis). University of Tennessee, Knoxville.
- Pourmand, A., Dauphas, N., Ireland, T.J., 2012. A novel extraction chromatography and MC-ICP-MS technique for rapid analysis of REE, Sc and Y: Revising CI-chondrite and Post-Archean Australian Shale (PAAS) abundances. *Chem. Geol.* 291, 38–54. <https://doi.org/10.1016/j.chemgeo.2011.08.011>
- Reed, M.H., Palandri, J., 2006. Sulfide Mineral Precipitation from Hydrothermal Fluids. *Rev. Mineral. Geochem.* 61, 609–631. <https://doi.org/10.2138/rmg.2006.61.11>
- Reich, M., Chryssoulis, S.L., Deditius, A., Palacios, C., Zúñiga, A., Weldt, M., Alvear, M., 2010. “Invisible” silver and gold in supergene digenite (Cu_{1.8}S). *Geochim. Cosmochim. Acta* 74, 6157–6173. <https://doi.org/10.1016/j.gca.2010.07.026>
- Reich, M., Palacios, C., Barra, F., Chryssoulis, S., 2013. “Invisible” silver in chalcopyrite and bornite from the Mantos Blancos Cu deposit, northern Chile. *Eur. J. Mineral.* 25, 453–460. <https://doi.org/10.1127/0935-1221/2013/0025-2287>
- Riciputi, L.R., Cole, D.L., Machel, H.G., 1996. Sulfide formation in reservoir carbonates of the Devonian Nisku Formation, Alberta, Canada. *Geochim. Cosmochim. Acta* 60, 325–336.
- Robinson, J., Atkinson, B., 2012. Technical report on the exploration history and current status of the Storm Project, Somerset Island, Nunavut (Technical report).

Rose, A.W., 1989. Mobility of copper and other heavy metals in sedimentary environments, in: Boyle, R.W., Brown, A.C., Jefferson, C.W., Jowett, E.C., Kirkham, R. (Eds.), Geological Association of Canada Special Paper, Sediment-Hosted Stratiform Copper Deposits. pp. 97–110.

Rose, A.W., 1976. The effect of cuprous chloride complexes in the origin of red-bed copper and related deposits. *Econ. Geol.* 71, 1036–1048.

Rose, A.W., Smith, A.T., Lustwerk, R.L., Ohmoto, H., Hoy, L.D., 1986. Geochemical aspects of stratiform and red-bed copper deposits in the Catskill Formation (Pennsylvania, USA) and Redstone area (Canada); sequence of mineralization in sediment-hosted copper deposits (Part 3), in: Friedeich, G.H., Genkin, A.D., Naldrett, A.J., Ridge, J.D., Sillitoe, R.H., Vokes, F.M. (Eds.), Special Publication of the Society for Geology Applied to Mineral Deposits, Geology and Metallogeny of Copper Deposits. pp. 412–421.

Schwinn, G., Markl, G., 2005. REE systematics in hydrothermal fluorite. *Chem. Geol.* 216, 225–248. <https://doi.org/10.1016/j.chemgeo.2004.11.012>

Selby, D., Creaser, R.A., Dewing, K., Fowler, M., 2005. Evaluation of bitumen as a (super 187) Re- (super 187) Os geochronometer for hydrocarbon maturation and migration; a test case from the Polaris MVT deposit, Canada. *Earth Planet. Sci. Lett.* 235, 1-15.

Selley, D., Broughton, D., Scott, R., Hitzman, M.W., Bull, S., Large, R.R., McGoldbrick, P., Croaker, M., Pollington, N., 2005. A new look at the geology of the Zambian Copperbelt. *Econ. Geol.* 100, 965–1000.

Seo, J.H., Lee, S.K., Lee, I., 2007. Quantum chemical calculations of equilibrium copper (I) isotope fractionations in ore-forming fluids. *Chem. Geol.* 243, 225–237.

<https://doi.org/10.1016/j.chemgeo.2007.05.025>

Shelton, K.L., Burstein, I.B., Hagni, R.D., Vierrether, C.B., Grant, S.K., Hennigh, Q.T., Bradley, M.F., Brandom, R.T., 1995. Sulfur isotope evidence for penetration of MVT fluids into igneous basement rocks, southeast Missouri, USA. *Miner. Deposita* 30, 339–350.

Shelton, K.L., Gregg, J.M., Johnson, A.W., 2009. Replacement dolomites and ore sulfides as recorders of multiple fluids and fluid sources in the southeast Missouri Mississippi Valley-type district: halogen-⁸⁷Sr/⁸⁶Sr- δ^{18} O- δ^{34} S systematics in the Bonneterre dolomite. *Econ. Geol.* 104, 733–748.

Sikka, D.B., Petruk, W., Nehru, C.E., Zhang, Z., 1991. Geochemistry of secondary copper minerals from Proterozoic porphyry copper deposit, Malanjkhand, India. *Ore Geol. Rev.* 6, 257–290. [https://doi.org/10.1016/0169-1368\(91\)90026-4](https://doi.org/10.1016/0169-1368(91)90026-4)

Sillitoe, R.H., 2005. Supergene oxidized and enriched porphyry copper and related deposits. *Econ. Geol.* 100, 723–768.

Sillitoe, R.H., Clark, A.H., 1969. Copper and copper-iron sulfides as the initial products of supergene oxidation, Copiapó mining district northern Chile. *Am. Mineral.* 54, 1684–1710.

Stewart, W.D., 1983. Late Proterozoic to Early Tertiary stratigraphy of Somerset Island and northern Boothia Peninsula, District of Franklin, N.W.T. *Geol. Surv. Can. Pap.* 83–26, 85.

Stewart, W.D., Kerr, J.W., 1984. Geology of Somerset Island north, District of Franklin. Geological Survey of Canada, map 1595A.

- Sverjensky, D.A., 1984. Europium redox equilibrium in aqueous solutions. *Earth Planet. Sci. Lett.* 67, 70–78.
- Taylor, H.P., 1977. Water/rock interactions and the origin of H₂O in granitic batholiths. *Geol. Soc. Lond.* 133, 509–558.
- Tegner, C., Storey, M., Holm, P.M., Thorarinsson, S.B., Zhao, X., Lo, C.-H., Knudsen, M.F., 2011. Magmatism and Eureka deformation in the High Arctic Large Igneous Province: 40Ar–39Ar age of Kap Washington Group volcanics, North Greenland. *Earth Planet. Sci. Lett.* 303, 203–214. <https://doi.org/10.1016/j.epsl.2010.12.047>
- Torres-Ruiz, J., 2006. Geochemical Constraints on the Genesis of the Marquesado Iron Ore Deposits, Betic Cordillera, Spain REE, C, O, and Sr Isotope Data. *Econ. Geol.* 101, 667–677.
- Torsvik, T.H., Van der Voo, R., Preeden, U., Mac Niocaill, C., Steinberger, B., Doubrovine, P.V., van Hinsbergen, D.J.J., Domeier, M., Gaina, C., Tohver, E., Meert, J.G., McCausland, P.J.A., Cocks, L.R.M., 2012. Phanerozoic polar wander, palaeogeography and dynamics. *Earth-Sci. Rev.* 114, 325–368. <https://doi.org/10.1016/j.earscirev.2012.06.007>
- Trettin, H.P., 1991. Middle and Late Tertiary tectonic and physiographic developments, in: Trettin, H.P. (Ed.), *Geology of the Innuitian Orogen and Arctic Platform of Canada and Greenland*, Geological Survey of Canada, *Geology of Canada*. pp. 493–496.
- Trettin, H.P., Mayr, U., Long, D.G.F., Packard, J.J., 1991. Cambrian to Early Devonian basin development, sedimentation and volcanism, in: Trettin, H.P. (Ed.), *Geology of the Innuitian Orogen and Arctic Platform of Canada and Greenland*, Geological Survey of Canada, *Geology of Canada*. pp. 163–238.

Tuke, M.F., Dineley, D.L., Rust, B.R., 1966. The basal sedimentary rocks in Somerset Island, N.W.T. *Can. J. Earth Sci.* 3, 697–711.

Turner, E.C., 2011. Structural and stratigraphical controls on carbonate-hosted base metal mineralization in the Mesoproterozoic Borden Basin (Nanisivik District), Nunavut. *Econ. Geol.* 106, 1197-1223.

Turner, E.C., 2018. Neoproterozoic carbonate lithofacies and ore distribution at the Kipushi Cu-Zn deposit, Democratic Republic of Congo, and Gayna River Zn camp, Northwest Territories, Canada. *Econ. Geol.* 113, 779-788.

Turner, E.C., Dewing, K., 2004. Geology of Little Cornwallis Island and Rookery Creek (Cornwallis Island), Nunavut. *Geol. Surv. Can. Open File* 1780.

Turner, E.C., Kamber, B.S., 2012. Arctic Bay Formation, Borden Basin, Nunavut (Canada): Basin evolution, black shale, and dissolved metal systematics in the Mesoproterozoic ocean. *Precambrian Res.* 208–211, 1–18. <https://doi.org/10.1016/j.precamres.2012.03.006>

Turner, E.C., Long, D.G.F., Rainbird, R.H., Petrus, J.A., Rayner, N.M., 2016. Late Mesoproterozoic rifting in Arctic Canada during Rodinia assembly: impactogens, trans-continental far-field stress and zinc mineralisation. *Terra Nova* 28, 188–194. <https://doi.org/10.1111/ter.12207>

Wall, A.J., Mathur, R., Post, J.E., Heaney, P.J., 2011. Cu isotope fractionation during bornite dissolution: An in situ X-ray diffraction analysis. *Ore Geol. Rev.* 42, 62–70. <https://doi.org/10.1016/j.oregeorev.2011.01.001>

Ward, W.C., Halley, R.B., 1985. Dolomitization in a mixing zone of near-seawater composition, Late Pleistocene, northeastern Yucatan Peninsula. *J. Sediment. Petrol.* 55, 407–420.

Whiteside, L.S., Goble, R.J., 1986. Structural and compositional changes in copper sulfides during leaching and dissolution. *Can. Mineral.* 24, 247–258.

Wilkinson, J.J., Eyre, S.L., Boyce, A.J., 2005. Ore-forming processes in Irish-type carbonate-hosted Zn-Pb deposits: evidence from mineralogy, chemistry, and isotopic composition of sulfides at the Lisheen Mine. *Econ. Geol.* 100, 63–86.

Xiao, Z., Gammons, C.H., Williams-Jones, A.E., 1998. Experimental study of copper (I) chloride complexing in hydrothermal solutions at 40 to 300 C and saturated water vapor pressure. *Geochim. Cosmochim. Acta* 62, 2949–2964.

Yund, R.A., Kullerud, G., 1966. Thermal stability of assemblages in the Cu-Fe-S system. *J. Petrol.* 7, 454–488.

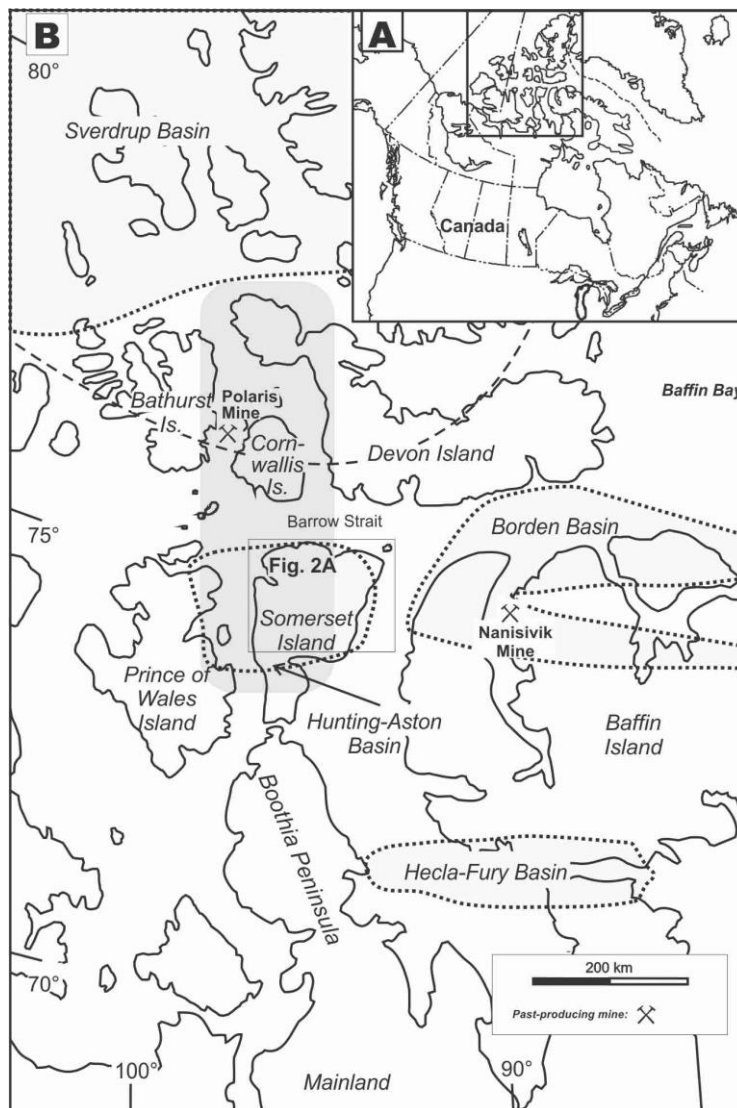


Figure 3-1: Study location

Figure 1. (A) General map of Canada and (B) the Arctic archipelago showing location of past-producing mines and the Cornwallis district (shaded), Mesoproterozoic basins (dotted lines), and the Ellesmerian orogenic front (dashed line).

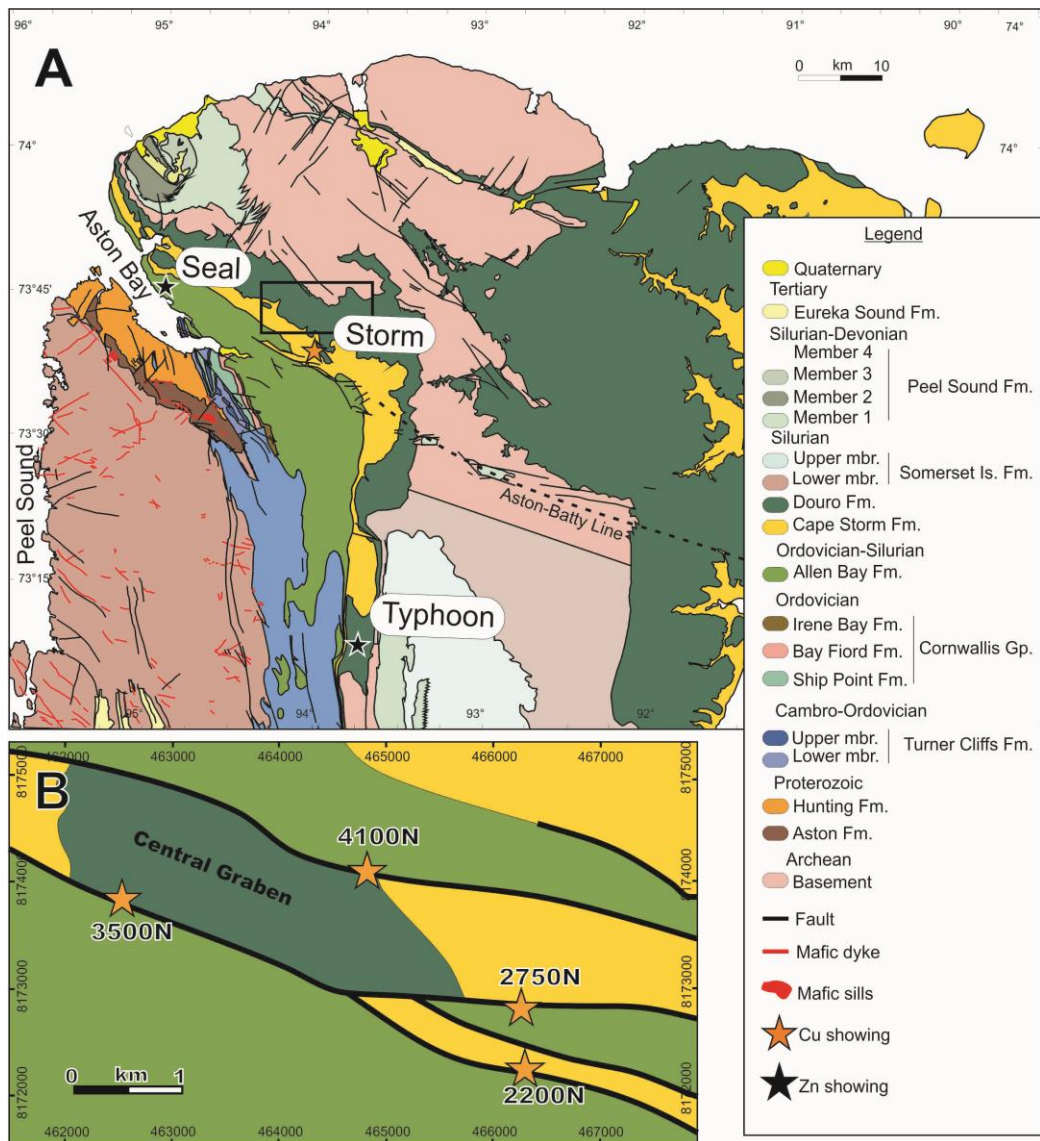


Figure 3-2: Geological map of Somerset Island

(A) Geology of Somerset Island (after Stewart and Kerr, 1984) shows base-metal showings on a northwest-trending fault zone that is parallel to regional Mesoproterozoic basin structures (Aston-Batty line; dashed line). (B) Local geology around the Storm showing shows the location of mineralised zones along normal faults. Samples used in this study are from 2750N, 3500N, and 4100N zones (NAD83, zone 15). Typhoon showing is the southernmost known showing in the Cornwallis district.

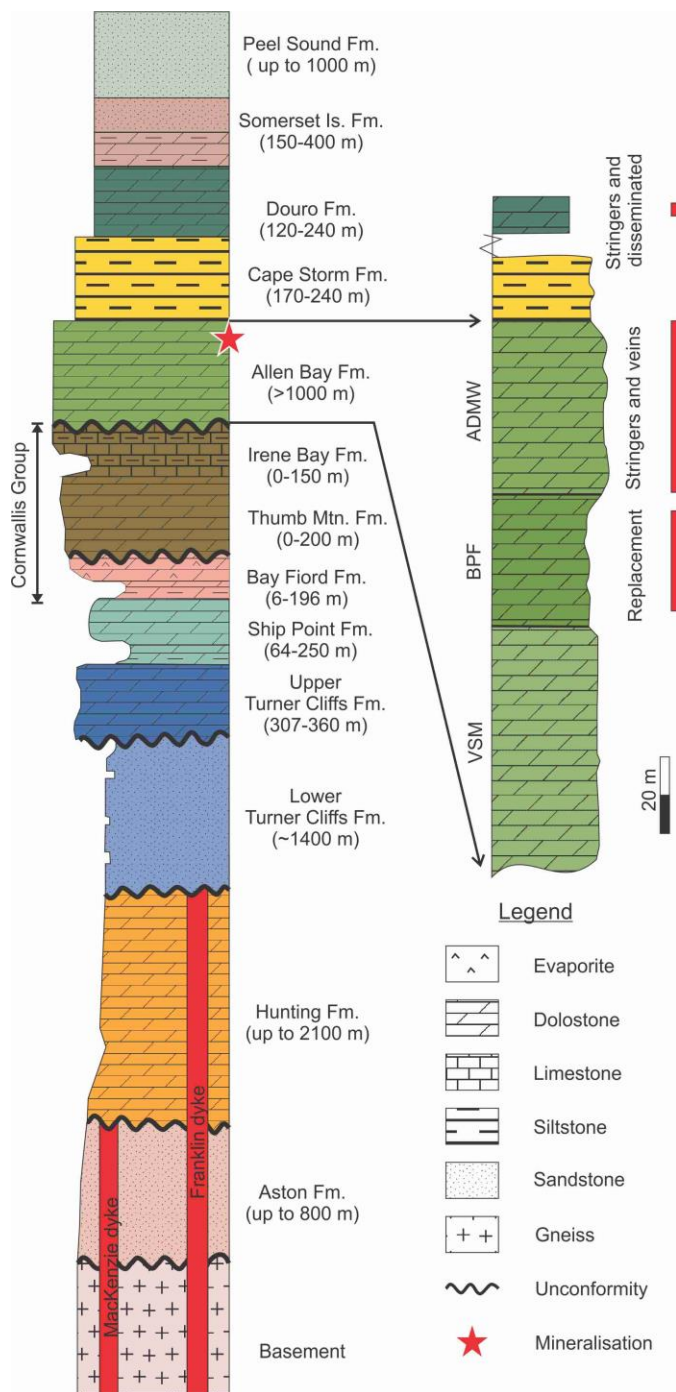
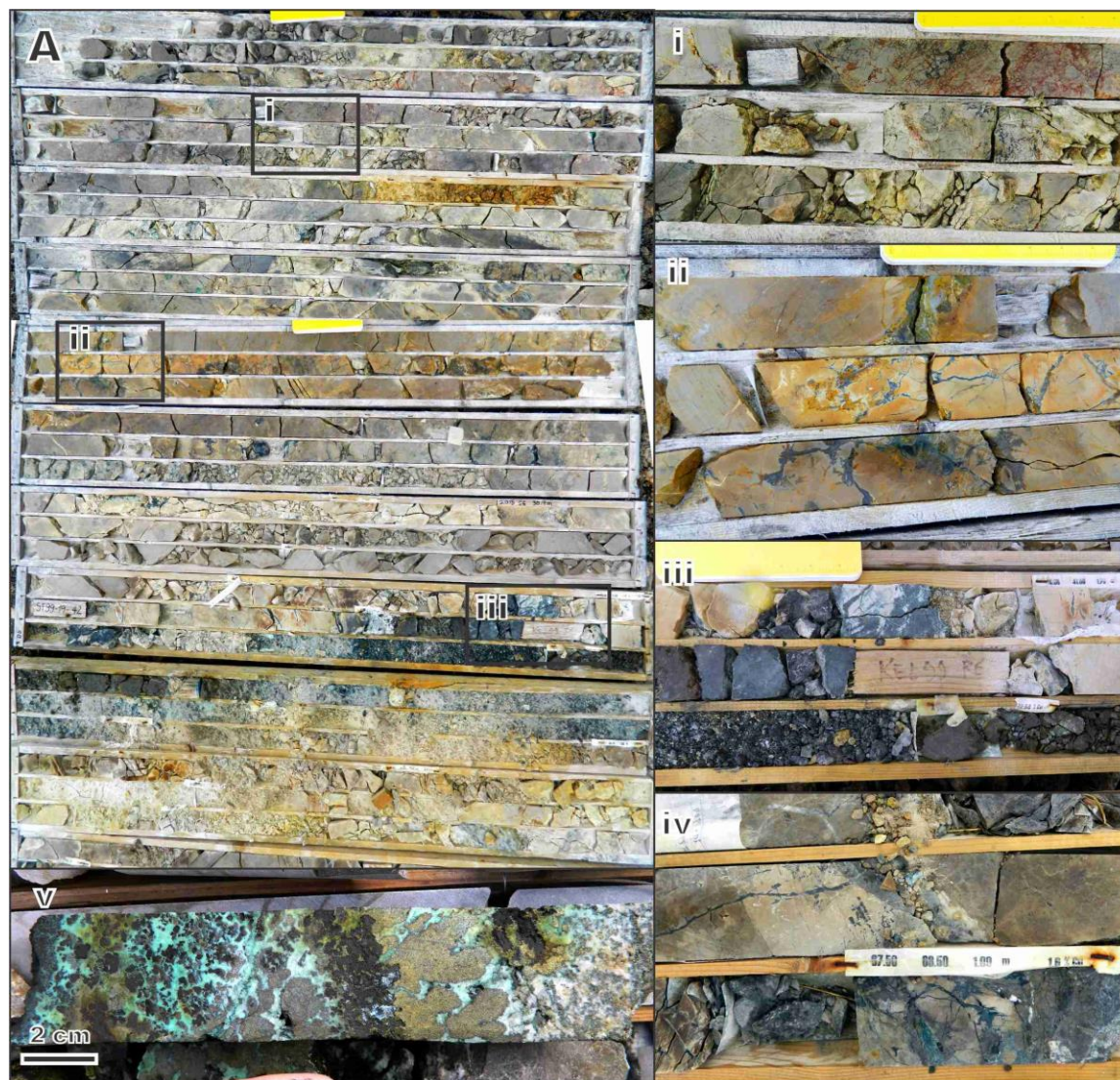


Figure 3-3: Simplified stratigraphy

. Simplified stratigraphic column of the geology at Storm (modified after Robinson and Atkinson, 2012). Enlargement of the Allen Bay Formation shows the stratigraphic location of mineralisation and informal members of the formation (ADMW – alternating dolomudstone and

dolowackestone; BPF – brown dolopackstone and dolofloatstone; VSM variable stromatoporoid).





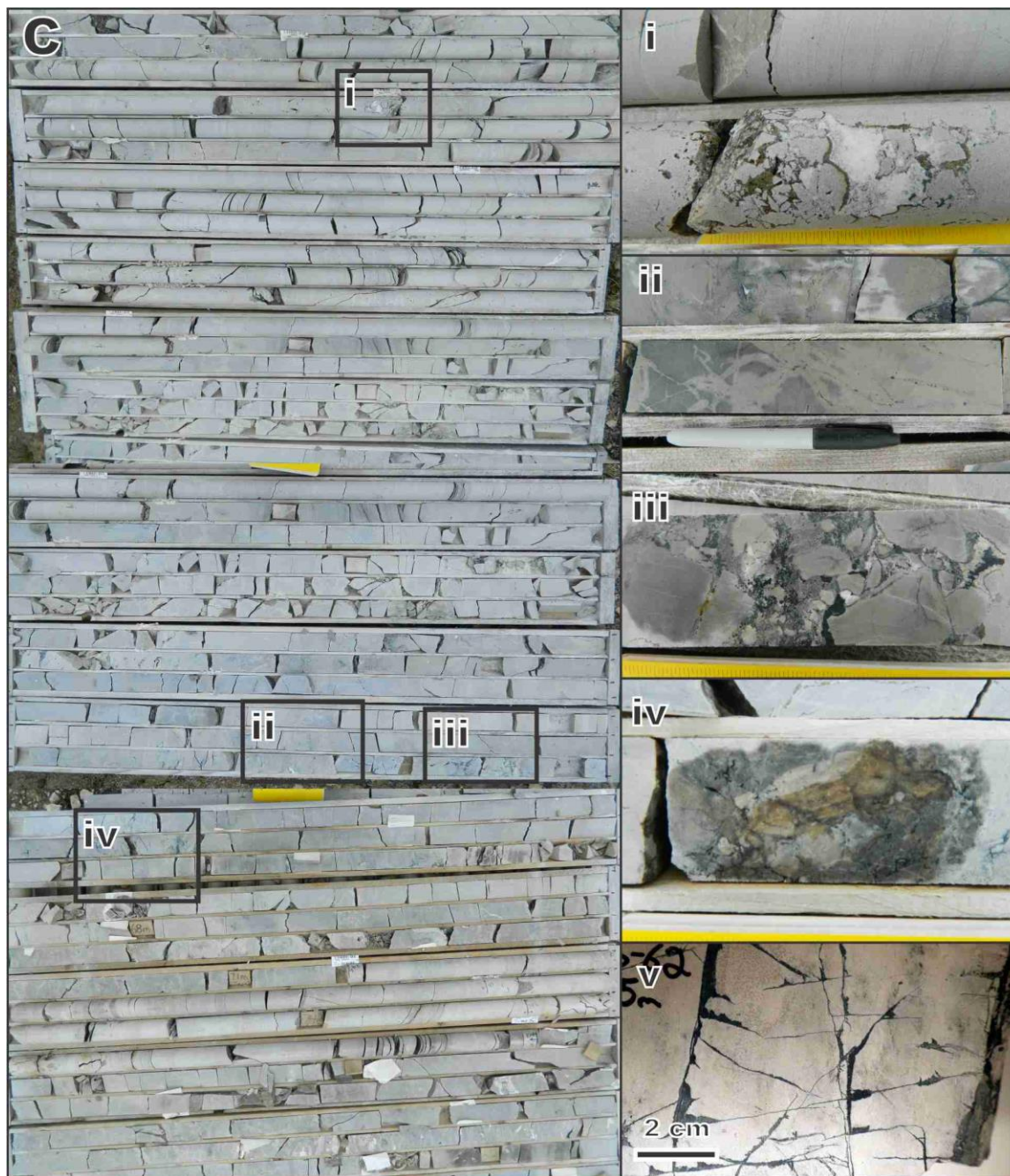


Figure 3-4: Representative Storm copper core photographs

Representative core photos show mineralisation textures from (A) 2750N, (B) 3500N, and (C) 4100N. (A) Mineralisation in brown dolopackstone and dolofloatstone (BPF) from 2750N: (i) chalcopyrite veinlets; (ii) geerite breccia mineralisation; (iii) carbonate replacement by geerite; (iv) dolostone alteration around mineralisation; (v) chalcopyrite mineralisation in the variable stromatoporoid member (VSM). (B) 3500N mineralisation in BPF and VSM: (i) carbonate

replacement by geerite in BPF; (ii), (iii), and (iv) breccia mineralization in VSM, by geerite later altered to atacamite, cuprite, and malachite. (C) 4100N mineralisation is typically hosted in the upper alternating dolomudstone and dolowackestone (ADMW): (i) veins and breccia with gangue and sulphide minerals commonly have mineralisation on one side of clasts/vein walls; (ii) alteration of dolostone along fractures near mineralised areas; (iii) and (iv) breccia-hosted mineralisation is primarily geerite; (v) veinlets of geerite in the overlying Cape Storm Formation.

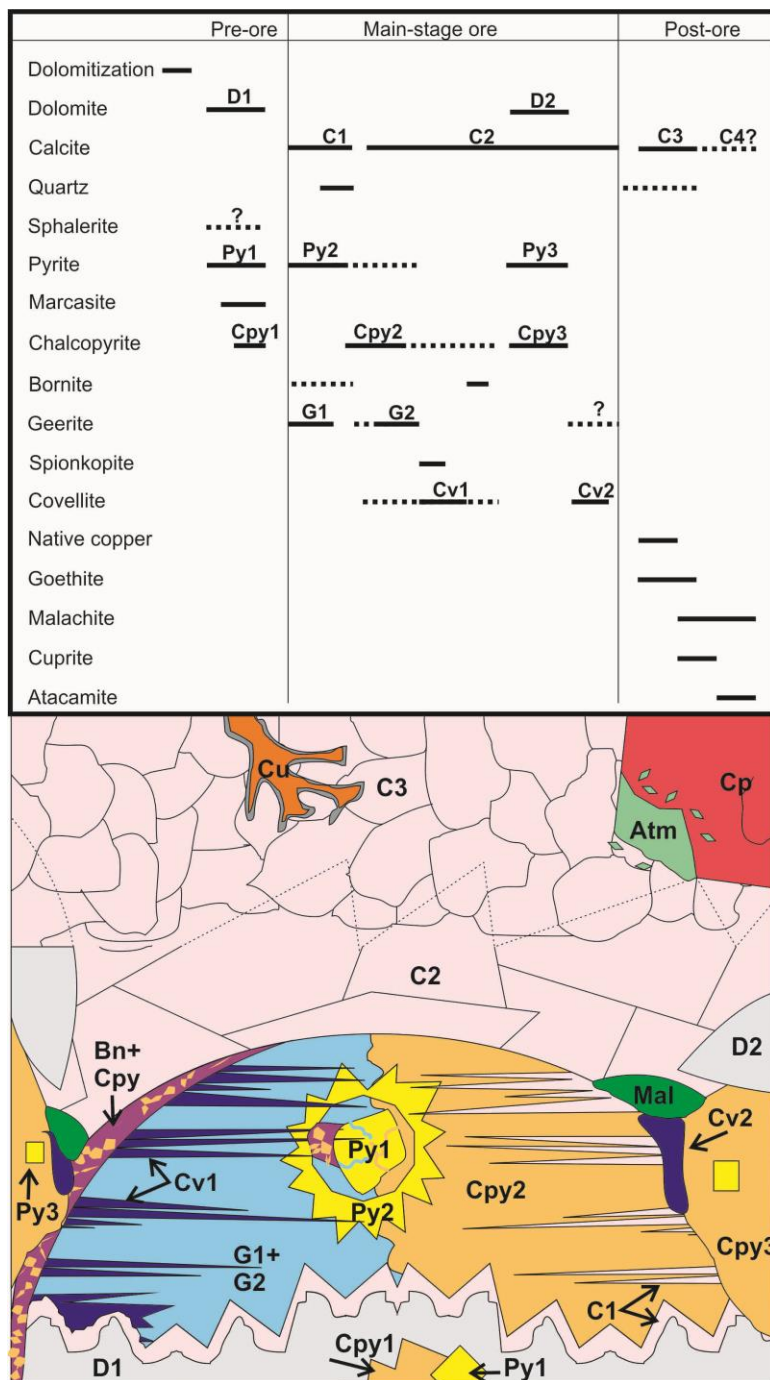
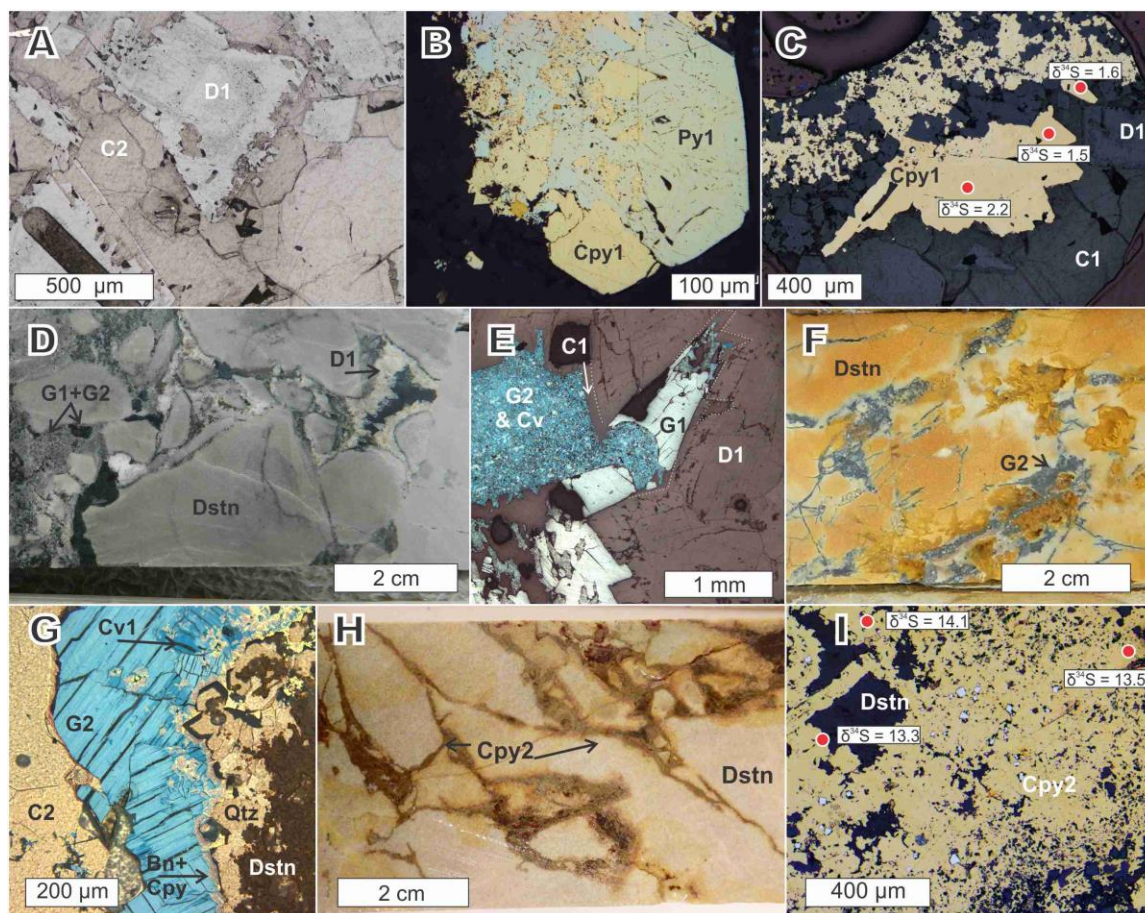


Figure 3-5: Simplified paragenetic diagram

Simplified paragenetic diagram for mineralisation at Storm copper. The relationship between geerite and chalcopyrite is inferred based on relative paragenetic timing with other minerals, and geochemistry.



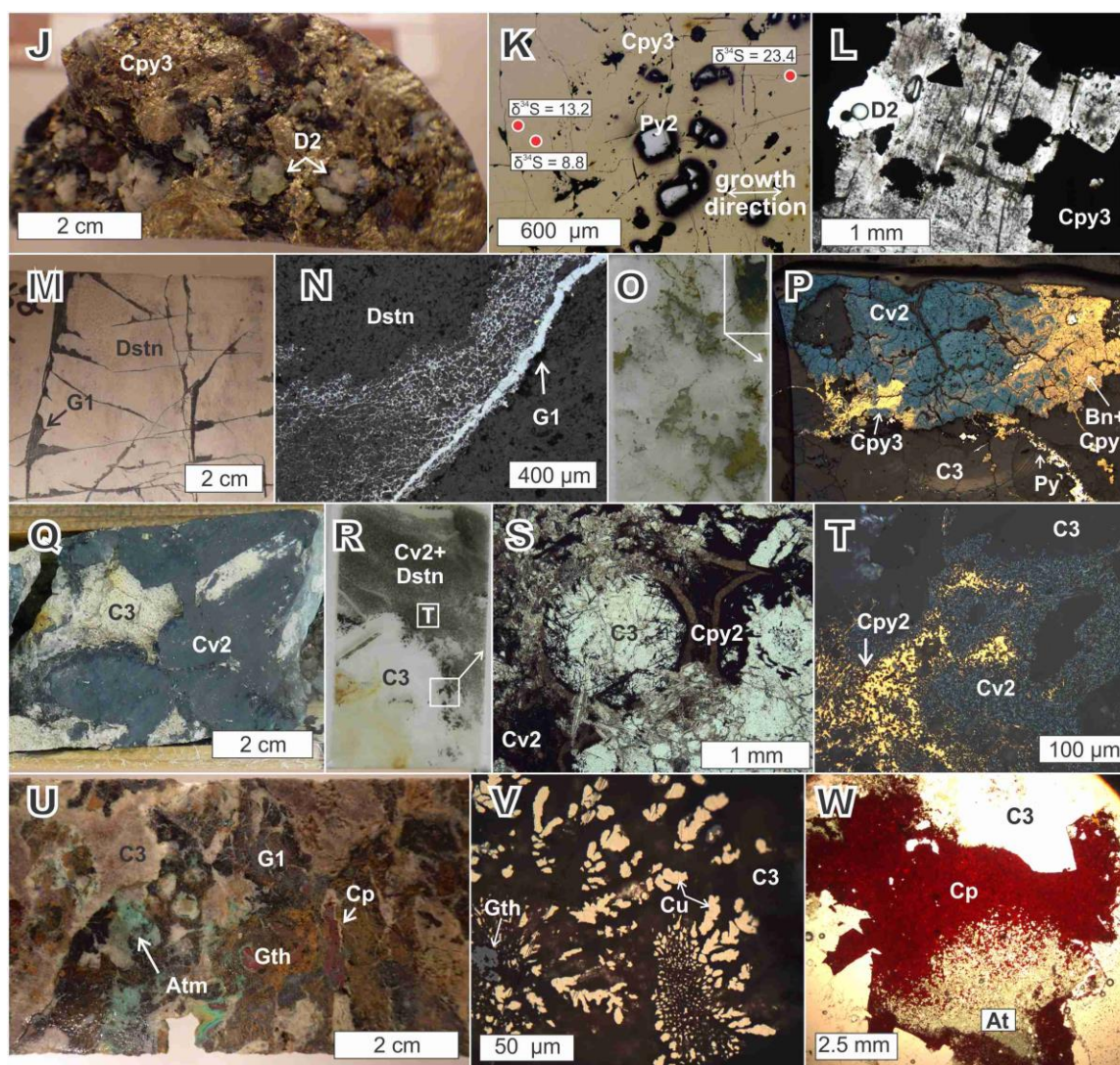


Figure 3-6: Storm mineralogy

Storm mineralogy. (A) Reflected-light (RL) image of primary dolomite (D1) replaced by calcite 2 (C2) with corroded edges (thin section). (B) RL image of pre-ore chalcopyrite 1 (Cpy1), pyrite 1 (Py1), and marcasite in a D1-cemented vein. (C) RL image of Cpy1, with locations of SIMS S isotope values (per mil). (D) Core photo of brecciated mineralisation at 4100N showing relationship between geerite (G1, G2) and D1. (E) RL image of G1 and G2 in (D) shows D1 replaced by C1 along its edges and G2 replaced/intergrown with covellite 1 (Cv1). (F) Core photo of G2 mineralisation from 2750N. (G) Combined RL and plane-polarised light (PPL) image of G2 replaced by Cv1, followed by bornite (Bn) forming a rim, and chalcopyrite. (H) Core image of breccia mineralisation of Cpy2. (I) RL image of Cpy 2 and the location of SIMS S

isotope values. (J) Core photo of massive Cpy3 with intergrown D2 cement. (K) RL image of Cpy3 replacing Py2 and location of SIMS isotope analyses. (L) PPL image of Cpy3 and intergrown D2 cement that has a high density of fluid inclusions. (M) Core image of carbonate replacement mineralisation along fractures by G1. (N) RL image of mineralisation in (M). (O) Thin section photo of mineralisation from 2750N shows the scale of localised alteration fronts. (P) RL image from area in (P) that shows bornite that was replaced by chalcopyrite2, which were both replaced by Cpy3, and later Cv2. (Q and R) Core and thin section of replacement Cv2 mineralisation. (S) PPL image from (R) of Cpy2 that was replaced by Cv2. (T) RL image of Cpy2 replaced by Cv2. (U) Core image of mineralisation at 3500N showing cuprite (Cp) and atacamite (Atm), which are apparently exclusive to this zone. (V) RL image of dendritic native Cu surrounded by C3 and goethite (Gth) from 3500N. (W) PPL image of cuprite (Cp) replaced by atacamite (At).

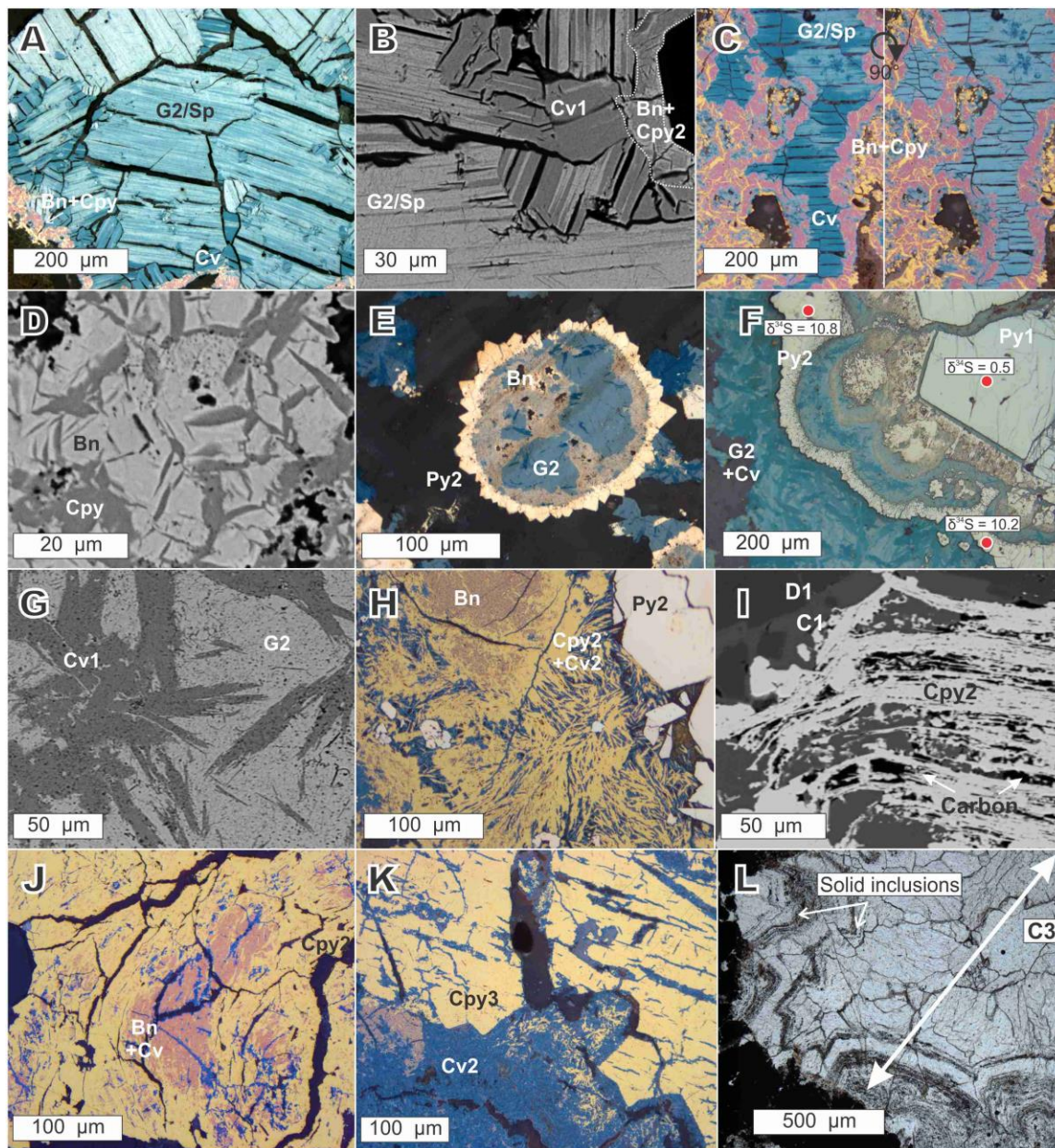


Figure 3-7: Storm mineral textures

Mineral textures. (A and B) RL image of intergrown gerite 2 (G2) and spionkopite (Sp) from 2750N replaced by Cv, and rimmed by bornite (Bn) that has exsolution-textured chalcopyrite replacement. The two images in C are the same but rotated 90° to show bireflectivity of Cv. (C) Back-scattered electron (BSE) image of relationship of G2 and Cv1. (D) BSE image of exsolution-textured chalcopyrite (Cpy) in bornite (Bn). (E) RL image of bornite replacement of G2 and Cv at 4100N that is limited to areas of pyrite dissolution. (F) Geerite 2 is intergrown with

pyrite 2 (Py2), which forms atoll-like structures around Py1. Spots indicate SIMS analyses for S, in permil relative to CDT. (G) BSE image of G2 and Cv1 from F. (H and I) RL and BSE images, respectively, of chalcopyrite 2 (Cpy2) exsolution texture and its intergrowth with C1 and amorphous carbon. (J) RL image of Cpy2 that replaced bornite and covellite and appears to grade into the exsolution-textured chalcopyrite. (K) RL image that shows Cv2 preferentially replacing bornite over Cpy3, and that remnant exsolution-textured chalcopyrite is locally preserved in covellite, after bornite replacement. (L) PPL image of the latest calcite cement (C3) that replaced a previous mineral and filled void space. The only indication of the previous mineral is its outline preserved as inclusions in C3. C3 (arrow) includes all transparent minerals in view.

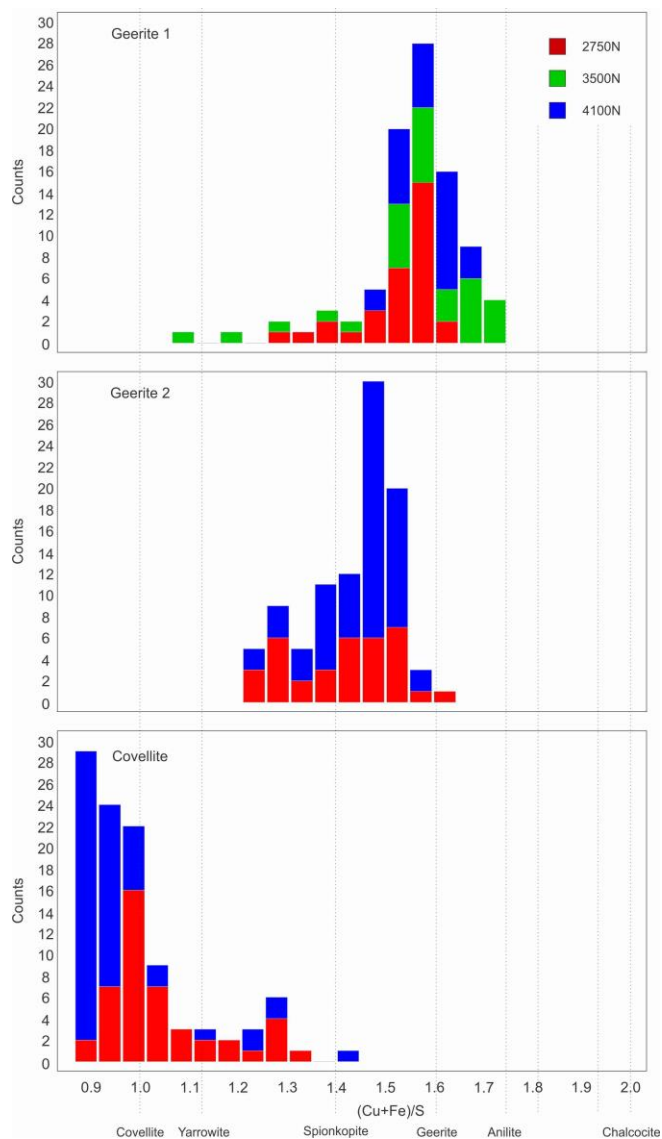


Figure 3-8: Storm Cu-sulphide composition

Composition of Cu-sulphides from three zones at Storm copper. (A) First generation of geerite has a mode of $\text{Cu}_{1.6}\text{S}$ for all three zones. (B) Second generation of geerite has noticeable decrease in Cu abundance to $\text{Cu}_{1.5}\text{S}$, but is still in the natural range reported by Goble and Robinson (1980). Geerite 2 is not present at 3500N. (C) Covellite chemistry from 2750N clusters at ideal CuS , whereas 4100N covellite is depleted to $\text{Cu}_{0.9}\text{S}$; no covellite is present at 3500N.

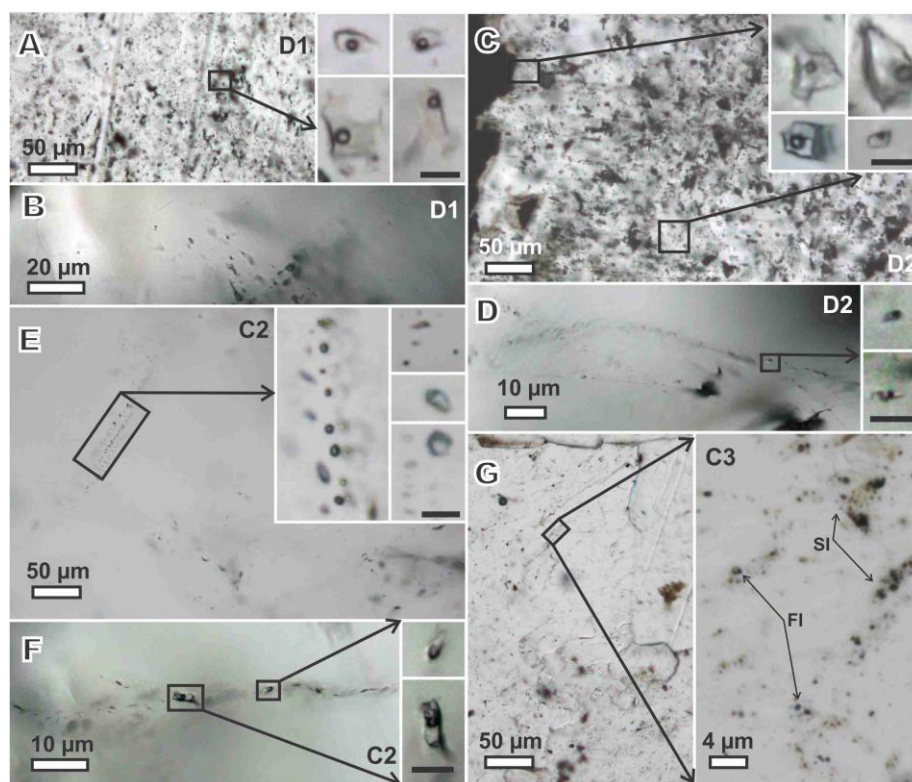


Figure 3-9: Storm fluid inclusion photomicrographs

Photomicrographs of fluid inclusions in dolomite (D) and calcite (C) cements; note the small inclusion size. (A) and (B) D1 cements densely populated by (A) primary and (B) secondary fluid inclusions with uniform L-V ratios (insets); vertical planes in (A) are crystallographic growth planes and insets are from different FIAs (not shown). (C) and (D) D2 cements nucleated on Cpy3 (left) densely populated by (C) primary and (D) secondary fluid inclusions along an arcuate fracture with consistent L-V ratios (inset). (E) C2 cement contains sparse fluid inclusions that are small or have variable L-V ratios. (F) Secondary fluid inclusions along a fracture in C2 cement are small, but have uniform L-V ratios. These inclusions cross growth planes in the calcite. (G) C3 cements with very small ($<1 \mu\text{m}$) primary fluid (FI) and solid (SI) inclusions whose size precludes microthermometric analysis. Scale bar in insets is $4 \mu\text{m}$.

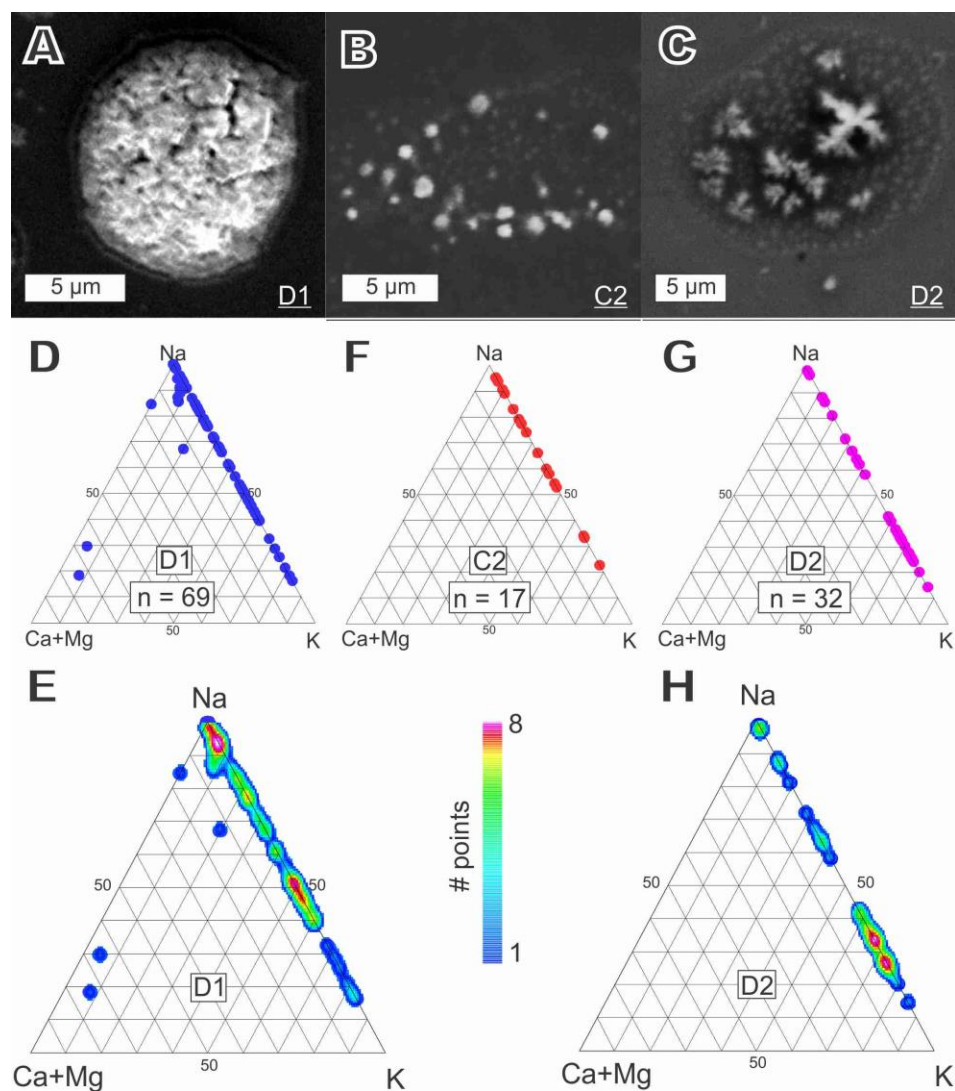


Figure 3-10: Evaporate mound images and composition

Evaporate mounds and their compositions. Back-scattered electron images of evaporate mounds showing morphologies (A = domical; B = anedral clusters; C = dendritic) that reflect their different compositions. Results of raster analysis of mounds are plotted on ternary diagrams in D, F, and G, whereas E and H are density plots of compositions from (D) and (G), respectively. The density plots indicate two compositional groups in D1, but only one in D2. D1- dolomite 1, C2 – calcite 2, D2 – dolomite 2.

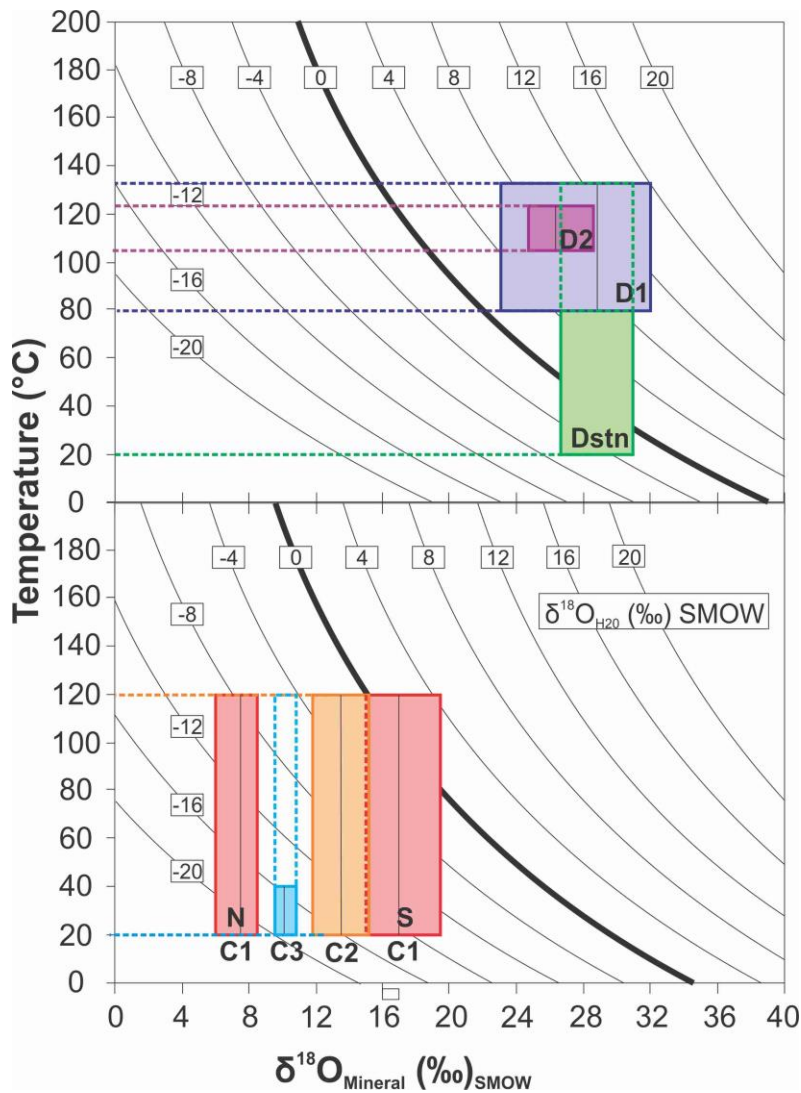


Figure 3-11: Oxygen isotope diagram

Oxygen isotope diagrams for the Allen Bay Formation and its cements show the range of possible $\delta^{18}\text{O}$ values of the precipitating fluids. Curved lines are isopleths calculated using Horita (2014) for dolomite-water and O'Neil et al. (1969) for calcite-water fractionation.

Homogenisation temperatures (T_h) and reasonable burial temperatures were used as temperature constraints. Heavy black lines represent average of measured isotope values of mineral. Dstn – Allen Bay Formation dolostone, D1 – dolomite 1, D2 – dolomite 2, C1 – calcite 1, C2 – calcite 2, C3 – calcite 3.

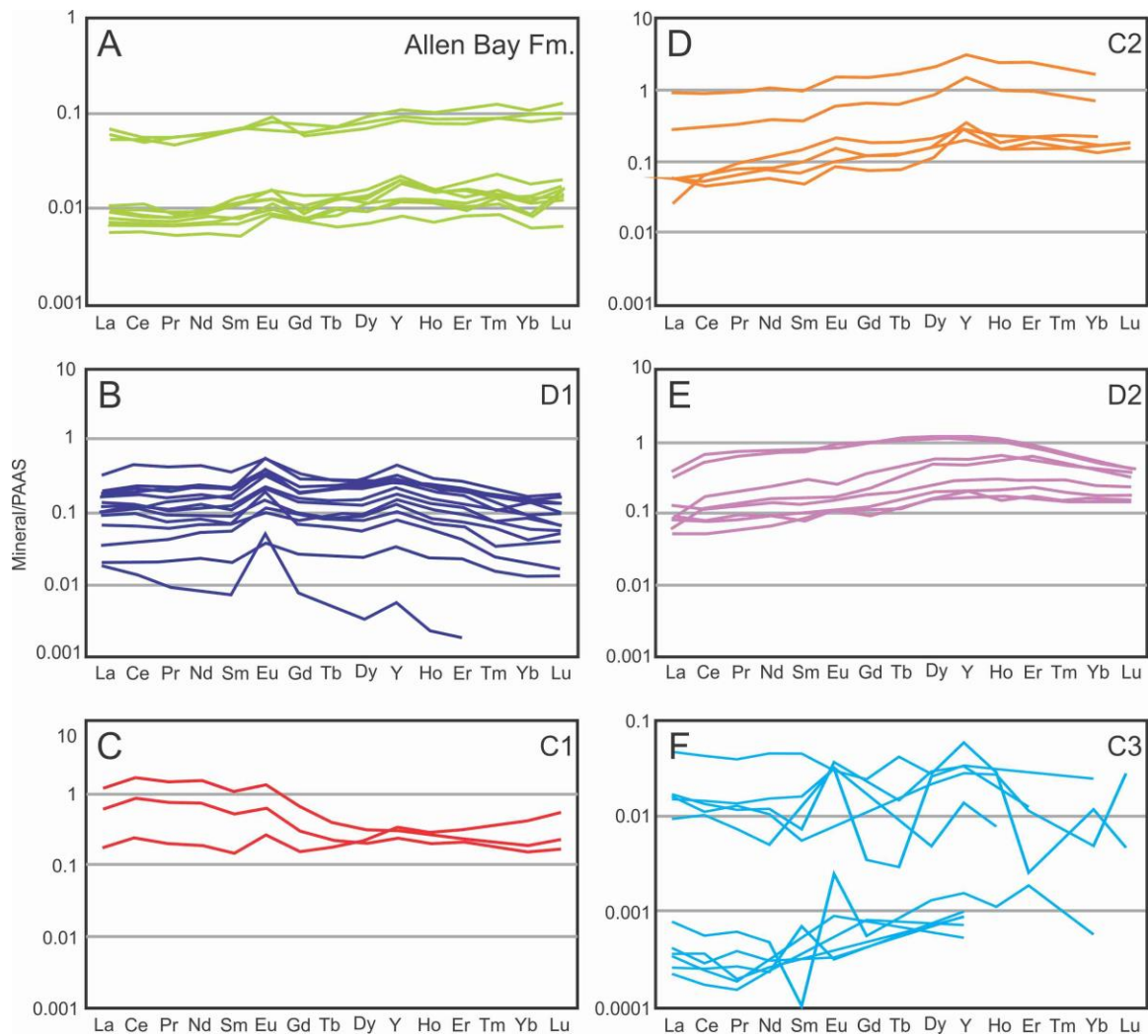


Figure 3-12: PAAS-normalised REE+Y diagram of carbonate gangue minerals

PAAS-normalised REEY diagrams for Allen Bay Formation, dolomite 1 (D1), calcite 1 (C1), calcite 2 (C2), dolomite 2 (D2), and calcite 3 (C3).

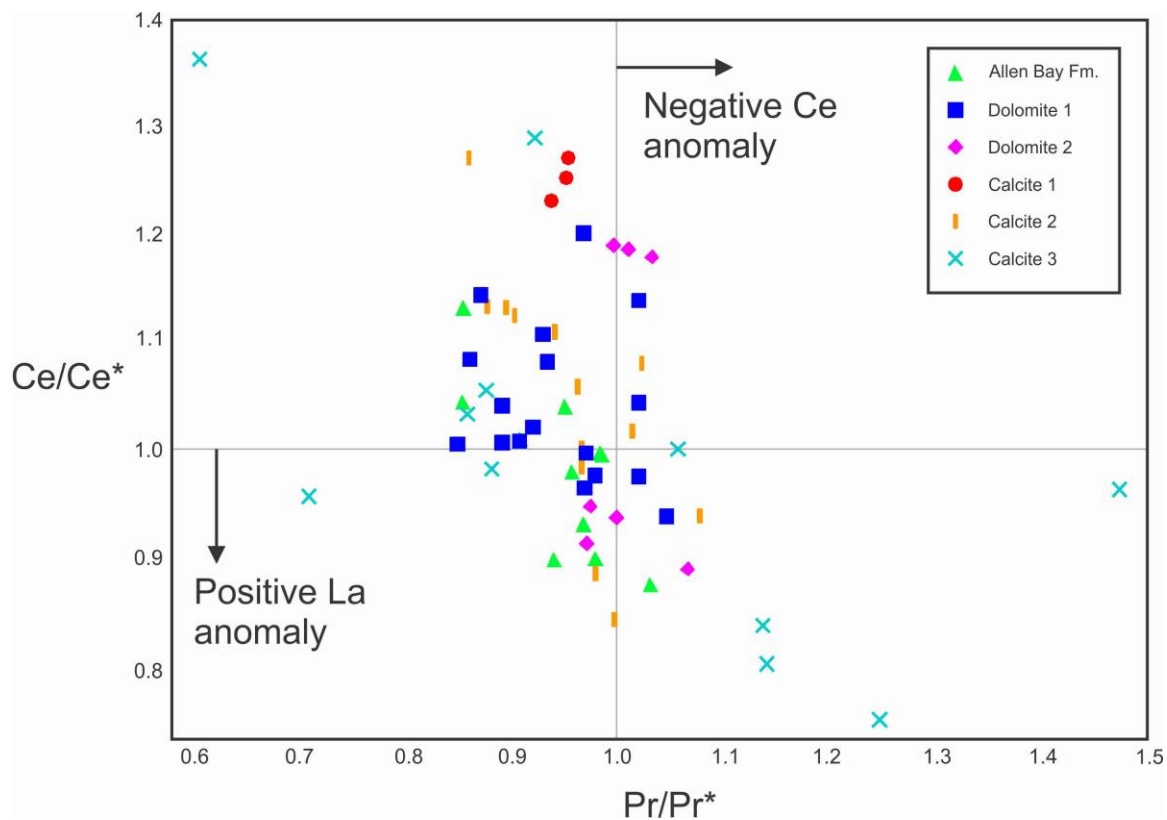


Figure 3-13: Anomaly discrimination diagram

A REEY discrimination diagram after Bau et al. (1997) used to verify La and Ce anomalies. The majority of samples have neutral or positive Ce and negative La anomalies, when normalised to PAAS (subscript SN). D1 – dolomite 1, C1 – calcite 1, C2 – calcite 2, D2, dolomite 2, C3 – calcite 3. $Ce^* = Ce / (0.5 * La_{SN} + 0.5 * Pr_{SN})$. $Pr^* = Pr / (0.5 * Ce_{SN} + 0.5 * Nd_{SN})$.

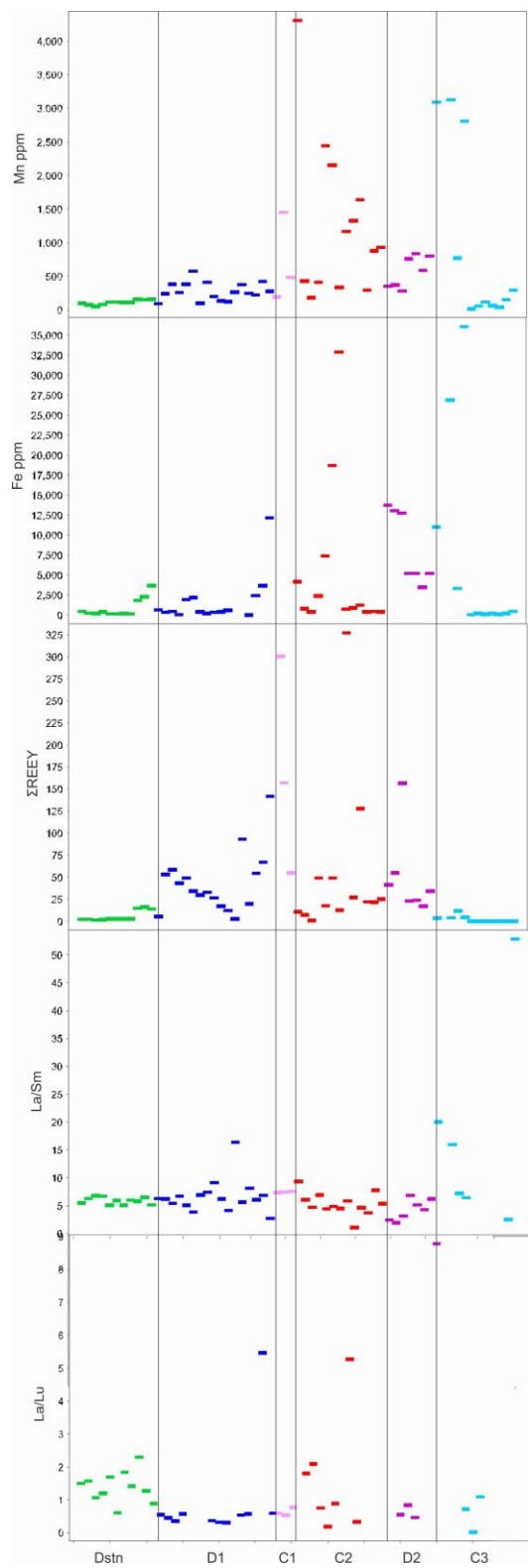


Figure 3-14: Trace element composition of carbonate gangue minerals

Summary diagram of trace element and REE chemistry of carbonate minerals through the paragenesis. Minerals are arranged in paragenetic order from left to right, with field size a function of data points, rather than time.

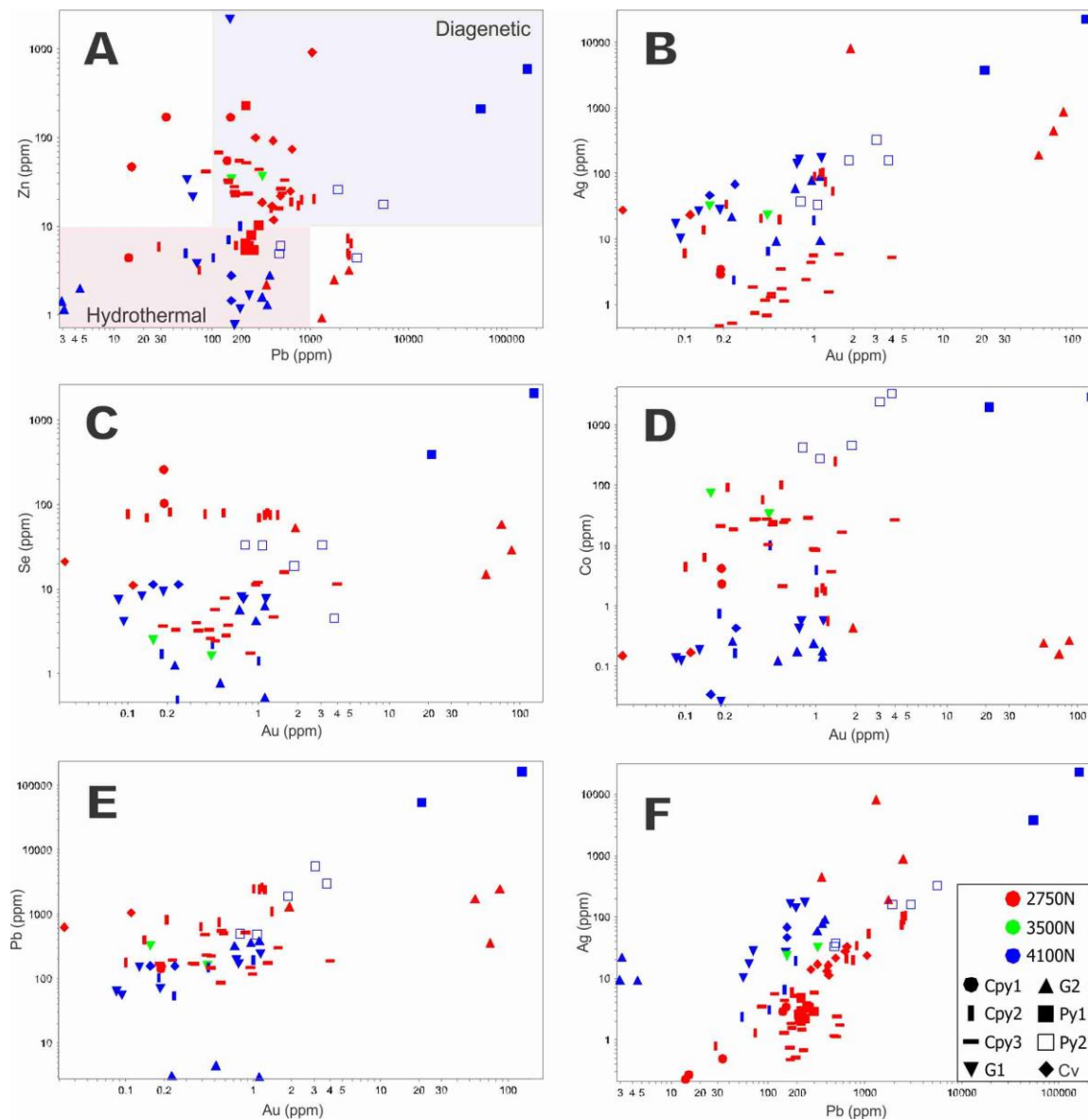


Figure 3-15: Sulphide trace element composition

Bivariate plots of sulphide trace element compositions. Shaded boxes in (A) indicate typical compositions of hydrothermal and diagenetic pyrite (Large et al. 2012, 2009).

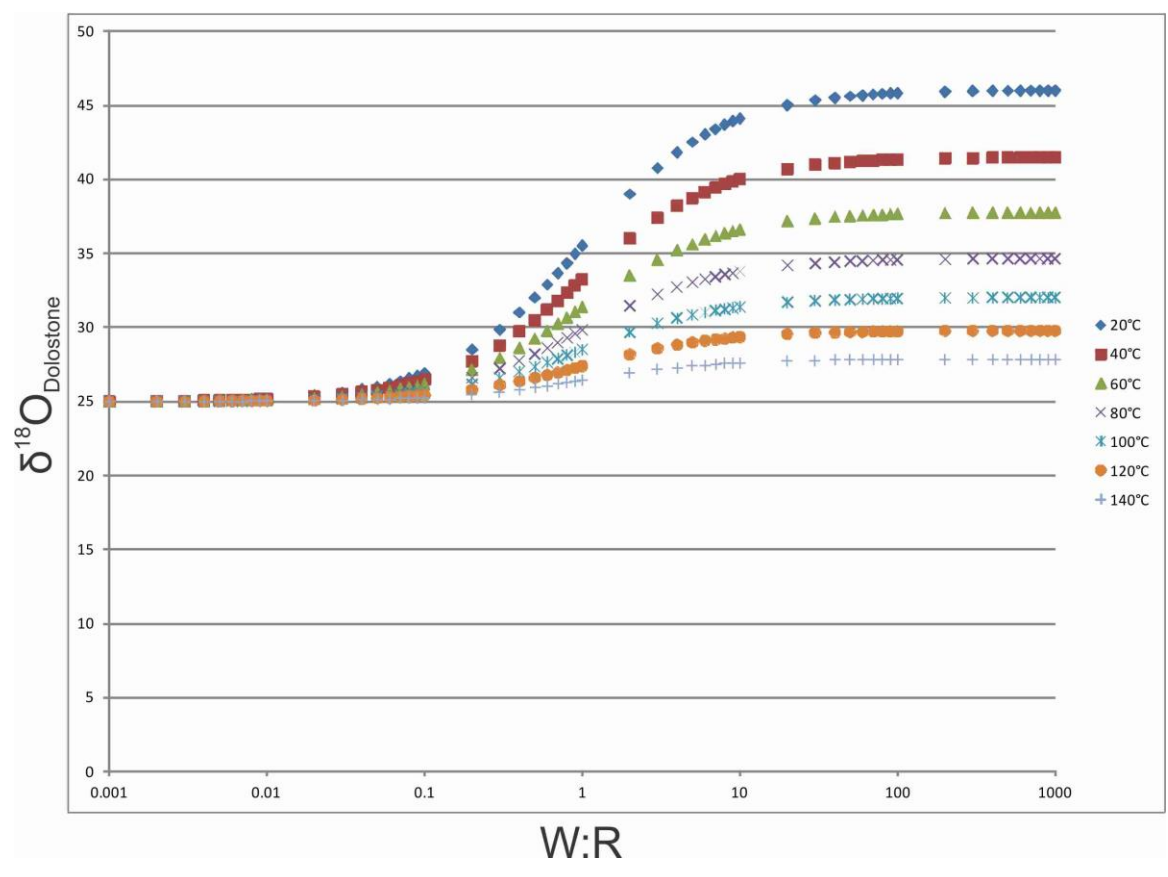


Figure 3-16: Water-rock ratio diagram

Water-rock ratio diagram showing results of calculations using equation of Taylor (1977). The lines show that, for an initial dolostone composition of 25‰, a fluid of the same composition and temperature as D1 (12‰ and ~100°C, respectively) requires a W:R of 2-20 to alter the dolostone to the measured 30‰ around veins.

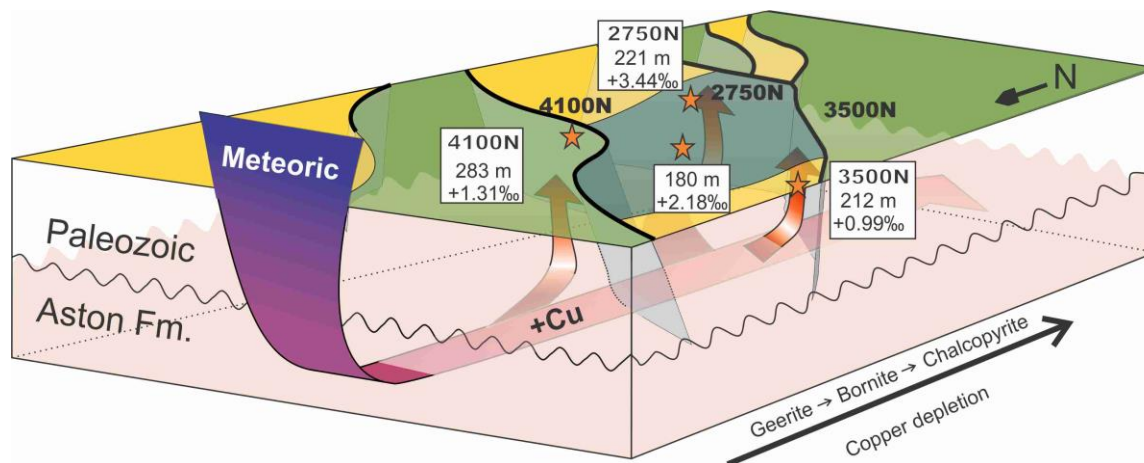


Figure 3-17: Mineralising fluid flow diagram for Storm

Mineralising fluid-flow for Storm was predominantly from the (present-day) north.

Mineralisation was facilitated by downward migration of meteoric water that originated in the north (4100N) and migrated through red-beds (Aston Formation) south and west towards 3500N and 2750N zones. Data in white boxes are $\delta^{65}\text{Cu}$ values of mineralisation (stars) at different elevations above present-day sea level. Copper minerals record progressive enrichment in $\delta^{65}\text{Cu}$ values along the fluid path and up faults.

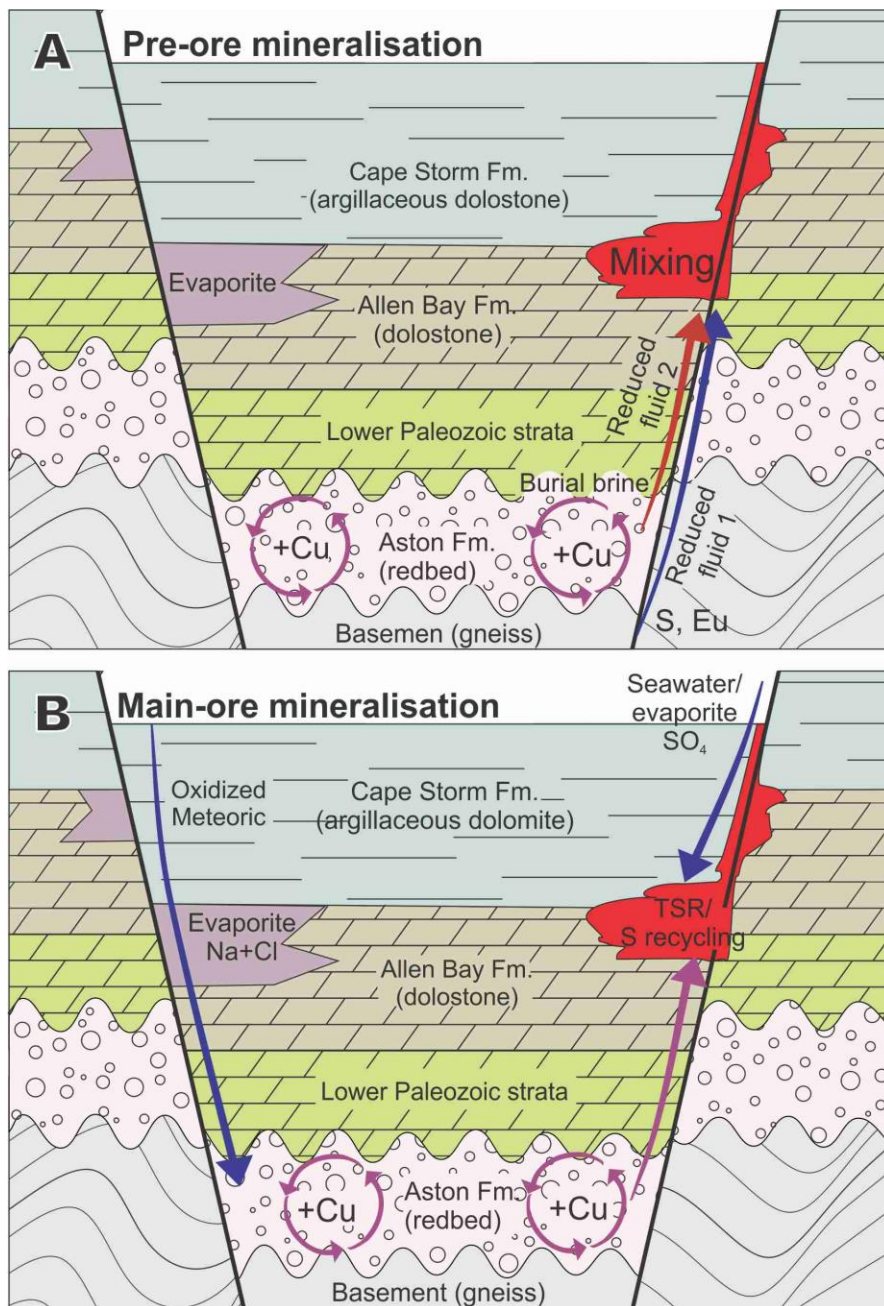


Figure 3-18: Mineralisation model for Storm

Mineralisation history of Storm. (A) Pre-ore mineralisation involved two reduced fluids that mixed on-site under the semi-impermeable, argillaceous Cape Storm Formation. Fluid 1 was basement-equilibrated and acquired magmatic-sourced S and Eu. Fluid 2 was a burial brine that leached Cu from Aston Formation red-beds (B) Main-stage ore resulted from prolonged oxidised meteoric fluid leaching of Cu from the underlying Aston Formation and transporting it up faults

to be reduced in a stratigraphic-structural trap by thermochemically reduced sulphate, organic matter, and/or diagenetic pyrite. Not to scale; no vertical scale implied.

Table 3-1: Microthermometric data for Storm

Microthermometric data for ore-related minerals at Storm.

FIA = fluid inclusion assemblage, FI = fluid inclusion, Avg = average, T_h = homogenisation temperature, T_m = ice-melting temperature

| Mineral | Stage | FIA# | # Fis | Range T_h | Avg T_h | range T_m | avg T_m | Salinity (wt. % NaCl equiv.) |
|----------|-------|------|-------|----------------|-----------|-----------------|-----------|---------------------------------------|
| Dolomite | D1 | 1 | 2 | 102- 106 | 104 | | | |
| | | 2 | 6 | 110- 130 | 117 | -13 | -13 | 16.9 |
| | | 3 | 12 | 76-104 | 83 | | | |
| | D2 | 1 | 7 | 105- 125 | 115 | | | |
| | | 2 | 7 | 97-130 | 107 | | | |
| Calcite | C2 | 1 | 8 | 102- 190* | 138 | -0.1 to -0.2 | -0.1 | 0.4 |

Table 3-2: Stable isotope data (SIMS) for Storm sulphides and carbonates

| Ore-stage | Sulfide | Stage | $\delta^{34}\text{S}_{\text{CDT}}$ (‰) | 1σ (‰) | Carbonate | Stage | $\delta^{18}\text{O}_{\text{v-SMOW}}$ (‰) | 1σ (‰) |
|-----------|--------------|-------|---|---------------|-----------|-------|--|------------------|
| Pre | Chalcopyrite | Cpy1 | 2.2 | 0.3 | Dolomite | Dstn | 31.6 | 1.2 |
| | Chalcopyrite | Cpy1 | 1.6 | 1.3 | Dolomite | D1 | 26.3 | 1.2 |
| | Chalcopyrite | Cpy1 | 1.5 | 2.3 | Dolomite | D1 | 23.8 | 1.2 |
| | Pyrite | Py1 | 0.8 | 0.3 | Dolomite | D1 | 28.1 | 1.2 |
| | Pyrite | Py1 | -1.4 | 0.3 | Dolomite | D1 | 30.5 | 1.2 |
| | Pyrite | Py1 | 6.9 | 0.3 | Dolomite | D1 | 29.2 | 1.2 |
| | Pyrite | Py1 | 0.9 | 0.3 | Dolomite | D1 | 29.0 | 1.2 |
| | Pyrite | Py1 | 0.5 | 0.3 | Dolomite | D1 | 31.2 | 1.2 |
| | Pyrite | Py1 | 2.4 | 0.3 | Dolomite | D1 | 29.1 | 1.2 |
| | | | | | Dolomite | D1 | 32.0 | 1.2 |
| Main | Chalcopyrite | Cpy2 | 10.0 | 0.3 | Calcite | C1 | 7.0 | 1.2 |
| | Chalcopyrite | Cpy2 | 13.3 | 0.3 | Calcite | C1 | 7.6 | 1.2 |
| | Chalcopyrite | Cpy2 | 13.5 | 0.3 | Calcite | C1 | 6.3 | 1.2 |
| | Chalcopyrite | Cpy2 | 8.7 | 0.3 | Calcite | C1 | 8.0 | 1.2 |
| | Pyrite | Py2 | 10.8 | 0.3 | Calcite | C1 | 8.6 | 1.2 |
| | Pyrite | Py2 | 10.2 | 0.3 | Calcite | C1 | 17.0 | 1.2 |
| | Pyrite | Py2 | 11.2 | 0.3 | Calcite | C1 | 19.4 | 1.2 |
| | Chalcopyrite | Cpy3 | 8.8 | 0.3 | Calcite | C1 | 18.7 | 1.2 |
| | Chalcopyrite | Cpy3 | 23.4 | 0.3 | Calcite | C1 | 14.8 | 1.2 |
| | Chalcopyrite | Cpy3 | 22.2 | 0.3 | Calcite | C1 | 16.6 | 1.2 |
| | Chalcopyrite | Cpy3 | 13.2 | 0.3 | Calcite | C2 | 13.4 | 1.2 |
| | Pyrite | Py3 | 17.7 | 0.3 | Calcite | C2 | 15.3 | 1.2 |

| | | | | |
|------|----------|----|------|-----|
| | Calcite | C2 | 12.0 | 1.2 |
| | Dolomite | D2 | 24.3 | 1.2 |
| | Dolomite | D2 | 26.0 | 1.2 |
| | Dolomite | D2 | 28.5 | 1.2 |
| | Dolomite | D2 | 25.3 | 1.2 |
| | Dolomite | D2 | 30.0 | 1.2 |
| | Dolomite | D2 | 29.3 | 1.2 |
| Post | Calcite | C3 | 10.7 | 1.2 |
| | Calcite | C3 | 9.7 | 1.2 |
| | Calcite | C3 | 10.2 | 1.2 |
| | Calcite | C3 | 10.7 | 1.2 |
| | Calcite | C3 | 9.9 | 1.2 |
| | Calcite | C3 | 9.8 | 1.2 |
| | Calcite | C3 | 9.8 | 1.2 |

Table 3-3: Copper isotope measurements from Cu minerals from 2750N, 3500N, and 4100N, at different depths.

| 2750N | | | | |
|-----------|---------------------------|--------------|-------|----------------------------------|
| Down hole | Elevation above sea level | Mineral | Stage | $\delta^{65}\text{Cu}$ (per mil) |
| Float | | Geerite | G1 | 0.01 |
| Float | | Bornite | Bn | 0.02 |
| Float | | Malachite | Mal | -0.33 |
| 25 m | 221 | Chalcopyrite | Cpy2 | 3.44 |
| 42 m | 208 | Chalcopyrite | Cpy2 | 0.88 |
| 62 m | 194 | Chalcopyrite | CPy1 | -0.07 |
| 78 m | 180 | Chalcopyrite | Cpy2 | 2.18 |
| 29 m | 158 | Chalcopyrite | Cpy3 | 0.14 |
| 29 m | 158 | Covellite | Cv2 | 1.31 |
| 102 m | 153 | Chalcopyrite | Cpy3 | 0.18 |
| 4100N | | | | |
| Down hole | Elevation above sea level | Mineral | Stage | $\delta^{65}\text{Cu}$ (per mil) |
| 12 m | 294 | Geerite | G1 | 0.43 |
| 24 m | 283 | Chalcopyrite | Cpy2 | 1.31 |
| 62 m | 243 | Geerite | G1 | -0.1 |
| 81 m | 214 | Native Cu | Cu | 0.04 |
| 3500N | | | | |

| Down hole | Elevation above sea level | Mineral | Stage | $\delta^{65}\text{Cu}$ (per mil) |
|-----------|---------------------------|--------------|-------|----------------------------------|
| float | | Geerite | G1 | 0.01 |
| 9 m | 212 | Chalcopyrite | Cpy2 | 0.99 |
| 16 m | 209 | Geerite | G1 | 0.05 |
| 33 m | 197 | Native Cu | Cu | 0.22 |
| 33 m | 197 | Malachite | Mal | 0.78 |
| 33 m | 197 | Cuprite | Cp | 0.09 |
| 33 m | 197 | Geerite | G1 | -0.17 |
| 65 m | 175 | Geerite | G1 | -0.06 |

Table 3-4: Summary of averaged geochemical data for different mineralisation stages.

| Stage | T _h (°C) | Salinity (wt. % NaCl equiv.) | δ ¹⁸ O _{SMOW} (‰) | δ ³⁴ S _{CDT} (‰) | δ ⁶⁵ Cu _{NIST} (‰) | Fluid redox | Fluid composition | Interpretation |
|----------------|---------------------|---------------------------------------|--|---|---|----------------|----------------------|---|
| pre- ore | 101 | 17 | 28.8 | 1.7 | 0.1 | reduced | Na & Na+K | Mixing of reduced basin-derived fluids |
| main ore I | 102- 190 | 0.4 | 13.5 | 11.1 | 1.8 | oxidised | Na- dominant | Low-latitude meteoric water dissolved evaporites and leached Cu from red bed |
| main ore II | 111 | moderate | 27.2 | 16.9 | 0.1 | reduced | Na+K- dominant | Mixing of basin-derived fluids |
| post- ore | <30* | low | 10 | NA | NA | oxidised | NA | High-latitude meteoric fluid |

Chapter 4

4 Diagenetic evaluation of a possible red-bed source for anomalous Cu in the Paleozoic-carbonate-hosted Cornwallis Zn-Pb district, NU

Mathieu, J. and Turner, E.C.

Abstract

The Mesoproterozoic Aston Formation on Kuuganajup Nunanga (Somerset Island), Canada, is a red sandstone situated stratigraphically below the Storm copper deposit, an anomalous Cu deposit in the Paleozoic-carbonate-hosted Cornwallis Zn-Pb district. It experienced a history of successive burial and exhumation episodes, reaching a maximum burial (>3 km) by the onset of the Devonian Ellesmerian orogeny, and a series of mostly Paleozoic fluid migrations. A petrographic and in situ SIMS oxygen isotope study was undertaken to identify diagenetic events and their relative timing in order to assess the possibility that this redbed unit was the Cu source of the Storm Cu deposit. Most framework grains in the sandstone are fractured quartz with long, concavo-convex grain contacts, of which some are sutured (pressure-solved); the characteristics of these contacts and the paragenesis of associated mineral phases outlines the diagenetic history of the sandstone. Two episodes of hematite precipitation (early and late) are indicated by patterns in the distribution of 1-100 μm -thick hematite coatings on quartz clasts: hematite coatings are present on all surfaces of some grains, including pressure-solved contacts, whereas other sutured grains lack hematite along sutured contacts but are otherwise completely veneered with hematite. Mafic grains, which would be expected in this material based on nearby exposed gneissic basement, are now absent, and may have reacted to supply the iron involved in hematite precipitation. Quartz cement that precipitated after the late hematite yields an average $\delta^{18}\text{O}$ value of 14.4‰ (SMOW). Calculated $\delta^{18}\text{O}_{\text{H}_2\text{O}}$ values indicate that this quartz was probably precipitated by a warm (100° to 130°C), externally derived, low- to mid-latitude (20-30°N), oxidised meteoric fluid during the Carboniferous, after maximum burial conditions, and was probably associated with the late hematite coatings. This relationship indicates that porosity and permeability were sufficient for the circulation of fluids in the Paleozoic, including possible mineralising fluids during the Carboniferous. The sandstone was bleached by a more reduced

fluid prior to (near-) maximum burial, indicated by the absence of hematite at pressure-solved grain contacts and secondarily reddened by the circulation of oxidised Carboniferous meteoric fluid. This sequence is similar to documented fluid types responsible for the overlying Storm copper deposit. The oxidised fluids responsible for the late reddening of the Aston Formation sandstone have characteristics that are compatible with their acting as a metal source for the regionally anomalous Storm copper deposit.

4.1 INTRODUCTION

Stratiform copper deposits are the second-most-important source of Cu globally after porphyry Cu, and contribute ~11% of Cu globally (Mudd and Jowitt, 2018). Red terrigenous strata near these deposits are typically the inferred metal source for these deposits (Haynes, 1986; Everett et al., 2003; Hitzman et al., 2005; Brown, 2005, 2009). It is understood that the sediment was not originally red when deposited, but instead that the colour is a diagenetic product produced when mafic and other labile minerals in the sediment were exposed to oxidised fluids (Zielinski et al., 1983; Walker, 1989; Brown, 2009), liberating iron that then precipitated as a ferric iron coating (cement) around sedimentary particles. This process gradually reddens sediment over perhaps several millions of years, as has been demonstrated in Cenozoic strata in the western USA (Zielinski et al., 1983; Walker 1989). The importance of the reddening process in the context of stratiform Cu deposits is that the oxidised fluid mobilises iron, copper, and other metals from the mafic minerals. The iron is reprecipitated as Fe-oxide, such as goethite or limonite, which can easily adsorb the other leached metals. During later fluid circulation, the adsorbed metals can be liberated, transported to more reducing areas, and precipitated as sedimentary-rock-hosted Cu deposits.

Originally, it was thought that redbeds controlled the redox conditions of a circulating mineralised fluid, but Eh-pH conditions are not necessarily adequate for Cu to be in solution

based only on the stability and presence of hematite (Brown, 2009). The Eh-pH and salinity conditions required to liberate Cu and other metals from mafic minerals, and at the same time to precipitate iron hydroxides (limonite/goethite) must be moderately oxidised, slightly acidic to neutral, and saline (Brown 2009). The oxidised sediment that results from the reddening process allows for prolonged or subsequent oxidised fluid(s) to migrate through them and broaden the extent of oxidised conditions, thus gradually reddening a sediment body. Brown (2009) and Zielinski et al. (1983) demonstrated that large amounts of Cu (and other metals) can be liberated from and transported away from a source sedimentary rock by the reddening process, and that unreasonably large volumes of red-bed sandstone are not required, as once thought (Hitzman et al., 2005).

Although a (moderately) saline, chloride-dominated fluid is accepted as the copper-mobilising fluid in redbed Cu deposits (e.g., Hitzman et al., 2005), the source of this fluid is not agreed upon (Brown, 2005; 2009). The most favourable fluid type for dissolving Cu in an Fe-OH system is a slightly acidic, atmosphere-equilibrated fluid (i.e., meteoric water; Rose, 1976; Brown, 2005; 2009).

Another common diagenetic change associated with sedimentary-rock-hosted ore deposits is bleaching (Wahab, 1998; Beitler et al., 2005; Hitzman et al., 2005; Wilkinson et al., 2005; Gorenc and Chang, 2015). Bleaching of sandstone can occur during hydrocarbon migration, which dissolves hematite and precipitates the iron as pyrite (Surdam et al., 1993; Garden et al., 2001; Rainoldi et al., 2014). The removal of hematite and associated metals changes the rock colour from red to grey or white (Everett et al., 2003; Hitzman et al., 2005; Macintyre, 2006; Rainoldi et al., 2014). The timing of diagenetic events in possible source rock(s), particularly

cementation, reddening, and bleaching, are therefore important in evaluating the possible metal source(s) of sedimentary-rock-hosted base-metal deposits.

Strata of Canada's Arctic archipelago contain numerous mineralised areas (Dewing et al., 2007a), including two past-producing mines (Polaris and Nanisivik Zn-Pb deposits). The Cornwallis district in Canada's Arctic archipelago (Fig. 1) includes more than 80 carbonate-hosted mineralised showings, including the past-producing Polaris Zn-Pb deposit (Kerr, 1977b; Randell and Anderson, 1996; Randell et al., 1996; Savard et al., 2000; Dewing et al., 2007b; Reid et al., 2013a,b). The southernmost part of the Cornwallis district, on Kuuganajup Nunanga (Somerset Island), includes an anomalous carbonate-rock-hosted copper deposit (Storm copper; Dewing et al., 2007b; Mathieu et al., 2018). The Storm copper deposit is hosted by Ordovician-Silurian age dolostone of the Allen Bay Formation, which is situated stratigraphically between underlying Proterozoic red sandstone (Aston Formation) and overlying Silurian-Devonian red sandstone (Peel Sound Formation). An integrated geochemical study of the deposit (Mathieu et al., 2018) determined that the mineralising fluid was a south-migrating, meteoric-derived fluid that interacted with sedimentary rocks and deposited the main ore stage during the late Devonian-Carboniferous, and that the Aston Formation may have been the metal source.

Most studies of sedimentary-rock-hosted ore deposits and districts focus on ore and alteration in the immediate vicinity of ore, but the prerequisites required for the formation of ore deposits involve large geographic areas and substantial stratigraphic successions, of which the relevant characteristics are commonly merely assumed. In many sedimentary-rock-hosted ore districts, the presumed source rocks are unexposed, or too fine-grained to harbour evidence of the type of diagenesis or subtle alteration that would result from the passage of metal-scavenging fluids. In some cases, the characteristics of metal source-rocks and of the aquifers through which

mineralising fluids migrate can be crudely deciphered using geochemical approaches focussed on ore and gangue minerals (e.g., Goldhaber et al., 1995; Wilde et al., 2006; Everett et al., 2003; Garcia-Alonso et al., 2011; Debruyne et al., 2016), without approaching the putative source or aquifer material. Diagenetic studies focussed specifically on presumed source rocks in base-metal districts are relatively few (e.g., Hiatt et al., 2003; Beyer et al., 2011; Tornos and Heinrich, 2008; Simbo et al., 2019; Everett et al., 2003; Rajabour et al., 2017; Bonnetti et al., 2015; Polito et al., 2006), yet the presumed source of metals in redbed copper deposits is coarse-grained terrigenous clastic strata (Hitzman et al., 2005) that could readily lend themselves to diagenetic study using simple techniques. Deciphering the diagenetic history of suspected source rocks could add substantially to the understanding of both individual deposits and whole districts by highlighting the types and timing of fluid events that affected source rocks through time, as reflected in mineral precipitation and dissolution episodes, and the evolution of porosity-permeability relationships through time.

This petrographic and isotopic study addresses Aston Formation red and grey sandstones to (1) outline the diagenetic events and burial history of this formation; (2) characterise the succession of diagenetic fluids; (3) compare the fluid history recorded in the Aston Formation with the fluid history at Storm copper; and (4) determine whether the Aston Formation may have contributed metals to mineralising fluids responsible for the Storm copper deposit.

4.2 GEOLOGICAL BACKGROUND

A collection of Mesoproterozoic basins in the Canadian Arctic archipelago are termed the Bylot basins (Fig. 1) and include the Borden (Baffin and Devon islands), Fury and Hecla (Baffin

Island), Thule (Greenland and Ellesmere islands), and Hunting-Aston (Somerset and Prince of Wales islands) basins (Jackson and Iannelli, 1981), although Mayr et al. (2004) suggested that the Hunting-Aston basin may be older. Jackson and Iannelli (1981) concluded that these basins were aulacogens associated with extension during the Mackenzie magmatic event (~1270 Ma; Fahrig et al., 1981; LeCheminant and Heaman, 1989), however, Long and Turner (2012) concluded that they may have been trans-tensional sag basins prior to rifting. The Hunting-Aston basin is overlain by Paleozoic strata that were deposited on the Franklin shelf (Trettin et al., 1991). Far-field, west-directed compressional stresses during the Silurian-Devonian associated with the Caledonian orogeny resulted in the Boothia uplift (Miall, 1986; Oliver, 2001; Morris et al., 2005), a north-trending feature that is cored by basement rocks and extends from the mainland (Boothia Peninsula) in the south to the Grinnell Peninsula (Devon Island) in the north (Okulitch et al., 1991). South-directed stresses in the Late Devonian-Carboniferous resulted in the Ellesmerian orogeny (Harrison et al., 1991), a west-trending deformation front that affected the islands north of the Barrow strait and deposited a thick clastic wedge (6-10 km) in its foreland basin on most of the islands (Embry, 1991; Dewing and Obermajer, 2009). Deposition in the Franklin basin effectively ceased with the waning of the Ellesmerian orogeny and the opening of the Carboniferous-Cretaceous Sverdrup Basin to the northwest of the Cornwallis district (Davies and Nassichuk, 1991), which became the primary depocentre in the High Arctic. Rotation of Greenland relative to Laurentia caused the Eurekan orogeny during the Cretaceous-Oligocene, which resulted in compressive stresses in the north (Ellesmere Island) and extensional stresses in the South (Baffin Bay; Tegner et al., 2011; Piepjohn et al., 2016), with no apparent affect on islands south of Barrow Strait.

Proterozoic redbed sandstone of the Aston Formation is exposed in a small area on northern Somerset Island (<50 km x <3 km; Figs. 2, 3). It nonconformably overlies amphibolite- to granulite-facies Archean quartzo-feldspathic and mafic basement gneiss (Brown et al., 1969; Frisch, 2011) along a northwest-trending contact, dipping gently northeast under the Mesoproterozoic Hunting Formation and a thick succession of Paleozoic carbonate rocks. Although the Aston Formation unconformably underlies Mesoproterozoic strata (Hunting Formation; Tuke et al., 1966; Dixon et al., 1971; Dixon, 1974; Butterfield et al., 1990; Butterfield, 2000), it is assumed to be much older than, and unrelated to, the late Mesoproterozoic Bylot basins in the central Arctic islands of Canada (Fahrig et al., 1981; Jackson and Iannelli, 1981). The formation's present thickness is ~800 m (Fig. 4), but originally may have been substantially thicker (Mayr et al., 2004); it is unclear whether its complete absence between basement and the Hunting Formation in some fault-related regions along depositional strike is owing to synsedimentary faulting and geographically variable subsidence, or to later removal (Tuke et al., 1966). No stratigraphic unit resembling the Aston Formation is present in the other Mesoproterozoic Bylot basins, and although the formation presumably underlies the Paleozoic succession east of the exposure area, its geographic extent seems to be limited to northern Somerset Island, and perhaps only a small part thereof.

The Aston Formation is sandstone-dominated, with minor basal conglomerate and siltstone. The formation consists of medium- to coarse-grained quartz sandstone with cross, trough, and planar lamination, and ripple marks, all of shallow-marine origin (Tuke et al., 1966; Long and Turner, 2012). Paleocurrents suggest that most of the sediment was derived locally from basement gneiss to the (present-day) west of the Boothia arch, which is in agreement with the strained and monocrystalline predominance of detrital quartz grains (Dixon et al., 1971). Sediment reworking

in the shallow-marine environment may have been responsible for the removal of silt-sized grains (Dixon et al., 1971). Dixon et al. (1971) noted that feldspar content decreases and compositional maturity of the sandstone increases up-section, and related these trends to greater transport duration and decreased subsidence rate through time. The Aston Formation is cross-cut by Mackenzie dykes and sills (1270 Ma; Mayr et al., 2004; LeCheminant and Heaman, 1989).

The overlying Mesoproterozoic Hunting Formation is a ~1.3-km-thick carbonate succession (Tuke et al., 1966; Dixon, 1974) and, together with the Aston Formation, is cross-cut by Franklin-aged dykes (723 Ma; Heaman et al., 1992). Aston-Formation-derived quartz sand grains are present locally in the pink upper Hunting Formation (Fig. 5). Overlying the Proterozoic strata are approximately 3 km of Paleozoic carbonate strata (Fig. 4; Miall and Kerr, 1977; 1980). The youngest preserved Paleozoic formation (member 4 of the Peel Sound Formation) was deposited in the Early Devonian (Lochkovian; Thorsteinsson, 1980) and is composed of clastic material shed from rocks in the Boothia uplift, including Aston Formation clasts (Miall and Gibling, 1978; Stewart, 1987). The Devonian-Carboniferous Ellesmerian orogeny deposited a widespread clastic wedge over most of the arctic islands, approximately 6 km thick (Embry, 1991), possibly as much as 9 km thick on Banks Island (Dewing and Obermajer, 2009), but no strata related to this orogeny are preserved on Somerset Island.

Of the major Phanerozoic tectonic episodes, the Ellesmerian orogeny has the only apparent association with a fluid migration event thought to have been critical to the diagenetic and mineral potential of the Cornwallis district of the Canadian Arctic islands (Kerr, 1977a, b; Randell and Anderson, 1996; Rose, 1999; Savard et al., 2000; Mitchell et al., 2004; Reid et al., 2013a, b; Mathieu et al., 2018).

The Storm copper deposit on Somerset Island is a carbonate-rock-replacement deposit that is divided into three paragenetic stages: pre-, main-, and post-ore (Mathieu et al., 2018). The pre-ore stage precipitated dolomite cement and chalcopyrite from a mixture of a reduced basement-derived-equilibrated fluid and a regional sulphate-bearing fluid that circulated at the onset of the Ellesmerian orogeny. During the main-ore stage, Cu-sulphides (chalcopyrite, bornite, chalcocite-group, and covellite) and calcite were precipitated from an oxidised, low-latitude meteoric fluid that interacted with sedimentary strata, probably a redbed, associated with the waning of the Ellesmerian orogeny. Post-ore fluids were precipitated from higher-latitude meteoric fluid.

A geochemical study of various mineral showings in the Cornwallis district (Chapter 2) indicates that mineralisation in the district was the result of a regional metalliferous fluid mobilised by the Ellesmerian orogeny. Following the Ellesmerian orogeny, the main regional fluid was supplanted by a low-latitude meteoric fluid.

4.3 MATERIALS and METHODS

Somerset Island is difficult to access during the few summer weeks of the year that are appropriate for geological work. Sea-ice cover between a helicopter base at Resolute Bay (Cornwallis Island) and Somerset Island is generally low during the summer weeks when snow-cover on land is lowest, and helicopter access is not possible when there is open water. Owing to the rocky landscape (Felsenmeer and glacial drift), areas suitable for the landing of bush-planes fitted with tundra tires are few and become dry enough for landings only halfway through the short workable summer interval. Much of the landscape is too rocky for travel using all-terrain

vehicles, and so field research must be done on foot from backpacking-style base camps that are commonly not ideally situated relative to the useful exposures. For these reasons of extreme time limitation and inimical geographic conditions, the Proterozoic strata of Somerset Island have not been well studied.

The Aston Formation red and grey sandstone samples used in this study were collected along a stratigraphic transect through the formation following a river valley that intermittently exposes the gently northeast-dipping strata (Table 1; Fig. 6). Because the exposure is poor and intermittent, many of the samples were collected from in situ frost-shattered bedrock (Felsenmeer; Fig. 3).

Petrographic study conducted on polished thin sections (30 μm thick) used transmitted, reflected, oblique, and ultraviolet (385 nm) light sourced from an Olympus BX-41 petrographic microscope. The resulting descriptions were used to identify sediment grain composition and character, visually estimate component proportions, characterise diagenetic cements, locate and classify fluid inclusions, and establish a paragenesis. Cathodoluminescence (CL) images were captured with a MAAS, Inc. (Nuclide Corporation) ELM-2E luminoscope with a cold cathode electron gun, mounted on a standard petrographic microscope. The following operating conditions were reported: accelerating voltage of 15 kV, beam current of approximately 5 mA and an operating vacuum of 50-100 millitorr.

A JEOL 6400 scanning electron microscope fitted with an Oxford INCA EDS detector was used to image textural relationships and identify mineral and geochemical compositions. Operating conditions were an accelerator voltage of 20 kV, 1.005 nA beam current, and 5-second counting time.

In situ measurement of $\delta^{18}\text{O}$ values of quartz grains and quartz cement were made using secondary ion mass spectrometry (SIMS) at the University of Manitoba, Canada. Samples were sputter-coated with Au. A CAMECA 7f secondary-ion mass spectrometer operated with a 300 V sample offset, -8.7 kV secondary accelerating voltage, and 225 μm slit diameter combined with a mass-resolving power of 350 analysed samples with a 4 nA Cs^+ primary ion beam accelerated to 10 kV onto the sample with a 15 μm beam diameter. Detection of ions was performed using an ETP 133H electron multiplier. The quartz standard UWQ-1 of Kelly et al. (2007) was used as an internal standard. Data are reported in standard per mil (‰) referenced to V-SMOW with spot-to-spot reproducibility of 0.7-0.8‰.

4.4 RESULTS

4.4.1 Hand Samples

Samples consist of red (unbleached) and grey (bleached) sandstone (Fig. 3, 7).

4.4.2 Thin sections

Unbleached material has iron-oxide coatings around most detrital particles and, in particular, around very fine grains that causes the red appearance of the samples (Fig. 7A-F). Bleached samples have little to no iron-oxide coatings and are various shades of grey (Fig. 7G-I). A gradation of hues from red to grey reflects variable amounts of iron-oxides. Some samples exhibit patches or layers containing iron-oxides, whereas the rest of the sample has none (Fig. 7J-L). Typically, coarser-grained grey sandstone layers lack hematite and finer-grained

sandstone layers are red. Well-sorted bleached samples generally lack iron-oxide coatings completely (Fig. 7H, I).

4.4.3 Framework grains

Sedimentary particle size ranges from very fine sand (65 μm) to medium sand (0.5 mm), and sandstone texture is well sorted with some samples having poorly sorted sections. Sedimentary grains are predominantly well- to sub-rounded and sub-spherical. Horizontal layers of different, uniform, grain size are present in some samples. Framework grains generally have long, subtly concavo-convex contacts that are predominantly horizontal or oblique to the depositional way up (Fig. 8A, B), with subordinate point and irregular-amplitude sutured contacts with no apparent preferred orientation (Fig. 8C), although the large stylolitic contacts appear to be horizontal (Fig. 8D-F), collectively forming a fitted framework. Sutured contacts appear to be predominant in bleached samples or bleached areas of samples, and are apparently proportional to level of sorting (better sorted samples have more sutured contacts). Sutured grains have no hematite at the contact, unless it is in small ($\sim 2\text{-}5\ \mu\text{m}$) corrosion pits filled with phyllosilicates. Generally, grains, particularly sutured grains, have corrosion along grain margins and contacts, leaving gaps less than 2 μm wide that are filled typically by phyllosilicates and/or hematite (Fig. 8C).

The Aston Formation consists primarily of uniformly luminescent detrital quartz (typically 80-90% of grains) and potassium feldspar (10-20% of grains), with minor amounts of lithic fragments. Quartz grains are predominantly strained (50-60%) and monocrystalline (40-50%), with subordinate polycrystalline quartz (typically <10%). Fractures are common in quartz grains. Potassium feldspar grains typically have tartan twinning in cross-polarised light, and appear cloudy; reflected-light and back-scattered electron images show a pitted-like texture of the grains (Fig. 9). Minor amounts of feldspar with perthite twinning or with no apparent twinning are

present. Lithic fragments are primarily chert or quartzite, with small amounts of granitic gneiss fragments. Mafic clasts are present in trace quantities.

Very fine grains of rounded to sub-angular, opaque, detrital Fe(-Ti)-oxide minerals (Fig. 10) are present (<1%) scattered in almost all of the samples, regardless of whether the rock is unbleached or bleached, but are apparently more common in bleached samples. Some of these grains have intergrown exsolution lamellae (Fig. 10A) or patches of Fe-oxides (hematite) and Ti-oxides (rutile) (Fig. 10B), and some grains have uniform hematite rims (up to 70 μm thick) surrounding cores of mixed Fe-Ti-oxides (Fig. 10B). Hematite grains are present in both bleached and unbleached sandstone, but are more common in unbleached material. These grains are typically (sub-)rounded and average 100 μm . Grains are distinct from surrounding grains and not incorporated in lithic fragments; some have corroded edges. Some of these grains appear to be composed of several smaller crystals amalgamated together with 'pore space' (Fig. 10C); others appear to be a single crystal. Some hematite grains in bleached and unbleached samples are <10 μm and appear to be partially dissolved in fine-grain matrix (illite?).

4.4.4 Cement

Very little matrix is present in the Aston Formation. Cement accounts for approximately 5-10 % of rock volume.

Iron oxide (hematite) coats and cements sand particles; it is also present along some of the fractures in quartz particles. In plane-polarised light, this cement is (almost opaque) brown,

whereas in oblique incident light, it is red to red-orange (Fig. 8A, 11). This cement evenly coats grains to a thickness of 1-10 μm and where mixed with illite between grains in unbleached material has a thickness of up to 100 μm . It unevenly coats few grains (if any) in bleached material; along most concavo-convex or sutured contacts, it is absent (Fig. 8C-E, 11A, B); this is not readily apparent in plane-polarised light, but is evident in oblique light. Some pressure-solved contacts have hematite present in corroded pits that are also filled by clay minerals (illite?), rather than an actual coating of the grain. The coatings lack any obvious crystallinity (based on petrographic evidence) and appear to be composed of colloid-like hematite that is trapped around the outside surface of a grain (Fig. 11A, C, E). Two phases of hematite coating are present (H1 and H2), which are most obvious when they are separated by a thin veneer of quartz (Fig. 11C). When present, H1 consists of thin (1-3 μm) layers of 'colloidal' hematite entrapped by quartz overgrowths around a grain. At concavo-convex grain contacts, H1 is preserved between the grains (Fig. 8A). Hematite 2 (H2) is typically thicker (up to 100 μm) than H1 and coats grains or quartz overgrowths and is mixed with phyllosilicates between grains or in corroded pits at grain contacts. At pressure-solution grain contacts, H2 envelops the two grains (Fig. 11A, B). Some H2 has been incorporated into late quartz cement (Q2; Fig. 11E, F), but does not coat Q2.

Two generations of quartz cement are present: thin, early veneers (Q1) and late, pore-occluding crystals (Q2; Fig. 12). The first quartz cement (Q1) forms thin (up to 100 μm), non-luminescent, syntaxial overgrowths on detrital quartz particles, and overgrows early hematite (H1 coatings around the grains (Fig. 11C, D, 12A-D). These Q1 overgrowths are typically <100 μm thick and pinch out at pressure-solved contacts (Fig. 12A, B). The transition from detrital grain to overgrowth is detectable by the overgrowth's lack of fluid inclusions and by the presence of H1

coatings along the grain boundary. There is no physical separation that can be detected between the grain and overgrowth (i.e., smooth surface under reflected light; Fig. 12B, D). Where Q1 is in contact with pores filled by phyllosilicates, it has corroded edges (Fig. 12C, D). Late quartz 2 (Q2) is the main pore-filling cement, and overgrows H2, if present (Fig. 11C-F); this cement is non-luminescent (Fig. 12G), hundreds of micrometres thick, has no fluid inclusions and sparse fracturing. Unbleached samples typically have more Q2 than bleached samples, with some bleached samples having no Q2. In some samples, detrital grains appear to be “floating” in Q2 (Fig. 12G). Most Q2 is separated from grains (and Q1) by a phyllosilicate (illite?) coating that, under reflected light, results in a visible gap that is typically $<2 \mu\text{m}$ wide (Fig. 11F, 12B); these gaps typically contain hematite and/or phyllosilicates and have corroded edges. This cement surrounds grains that have pressure dissolution contacts (Fig. 12G). In some samples, Q2 that overgrows H2 appears to incorporate some of the hematite ‘colloids’ (Fig. 11E, F).

Authigenic K-feldspar is present around some detrital feldspar (uniformly brightly luminescent) particles in the form of cloudy overgrowths (Fig. 9G-J), commonly in optical continuity with the underlying feldspar particle. At a micro-scale, the authigenic K-feldspar cement is more porous than the detrital grain it overgrows (Fig. 9I, J).

4.4.5 Phyllosilicates

Phyllosilicate minerals (muscovite and illite) are present in minor abundances in sandstone pores (Fig. 12C, D), primarily in bleached samples, where there is an apparently inverse relationship with sorting (better sorted = fewer phyllosilicates). They are also found as grain coatings ($<2 \mu\text{m}$ thick) even at grain pressure-solution contacts (Fig. 9C-F, 8C). Phyllosilicate mineralogy plots

along two trends in a Si-Al-K ternary diagram (Fig. 13A): one between muscovite and Fe-Mg-free illite, and one from muscovite to Fe-Mg-bearing illite. The phyllosilicate that plots closest to a muscovite composition ('muscovite') is present as comparatively large (~25 μm) euhedral plates that infill the larger irregular pores (Fig. 13B-F) in bleached samples, whereas the Fe-Mg-bearing illite ('illite') is fine-grained and is concentrated between grains (Fig. 13G), in corroded pits, and especially around dissolved K-feldspar (Fig. 9C-J).

Illite coats most grains with a veneer that is present between grains that have a small gap (<2 μm) between corroded grain edges or pits (up to 200 μm). Because some Q1 has corrosion features filled by phyllosilicates (Fig. 12C, D), this indicates a post-Q1 process. Cloudy K-feldspar grains and cement have pits that may be related to twinning that are filled with illite that extend to and around the grain margin (Fig. 9C-J). Some grains have illite that isolates, rounded fragments in optical continuity with the detrital grain (Fig. 13H, I). Hematite 2 is often mixed with illite. In samples that have H1 removed at grain contacts (i.e., bleached), H2 can be present in the corroded gaps/pits between grains that are associated with illite.

Muscovite-filled pores have corroded edges with the grains/cement in contact with the pore (Fig. 12C, D, 13B-F), making it difficult to determine if the pores were primary and the grain edges dissolved or if the pore space was the product of dissolution to allow for the infilling by muscovite. These pores are limited to bleached samples and have no H2 associated with muscovite. Muscovite crystals are apparently oriented randomly and undeformed (Fig. 13D). No timing constraints, except for post-dating Q1, were decipherable for muscovite and the pores it fills.

4.4.6 Porosity

Little primary porosity remains in Aston Formation sandstones, but there is approximately 1-10% secondary porosity. Oversized pores with corroded edges and irregular shapes (Fig. 14A-E) suggest porosity developed by dissolution. Some of these pores are empty (Fig. 14), whereas others were filled with phyllosilicates (Fig. 12C, D, 13B-F); some appear to post-date phyllosilicate infilling because of the void butting up against phyllosilicates (Fig. 14A, B); some are connected by narrow passages (Fig. 14C). Corroded edges along pores cut across grains and Q1 (Fig. 12C, D). Some of these pores are rounded and have concentric fractures around the margin of the void and probably represent grains plucked during thin section preparation (Fig. 14D).

4.4.7 Oxygen isotopes

Measured $\delta^{18}\text{O}$ values of quartz clasts and quartz cement (Q2) from two samples (Fig. 15) yielded averages of 8.8 ($1\sigma = \pm 1.1\text{‰}_{\text{SMOW}}$; $n=6$; range = 7.5-10.1‰) and 14.4 ($1\sigma = \pm 1.9\text{‰}$; $n=7$; range = 11.8-16.9‰), respectively.

4.5 INTERPRETATION

4.5.1 Sandstone composition and fabric

Aston Formation sandstone is dominated by strained, monocrystalline quartz grains, reflecting its main source area in nearby basement rock exposures. In basins that have a local source from

uplifted basement rocks, unstable mafic clasts would be expected to be present, and if they are not, it may indicate that they were dissolved, which would release Fe (Walker, 1976). Iron that is released during initial reddening events typically does not travel far due to its tendency to adsorb onto oxyhydroxides (Zielinski et al., 1983; Walker 1989; Rose and Bianchi-Mosquera, 1993). Based on paleocurrents and clast composition, the Boothia arch was probably the source of Aston Formation sediment (Tuke et al., 1966; Dixon et al., 1971; Long and Turner, 2012), and as such, the lack of mafic clasts probably indicates the dissolution of these types of grains.

The sandstone is dominated by fitted fabric, in which adjacent framework grains generally have long, gently concavo-convex contacts rather than point contacts, indicating extensive pressure solution. Pressure-solution took place after the development of at least one episode of hematite coating and after Q1, because the hematite veneers are preserved along pressure-solved grain contacts (behaving as an insoluble residue), whereas Q1 pinches out at pressure-solved contacts. After the main episode of porosity loss through pressure-solution, interparticle pore volume would have been ~10% until the time of their eventual occlusion during Q2 cement precipitation.

4.5.2 Fe-oxide coatings:

The red colour of Aston Formation sandstone developed through precipitation of Fe-oxide cement that coated sand particles during diagenesis; the Aston Formation sand was, therefore, probably not red at the time of its deposition. The reddening process requires the circulation of an oxygen-bearing fluid (Rose, 1989; Brown, 2005, 2009). The reddening of sediment is typically considered shallow (Zielinski et al., 1983), with indications of reddening occurring to depths near 1 km (McBride, 2016), similar penetration depths of oxygenated meteoric fluid have

been determined in other studies as well (e.g., Machel, 2001; Brown et al., 2004; Rasmussen et al., 2014; Yuan et al., 2017). Faults and fracture networks can, however, increase the penetration depth of meteoric water (e.g., Diamond et al., 2018). Therefore an appropriate limiting depth of less than 1 km burial for reddening, in accordance with the shallow burial regime of Machel (2001).. This reddening fluid dissolves Fe-bearing (typically mafic) minerals, releasing Fe into solution where it can precipitate on grains as an Fe-oxyhydroxide (Zielinski et al., 1983; Weibel, 1998; Brown, 2005). This process is common, gradual, and can take several million years (Zielinski et al., 1983; Brown, 2005), but is still considered to be an early diagenetic phenomenon (e.g., Zielinski et al., 1983; Ryan, 1989; Rose and Bianchi-Mosquera, 1993; Eichhubl et al., 2004), but it can also develop during late diagenesis if conditions allow for the circulation of oxidised fluid, such as after uplift and exposure (Wahab, 1998).

The main Fe-oxide cements in oxidised clastic sedimentary rocks are hematite and goethite/limonite. Typically, goethite is metastable and recrystallises to hematite (Zielinski et al., 1983); it can resemble hematite in plane-polarised light, but under oblique light, goethite is yellow to yellow-orange. The red colour of coatings in Aston Formation material indicates hematite (Figs. 8A and 11).

Because hematite is highly insoluble during quartz pressure-solution (Morey and Hesselgesser, 1951) and H₂ is generally absent at concavo-convex and sutured quartz-grain contacts but coats the free surfaces of pressure-solved grains, H₂ precipitation is interpreted to have post-dated pressure solution. However, because the overlying Hunting Formation is locally pink due to the presence of Aston Formation grains with hematite coatings (Fig. 5), hematite cement must predate Hunting Formation deposition, which may not have been thick enough to cause pressure solution in the underlying Aston Formation (quartz pressure-solution requires >2 km burial).

These two contradicting temporal constraints for hematite timing suggest that at least two episodes of hematite precipitation took place - early diagenesis (H1) and late diagenesis (H2) - a conclusion that is supported by petrographic evidence. There is no available evidence that the two hematite coatings differ compositionally.

Ilmenite is a common heavy mineral in sedimentary rocks and typically alters during diagenesis to heterogeneous clasts composed of mixed TiO_2 (rutile/anatase) and Fe-oxide (hematite or magnetite) minerals (Ramdohr, 1969, Weibel and Friis, 2004; Pe-Piper et al., 2005; de Oliveira and Truckenbront, 2019). The alteration of ilmenite may have supplied the Fe for the thick homogeneous hematite overgrowths on the mixed hematite- TiO_2 grains (Fig. 10B), similar to the alteration documented by Weibel and Friis (2004). It is unlikely that rutile was depositional and later altered to hematite, because rutile is the most stable TiO_2 mineral in surface and diagenetic conditions (Meinhold, 2010), and unlikely to be dissolved and/or replaced during diagenesis, in addition to the rutile-hematite exsolution in some grains being related to source rocks, rather than diagenetic alteration. Based on the thickness of hematite overgrowths on these opaque minerals, the overgrowths may indicate a separate hematite-precipitating event between the early and late hematite stages. It is, however, difficult to relate these overgrowths to other diagenetic events because of the spatial separation from other stages.

4.5.3 Alteration:

Oversized, irregular pores, typically with corroded edges, indicate dissolution of particle surfaces at pore margins (Walker, 1967). Some of these pores are filled with euhedral muscovite (Fig. 13D), suggesting that some detrital particles had been dissolved prior to infilling of muscovite.

Corroded detrital quartz grains and Q1 in contact with these filled secondary pores indicate that the clay was present during burial, because of the increased solubility of quartz by in the presence of clay (i.e., clay-induced dissolution; Siever, 1962; Bjørkum, 1996).

Sodic and potassic alteration are generally expected in a red-bed succession owing to fluid interaction (Hitzman et al., 2005). The absence of plagioclase in siliciclastic stratigraphic units, such as in the Zambian copperbelt, is attributed to its replacement by K-feldspar during potassic alteration (Selley et al., 2005). Similarly, there is a predominance of K-feldspar over plagioclase in the Aston Formation, however, this is probably due to the removal/absence of plagioclase, rather than the alteration of plagioclase to K-feldspar, because K-feldspar grains typically have primary twinning features, although some K-feldspar grains lack the primary, “high temperature” tartan twinning, which may be related to a “low temperature” origin, such as alteration. The predominance of K-bearing clays over Na clays in the Aston Formation may be a function of potassic alteration. Kaolinite is generally the most common phyllosilicate alteration product of feldspars (plagioclase and K-feldspar) during diagenesis (Lanson et al., 2002; Yuan et al., 2015), but kaolinite is apparently absent in Aston Formation material, and illite is the predominant clay mineral. This could be the result of kaolinite being altered to illite, the transformation of smectite to illite, or, the direct precipitation of illite from the alteration of K-feldspar. Several diagenetic parameters affect the precipitation of illite, the most notable of which are temperature and the activities of K^+ and H^+ (Lanson et al., 2002). The predominance of K-rich illite over K-free kaolinite in the Aston Formation may indicate higher K activity, possibly related to dissolution of K-feldspar (Berger et al., 1997; Molenaar et al., 2015; Yuan et al., 2019), which is observed in the porous detrital K-feldspar grains and cement. Illite is more common than kaolinite at temperatures $>70^{\circ}C$, which may indicate kinetic controls (Lanson et al., 1996, 2002; Yuan et al.,

2015, 2019), with increased crystallinity of illite being related to increased temperatures (Lanson et al., 1996). That illite (muscovite) in secondary pores is euhedral (Fig. 13D) may therefore be related to temperatures reached during or near maximum burial.

Most rebeds contain carbonate (usually calcite) as an early to middle diagenetic cement (Schluger, 1976; Wahab, 1998; Weibel, 1998; Beitler et al., 2005; Heidari et al., 2013; Elshahat, 2017). This cement prevents physical compaction and occlusion of pore space by other more insoluble cements, such as quartz, such that when a later fluid interacts with the rock the calcite can dissolve, leaving porosity. The apparent absence of calcite cement in the Aston Formation may indicate either that it was formerly present but dissolved during diagenesis, as in other studies (e.g., Wahab, 1998; Yuan et al., 2017), or perhaps that calcite cement was never present, due to unfavourable conditions. It is possible that the pore space now occupied by illite was once occupied by now-dissolved calcite cement, but with the lack of any Ca minerals, and no calcite documented elsewhere, it is difficult to determine.

The porous texture of cloudy feldspar grains (Fig. 9) could have developed from the initial weathering process during erosion and deposition or a pre-depositional process, but because the authigenic feldspar cement is also porous, some degree of feldspar alteration must have taken place during diagenesis. The higher amounts of structural defects in authigenic K-feldspar than in detrital grains (e.g., Martin, 1971; McBride, 2015; Yuan et al., 2019) may have resulted in a higher rate of dissolution or alteration of the cement versus detrital (igneous) feldspar grains. The alteration of K-feldspar is a probable source of the illite coatings and in-fill. The apparent absence of muscovite in red samples suggests a relationship to the bleaching fluid, which may be related to increased dissolution of K-feldspar with reducing ('bleaching') fluids, as has been observed in the Navajo sandstones (Beitler et al., 2005).

In unbleached material, ilmenite (hematite-TiO₂) particles are apparently absent, and only hematite grains are present. It is not evident if this is because the hematite (a) was deposited as a detrital mineral and underwent no alteration, (b) completely replaced another iron oxide (e.g., magnetite), or (c) is the coincidental section through thick hematite cement overgrowths, and not particles at all. It is therefore difficult to determine the timing of this alteration relative to other diagenetic events, but it probably post-dates early hematite (H1) cements and pre-dates late quartz (Q2) cement and may be related to precipitation of H2. The hematite rinds on ilmenite grains is a typical feature of reddening during diagenesis (Weibel and Friis, 2004). That these grains with hematite rims are present in bleached samples, indicates that bleaching post-dates reddening, or at least the oxidised alteration of ilmenite. It is possible that a secondary oxidising alteration of previously altered ilmenite could have hematised the entire ilmenite grain, rather than just form a rind, which would explain the lack of coated ilmenite grains and predominance of hematite grains in unbleached samples.

The secondary porosity that was produced by dissolution of grains, most of which has been occupied by illite, probably formed after or during the final episode of mechanical compaction during burial because the pores and the infilling clays are relatively undeformed. It would be expected that, if dissolution took place before mechanical compaction, the pores would be deformed (Wilkinson et al., 2001).

4.5.4 Bleaching:

Removal of hematite cement from around sedimentary particles produced bleached sandstone.

The predominance of illite in bleached samples, as compared to unbleached material may

indicate that it is a product of hematite or feldspar alteration. Bleaching of the Navajo Red sandstone was accompanied by an increase in K-feldspar dissolution and the precipitation of clay minerals (Beitler et al., 2005). Early quartz overgrowths (Q1) that preserve H1 hematite coatings in bleached samples of this study indicate that bleaching post-dated both early hematite deposition and Q1 precipitation. However, the removal of H1 at long concavo-convex contacts indicate that bleaching pre-dates extensive burial.

The apparent lack of pyrite in the Aston Formation sandstone, which is a common product of bleaching (e.g., Weibel, 1998; Beitler et al., 2005; Macintyre, 2006), could be due to sampling bias, the subsequent removal/alteration of pyrite, or there not being sulphate present to reduce during bleaching that could have precipitated pyrite. Alternatively, it is possible that bleaching was actually just the inhibition of reddening by local conditions, such as pH or the presence of organic matter (Weibel, 1998; Weibel and Friis, 2004). Sample D9 (red) has spots up to approximately 500 μm across that are not red (Fig. 7D-F) and could indicate local conditions that would have inhibited hematite precipitation. Large-scale (lithostratigraphic) bleached areas are typically the result of external reducing fluids, usually hydrocarbon-bearing, removing hematite (Shebl and Surdam, 1996; Beitler et al., 2005; Hitzman et al., 2005; Macintyre, 2006; Rainoldi et al., 2014; McBride, 2015), rather than local preclusion of hematite formation due to reducing conditions. The lack of bitumen or hydrocarbon-bearing fluid inclusions in Aston Formation sandstone or in Storm Cu samples (Mathieu et al., 2018) makes it difficult to relate redbed bleaching to the migration of a hydrocarbon fluid.

4.5.5 Quartz cement and its $\delta^{18}\text{O}$ values

In order to interpret the oxygen isotope data from quartz cement, it is necessary to determine whether Q2 resulted from recrystallisation of an early low-temperature phase or if it was precipitated directly as coarsely crystalline quartz cement. Amorphous silica typically forms laminated precipitates or fibrous chrysocolla, both with easily identified optical and CL characteristics (Goldstein and Rossi, 2002). Although recrystallisation of such cements to quartz can obliterate their crystal structure and optical properties, the original CL patterns, conferred by patterns in trace element distribution, are generally preserved (Goldstein and Rossi, 2002). The homogeneously non-luminescent, coarsely crystalline Q2 cement in this study (Fig. 12G) probably precipitated as large, simple quartz cement crystals directly from solution, and therefore its oxygen isotopic values should record characteristics of the precipitating fluid.

In the absence of a proper temperature constraint for quartz cement (Q2) precipitation, three possible temperature ranges and fluid isotopic compositions (Fig. 15) were used to calculate the possible characteristics of the quartz-precipitating fluid. Seawater is one of the most common diagenetic fluids and a possible identity for the quartz-precipitating fluid. Using a range of $\delta^{18}\text{O}_{\text{H}_2\text{O}}$ values from -4 to +4‰ with the average quartz cement $\delta^{18}\text{O}$ value (14.4‰) and the H_2O -quartz fractionation equation of Sharp and Kirschner (1994), the temperature of precipitation is calculated to be between 141° (for -4‰) and 251°C (for 4‰) if the fluid were seawater-derived. Such temperatures would relate to burial depths of approximately 4 and 7 km, respectively, using a geothermal gradient of 30°C/km and surface temperature of 30°C.

Meteoric water is another common diagenetic fluid; its isotopic composition is a function of latitude (e.g., Yurtsever and Gat, 1981; Luz and Barkan, 2010). Meteoric oxygen isotope values for latitudes between 20° and 30°N were chosen for temperature calculations because the meteoric water that precipitated the Storm copper deposit indicates these latitudes (Mathieu et

al., 2018), based on paleotectonic reconstructions of Cocks and Torsvik (2011) and Torsvik et al. (2012). Using present-day oxygen isotope values of meteoric water for these latitudes (-8‰ to -2‰; Yurtsever and Gat, 1981; Luz and Barkan, 2010), calculated temperatures range from ~105°C (for -8‰) to 160°C (for -2‰). This temperature range and associated paleolatitude are within the respective ranges typical of sedimentary-rock-hosted stratiform Cu deposits (Hitzman et al., 2005).

The final calculation assumes a fluid in equilibrium with ambient burial temperatures during or after hematite precipitation (i.e., <1 km). Using a surface temperature of 30°C and geothermal gradient of 30°C/km, ambient burial temperature would be less than 60°C, and using the average quartz cement $\delta^{18}\text{O}$ value (14.4‰) in the fractionation equation yields calculated $\delta^{18}\text{O}_{\text{H}_2\text{O}}$ values between -22.5‰ (for 30°C) and -15.6‰ (for 60°C). These calculated values coincide with mid- to high-latitude (50° to 60°N) meteoric water, based on present-day values (Yurtsever and Gat, 1981; Luz and Barkan, 2010; Delavau et al., 2011), which could indicate precipitation during the Jurassic or Cretaceous.

4.6 DISCUSSION

The timing of diagenetic events and the fluids that were involved are important in determining whether a red-bed unit may have been the metal source for an ore deposit. This section discusses the characteristics and paragenesis of the major diagenetic events and their associated fluids recorded in the Aston Formation, and how they relate to mineralisation of the overlying Storm copper deposit. The main diagenetic events, in paragenetic order (Fig. 16), are (1) development

of H1 hematite coatings; (2) precipitation of Q1 quartz cement; (3) irregular, incomplete removal of some H1 by reduction ('bleaching'); (4) alteration of non-quartz minerals to illite and/or muscovite; (5) pressure-solution; (6) development of H2 coatings; and (7) occlusion of most remaining porosity by Q2.

4.6.1 Burial history and reddening of the Aston Formation sandstone

Porosity reduction is a key factor in host-rock quality for metal and hydrocarbon deposits, and therefore an understanding of the burial history is required. Most porosity reduction in sandstone comes from pressure-solution and quartz cementation (Bell, 1978; McBride, 1989; Bjørlykke and Egeberg, 1993; van Noort et al., 2008). Permeability is considered to be effective for fluid circulation as long as porosity is above a 2-4% threshold (Mavko and Nur, 1997). In the Aston Formation, because pore occlusion by quartz cement Q2 post-dated most of the diagenetic events, the sandstone probably had adequate porosity and permeability to allow for fluid circulation at all times prior to Q2 quartz cementation.

Deformation of quartz grains is predominantly brittle up to 2 km burial depth (Bell, 1980; van Noort et al., 2008). Evidence of pressure-solution, such as concavo-convex and sutured grain contacts, becomes abundant after 1.5 km with a geothermal gradient of 40°C/km (Taylor 1950; Ramm 1992; Bjørlykke and Egeberg, 1993; van Noort et al. 2008). With more normal geothermal gradients (i.e., 20-30°C/km), pressure-solution of quartz grains becomes possible below 2 km and is more common below 3 km. Interstitial clay can enhance dissolution of quartz under pressure (Siever, 1962; Bjørkum, 1996), and clay coatings can inhibit syntaxial cementation (Walderhaug, 1996). The minor amount of clay in Aston Formation sandstone indicates that pressure-solution of quartz was not greatly affected by the presence of detrital or alteration clay minerals. However, local accumulations of clay material at grain boundaries

resulted in corrosion along particle and Q1 surfaces in contact with the clay. Small-scale corroded edges of detrital quartz associated with clay minerals (Fig. 12C, D, 13B-D) indicates clay-induced dissolution of quartz. That these clays are between sutured grains indicates that they were present prior to burial depths sufficient for pressure solution, which would have prevented infiltration by clay minerals. The temperature dependence of illite (requiring higher temperature than kaolinite) suggests that kaolinite could have been present during burial and underwent transformation to illite at burial depths of at least 2 km. Because pressure-solved grain contacts are abundant in the Aston Formation, it must have been buried to at least 2 km, but probably more than 3 km at some point in its burial history.

The Proterozoic to Recent stratigraphic succession exposed on northern Somerset Island contains evidence of at least three major subaerial exposure events, as indicated by substantial gaps in the stratigraphic succession (Fig. 4): major unconformities are present between the Aston and Hunting formations, between the Hunting Formation and Paleozoic strata, and between Paleozoic and (Mesozoic-) Cenozoic strata. Furthermore, two major compressional tectonic events affected the area: (1) far-field effects of the Late Silurian to Early Devonian Caledonian orogeny produced the Boothia uplift (Fig. 1; Miall 1986, Oliver, 2001; Morris et al., 2005), and (2) the Late Devonian to Early Carboniferous Ellesmerian orogeny (Harrison et al., 1991) produced an orogen some 300 km north of Somerset Island (Fig. 1), together with a thick south-prograding clastic wedge. Other major tectonic events in northern Laurentia that have as yet no known widespread tectonic, stratigraphic, or diagenetic expression on Somerset Island include Early Carboniferous extension to form the Sverdrup basin (Davies and Nassichuk, 1991), some 400 km north of Somerset Island, and the early Cenozoic Eurekan orogeny (Kerr, 1977a; Tegner et al., 2011; Piepjohn et al., 2016), which produced a fold belt in the northern Arctic islands but

extensional structures (locally associated with limited terrigenous clastic accumulations) in the southern Arctic islands.

This suite of events suggests multiple times during which the Aston Formation could have become reddened by circulating oxidised fluid (i.e., at less than 1 km burial); two separate reddening events (at least) are indicated by the petrography and paragenesis. Discounting the remote Sverdrup and Eureka events, and considering only basic geological factors, the possible times for generation and movement of oxidised crustal fluid are (1) during initial burial of the Aston Formation (i.e., early diagenesis); (2) during Neoproterozoic exposure of the land surface after Hunting Formation deposition but prior to deposition of Paleozoic strata; (3) during exposure from the development of the Boothia uplift; (4) during development of the Ellesmerian mountain belt and foreland basin; and (5) during episode(s) of exposure post-dating all Paleozoic tectonic events.

Like most redbeds (e.g., Zeilinski et al., 1983; Weibel, 1998; Beitler et al., 2005; Perri et al., 2013; Busch et al., 2017), the reddening process of the Aston Formation was probably early, coating the grains with hematite. The presence of hematite coated grains in the overlying Hunting Formation (Fig. 5) indicates that the Aston Formation was reddened prior to deposition of the Hunting Formation. The lack of cemented- or sutured-grain clasts in the Hunting Formation may represent the lack of an appropriate thickness of the Aston Formation to produce pressure-solved features, thereby suggesting that the thickness of the Aston Formation may have been less than 1.5-2 km. Possible thickness of the Aston Formation on Prince of Wales Island, based on seismic data (Mayr et al., 2004), may be in this thickness range. Because H2 post-dates pressure solution, the hematite-coated grains in the Hunting must be related to H1. The second reddening event must have post-dated the Hunting Formation deposition.

The preserved thickness of the Hunting Formation on Somerset Island is 1.1-1.3 km thick (Dixon, 1974), with a possible thickness of several kilometres on Prince of Wales Island, based on seismic analyses (Mayr et al., 2004). Possible thickness of the Hunting Formation could have been sufficient for the pressure solution of quartz grains, producing concave-convex and sutured contacts. Exposure in the Neoproterozoic-Cambrian, which caused the unconformity between Proterozoic and Paleozoic strata, could have allowed for the migration of H₂-precipitating fluid

The uplift and exposure during the Boothia uplift event was not uniform along the uplift, with northern parts not being as exposed as southern parts for weathering and erosion (Thorsteinsson, 1980; Okulitch et al., 1991). With similar paragenetic phases present in the northern part of the uplift, a regional fluid is expected to have been responsible, rather than a local oxidised fluid present only in the southern part of the Boothia uplift. The Peel Sound Formation, derived from sediment shed from the Boothia uplift, contains clasts of Aston Formation in its youngest member described as quartzite or quartz sandstone (Miall, 1969, 1970), however, no petrographic description of these clasts was provided, making it difficult to determine which paragenetic phases were present at the time of deposition.

An oxidised, meteoric fluid associated with the Ellesmerian orogeny in the Late Devonian to Carboniferous is recorded regionally in the Cornwallis Zn-Pb district, including the main Cu mineralising fluid at the Storm Cu deposit on Somerset Island (Mathieu et al., 2018). This fluid could have resulted in the precipitation of H₂ that would have post-dated burial below 2 km, which could have been associated with the deposition of the Hunting Formation or the accumulation of Paleozoic strata.

Oxygen isotope values of quartz cement (see Quartz timing below), which post-dates H2, indicate low paleolatitudes that are inconsistent with the study site location following the Paleozoic, based on paleogeographic reconstructions (Cocks and Torsvik, 2011; Torsvik et al., 2012); therefore, H2 could not have been from the exposure following the Ellesmerian orogeny.

In summary, the most probable time interval for the precipitation of H1 is between the deposition of the Aston and Hunting Formation, whereas H2 is most probable during the migration of oxidised fluid flow related to the Ellesmerian orogeny with a less probable timing during the Boothia uplift exposure. A detailed petrographic study of the Peel Sound Formation would aid in determining the timing of H2, but the documented circulation of appropriate fluids with the Ellesmerian orogeny is the preferred timing.

4.6.2 Timing and origin of quartz cement and its effect on porosity

Quartz cementation is a major component of siliciclastic rock diagenesis (McBride, 1989; Bjørlykke and Egeberg, 1993; Bjørlykke, 1994), and may change an aquifer into an aquitard during burial (Hiatt et al., 2003; Kyser, 2007). It is important, therefore, to understand the timing of quartz cementation in the present study area. Petrographic relationships show at least two episodes of quartz precipitation: an early, minor Q1 that post-dates H1 and pre-dates pressure solution, and late Q2, the volumetrically more important of the two, which post-dates H2.

Q1 consists of thin syntaxial quartz overgrowths, probably produced during early diagenesis because it experienced pressure solution with adjacent grains and does not surround pressure solution contacts. Low temperatures (<70°C) associated with shallow burial (<2 km) during early diagenesis would have resulted in slow rates of quartz precipitation (Siever, 1962, Walderhaug,

1996; Worden, 2018), which resulted in thin cements. Therefore, the volumetrically minor early Q1 cement probably did not affect porosity significantly.

Because Q2 is either (almost) syngenetic with or post-dates H2, there are three possible times at which Q2 could have precipitated: (1) following exposure of the Boothia uplift (Late Silurian to Early Devonian) but before the Ellesmerian orogeny, (2) during the late stages of the Ellesmerian orogeny (Late Devonian to Carboniferous), and (3) after the Ellesmerian orogeny (younger than the Carboniferous). Two probable fluid isotopic conditions are yielded by calculations based on $\delta^{18}\text{O}_{\text{Q2}}$ (Fig. 15): a cool, high-latitude fluid and a hot, low-latitude fluid. A possible high-latitude (50° - 60°N) meteoric fluid calculated with ambient burial (>1 km) temperatures would indicate quartz precipitation in either the Jurassic-Cretaceous, based on the paleogeographic reconstructions of Cocks and Torsvik (2011) and Torsvik et al. (2012), or the Pliocene, based on recorded oxygen isotope values of fossils on Ellesmere Island (Csank et al., 2011); both of these possibilities post-date the time of meteoric fluid circulation responsible for main-stage mineralisation at Storm copper (Late Devonian to Carboniferous; Mathieu et al., 2018) as well as the regional meteoric fluid that post-dates Zn-Pb mineralisation in the Cornwallis district (Mathieu et al., in prep.). The Storm copper paragenesis does include a low-temperature ($<25^{\circ}\text{C}$) high-latitude meteoric fluid in the post-ore fluid history (Mathieu et al., 2018), however, a fluid below 25°C cannot precipitate quartz at a sufficient rate to account for the volume of Q2, and so Q2 in the Aston Formation was probably not contemporaneous with post-ore mineralisation at Storm.

The temperature range (~ 105 - 160°C), based on the assumption of the precipitating fluid being a low- to mid-latitude (20° to 30°N) fluid of meteoric origin, is beyond ambient burial (<1 km) temperatures (Fig. 15C), and requires the circulation of an external, relatively hot fluid to

precipitate abundant quartz cement. This temperature range would be conducive to the precipitation of quartz cement with sufficient reaction kinetics to account for the volume of Q2 (Siever, 1962, Fournier, 1985; Walderhaug, 1996; Worden, 2018) and is within the temperature range (~150°C) of the regional, meteoric fluids in the Cornwallis district (Mathieu et al., in prep.).

Regardless of whether quartz cementation accompanied reddening (and H2) or not, what is important is that porosity of the Aston Formation was not occluded by quartz cement at the time of oxidised fluid circulation (second reddening). This allows the possibility of Aston Formation sandstone acting as an aquifer and Cu source for the Storm deposit after H2 deposition but before Q2 precipitation.

Silica that is used in diagenetic quartz cementation is typically sourced from biogenic material, pressure-solution of detrital grains, clay-transformation reactions (e.g., smectite-illite), or dissolution of silicate minerals. Biogenic silica is absent in the Proterozoic Aston Formation. Because Q2 quartz cementation took place at < 1 km depth (post-dates H2, which post-dates burial), pressure solution is an unlikely Si source; although clay-induced dissolution along grain contacts can produce sufficient Si for quartz cementation (Bjørkum, 1996; Hanson et al., 2017; Ogebule et al., 2020). Smectite-illite transformation in shale can provide copious amounts of Si (Lynch et al., 1997), but mudrock is unimportant in the local stratigraphy. Detrital feldspar grains and nearby igneous dykes could have supplied Si through dissolution. The altered detrital and authigenic K-feldspars that predate Q2 growth could have supplied the Si used in quartz cementation.

If Q2 were precipitated from the pressure solution of quartz during burial, the timing of Q2 would be limited to the Paleozoic. Paleogeographic reconstructions (Cocks and Torsvik, 2011; Torsvik et al., 2012) place the Somerset Island in tropical latitudes. Low-latitude (approximate position during Silurian-Devonian) fluid isotopic compositions ($\delta^{18}\text{O}$ value of ~ 0 ‰) would require temperatures between approximately 130 and 240°C, which equates to approximately 3.5 and 7 km burial, unless the precipitating fluid was in isotopic equilibrium with the detrital quartz grains ($\delta^{18}\text{O}$ value of ~ 8 ‰), in which case unreasonable temperatures over 300°C (10 km burial) would be needed. The 3.5-7 km range could have been attained by burial by the time of the Boothia uplift and Ellesmerian orogeny (possible maximum of 6 km). A Silurian-Devonian age of Q2 would limit H2 precipitation to the late Neoproterozoic-early Paleozoic, prior to >1 km of burial. Although it is possible that Q2 can be associated with burial in the Paleozoic, the apparently close temporal association with H2 (incorporated in Q2), which requires <1 km burial and the timing of regional fluid migration (Devonian to Carboniferous) do not fit with this interpretation.

The most probable timing of Q2 is during the end stages of the Ellesmerian orogeny that is associated with circulation of a hot regional, meteoric water that could have altered silicates to produce sufficient silica for cementation.

4.6.3 Bleaching

Bleaching of redbeds through the circulation of reduced fluids that removed hematite (and therefore the red colour) is a common phenomenon in red-bed districts (e.g., Wilkinson et al., 2005; Beitler et al., 2005; MacIntyre, 2006; Gorenc and Chan, 2015). The timing of Aston Formation bleaching post-dates early hematite cement and early quartz overgrowth. Bleaching must have taken place before sufficient burial for pressure solution, because hematite grain

coatings are absent at pressure-solved grain contacts, especially sutured contacts, which requires hematite removal prior to chemical compaction. The presence of hematite at some concavo-convex grain contacts indicates that the sandstone was bleached, rather than that the sediment never had hematite coatings. It also indicates that bleaching was incomplete and patchy. The possible timing of bleaching could have been during burial of the Aston Formation, during Hunting Formation before thickness was sufficient for quartz pressure solution, and in the Paleozoic prior to sufficient burial for quartz pressure solution. After the Ellesmerian orogeny, Somerset Island was a locale of erosion rather than deposition, therefore no further opportunities for quartz pressure solution after bleaching; also, there was no major driving mechanism for reduced fluid migration through the region, after the Ellesmerian orogeny.

Hematite-coated grains in the Hunting Formation indicate that bleaching post-dated most Hunting Formation deposition. Mobilisation of a reduced fluid in equilibrium with basement rocks is associated with the Ellesmerian orogeny (Mathieu et al., 2018). The maximum (preserved) thickness of the Paleozoic succession would have been attained by the onset of the Ellesmerian orogeny, allowing for quartz pressure solution to occur, therefore, the bleaching would have had to have been temporally associated with burial and could explain the patchiness of the bleaching. A diagenetic history of the Peel Sound Formation (the youngest preserved Paleozoic rocks) may elucidate if there was any burial of this formation that may have been related to the Ellesmerian orogeny, as well as indicating whether bleaching was before or after Peel Sound Formation deposition.

The Ellesmerian orogeny, and therefore (near) maximum burial, is the most reasonable time for reduced fluid mobilisation through the Aston Formation. The Eurekan orogeny caused some

fault reactivation and movement in the Cenozoic on Somerset Island (Kerr, 1977a), but no evidence of fluid mobilisation is associated with it at Storm.

4.6.4 Aston Formation as an aquifer or aquitard

Hiatt et al. (2003), Polito et al. (2006), Hiatt et al. (2007), Kyser (2007), and Beyer et al. (2011) noted that depositional aquifers have a tendency to become diagenetic aquitards because of early cementation of porous and permeable sandstones, whereas depositional aquitards can become aquifers by being either relatively more permeable/porous than the diagenetic aquitard or through dissolution. Bleached samples of the Aston Formation typically have no Q2 (or very little) and more sutured contacts compared to unbleached samples. Sample D11 (bleached) for example, is the best sorted sample and would have been a good depositional aquifer. This sample is composed almost entirely of sutured grains of quartz; it has the most abundant Q1 cement of the samples, with no feldspar framework grains, no H2, and no Q2. The absence in this sample of paragenetic stages after Q1 indicates that it became a diagenetic aquitard, preventing the flow of diagenetic fluids. The more poorly sorted samples, or sections of samples, are typically more abundant in H2 and Q2 and may indicate that these samples acted as depositional aquitards, relative to the well-sorted samples, but became diagenetic aquifers for the later reddening and Q2-precipitating fluids. It is possible, therefore, that diagenetic fluid flow was facies controlled, similar to sandstones in the Berants Sea (Hanson et al., 2017) and McArthur Basin (Australia; Polito et al., 2006), where different facies controlled different amounts of cementation.

4.6.5 Relationship to Storm mineralising fluids

The mineral paragenesis of the Storm deposit is divided into pre-ore, main-ore, and post-ore stages (Mathieu et al., 2018). Pre-ore mineralisation resulted from reduced fluids that equilibrated with basement (-derived) rocks and then mixed with a regional metalliferous fluid at the site of precipitation during the onset of the Ellesmerian orogeny. This reduced fluid's geochemical characteristics are similar to those of the reducing fluid that bleached the Aston Formation at approximately the time of maximum burial. Metals can be liberated along with Fe by the bleaching process, in relatively minor amounts compared to the reddening process, and would explain the trace element geochemistry (e.g., abundant Co) of pre-ore sulphides at Storm (Mathieu et al., 2018). This process is similar to relationships documented in the Irish midlands, where bleached redbeds were the source of trace element concentrations (e.g., Co, Ni, and Cu) in sulphides (Wilkinson et al., 2005). The reduced fluid responsible for bleaching the Aston Formation may have contributed to the small amount of pre-ore Storm copper mineralisation.

The main-ore stage at Storm is associated with a post (or late)-Ellesmerian (i.e., maximum burial) oxidised meteoric fluid that transported Cu (and other base metals) as a chloride complex was delivered to the Storm area and reduced on site (Mathieu et al., 2018). The introduction of an oxidised, Na-enhanced meteoric fluid after circulation of a reduced fluid and maximum burial is similar to the diagenetic history of the Aston Formation [i.e., reduced bleaching fluid circulation was followed by oxidised (reddening) fluid circulation]. Copper adsorbed onto the oxyhydroxide would have been released into the fluid from the recrystallisation of the oxyhydroxide to hematite during the reddening process by oxidised meteoric fluid (Brown, 2005; 2009) agrees with the fluid history of the Storm copper deposit. A late Paleozoic, mid-latitude meteoric water responsible for quartz cementation and reddening in the Aston Formation, and

responsible for the main-ore stage at Storm, agrees with age estimates for the main-ore at Storm copper (Mathieu et al., 2018) and with the age and geographic position of sediment-hosted stratiform Cu deposits globally (Hitzman et al., 2005).

Circulation of hot mineralising fluids of the carbonate-rock-hosted Zn-Pb (MVT) deposits in the Illinois basin gradually occluded source rock pores with quartz cement during (or shortly after) precipitation of the deposits (Hyodo et al., 2014). A similar situation could have taken place for the Storm copper deposit, in that the mineralising fluid probably circulated through the Aston Formation sandstone while initially transporting Cu away from, but eventually precipitating quartz cement in, the sandstone source rock shortly afterwards. This may also be reflected in some early Q2 (i.e., closest to grain margins) that appears to incorporate some hematite ‘colloids’ (Fig. 11E, F). Therefore, the diagenetic history of the Aston Formation documented in this study is compatible with the paragenetic history of the overlying Storm copper deposit, and the Aston Formation redbeds were plausibly the metal source for the Storm deposit.

4.7 Conclusions

The diagenetic and fluid histories recorded in the Aston Formation redbed succession indicate multiple fluid circulation events since the formation’s deposition in the Proterozoic. Precipitation of early hematite grain-coatings and early quartz cement took place in the Proterozoic. At some later time, and at deeper burial (>1.5 km), extensive pressure-solution of sandstone quartz particles occurred. A mid-Paleozoic reducing fluid, plausibly related to the pre-ore event at Storm, bleached (reduced) some of the early hematite, and may be associated with the reduced

fluid responsible for pre-ore mineralization at Storm Cu. The most important fluid migration event, in terms of porosity reduction and Cu transportation, took place after maximum burial, in the late Paleozoic, with the circulation of low-latitude meteoric water. This warm fluid produced a second generation of hematite grain coatings in the Aston Formation, but also liberated Cu, which migrated a short distance and was reduced at the Storm copper deposit. The last paragenetic phase was pore-occluding quartz cementation with silica probably sourced from silicate dissolution, probably a combination of feldspar and clay-induced quartz dissolution. The presence of an anomalous Cu deposit in a Zn-Pb district can therefore be explained by the diagenetic history of a geographically limited metal-source unit. Based primarily on field and petrographic evidence, this study demonstrates that metal liberation by diagenetic reddening (oxidation) of subsurface siliciclastic units is a geochemically and geologically viable source of Cu in sedimentary-rock-hosted Cu deposits.

4.8 Acknowledgements

Financial support was supplied in part by a grant through the Geological Survey of Canada GEM-II program; field support, logistics, and analytical support were through a NSERC-Discovery Grant to E. Turner and Polar Continental Shelf Project (NRCan).

4.9 References

- Beitler, B., Parry, W.T., Chan, M.A., 2005. Fingerprints of fluid flow: chemical diagenetic history of the Jurassic Navajo sandstone, southern Utah, U.S.A. *Journal of Sedimentary Research*, **75**, 547-561.
- Bell, F.G., 1978. Petrographical factors relating to porosity and permeability in the Fell Sandstone. *Journal of Engineering Geology*, **11**: 113-126.
- Berger, G., Lacharpagne, J.C., Velde, B., Beaufort, D., Lanson, B., 1997. Kinetic constraints for mineral reactions in sandstone/shales sequences and modelling of the effect of the organic diagenesis. *Applied Geochemistry*, **12**, 23-35.
- Beyer, S.R., Hiatt, E.E., Kyser, K., Dalrymple, R.W., Pettman, C., 2011. Hydrogeology, sequence stratigraphy and diagenesis in the Paleoproterozoic western Thelon Basin: Influences on unconformity-related uranium mineralization. *Precambrian Research*, **187**, 293-312.
- Beyer, S.R., Hiatt, E.E., Kyser, K., Drever, G.L., Marlatt, J., 2015. Stratigraphy, diagenesis and geological evolution of the Paleoproterozoic Roraima Basin, Guyana: Links to tectonic events on the Amazon Craton and assessment for the uranium mineralization potential. *Precambrian Research*, **267**, 227-249.
- Bjørkum, P.A., 1996. How important is pressure in causing dissolution of quartz in sandstones? *Journal of Sedimentary Research*, **66**, 147-154.
- Bjørlykke, K., 1998. Clay mineral diagenesis in sedimentary basins – A key to the prediction of rock properties. Examples from the North Sea Basin. *Clay Minerals*, **33**, 15-34.

- Bjørlykke and Egeberg, 1993. Quartz cementation in sedimentary basins. *AAPG Bulletin*, **77**: 1538-1548.
- Bonnetti, C., Cuney, M., Malartre, F., Michels, R., Liu, X., Peng, Y., 2015. The Nuheting deposit, Erlan Basin, NE China: Synsedimentary to diagenetic uranium mineralization. *Ore Geology Reviews*, **69**, 118-139.
- Brown, M.C. Oliver, N.H.S., Dickens, G.R., 2004. Veins and hydrothermal fluid flow in the Mt. Whaleback Iron Ore District, eastern Hamersley Province, Western Australia. *Precambrian Research*, **128**, 441-474.
- Brown, A.C., 2005. Refinements for footwall red-bed diagenesis in the Sediment-hosted stratiform copper deposits model. *Economic Geology*, **100**: 763-771
- Brown, A.C., 2009. A process-based approach to estimating the copper derived from red beds in the sediment-hosted stratiform copper deposit model. *Economic Geology*, **104**: 857-868.
- Brown, R.L., Dalziel, I.W.D., Rust, B.R., 1969. The structure, metamorphism, and development of the Boothia Arch, Arctic Canada. *Canadian Journal of Earth Sciences*, **6**: 525-543.
- Busch, B., Hilgers, C., Gronen, L., Adelman, D., 2017. Cementation and structural diagenesis of fluvio-aeolian Rotliegend sandstones, northern England. *Journal of the Geological Society*, **174**, 855-868.
- Butterfield, N.J., 2000. *Bangiomorpha pubescens* n. gen., n. sp.: implications for the evolution of sex, multicellularity, and the Mesoproterozoic/Neoproterozoic radiation of eukaryotes. *Paleobiology*, **26**, 386-404.

- Butterfield, N.J., Knoll, A.H., Swett, K., 1990. A Bangiophyte Red Alga from the Proterozoic of Arctic Canada. *Science*, **250**, 104-107.
- Cocks, L.R.M., Torsvik, T.H., 2011. The Palaeozoic geography of Laurentia and western Laurussia: A stable craton with mobile margins. *Earth-Science Reviews*, **106**, 1-51.
- Csank, A.Z., Patterson, W.P., Eglington, B.M., Rybczynski, N., Basinger, J.F., 2011. Climate variability in the Early Pliocene Arctic: Annually resolved evidence from stable isotope values of sub-fossil wood, Ellesmere Island, Canada. *Palaeogeography, Palaeoclimatology, Palaeoecology* **308**, 339-349.
- Davies, G.R., Nassichuk, W.W., 1991. Carboniferous and Permian history of the Sverdrup Basin, Arctic Islands, in: Trettin, H.P. (Ed.), *Geology of the Inuitian Orogen and Arctic Platform of Canada and Greenland*, Geological Survey of Canada, *Geology of Canada*. pp. 345–368.
- de Oliveira, R.S., Truckenbrodt, W., 2019. Provenance and diagenesis of Guama Sandstone, northeastern Pera, Brazil: A Silurian link between the Amazonas and Parnaíba basins. *Journal of South American Earth Sciences*, **90**, 265-281.
- Debruyne, A., Hulsbosch, N., Muchez, P., 2016. Unravelling rare earth element signatures in hydrothermal carbonate minerals using a source-sink system. *Ore Geology Reviews*, **72**, 232-252.
- Delavau, C., Stadnyk, T., Birks, J., 2011. Model based spatial distribution of oxygen-18 isotopes in precipitation across Canada. *Canadian Water Resources Journal*, **36**, 313-330.

- Dewing, K., Obermajer, M., 2009. Lower Paleozoic thermal maturity and hydrocarbon potential of the Canadian Arctic Archipelago. *Bulletin of Canadian Petroleum Geology*, **57**, 141–166.
- Dewing, K., Turner, E., and Harrison, J.C., 2007a, Geological history, mineral occurrences and mineral potential of the sedimentary rocks of the Canadian Arctic Archipelago, *in* Goodfellow, W.D., ed., *Mineral Deposits of Canada: A Synthesis of Major Deposit-Types, District Metallogeny, the Evolution of Geological Provinces, and Exploration Methods*: Geological Association of Canada, Mineral Deposits Division, Special Publication No. 5, p. 733-753.
- Dewing, K., Sharp, R.J., Turner, E., 2007, Synopsis of the Polaris Zn-Pb District, Canadian Arctic Islands, Nunavut, *in* Goodfellow, W.D., ed., *Mineral Deposits of Canada: A Synthesis of Major Deposit-Types, District Metallogeny, the Evolution of Geological Provinces, and Exploration Methods*: Geological Association of Canada, Mineral Deposits Division, Special Publication No. 5, p. 655-672.
- Diamond, L.W., Wanner, C., Weber, H.N., 2018. Penetration depth of meteoric water in orogenic geothermal systems. *Geology*, **46**, 1063-1066.
- Dixon, J., 1974. Revised stratigraphy of the Hunting Formation (Proterozoic), Somerset Island, Northwest Territories. *Canadian Journal of Earth Science*, **11**: 635-642.
- Dixon, O.A., Williams, S.R., Dixon, J., 1971. The Aston Formation (? Proterozoic) on Prince of Wales Island, Arctic Canada. *Canadian Journal of Earth Sciences*, **8**: 732-742.

- Eichhubl, P., Taylor, W.L., Pollard, D.D., Aydin, A., 2004. Paleo-fluid flow and deformation in the Aztec Sandstone at the Valley of Fire, Nevada – Evidence for the coupling of hydrogeologic, diagenetic, and tectonic processes. *GSA Bulletin*, **116**: 1120-1136.
- Elshahat, O.R., 2017. Diagenesis and reservoir quality of the Nubia sandstone and Nukhul formations in Zeit Bay oil field, Gulf of Suez, Egypt. *Sedimentology of Egypt*, **23**: 17-32.
- Embry, A.F., 1991a. Middle-Upper Devonian clastic wedge of the Arctic Islands. In: Trettin, H.P. (Ed.), *Geology of the Inuitian Orogen and Arctic Platform of Canada and Greenland*. Geological Survey of Canada, *Geology of Canada*, pp. 261–291.
- Everett, C.E., Rye, D.M., Ellam, R.M., 2003. Source or sink? An assessment of the role of the Old Red Sandstone in the genesis of the Irish Zn-Pb deposits. *Economic Geology*, **98**: 31-50.
- Fahrig, W.F., Christie, K.W., Jones, D.L., 1981. Paleomagnetism of the Bylot basins: evidence for Mackenzie continental tensional tectonics. *Geological Survey of Canada Paper* 81–10, 303–312.
- Fournier, R.O., 1985. The Behavior of silica in hydrothermal solutions. In: Berger, B.R. (Ed.), *Geology and Geochemistry of Epithermal Systems, Reviews in Economic Geology*, no. 2, p. 45-61.
- Frisch, T., 2011. *Geology, Precambrian geology of northern Boothia Peninsula and Somerset Island, Nunavut*. GSC Open File 6051, map 1:250000.

- Garcia-Alonso, D., Canet, C., González-Partida, E., Villanueva-Estrada, R.E., Prol-Ledesma, R.M., Alfonso, P., Caballero-Martinez, J.A., Cruz, R.L., 2011. The Cretaceous sediment-hosted copper deposits of San Marcos (Coahuila, Northeastern Mexico): An approach to ore-forming processes. *Journal of South American Earth Sciences*, **31**, 432-443.
- Garden, I.R., Guscott, S.C., Burley, S.D., Foxford, K.A., Walsh, J.J., Marshall, J., 2001. An exhumed palaeo-hydrocarbon migration fairway in a faulted carrier system, Entrada Sandstone of SE Utah, U.S.A. *Geofluids*, **1**, 195-213.
- Goldhaber, M.B., Church, S.E., Doe, B.R., Aleinikoff, J.N., Brannon, J.C., Podosek, F.A., Mosier, E.L., Taylor, C.D., Gent, C.A., 1995. Lead and sulfur isotope investigation of Paleozoic sedimentary rocks from the southern midcontinent of the United States: implications for paleohydrology and ore genesis of the southeast Missouri lead belts. *Economic Geology*, **90**, 1875-1910.
- Goldstein, R.H., Rossi, C., 2002. Recrystallization in quartz overgrowths. *Journal of Sedimentary Research*, **72**, 432-440.
- Gorenc, M.A. and Chan, M.A., 2015. Hydrocarbon-induced diagenetic alteration of the Permian White Rim Sandstone, Elaterite Basin, southeast Utah. *AAPG Bulletin*, **99**: 807-829.
- Hansen, H.N., Løvstad, K., Müller, R., Jahren, J., 2017. Clay coating preserving high porosities in deeply buried intervals of the Stø Formation. *Marine and Petroleum Geology*, **88**, 648-658.
- Harrison, J.C., Fox, F.G., Okulitch, A.V., 1991. Late Devonian – Early Carboniferous deformation of the Parry Islands and Canrobert Hills fold belts, Bathurst and Melville

islands. In: Trettin, H.P. (Ed.), *Geology of the Innuitian Orogen and Arctic Platform of Canada and Greenland*. Geological Survey of Canada, *Geology of Canada*, pp. 321-333.

Haynes, D.W., 1986. Stratiform copper deposits hosted by low-energy sediments: II. Nature of source rocks and composition of metal-transporting water. *Economic Geology*, **81**: 266-280.

Heaman, L.M., Lecheminant, A.N., Rainbird, R.H., 1992. Nature and timing of Franklin igneous events, Canada: implications for a late Proterozoic mantle plume and the break-up of Laurentia. *Earth Planetary Science Letters*, **109**: 117–131.

Heidari, M., Momeni, A.A., Rafiei, B., Khodabakhsh, S., Torabi-Kaveh, M., 2013. Relationship between petrographic characteristics and the engineering properties of Jurassic sandstones, Hamedan, Iran. *Mechanical rock engineering*, **46**: 1091-1101.

Hiatt, E.E., Kyser, T.K., Dalrymple, R.W., 2003. Relationships among sedimentology, stratigraphy and diagenesis in the Proterozoic Thelon Basin, Nunavut, Canada: implications for paleoaquifers and sedimentary-hosted mineral deposits. *The Journal of Geochemical Exploration*, **80**, 221-240.

Hiatt, E.E., Kyser, T.K., Fayek, M., Polito, P., Holk, G.J., Riciputi, L.R., 2007. Early quartz cements and evolution of paleohydraulic properties of basal sandstones in three Paleoproterozoic continental basins: Evidence from in situ $\delta^{18}\text{O}$ analysis of quartz cements. *Chemical Geology*, **238**, 19-37.

Hitzman, M.W., Kirkham, R., Broughton, D., Thorson, J., Selley, D., 2005. The sediment hosted stratiform copper ore system. *Economic Geology*, **100**: 609–642.

- Hyodo, A., Kozdon, R., Pollington, A.D., Valley, J.W., 2014. Evolution of quartz cementation and burial history of the Eau Claire Formation based on in situ oxygen isotope analysis of quartz overgrowths. *Chemical Geology*, **384**, 168-180.
- Jackson, G.D., Iannelli, T.R., 1981. Rift-related cyclic sedimentation in the Neohelikian Borden Basin, northern Baffin Island. In: Campbell, F.H.A. (Ed.), *Proterozoic basins of Canada*. Geological Survey of Canada Paper, pp. 269–302.
- Kelly, J.L., Fu, B., Kita N.T. & Valley J.W., 2007. Optically continuous silcrete quartz cements of the St. Peter Sandstone: high precision oxygen isotope analysis by ion microprobe. *Geochimica et Cosmochimica Acta*, **71**: 3812-3832,
- Kerr, J.W., 1977a. Cornwallis Fold Belt and the mechanism of basement uplift. *Canadian Journal of Earth Science*, **14**, 1374-1401.
- Kerr, J.W., 1977b. Cornwallis lead-zinc district; Mississippi Valley-type deposits controlled by stratigraphy and tectonics. *Canadian Journal of Earth Science*, **14**, 1402-1426.
- Kyser, K., 2007. Fluids, basin analysis, and mineral deposits. *Geofluids*, **7**, 238-257.
- Lanson, B., Beaufort, D., Berger, G., Baradat, J., Lacharpagne, J.C., 1996. Late-stage diagenesis of clay minerals in porous rocks: Lower Permian Rotliegendes reservoir off-shore of The Netherlands. *Journal of Sedimentary Research*, **66**, 501-518.
- Lanson, B., Beaufort, D., Berger, G., Bauer, A., Cassagnabère, A., Meunier, A., 2002. Authigenic kaolin and illitic minerals during burial diagenesis of sandstones: a review. *Clay Minerals*, **37**, 1-22.

- LeCheminant, A.N., Heaman, L.M., 1989. Mackenzie igneous events, Canada: middle Proterozoic hotspot magmatism associated with ocean opening. *Earth and Planetary Science Letters*, **96**: 38-48.
- Long, D.G.F., Turner, E.C., 2012. Tectonic, sedimentary and metallogenic re-evaluation of basal strata in the Mesoproterozoic Bylot basins, Nunavut, Canada: Are unconformity-type uranium concentrations a realistic expectation? *Precambrian Research*, **214-215**, 192-209.
- Luz, B. and Barkan, E., 2010. Variations of $^{17}\text{O}/^{16}\text{O}$ and $^{18}\text{O}/^{16}\text{O}$ in meteoric waters. *Geochimica et Cosmochimica Acta*, **74**: 6276-6286.
- Lynch, F.L., Mack, L.E., Land, L.S., 1997. Diagenesis of illite/smectite and the origins of authigenic quartz and secondary porosity in sandstones. *Geochimica et Cosmochimica Acta*, 61: 1995-2006.
- Machel, H.G., 1999. Effects of groundwater flow on mineral diagenesis, with emphasis on carbonate aquifers. *Hydrogeology Journal*, **7**, 94–107.
- Mackintyre, T.J., 2006. Fault-controlled hydrocarbon-related bleaching and sediment-hosted copper mineralization of the Jurassic Wingate Sandstone at the Cashin Mine, Montrose County, Colorado. Unpublished M.Sc. thesis, Colorado School of Mines, Golden, Colorado, 360 p.
- Martin, R.F., 1971. Disordered authigenic feldspars of the series KAlSi_3O_8 - KBSi_3O_8 from southern California. *The American Mineralogist*, **56**, 281-291.

- Mathieu, J., Turner, E.C., Kontak, D.J., Fayek, M., Mathur, R., 2017. Atypical Cu mineralisation in the Cornwallis carbonate-hosted Zn district: Storm copper deposit, Arctic Canada. *Ore Geology Reviews*, **99**: 86-115.
- Mavko, G., and Nur, A., 1997, The effect of percolation threshold in the Kozeny-Carmen relation, *Geophysics*, **62**, 1480-1482.
- Mayr, U., Brent, T.A., de Freitas, T., Frisch, T., Nowlan, G.S., Okulitch, A.V., 2004. Geology of eastern Prince of Wales Island and adjacent smaller islands, Nunavut. GSC Bulletin 574, 99p.
- McBride, E.F., 1989. Quartz cement in sandstones: a review. *Earth-Science Reviews*, **26**, 69-112.
- McBride, E.F., 2015. Diagenesis of sandstones and carbonates of the Ignacii Quartzite and McCracken Sandstone Member of the Elbert Formation, southwestern Colorado, U.S.A. *Rocky Mountain Geology*, **51**, 69-80.
- Meinhold, G., 2010. Rutile and its applications in earth sciences. *Earth-Science Reviews*, **102**, 1-28.
- Miall, A.D., 1969. Sedimentary history of the Peel Sound Formation, Prince of Wales Island, Northwest Territories. Unpublished Ph.D. thesis, University of Ottawa, Ottawa, Ontario, 390p.
- Miall, A.D., 1970. Devonian alluvial fans, Prince of Wales Island, Arctic Canada. *Journal of Sedimentary Petrology*, **40**, 556-571.

- Miall, A.D., 1986. Effects of Caledonian tectonism in Arctic Canada. *Geology*, **14**: 904–907.
- Miall, A.D., Gibling, M.R., 1978. The Siluro-Devonian clastic wedge of Somerset Island, Arctic Canada, and some regional paleogeographic implications. *Sedimentary Geology*, **21**, 85-127.
- Miall, A.D., Kerr, J.W., 1977. Phanerozoic stratigraphy and sedimentology of Somerset Island. Geological Survey of Canada Paper, 77–1A, 99–106.
- Miall, A.D., Kerr, J.W., 1980. Cambrian to Upper Silurian stratigraphy, Somerset Island and northeastern Boothia Peninsula, District of Franklin, N.W.T. Geological Survey of Canada Bulletin, **315**: 1–17.
- Mitchell, I., Linnen, R.L., Creaser, R.A., 2004. The setting and age of the Bermuda Zn-Pb showing, Grinnell Peninsula, Devon Island: implications for MVT mineralization in the Canadian Arctic. *Exploration Mining Geology*, **13**, 109-118.
- Molenaar, N., Felder, M., Bär, K., Götz, A.E., 2015. What classic greywacke (litharenite) can reveal about feldspar diagenesis: An example from Permian Rotliegend sandstone in Hessen, Germany. *Sedimentary Geology*, **326**, 79-93.
- Morey, G., Hesselgesser, J.M., 1951. Solubility of minerals in superheated steam. *Economic Geology*, **46**, 821-835.
- Morris, G.A., Page, L., Martinez, V., 2005. New dates (415 Ma) for the Etive Dyke Swarm and the end of the Caledonian Orogeny in the SW Grampian Highlands of Scotland. *Journal of the Geological Society, London*, **162**, 741-744.

- Mudd, G., Jowitt, S.M., 2018. Growing global copper resources, reserves and production: Discovery is not the only control on supply. *Economic Geology*, **113**, 1235-1267.
- Ogebule, O.Y., Jahren, J., Mondol, N.H., 2020. Compaction, rock physics and rock properties of sandstones of the Stø Formation: Case study of five wells from the south-western Barents Sea, Norway. *Marine and Petroleum Geology*, **119**, 1-25.
- Okulitch, A.V., Packard, J.J., Zolnai, A.I., 1991. Late Silurian – Early Devonian deformation of the Boothia Uplift. In: Trettin, H.P. (Ed.), *Geology of the Inuitian Orogen and Arctic Platform of Canada and Greenland*. Geological Survey of Canada, *Geology of Canada*, pp. 302–307.
- Oliver, G.H., 2001. Reconstruction of the Grampian episode in Scotland: its place in the Caledonian Orogeny. *Tectonophysics*, **332**, 23-49.
- Pe-Piper, G., Piper, D.J., Dolansky, L. 2005. Alteration of ilmenite in the Cretaceous sandstones of Nova Scotia, southeastern Canada. *Clays and Clay Minerals*, **53**, 490-510.
- Perri, F., Critelli, S., Martin-Algarra, A., Martin-Martin, M., Perrone, V., Mongelli, G., Zattin, M., 2013. Triassic redbeds in the Malaguide Complex (Betic Cordillera – Spain): Petrography, geochemistry and geodynamic implications. *Earth-Science Reviews*, **117**, 1-28.
- Piepjohn, K., von Gosen, W., Tessensohn, F., 2016. The Eurekan deformation in the Arctic: an outline. *Journal of the Geological Society*, **173**, 1007–1024.

- Polito, P.A., Kyser, K., Jackson, M.J., 2006. The role of sandstone diagenesis and aquifer evolution in the formation of uranium and zinc-lead deposits, southern McArthur Basin, Northern Territory, Australia. *Economic Geology*, **101**, 1189-1209.
- Rainoldi, A.L., Franchini, M., Beaufort, D., Patrier, Giusiano, A., Impiccini, A., Pons, J., 2014. Large-scale bleaching of red beds related to upward migration of hydrocarbons: Los Chihuidos High, Neuquén basin, Argentina. *Journal of Sedimentary Research*, **84**: 373-393.
- Rajabpour, S., Abedini, A., Alipour, S., Lehmann, B., Jiang, S., 2017. Geology and geochemistry of the sediment-hosted Cheshmeh-Konan redbed-type copper deposit, NW Iran. *Ore Geology Reviews*, **86**, 154-171.
- Ramdohr, P., 1969. The ore minerals and their intergrowths. Pergamon Press, 1174 p.
- Ramm, M., 1992. Porosity-depth trends in reservoir sandstones: theoretical models related to Jurassic sandstones offshore Norway. *Marine and Petroleum Geology*, **9**: 553-567.
- Randell, R.N., Anderson, G.M., 1996. Geology of the Polaris Zn-Pb deposit and surrounding area, Canadian Arctic archipelago. *Society of Economic Geologists Special Publication No. 4*, 307-319.
- Randell, R.N., Héroux, Y., Chagnon, A., Anderson, G.M., 1997. Organic matter and clay minerals at the Polaris Zn-Pb deposit, Canadian Arctic archipelago. *Society of Economic Geologists Special Publication No. 4*, 320-329.

- Rasmussen, B., Krapež, B., Meier, D.B., 2014. Replacement origin for hematite in 2.5 Ga banded iron formation: Evidence for postdepositional oxidation of iron-bearing minerals. *GSA Bulletin*, **126** (3/4), 438-446.
- Reid, S., Dewing, K., Sharp, R., 2013a. Polaris as a guide to northern exploration: Ore textures, paragenesis and the origin of the carbonate-hosted Polaris Zn-Pb mine, Nunavut, Canada. *Ore Geology Reviews*, **51**, 27-42.
- Reid, S., Dewing, K., Sharp, R., 2013. Structural and diagenetic origin of breccias in the carbonate-hosted Polaris Zn-Pb deposit, Nunavut, Canada. *Ore Geology Reviews*, **55**, 110-124.
- Rose, A.W., 1976. The effect of cuprous chloride complexes in the origin of red-bed copper and related deposits. *Economic Geology*, **71**: 1036-1048.
- Rose, A.W., 1989. Mobility of copper and other heavy metals in sedimentary environments. *Geological Association of Canada Special Paper* **36**, 97-110.
- Rose, A.W., Bianchi-Mosquera, G.C., 1993. Adsorption of Cu, Pb, Zn, Co, Ni, and Ag on Goethite and Hematite: A control on metal mobilization from red beds into stratiform copper deposits. *Economic Geology*, **88**: 1226-1236.
- Rose, S.R.A., 1999. Sedimentology and diagenesis of the Lower Blue Fiord Formation Carbonates in a prospective Mississippi Valley-type (Pb-Zn) setting. Unpublished M.Sc. thesis, University of Calgary, Calgary, Alberta, Canada, 186 pp.

- Ryan, R.J., Boehner, R.C., Stea, R.R., and Rogers, P.J., 1989, Geology, geochemistry, and exploration applications for the Permo-Carboniferous redbed copper deposits of the Cumberland basin, Nova Scotia, Canada: Geological Association of Canada Special Paper 36, p. 245–256.
- Savard, M.M., Chi, G., Sami, T., Williams-Jones, A.E., Leigh, K., 2000. Fluid inclusion and carbon, oxygen, and strontium isotope study of the Polaris Mississippi Valley-type Zn-Pb deposit, Canadian Arctic archipelago: implications for ore genesis. *Mineralium Deposita*, **35**, 495-510.
- Schluger, P.R., 1976. Petrology and origin of the red beds of the Perry Formation New Brunswick, Canada, and Maine, USA. *Journal of Sedimentary Petrology*, **46**: 22-37.
- Selley, D., Broughton, D., Scott, R., Hitzman, M.W., Bull, S., Large, R.R., McGoldbrick, P., Croaker, M., Pollington, N., 2005. A new look at the geology of the Zambian Copperbelt. *Economic Geology*, **100**: 965–1000.
- Sharp, Z.D., Kirschner, D.L., 1994. Quartz-calcite oxygen isotope thermometry: a calibration based on natural isotopic variations. *Geochimica et Cosmochimica Acta*, **58**, 4491-4501.
- Shebi, M.A., Surdam, R.C., 1996. Redox reactions in hydrocarbon clastic reservoirs: experimental validation of this mechanism for porosity enhancement. *Chemical Geology*, **132**: 103-117.
- Siever, R., 1962. Silica solubility, 0°-200°C., and the diagenesis of siliceous sediments. *The Journal of Geology*, **70**, 127-150.

- Simbo, C.W., Potra, A., Samuelsen, J.R., 2019. A geochemical evaluation of the genetic relationship between Ouachita Mountains Paleozoic rocks and the Mississippi Valley-type mineralization in the southern Ozark Region, USA. *Ore Geology Reviews*, **112**, 18p.
- Stewart, W.D., 1983. Late Proterozoic to Early Tertiary stratigraphy of Somerset Island and northern Boothia Peninsula, District of Franklin, N.W.T. GSC Paper 83–26, 85.
- Surdam, R.C., Jiao, Z.S., MacGowan, D.B., 1993. Redox reactions involving hydrocarbons and mineral oxidants: a mechanism for significant porosity enhancement in sandstones. *American Association of Petroleum Geologist, Bulletin*, **77**, 1509-1518.
- Taylor, J.M., 1950. Pore space reduction in sandstone. *American Association of Petroleum Geology Bulletin*, **34**: 701-716.
- Tegner, C., Storey, M., Holm, P.M., Thorarinsson, S.B., Zhao, X., Lo, C.H., Knudsen, M.F., 2011. Magmatism and Eureka deformation in the high arctic large igneous province: ^{40}Ar - ^{39}Ar age of Kap Washington Group volcanics, North Greenland. *Earth and Planetary Science Letters*, **303**, 203-214.
- Thorsteinsson, R., 1980. Stratigraphy and conodonts of Upper Silurian and Lower Devonian rocks in the environs of the Boothia Uplift, Canadian Arctic Archipelago. *Geological Survey of Canada Bulletin* 292, 1-38.
- Tornos, F., Heinrich, C.A., 2008. Shale basins, sulfur-deficient ore brines and the formation of exhalative base metal deposits. *Chemical Geology*, **247**, 195-207.

- Torsvik, T.H., Van der Voo, R., Preeden, U., Niocaill, C.M., Steinberger, B., Doubrovine, P.V., van Hinsbergen, D.J.J., Domeier, M., Gaina, C., Tohver, E., Meert, J.G., McCausland, P.J.A., Cocks, L.R.M., 2012. Phanerozoic polar wander, palaeogeography and dynamics. *Earth-Science Reviews*, **114**: 325-368.
- Trettin, H.P., 1991. Tectonic Framework. In: Trettin, H.P. (Ed.), *Geology of the Inuitian Orogen and Arctic Platform of Canada and Greenland*. Geological Survey of Canada, *Geology of Canada*, pp. 59–66.
- Tuke, M.F., Dineley, D.L., Rust, B.R., 1966. The basal sedimentary rocks in Somerset Island, N.W.T. *Canadian Journal of Earth Sciences*, **3**: 697–711.
- von Noort, R., Spiers, C.J., Pennock, G.M., 2008. Compaction of granular quartz under hydrothermal conditions: controlling mechanisms and grain boundary processes. *Journal of Geophysical Research*, **113**: 1-23.
- Wahab, A.A., 1998. Diagenetic history of Cambrian quartzarenites, Ras Dib-Zeit Bay area, Gulf of Suez, eastern desert, Egypt. *Sedimentary Geology*, **121**: 121-140.
- Walderhaug, O., 1996. Kinetic modelling of quartz cementation and porosity loss in deeply buried sandstone reservoirs. *AAPG*, **80**, 731-745.
- Walker, T.R., 1967. Formation of red beds in modern and ancient deserts. *GSA Bulletin*, **78**, 353-368.
- Walker, T.R., 1976. Diagenetic origin of continental red beds. In: Falke, H. (Ed.) *The Continental Permian in Central, West, and South Europe*, p. 240-282.

- Walker, T.R., 1989. Application of diagenetic alterations in red beds to the origin of copper in stratiform copper deposits: Geological Association of Canada Special Paper **36**: p 85–96.
- Weibel, R., 1998. Diagenesis in oxidising and locally reducing conditions – an example from the Triassic Skagerrak Formation, Denmark. *Sedimentary Geology*, **121**, 259-276.
- Weibel, R., Friis, H., 2004. Opaque minerals as keys for distinguishing oxidising and reducing diagenetic conditions in the Lower Triassic Bunter Sandstone, North German Basin. *Sedimentary Geology*, **169**, 129-149.
- Wilde, A.R., Jones, P.A., Gessner, K., Aillères, L., Gregory, M.J., Duncan, R.J., 2006. A geochemical process model for the Mount Isa copper orebodies. *Economic Geology*, **101**, 1547-1567.
- Wilkinson, J.J., Eyre, S.L., Boyce, A.J., 2005. Ore-forming processes in Irish-type carbonate-hosted Zn-Pb deposits: Evidence from mineralogy, chemistry, and isotopic composition of sulfides at the Lisheen mine. *Economic Geology*, **100**, 63-86.
- Wilkinson, M., Milliken, K.L., Haszeldine, R.S., 2001. Systematic destruction of K-feldspar in deeply buried rift and passive margin sandstones. *Journal of Geological Society of London*, **158**, 675-683.
- Worden, R.H., Bukar, M., Shell, P., 2018. The effect of oil emplacement on quartz cementation in a deeply buried sandstone reservoir. *AAPG Bulletin*, **102**: 49-75.
- Yuan, G., Cao, Y., Gluyas, J., Li, X., Xi, K., Wang, Y., Jia, Z., Sun, P., Oxtoby, N., 2015. Feldspar dissolution, authigenic clays, and quartz cements in open and closed sandstone

- geochemical systems during diagenesis Typical examples from two sags in Bohai Bay Basin, east China. *AAPG Bulletin*, **99**, 2121-2154.
- Yuan, G., Cao, Y., Zhang, Y., Gluyas, J., 2017. Diagenesis and reservoir quality of sandstones with ancient “deep” incursion of meteoric freshwater – An example in the Nanpu Sag, Bohai Bay Basin, East China. *Marine and Petroleum Geology*, **82**, 444-464.
- Yuan, G., Gao, Y., Schulz, H., Hao, F., Gluyas, J., Liu, K., Yang, T., Wang, Y., Xi, K., Li, F., 2019. A review of feldspar alteration and its geological significance in sedimentary basins: From shallow aquifers to deep hydrocarbon reservoirs. *Earth-Science Reviews*, **191**, 114-140.
- Yurtsever, Y. and Gat, J.R., 1981. Atmospheric waters. In: Gat and Gofiantini (eds.) *Stable Isotope Hydrology Deuterium and Oxygen-18 in the Water Cycle*. IAEA technical report series 210, pp. 103-142.
- Zielinski, R.A., Bloch, S. and Walker, T.R., 1983. The mobility and distribution of heavy metals during the formation of first cycle red beds: *Economic Geology*, **78**: 1574–1589.

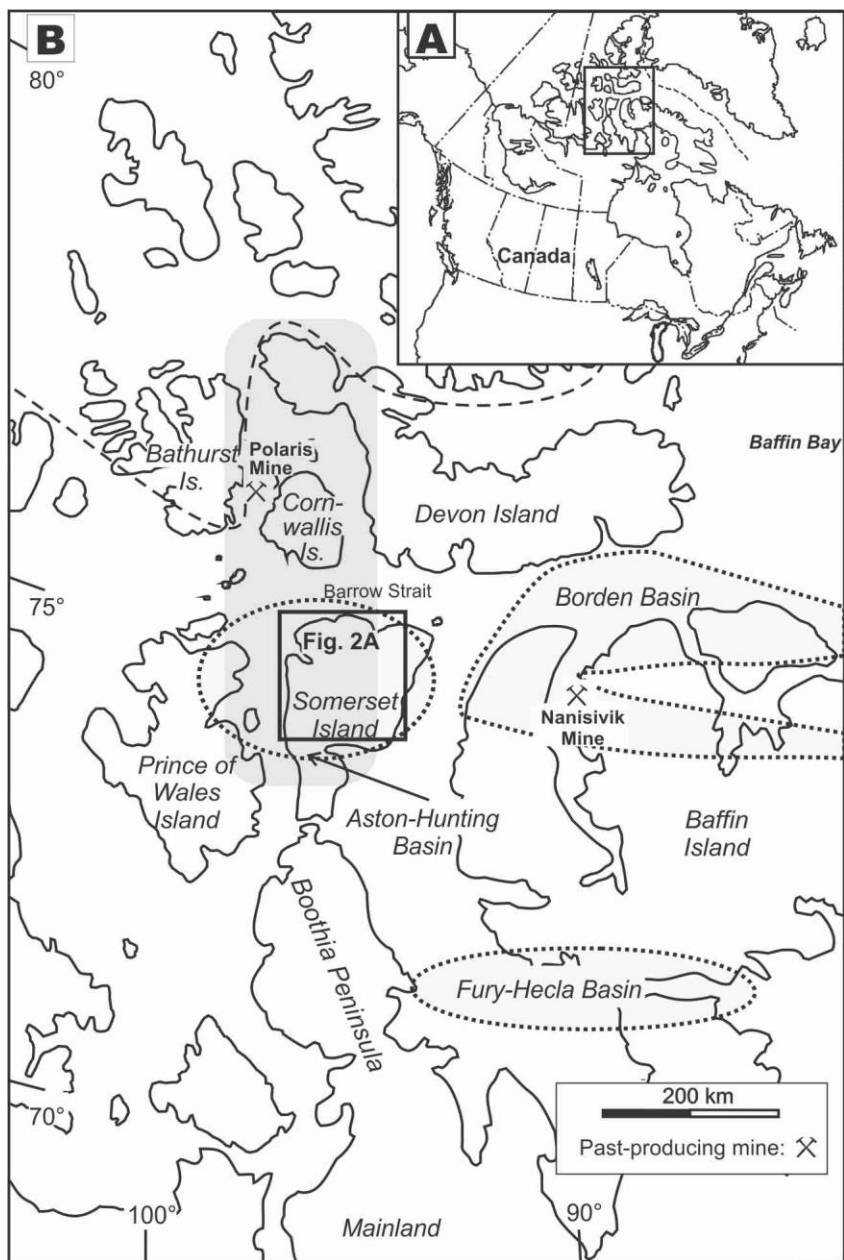


Figure 4-1: Study area

(A) Simplified map of Canada; outlined area is enlarged in (B). (B) Part of Canada's Arctic archipelago, showing the location of the Cornwallis district (shaded rectangle), Mesoproterozoic Bylot basins, past-producing mines, and the Ellesmerian orogenic front (dashed line).

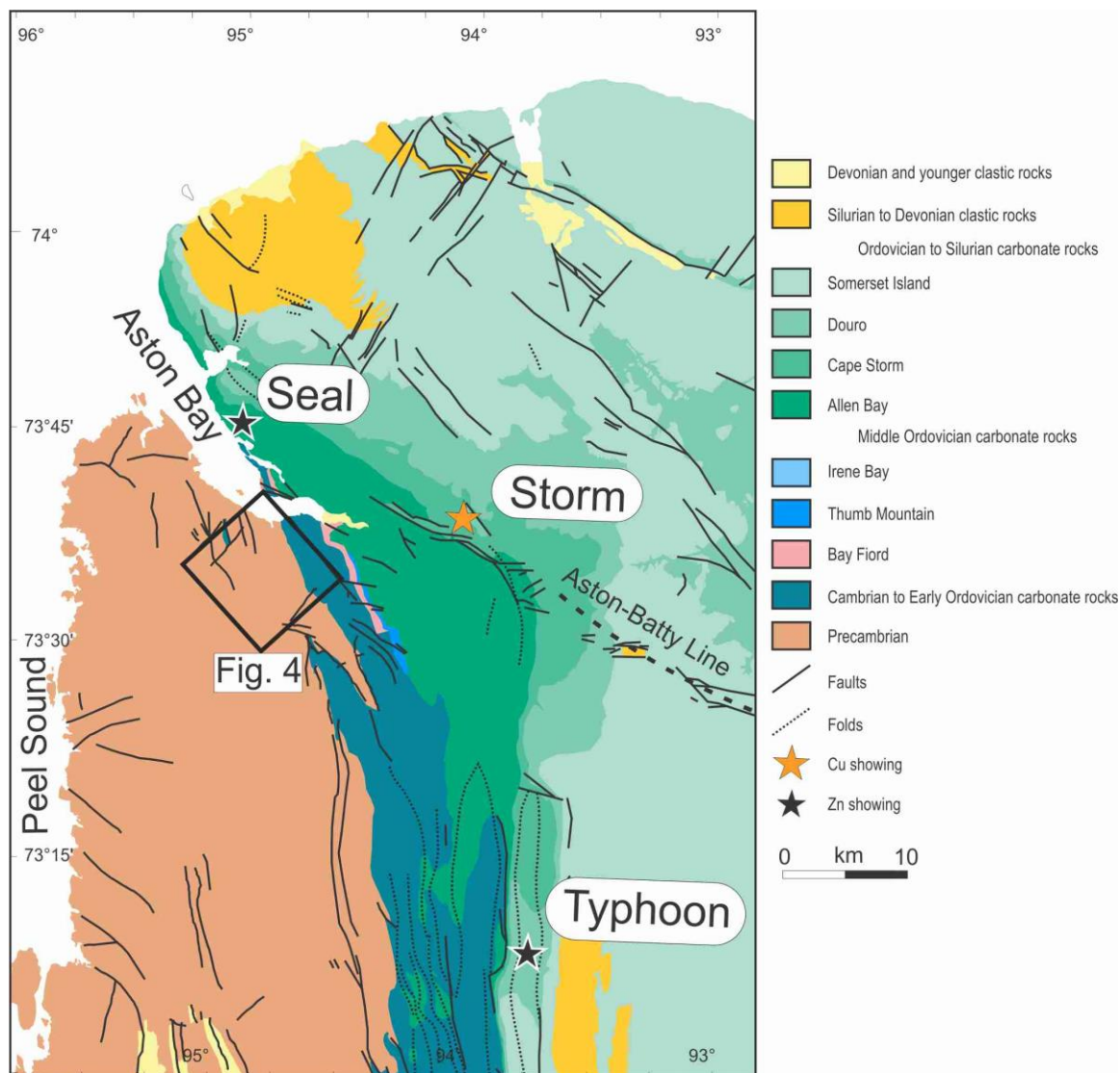


Figure 4-2: Geological map of Somerset Island

Geological map of northern Somerset Island (after Stewart and Kerr, 1984) showing the location of Cornwallis district base metal mineralisation along possible reactivated Mesoproterozoic basin structures (Aston-Batty line; Dewing et al., 2007b). Aston Formation (brown) extends at least some distance under Paleozoic strata. Black rectangle outlines area shown in Figure 6.



Figure 4-3: Typical exposure of the Aston Formation

Typical exposures of the Aston Formation. (A) Frost-shattered bedrock (Felsenmeer) has not been transported; river valley intermittent exposures in background. Near sample D3. Arrows indicate location of image 4B and 4C. (B) Typical red sandstone of Aston Formation. Near sample D5. (C) Interlayered red (diagenetically hematized) and grey (reduced) sandstone. Near sample D7.

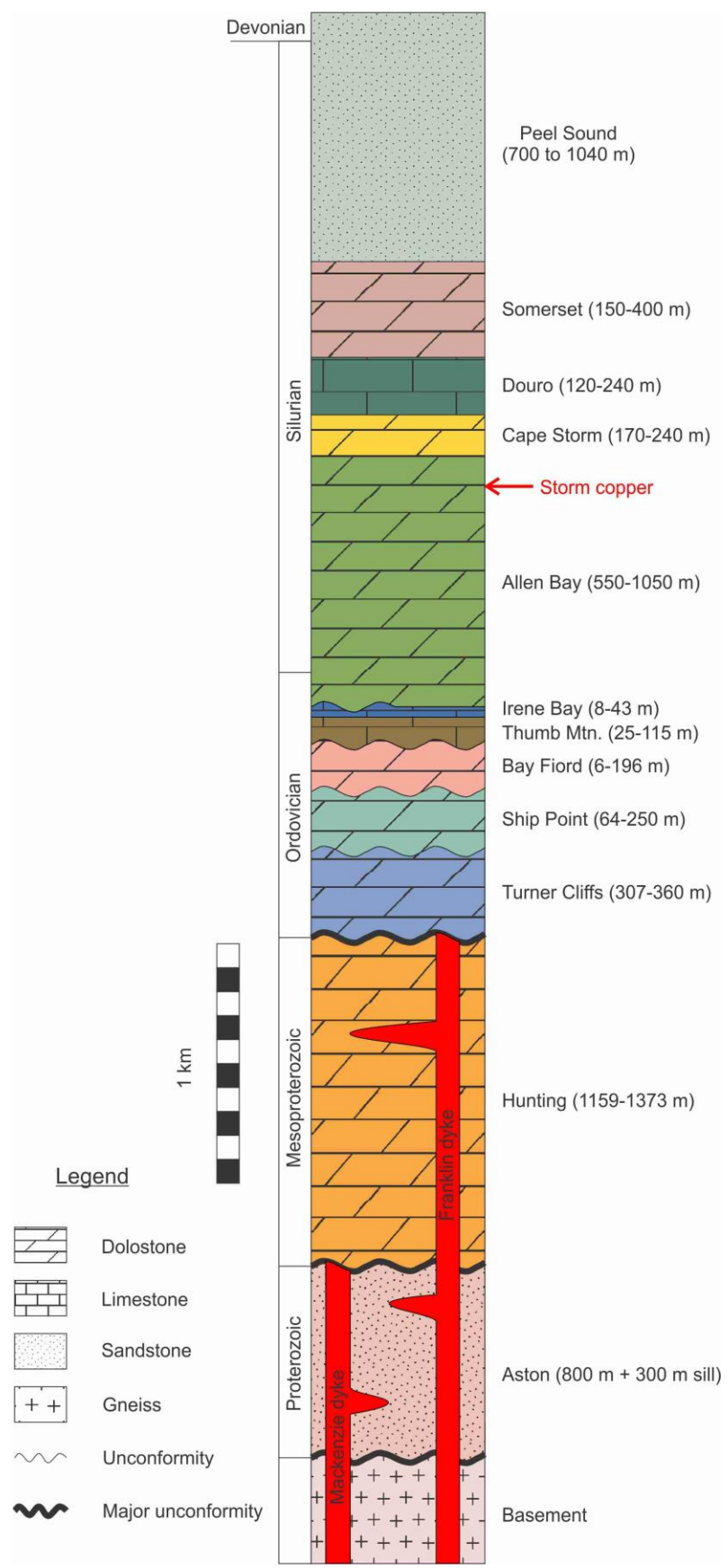


Figure 4-4: Simplified stratigraphy on Somerset Island

Simplified stratigraphic column of the geology on Somerset Island (modified from Tuke et al., 1966; Dixon, 1974; Miall and Kerr, 1980; Stewart, 1987) showing the position of the Storm copper deposit above Proterozoic Aston Formation red beds but below Silurian-Devonian Peel Sound Formation red beds.

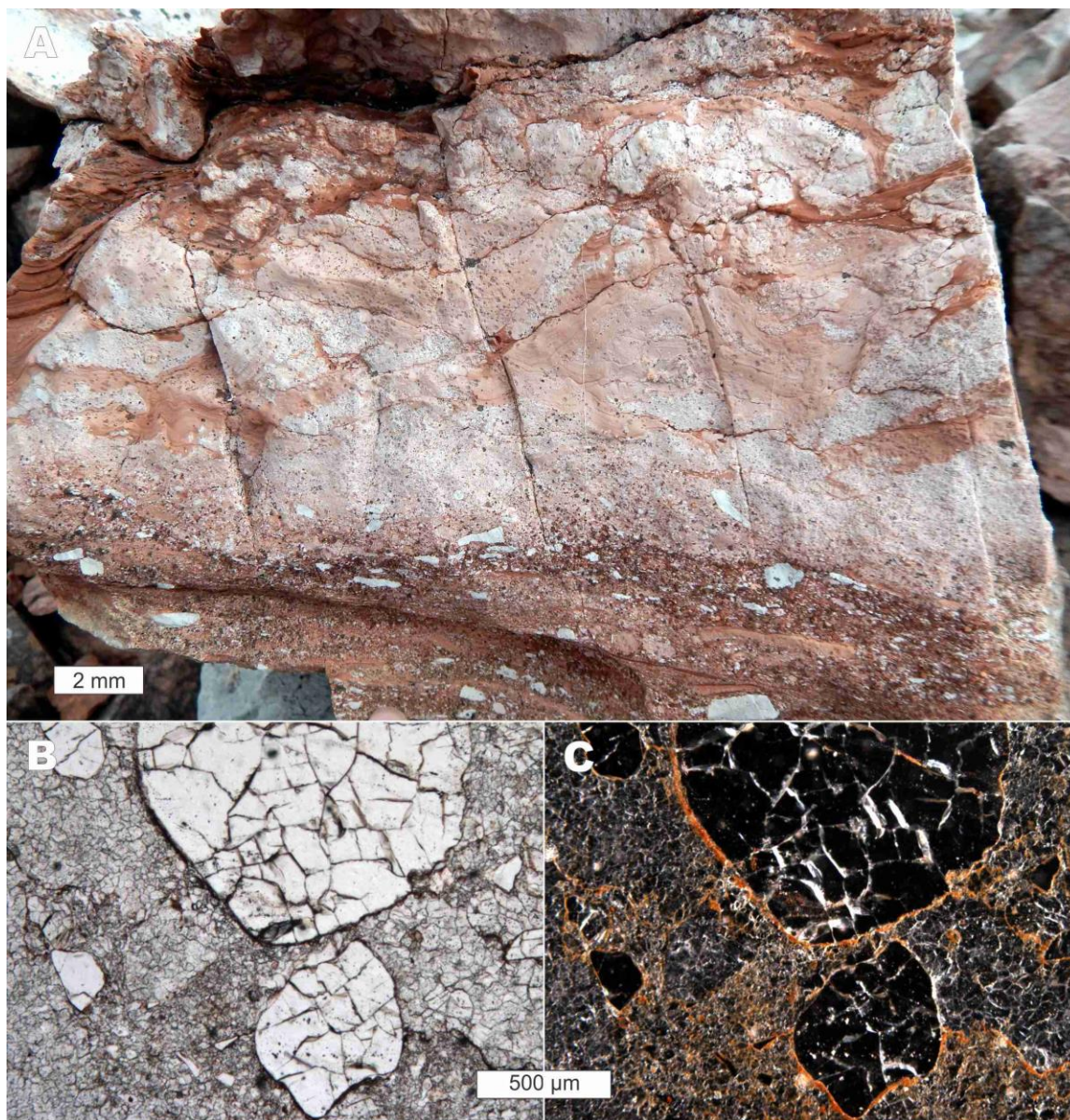


Figure 4-5: Hunting Formation features

Hunting Formation dolostone locally contains hematite-coated quartz grains inherited from Aston Formation. (A) A lag of reworked hematite-coated quartz grains and carbonate intraclasts in the upper Hunting Formation. (B) Partly hematite-coated quartz sand particles from samples in (A) under plane-polarised light. (C) Hematite-coated quartz sand clasts in oblique reflected light. The presence of reworked hematite-coated Aston Formation particles in Hunting Formation dolostone indicates that diagenetic hematite coatings developed in the burial environment after

Aston Formation deposition and before Hunting Formation deposition, and that Aston Formation was at least locally exposed during Hunting Formation deposition.

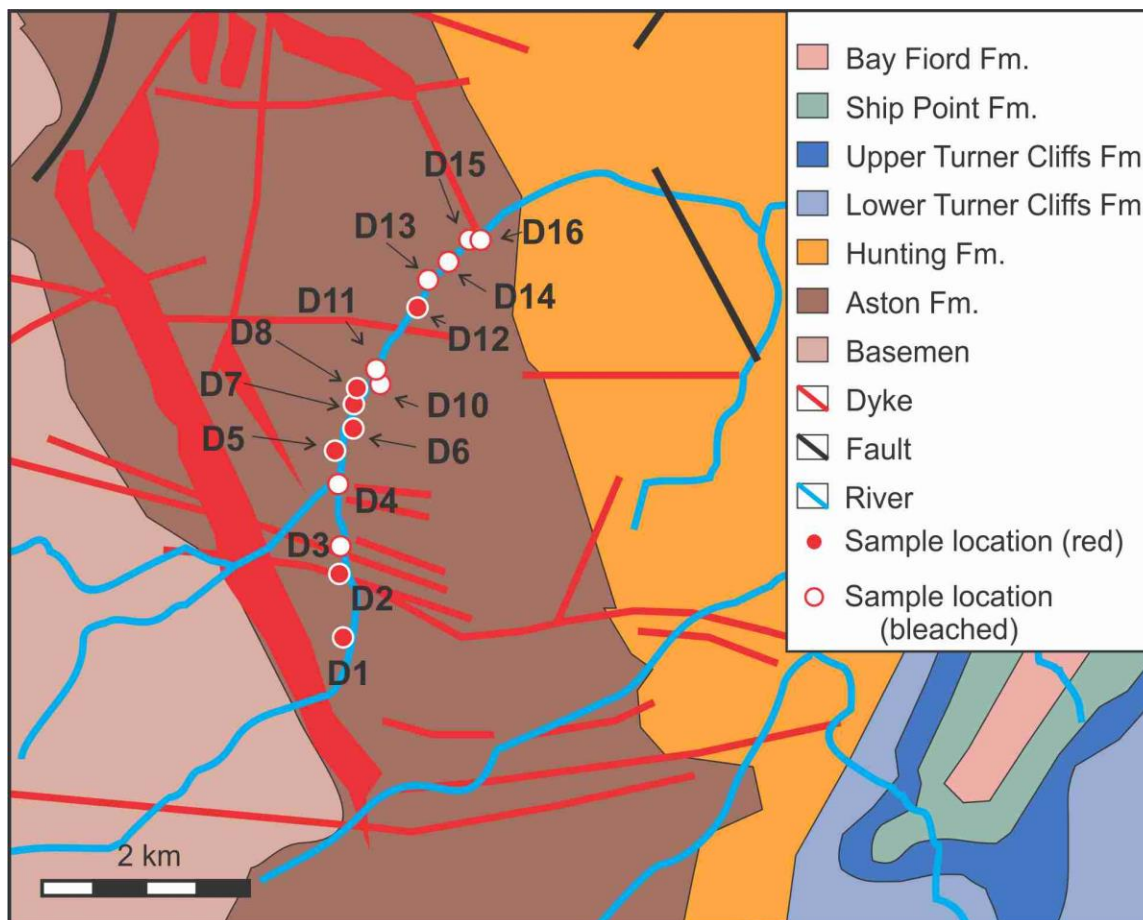


Figure 4-6: Simplified local geology of Hunting River, Somerset Island

Simplified local geology map of rectangle area in Figure 2 showing sample localities along a transect through the Aston Formation.

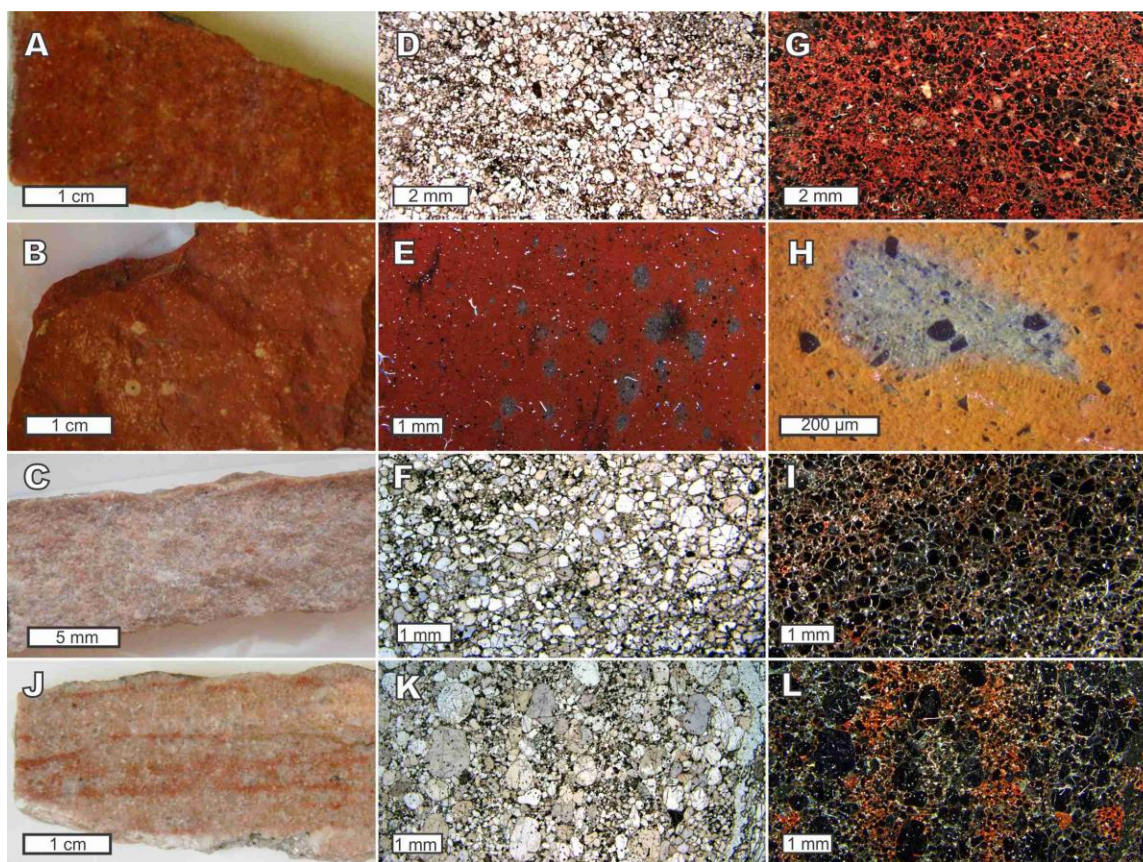


Figure 4-7: Representative samples of Aston Formation

Representative samples of the Aston Formation. (A-C) Typical unbleached material (sample D-2). (D-F) Typical bleached material (sample D-14). (G-I) Partly bleached samples contain patches of hematite-coated grains (sample D-10). (J-L) Reduced spots in red samples. Plane-polarised transmitted-light (B, E, H) and oblique reflected-light petrography (C, F, I, K, L) shows that rock colour is related to the amount of hematite cement around the grains and that oblique reflected light highlights the hematite cement.

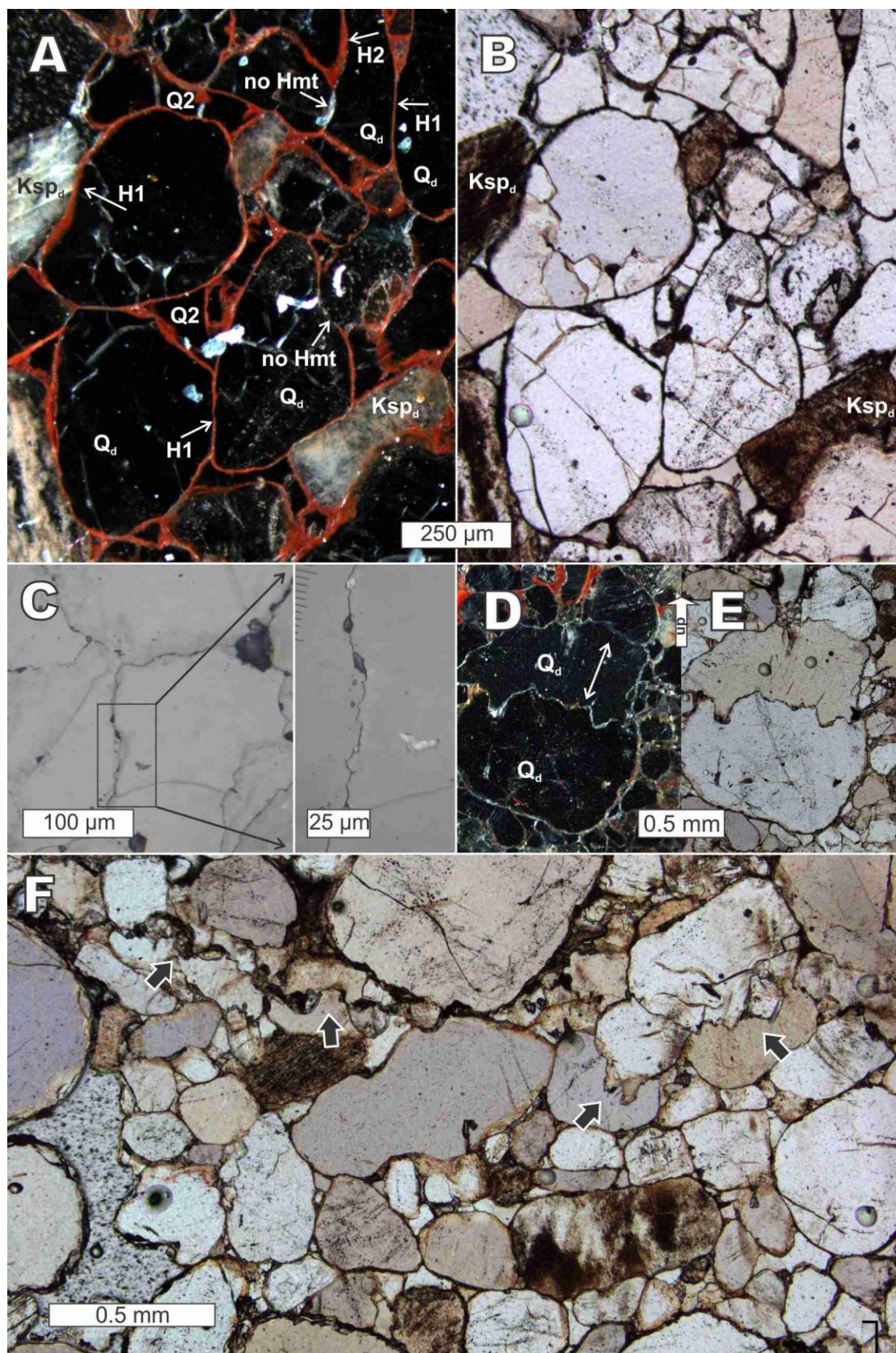


Figure 4-8: Aston Formation grain contacts

Photomicrographs of characteristic grain contacts Aston Formation sandstone. (A) Oblique incident and (B) plane-polarised transmitted light images showing typical long, concavo-convex grain contacts, some of which have hematite preserved between grains (sample D12). (C) Reflected-light micrograph of sutured grain contacts with irregular amplitude contacts, some of which have corrosion pits filled with clay (illite). (D) Oblique incident and (E) plane-polarised transmitted light micrographs of a stylolite through a quartz grains with no hematite along suture (sample D4). Up arrow indicates present-day up. (F) Plane-polarised transmitted-light image of a stylolite (arrows) through multiple quartz grains. (sample D4).

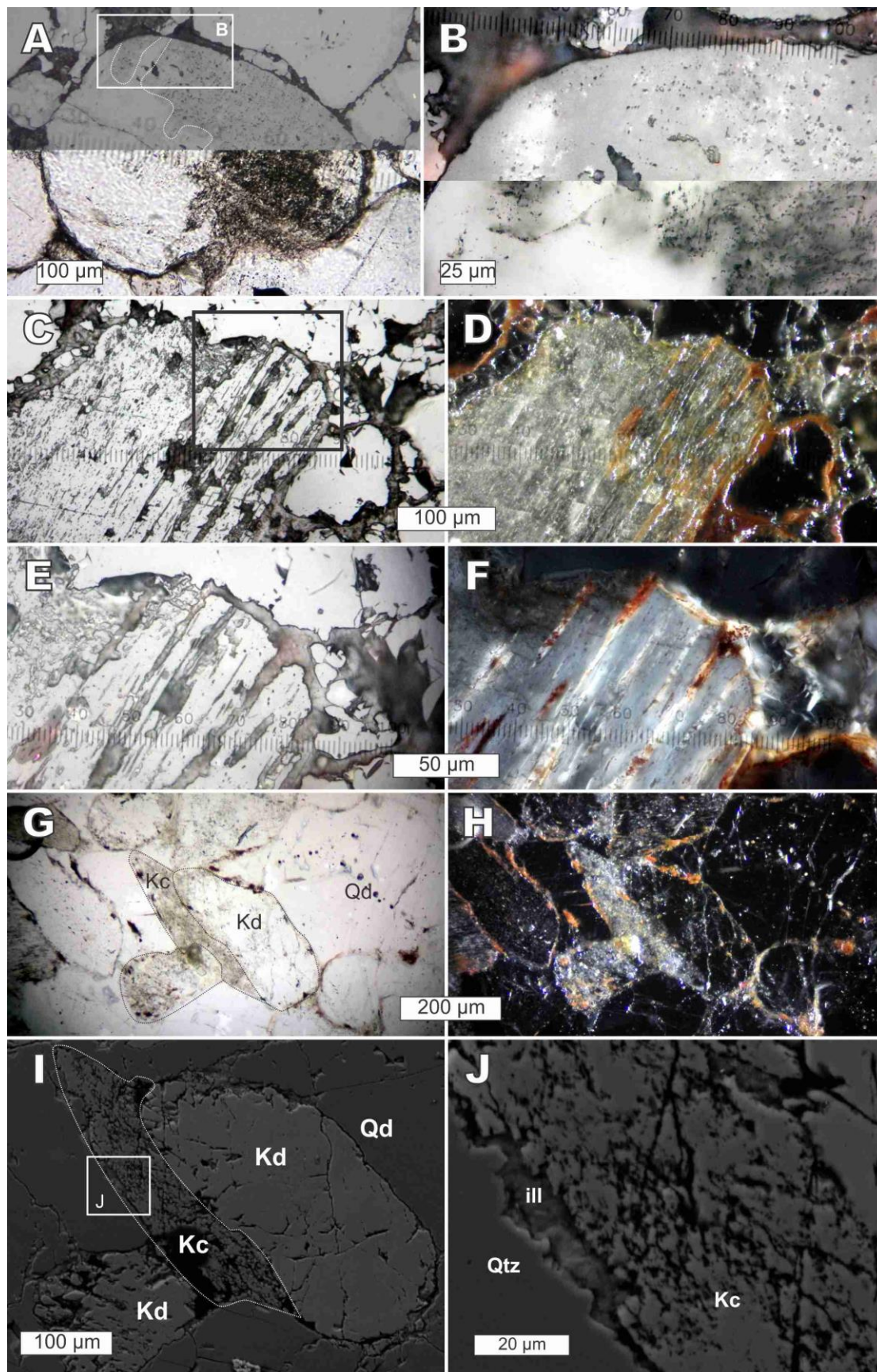


Figure 4-9: K-feldspar diagenetic features

Diagenetic features that are present in detrital K-feldspar. (A) Combined plane-polarised transmitted-light and reflected-light image of cloudy detrital grains as the result of pits (sample D7). (B) Close-up of area in A. (C) Reflected and (D) oblique reflected-light images of corrosion pits possibly related to twinning are filled with clay (illite) and hematite. (E and F) Detailed images of area in C shows illite and hematite fill pits and intrapore space. (reflected light in E, cross-polarised transmitted-light in F). (G) Plane-polarised transmitted-light, (H) oblique reflected-light, and (I) back-scatter electron images of authigenic K-feldspar cement (Kc) on detrital K-feldspar grains (Kd) shows an enhanced cloudy appearance than the detrital grain. (J) Detailed back-scattered electron image of area in (I) shows illite occupying the pores of the altered K-feldspar (sample D13).

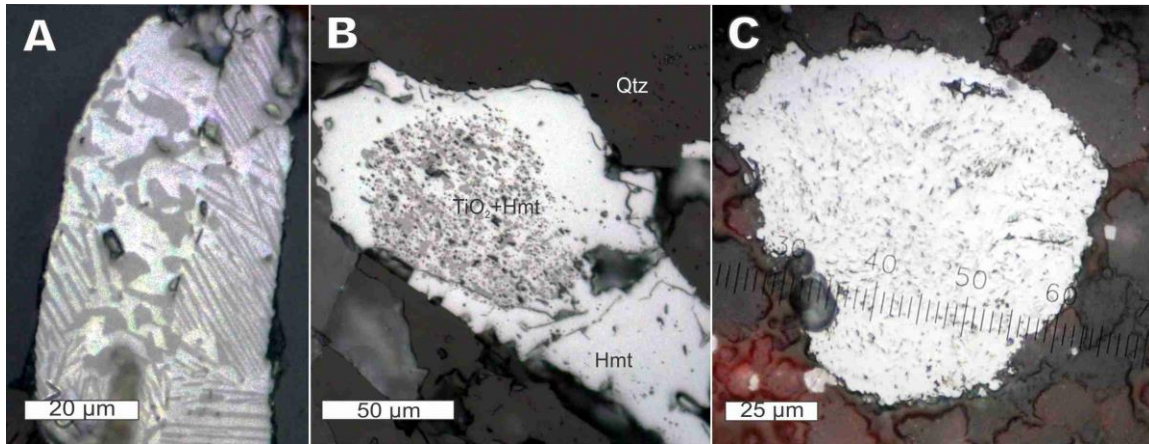


Figure 4-10: Aston Formation opaque grains

Typical opaque Ti-Fe-oxide detrital grains in reflected-light. (A) Exsolution texture of hematite (bright) and TiO_2 (rutile; dark) (sample D12). (B) Mixed hematite-rutile cores surrounded by rinds of homogeneous hematite (sample D11). (C) Hematite grains with porous texture in unbleached samples (sample D8).

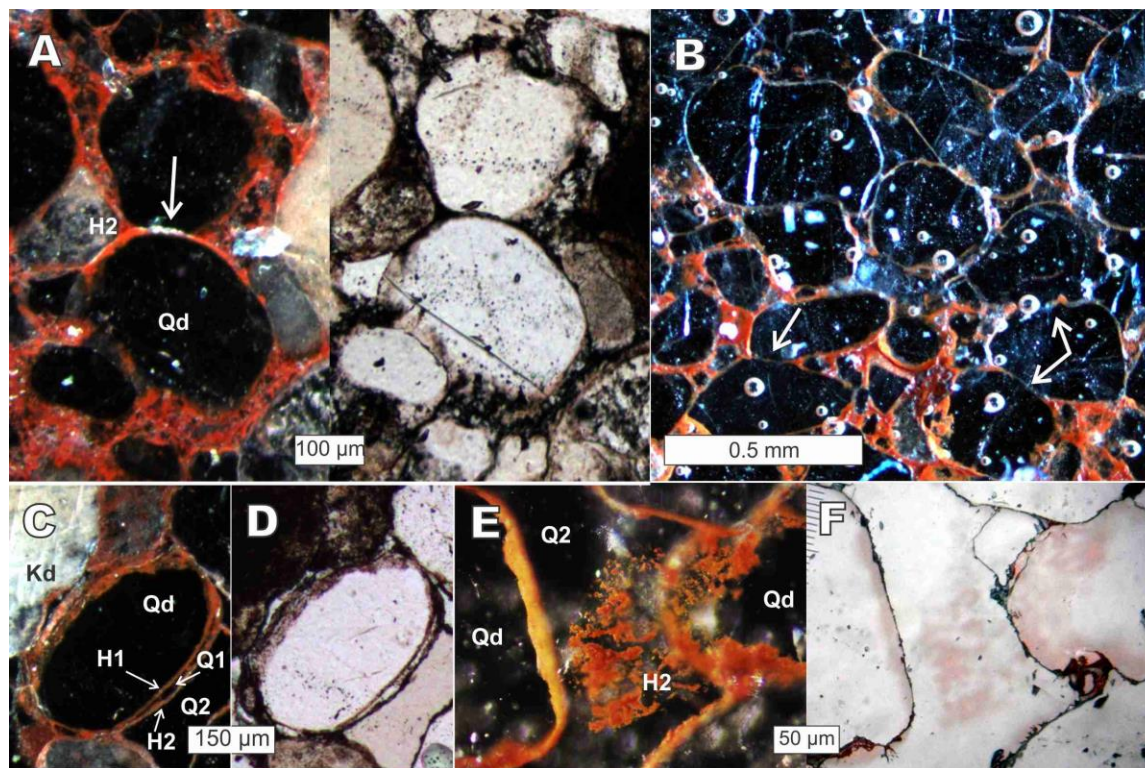


Figure 4-11: Aston Formation hematite cement

Typical features of hematite coatings on Aston Formation sandstone. (A) Oblique reflected-light and plane-polarised transmitted-light images shows hematite 2 (H2) is around, and thus post-dates, pressure-solved detrital quartz grains (Qd). The absence of H2 at the grain contact is highlighted by oblique reflected-light (sample D8). (B) Hematite 2 in red samples is abundant between grains mixed with illite and absent at most long, concavo-convex contacts (arrows) (sample D2). (C) Oblique reflected and plane-polarised transmitted-light images shows early hematite 1 (H1) grain coatings are overgrown by quartz overgrowths (Q1), which is then coated by a late hematite (H2) and pore-occluding quartz cement (Q2) (sample D12). (D) Oblique reflected light image shows ‘colloidal’ texture of H2 that is incorporated in Q2 cement (sample D7). (E) Reflected-light image of (D) that shows H2 is incorporated in Q2, rather than as a clast surrounded by Q2.

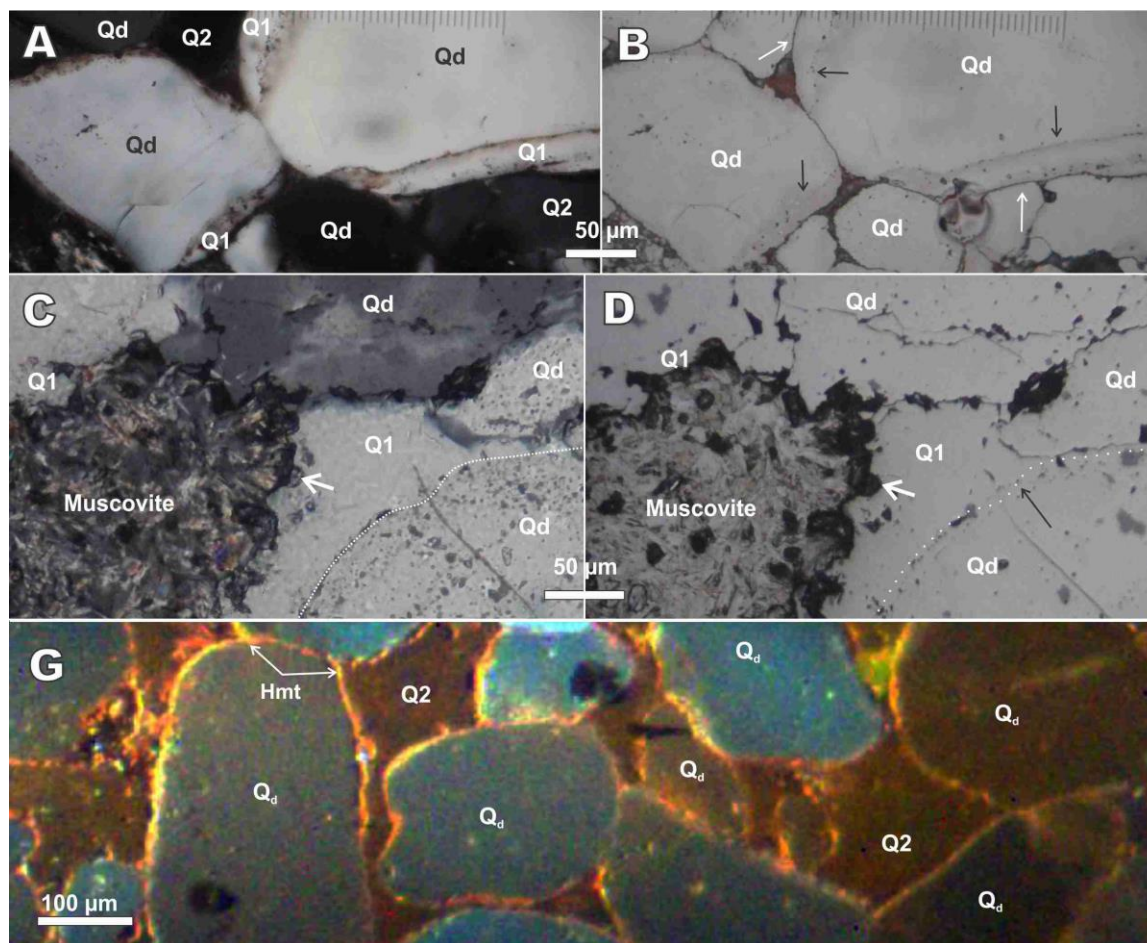


Figure 4-12: Aston Formation quartz cement

Typical features of quartz cement in Aston Formation sandstone. (A) Cross-polarised transmitted light and (B) reflected light images showing quartz overgrowth (Q1) pinches out at pressure solution grain contacts. Quartz overgrowth have a continuous grain-to-cement surface (black arrows), whereas late quartz cement (Q2) is separated from grains (and previous cements) by a thin gap ($<2 \mu\text{m}$; white arrows). (C) Cross-polarised transmitted light and (D) reflected light images showing Q1, with continuous surface to detrital grain (black arrow), and illite (muscovite)-filled pores with corroded edges (white arrows) (sample D10). (G) Cathodoluminescence image shows Q2 is homogeneously non-luminescent (sample D7).

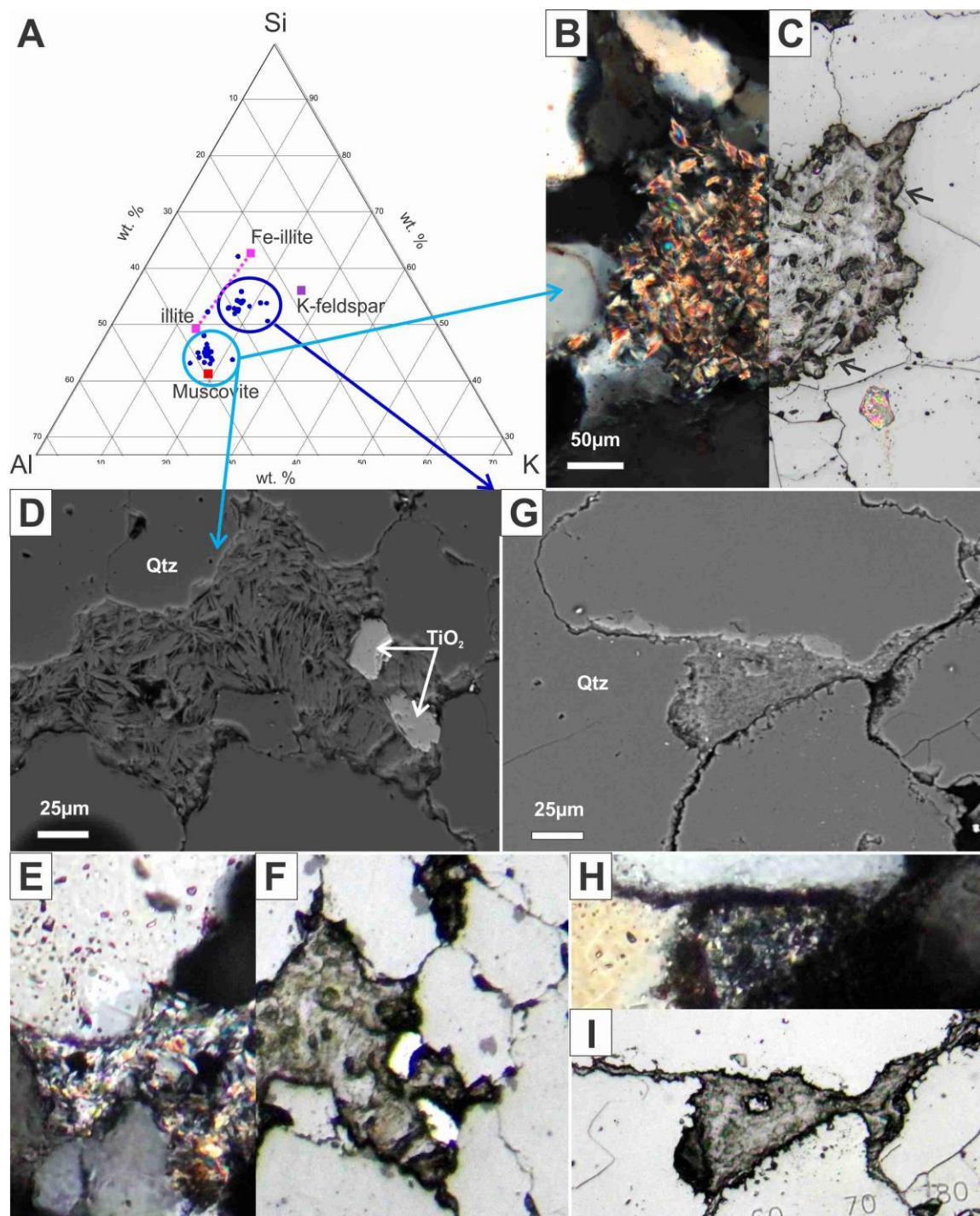


Figure 4-13: Aston Formation phyllosilicates

Two types of pore-filling phyllosilicate display two crystal sizes and chemical compositions. (A) Normalised K-Al-Si ternary diagram (in wt. %) of SEM-EDS analyses showing two compositions (blue circles) plotting along a muscovite-(Fe-Mg-free)illite trend or a muscovite-

(Fe-Mg-bearing)illite trend. (B) Cross-polarised transmitted-light and (C) reflected-light composite-image and (D) back-scattered electron image of comparatively large euhedral illite in sand-sized irregular pores with corroded edge contacts (arrows in C) on adjacent quartz grains (Qtz) (sample D10). (E) Cross-polarised and (F) plane-polarised transmitted-light images of (D) shows adjacent material is detrital quartz grains. (G) Back-scattered electron image showing comparatively small illite crystals along and between grains (sample D12). (H) Reflected-light and (I) cross-polarised transmitted-light images of dissolved detrital grains is replaced by illite (sample D16).

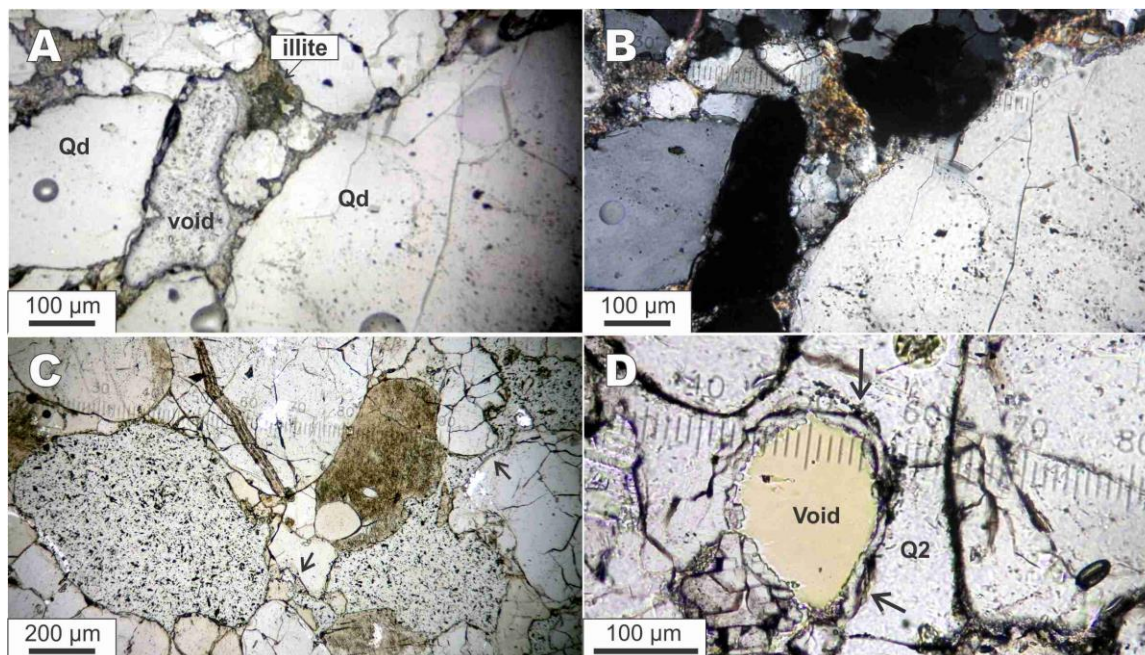


Figure 4-14: Aston Formation void characteristics

Secondary porosity in Aston Formation. (A) Plane-polarised and (B) cross-polarised transmitted-light images of irregular over-sized, undeformed pores that are surrounded by detrital grains and illite. (C) Cross-polarised transmitted-light and (D) reflected-light images shows irregular-shaped oversized pores filled with illite. (E) Plane-polarised transmitted-light image of connected oversized pores, suggesting dissolution rather than plucking. (F) Plane-polarised transmitted-light image of smooth pores in Q2 cement with concentric fractures around pore margin suggest plucking during sample preparation.

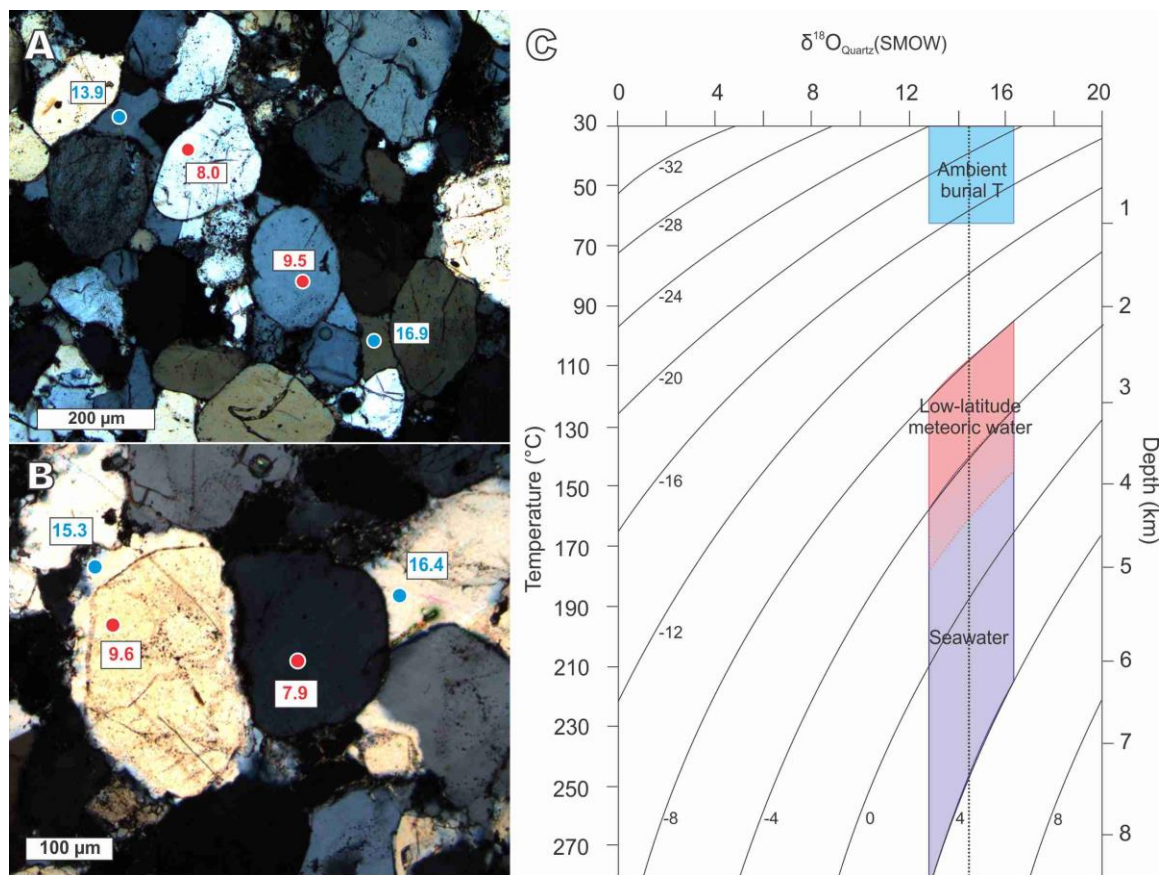


Figure 4-15: Aston Formation quartz SIMS oxygen isotope values

(A and B) Cross-polarised transmitted-light photo micrographs of Aston Formation sandstone showing detrital quartz grains and quartz cement, with locations of SIMS analyses and their respective oxygen isotope values (V-SMOW) (sample D3 and D14 for A and B, respectively). (C) Measured $\delta^{18}\text{O}$ values of quartz cement vs. temperature ($^{\circ}\text{C}$) and depth (using a surface temperature of 30°C and geothermal gradient of $30^{\circ}\text{C}/\text{km}$) with isopleths of equilibrium $\delta^{18}\text{O}_{\text{H}_2\text{O}}$ values calculated using the quartz-water fractionation equation of Sharp and Kirschner (1994). Vertical dashed line represents the average $\delta^{18}\text{O}$ value of quartz cement (14.4‰). Shaded areas represent reasonable fluid-source compositions of seawater (-4 to +4‰), low- to mid-latitude meteoric water (-2 to -8‰), and a fluid in equilibrium with a quartz sandstone at a temperature related to burial depths <1 km.

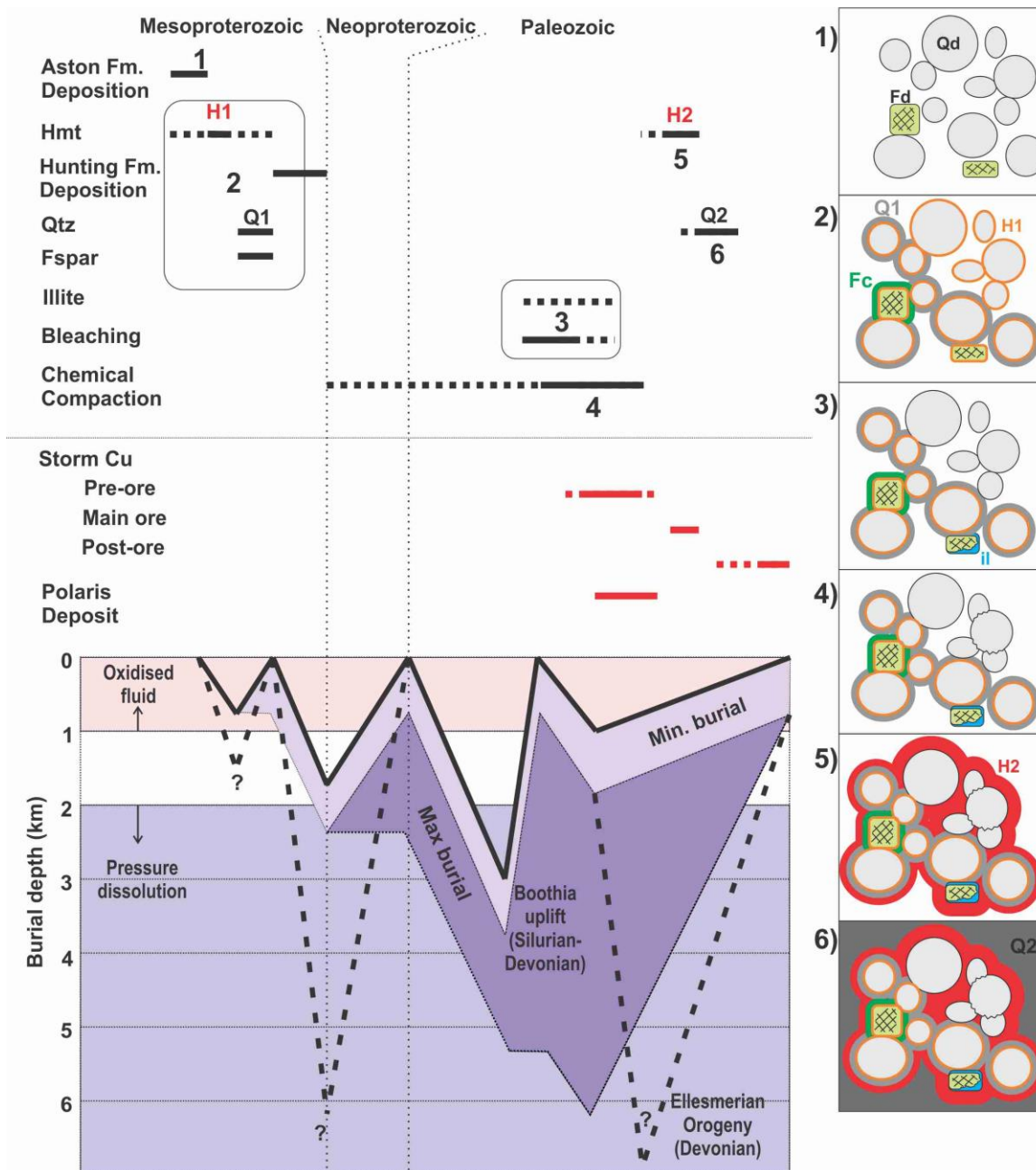


Figure 4-16: Paragenesis of Aston Formation

Proposed (A) paragenetic sequence and (B) burial history of the Aston Formation, highlighting Paleozoic diagenetic processes that coincide with paragenetic sequence previously documented at Storm copper (Mathieu et al., 2018). Polaris paragenesis based on Reid et al. (2013a). Minimum burial depths are provided by the maximum preserved thickness of strata between major unconformities (Fig. 4; Aston Formation = 800 m; Hunting Formation = 1.3 km; Paleozoic

strata = 3.9 km). Maximum burial depth is assumed as the maximum preserved thickness of strata with minimal removal (i.e., almost no removal) at major unconformities. (C) Simplified burial events experienced by Aston Formation: from (1) deposition (Proterozoic), (2) reddening 1 (Proterozoic), (3) bleaching and illitisation (Paleozoic), (4) pressure solution (Paleozoic), (5) reddening 2 (Paleozoic), and (6) quartz cementation (Paleozoic).

Table 4-1: Sample list with associated locations (shown on Figure 6) and colour.

| Sample | Northing | Easting | Colour |
|----------|----------|---------|----------|
| 16HR D1 | 442884 | 8164479 | Red |
| 16HR D2 | 442442 | 8164856 | Red |
| 16HR D3 | 442263 | 8165048 | Bleached |
| 16HR D4 | 441836 | 8165432 | Bleached |
| 16HR D5 | 441587 | 8165622 | Red |
| 16HR D6 | 441556 | 8165896 | Red |
| 16HR D7 | 441388 | 8166051 | Red |
| 16HR D8 | 441301 | 8166179 | Red |
| 16HR D10 | 441429 | 8166375 | Bleached |
| 16HR D11 | 441311 | 8166449 | Bleached |
| 16HR D12 | 441138 | 8167149 | Red |
| 16HR D13 | 441011 | 8167421 | Bleached |
| 16HR D14 | 441023 | 8167707 | Bleached |
| 16HR D15 | 441002 | 8168014 | Bleached |
| 16HR D16 | 441076 | 8168094 | Bleached |

Chapter 5

5 Concluding Statements

5.1 Conclusions

This thesis provides the first complete study of the fluids responsible for mineralisation in the Cornwallis district, including the first detailed study on the Storm copper deposit. During this study, the following questions have been answered:

- *What was the mineralising fluid(s) composition within the Cornwallis Zn-Pb district and what was the mechanism for sulphide precipitation?*

Mineralisation throughout the Cornwallis district was controlled by a uniform, regional, low-temperature, high-salinity, seawater-sourced fluid that dissolved evaporites in the subsurface and leached metals from the sedimentary succession to transport metals and sulphate together. This regional fluid interacted with accumulations of reduced sulphur at the site of mineralisation to precipitate sulphide minerals. Thermochemical sulphate reduction (TSR) of the regional fluid became the dominant source of reduced sulphur for precipitation, if there was a sufficient source of pre-existing reduced sulphur to initiate mineralisation, lowering kinetic controls of TSR processes and if there were sufficient reductants on site to allow for TSR. Varying degrees of TSR of the regional fluid affected the sulphur isotopic composition. The main control on the size (volume) of mineralisation in the Cornwallis district is the amount of fluid flow that could be accommodated by a site, and the ability to reduce sulphate at a sufficient rate.

- *What was the composition of the fluid(s) of the Storm copper deposit in the district and how does it relate to the regional fluid?*

Storm copper mineralisation records three episodes of fluid movement: early pre-ore, main-ore, and post-ore mineralisation. Fluids evolved from a reduced, basement-equilibrated fluid that mixed with a reduced sulphur fluid (pre-ore) to an oxidised low-latitude meteoric fluid (main-ore) to a high-latitude meteoric fluid responsible for post-ore mineralisation. Main-ore sulphur was supplied by a mixture of recycled sulphur and in situ reduction of sulphate. Pre-ore fluids are probably related to the main mineralising regional fluid, with the main-ore fluid being related to the regional fluid that post-dated Zn+Pb mineralisation in the district, with the Cu modifications supplied by local geology.

- *What was the source of copper for the Storm copper deposit?*

Geochemical evidence from Cu mineralisation at Storm copper (Chapter 3) suggest the Aston Formation red bed as a probable source of copper. Chapter 4 concludes that fluids with comparable composition and paragenetic order to those responsible for Storm copper mineralisation circulated through the Aston Formation red beds, resulting in its observed diagenetic features. These observations suggest that the Aston Formation was a probable Cu source for Storm copper mineralisation.

- *What are the implications of ore district controls and intra-district relationships?*

Topographically driven fluid flow is the most probable mechanism for allowing a regional fluid to pervade an entire basin with geochemically consistent characteristics and a uniform paragenetic change related to a meteoric recharge fluid. Mineralised showings in an ore district that was controlled by a regional fluid should therefore have shared characteristics, making them genetically linked, as has been assumed. It is possible that the concept of pre-existing sulphide

accumulations can be used to explain other ore districts worldwide that experienced a regional metal-bearing fluid.

5.2 Future work

In Chapter 2, purple sphalerite was common as the regionally consistent main sphalerite. It was observed that there was an apparent positive relationship between Cd concentration and the purple colour. The presence of purple sphalerite may be more common than originally thought, being observed in the Cornwallis district (Randell, 1994; this study), Australian Canning basin (Etminan and Hoffmann, 1989), the Chinese Fule Pb-Zn deposit (Si et al., 2011), Pb-Zn deposits in the midcontinent U.S. (Field et al., 2020), and the Congolese Kipushi deposit (personal observation). A more detailed study to determine the cause (crystallographic or geochemical) of this type of sphalerite is merited, because it may be used as an indicator to mineralisation processes.

Chapter 3 concludes with the Storm copper mineralisation fluid being related to regional Zn-Pb mineralizing fluid of the district; study of other Cu showings in the district may be merited to compare with the Storm copper deposit to elucidate the controlling factors of Cu mineralisation over Zn-Pb mineralisation. Copper showings in other Zn+Pb districts should be geochemically studied to identify any possible trends that may separate them from Cu-dominant districts/deposits.

Chapter 4 required some inference on the burial history of the Aston Formation; a petrographic study of the Siluro-Devonian Peel Sound Formation sandstone, which was derived from reworked Aston Formation (Miall, 1970; Miall and Gibling, 1978), could help identify which

paragenetic stages were present in the Aston sandstone at the time of Peel Sound Formation deposition.

The diagenetic study of possible ore-deposit source rocks is mainly limited to uranium deposits (e.g., Hiatt et al., 2003; 2007; Kyser, 2007; Beyer et al., 2011). Studies of possible source rocks for metals in other base-metal deposits, particularly redbed copper deposits, could be beneficial for producing new exploration criteria.

5.3 References

Beyer, S.R., Hiatt, E.E., Kyser, K., Drever, G.L., Marlatt, J., 2015. Stratigraphy, diagenesis and geological evolution of the Paleoproterozoic Roraima Basin, Guyana: Links to tectonic events on the Amazon Craton and assessment for the uranium mineralization potential. *Precambrian Research*, **267**, 227-249.

Etminan, H., Hofmann, C.F., 1989. Biomarkers in fluid inclusions: A new tool in constraining source regimes and its implications for the genesis of Mississippi Valley-type deposits. *Geology*, **17**, 19-22.

Field, J. D., Appold, M. S., Coveney, R. M., and Bodnar, R. J., 2020. Geochemical characteristics of trace occurrences of Mississippi Valley-type mineralization in the U.S. mid-continent: Implications for deposit growth: *Journal of Geochemical Exploration*, v. 213, 18p.

Hiatt, E.E., Kyser, T.K., Dalrymple, R.W., 2003. Relationships among sedimentology, stratigraphy and diagenesis in the Proterozoic Thelon Basin, Nunavut, Canada:

implications for paleoaquifers and sedimentary-hosted mineral deposits. *The Journal of Geochemical Exploration*, **80**, 221-240.

Hiatt, E.E., Kyser, T.K., Fayek, M., Polito, P., Holk, G.J., Riciputi, L.R., 2007. Early quartz cements and evolution of paleohydraulic properties of basal sandstones in three Paleoproterozoic continental basins: Evidence from in situ $\delta^{18}\text{O}$ analysis of quartz cements. *Chemical Geology*, **238**, 19-37.

Kyser, K., 2007. Fluids, basin analysis, and mineral deposits. *Geofluids*, **7**, 238-257.

Miall, A.D., 1970. Devonian alluvial fans, Prince of Wales Island, Arctic Canada. *Journal of Sedimentary Petrology*, **40**, 556-571.

Miall, A.D., Gibling, M.R., 1978. The Siluro-Devonian clastic wedge of Somerset Island, Arctic Canada, and some regional paleogeographic implications. *Sedimentary Geology*, **21**, 85-127.

Randell, R. N., 1994, Geology of the Polaris Zn-Pb Mississippi Valley-type deposit, Canadian Arctic Archipelago. Unpublished Ph.D. thesis, University of Toronto, Toronto, Ontario, 819 p.

Si, R., Gu, X., Xiao, C., Yu, H., Wang, Z., Chen, Y.-J., and Qiu, N., 2011. Geochemical character of trace elements in sphalerite from Fule Pb-Zn Deposit, Yunnan Province: *Journal of Mineralogy and Petrology*, v. 31, p. 34–40.